Numerieke analyse van het post-breukgedrag van gelamineerd glas onder impact en schokbelasting

Numerical Analysis of the Post-Fracture Response of Laminated Glass under Impact and Blast Loading

Joren Pelfrene

Promotor: prof. dr. ir. W. Van Paepegem
Proefschrift ingediend tot het behalen van de graad van
Doctor in de ingenieurswetenschappen: werktuigkunde-elektrotechniek

Vakgroep Toegepaste Materiaalwetenschappen
Voorzitter: prof. dr. ir. J. Degrieck
Faculteit Ingenieurswetenschappen en Architectuur
Academiejaar 2015 - 2016

UNIVERSITEIT GENT

ISBN 978-90-8578-927-7
NUR 929
Wettelijk depot: D/2016/10.500/59

Promotor

prof. dr. ir. W. Van Paepegem

Ghent University
Faculty of Engineering
Department of Materials Science and Technology

Examination Committee

prof. L. Taerwe (Chair)	Ghent University, Belgium
prof. W. Van Paepegem	Ghent University, Belgium
prof. J. Belis	Ghent University, Belgium
prof. W. De Corte	Ghent University, Belgium
dr. F. Gilabert-Villegas	Ghent University, Belgium
prof. J. Schneider	Technische Universität Darmstadt, Germany
prof. J.H. Nielsen	Denmark Technical University, Denmark
dr. P. D'haene	Eastman Chemical, Belgium

Research Institute

Ghent University
Department of Materials Science and Technology
Mechanics of Materials and Structures
Technologiepark 903
B-9052 Zwijnaarde
Belgium

Tel. +32 9 331 04 44
Joren.Pelfrene@UGent.be
Joren.Pelfrene@Posteo.be

This research is funded by the UGent BOF (Bijzonder Onderzoeksfonds) under grant number B/12091/01.

Acknowledgements

I am most gratefully indebted to my promotor, prof. Wim Van Paepegem, who favoured me with his continued support and trust. More than this, his enthusiasm led me to discover the joy and creativity in scientific research and numerical techniques. Together with my colleague Sam Van Dam, a pleasant collaboration existed on our spree of destruction to crack the mysteries of laminated glass. I owe much gratitude to Sam for his help over the years and wish him the best of luck in continuing our research work, as well as in his alternate identity as the Seam Doctor.

I also wish to thank prof. Joris Degrieck, who first sparked my interest in composite materials technology and welcomed me with every further step.

The support of our industrial partners Eastman Chemical and AGC Europe is gratefully acknowledged. For myself, in particular the discussions with dr. Pol D'haene have been invaluable. Also the opportunity to take part in the COST Action TU0905, under the gentle guidance of prof. Jan Belis, has opened the doorway to connect and interact with many experts in the field. Over the years, many have become good friends, most notably dr. Gergely Molnár and prof. Bojana Trajanoska who enjoyed cracking their heads over numerical problems as well and made part of the lively TG7, led by prof. Jens Nielsen. I am especially grateful to prof. Jens Schneider, who hosted me at his institute in Darmstadt to work with dr. Johannes 'Joschi' Kuntsche. Ever since, Joschi functioned as an office mate by proxy and has been a true pleasure to share ideas (and beers) with.

Thanks are also due to our colleagues at the Belgian RMA, prof. John Vantomme, dr. David Lecompte and Abderraouf Louar, for their input and feedback.

Furthermore, I wish to thank everyone at our department in Tech Lane Ghent Science Park. Owing to the cheerful presence of all colleagues I am still in doubt whether the past years were spent working hard or hardly working. A few people should be mentioned in particular: Sridhar, who supervised my

Master's thesis and continued to be a mentor afterwards; Geert, for encouraging free improvisation skills in teaching; Fran and David, for providing a solution when computers don't accept swearwords; Dung, for being a great friend and showing that one key trick in Fortran; Frederik and Mathijs, for having their door (banged) open countless times; Gabriele, for hospitality with french fries pizza; Siebe, for finally succeeding to build a composite skateboard; Ali, for nightly setar sessions; Ives, for kindheartedness and scuba stories, and Mathias, for frisbee practice and conversation about frisbee practice. I am also very grateful to our technical staff Luc, Pascal and Roger, and secretaries Ilse, Line and Martine who have provided a professional and enjoyable environment to work in. During the years as a PhD student, I have been lucky to receive the help of several thesis students; thank you, Suat, Roel, Glenn, Colin, Bert, Stef, Magali and Renaat.
More aubades are aimed for the ghosts Sjarlot, Motaar, Diri, Coupé and Lynn, irmãos Timon and Pol, 'cesco, 'cesca, the alien Diana, and Mondi jr.
Finally, I thank my mother and father for all their encouragement and support over the years, and for sustaining my diverse interests with their own.

Joren Pelfrene,
September 2016

Summary

Brittle by nature, glass windows are among the most vulnerable components of buildings and vehicles, and the projection of sharp glass debris is responsible for the majority of injuries in the event of a crash or explosion. Safety may be provided by laminating the glass with a transparent polymer interlayer to retain the glass shards upon fracture. In the post-crack phase, the broken laminate absorbs energy from the impact or blast by further deformation, until finally, the interlayer is torn and the panel fails. The most commonly used interlayer material is polyvinyl-butyral (PVB), which is capable of large deformation without tearing. PVB material can be produced with different elastic and adhesive properties, for which a working combination for safety performance can be found. A very soft interlayer may be torn too easily, while glazing with a very stiff interlayer may get blown away entirely by a blast wave. The adhesion between glass and PVB should be strong to withhold glass fragments, but allowing for some delamination reduces the strain in PVB ligaments that bridge the cracks and can, consequently, avoid failure of the panel by tearing. In the glass industry, the use of the PVB product is mostly based on experience. Neither the highly nonlinear viscoelastic mechanical behaviour of PVB interlayer, nor the adhesive strength and debonding energy are sufficiently known by the industry or described in scientific literature.

The performance of laminated glass in response to impact or blast loads can only really be evaluated by expensive experimental testing, which is also required for the qualification to international standards. Not only the elastic response up to fracture should be evaluated, but also the ensuing behaviour. If a numerical simulation method would allow to reliably assess the post-fracture response of the glazing, this could mean a great improvement for the cost-effectiveness and speed by which safe design of glazing can be achieved. Therefore, this work aims to investigate the numerical approaches that can be used to simulate the response of laminated glazing to impact or blast loading, also after the glass has fractured. First, the material constituents and adhesive properties of laminated glass are characterised for use in finite element modelling. Subsequently, various cases of impact and blast are simulated and compared with experimental test data for validation.

Several numerical approaches are investigated for the simulation of fracture and fragmentation of annealed float glass panels under dynamic loading. The most encountered method for this purpose is the rather crude element deletion technique, by which an element is removed from the mesh as it reaches the failure criterion, described in a damage model. A study is performed for different formulations of the damage model, which allows to identify several issues of incorrectness and numerical instability that can be experienced when modelling a very brittle material such as glass. This leads to the development of the *crack delay model*, which is able to avoid many of these problems. The proposed model is based on the concept of delay damage, which states that crack separation does not take place instantaneously, but is bounded by a maximum damage rate. The damage behaviour in the crack delay model is defined by three physical properties of brittle materials: critical stress, fracture energy and maximum crack propagation velocity. Even though numerical simulation with this method allows to capture the cracking behaviour of glass plates reasonably well in comparison with experimental data, the element deletion technique remains highly mesh sensitive, removes material from the analysis and leaves gaps the width of an element.
Therefore, two alternative methods are evaluated: smoothed particle hydrodynamics (SPH), as a meshfree particle method, and the use of cohesive zone elements at all interelement boundaries for the glass. However, the SPH method cannot be applied to model the fracture of glass under low velocity impact, because particles on either side of a crack remain in each other's influence domain. Consequently, no fragmentation takes place. Also the intrinsic cohesive zone approach is not suited, even when artificial compliance can be avoided by assigning a smalll thickness to the interface elements. In that case, a multitude of cracks are formed simultaneously, instantly reducing the flexural stiffness of the plate and thus impeding further crack propagation.

The PVB interlayer for laminated glass displays highly nonlinear visoelastic material behaviour with high sensitivity to the deformation rate and temperature. Moreover, PVB can be extended to very high elongations of over 250% of its original length. A number of uniaxial tensile tests are performed at different speeds to characterise the mechanical behaviour for strain rates between $10^{-3}\,\mathrm{s}^{-1}$ and $100\,\mathrm{s}^{-1}$. Subsequently, a numerical method is developed to calibrate a material model for the PVB by simulation of the uniaxial tests at the different testing speeds. The constitutive model uses a combination of viscoelasticity defined by a Prony series representation and a hyperelastic strain energy potential which defines the instantaneous material behaviour.

Adhesive debonding at the glass-PVB interface can be characterised by several experimental methods. However, these tests do not allow to measure the adhesive properties directly, except for pull-off tests for the fracture strength. By numerical simulation of steady state delamination in the 90° peel test and the

through-cracked tensile (TCT) test, also the fracture energy at the interface can be determined. The analyses show that very few simplifications can be allowed in the numerical models, especially for the material behaviour of the PVB interlayer.

With the developed material models, the response of laminated glazing to transient loading can be simulated. A standardised test case to assess human body impact is described by EN 12600. In this test, a 50 kg pendulum impactor, consisting of a deadweight surrounded by two tyres, is dropped onto a large glass panel in a rigid frame. In literature, several numerical approaches to the simulation of this test can be found. However, the representation of the impactor in these models is calibrated to match test results, rather than reflecting the physical nature, which may cast doubt over their general applicability. Therefore, a detailed model of the impactor is conceived, which could be validated for quasi-static compression, impacts at different drop heights against a force and pressure plate setup, and against a thick, monolithic glass panel. The numerical results for impact against laminated glazing without considering fracture are in fairly good agreement with the highly efficient calculation method for this test in SJ MEPLA software.

For the simulation of laminated glass fracture with the crack delay model, larger panels can be discretised in different ways. Comparison with drop weight tests shows that a configuration with continuum shell elements for the glass and solid elements for the interlayer performs best at capturing the elastic response, breakage and post-fracture response for cases with single-sided and two-sided fracture. However, the element deletion method allows only comparison of the global response, with test data for the force and deformation, and qualitative comparison of the crack pattern. Because of the inherent dependency of the mesh and element size, local behaviour in the laminated glass plate cannot be simulated accurately. Nonetheless, the simulated strains in PVB ligaments between the glass cracks do reach a very high level for those cases where the interlayer was torn in the experiments. If the reliability of the high strain prediction for such cases could be further confirmed, this might eventually allow for the evaluation of ultimate failure by tearing. Delamination at the interfaces has been included in the simulation of shocktube blast tests where test specimens with a lower adhesion grade showed to be less prone to tearing. In the simulation, however, delamination takes place to a rather high extent, which is likely due to the element size and does not seem realistic.

Samenvatting

Door de natuurlijke brosheid van glas behoort de beglazing tot de meest kwetsbare onderdelen in gebouwen en voertuigen, en het rondvliegen van scherpe glasscherven is verantwoordelijk voor de meeste verwondingen in een crash of explosie. Lamineren van glas met een transparante, polymeer tussenlaag kan de veiligheid verzekeren door de scherven tegen te houden bij breuk. Na breuk vangt het laminaat energie van de impact of schok op door verdere vervorming tot de tussenlaag uiteindelijk scheurt en het paneel faalt. Het meest gebruikelijke materiaal voor de tussenlaag is polyvinyl-butyral (PVB), dat in staat is sterk te vervormen vooraleer te scheuren. PVB kan geproduceerd worden met verschillende elastische en adhesieve eigenschappen. De veiligheid die na glasbreuk nog bereikt kan worden hangt grotendeels af van de combinatie hiervan. Immers, een slappe tussenlaag kan te makkelijk scheuren, terwijl een zeer stijve tussenlaag eerder tot gevolg heeft dat het gehele paneel van zijn bevestiging losgetrokken wordt. De adhesie tussen glas en PVB dient sterk genoeg te zijn om delaminatie van glasscherven tegen te houden, maar het toelaten van enige delaminatie is eveneens voordelig; hierdoor blijft de rek in het PVB-materiaal tussen de glasbreuken kleiner, hetgeen falen van het paneel door scheuren kan vermijden. In de glasindustrie is de samenstelling en het gebruik van PVB vooral gebaseerd op ervaring. Noch het sterk niet-lineair viscoelastische materiaalgedrag, noch de adhesiesterkte en delaminatie-energie zijn voldoende gekend in de industrie of beschreven in wetenschappelijke literatuur.

De prestatie van gelamineerd glas onder impact of explosiebelasting kan tot op heden enkel echt geëvalueerd worden m.b.v. dure experimentele testen, hetgeen ook vereist is voor kwalificatie naar internationale normen. Niet enkel de elastische respons tot op glasbreuk moet hierin beoordeeld worden, maar ook het daaropvolgende gedrag. Indien een numerieke simulatiemethode zou toelaten het post-breuk gedrag op een betrouwbare manier te voorspellen, kan dit een grote stap betekenen voor de kost-effectiviteit en snelheid waarmee een veilig ontwerp van de beglazing gemaakt kan worden. Om die reden beoogt dit werk de numerieke benaderingen te onderzoeken die toegepast kunnen worden voor het simuleren van de respons van gelamineerd glas op impact en schokbelasting, ook in de fase nadat het glas gebroken is. Eerst worden de materiaallagen en adhesie-eigenschappen van gelamineerd glas gekarakteriseerd voor

gebruik in eindige elementen analyse. Vervolgens worden verscheidene gevallen van impact en explosie gesimuleerd en vergeleken met experimentele test data voor validatie.

Verscheidene numerieke methoden zijn onderzocht voor het simuleren van breuk en fragmentatie van floatglas panelen onder dynamische belasting. De meest gebruikelijke methode hiervoor is de eerder rudimentaire element-erosie techniek, waarbij een element verwijderd wordt uit de mesh wanneer een criterium tot falen bereikt is, zoals beschreven wordt in een schademodel. Verschillende formuleringen voor het schademodel zijn bestudeerd, wat toelaat diverse incorrectheden en numerieke stabiliteitsproblemen te identificeren, die kunnen optreden bij het modelleren van bijzonder brosse materialen zoals glas. Dit gaf aanleiding tot het ontwikkelen van het 'crack delay' model, waarmee vele van deze problemen vermeden worden. Het voorgestelde breukmodel is gebaseerd op het feit dat het breukoppervlak niet ogenblikkelijk gescheiden wordt, maar dat er een maximale schadesnelheid bestaat. Het schadegedrag in het 'crack delay' model is gedefiniëerd door drie fysische eigenschappen van brosse materialen, nl. de breuksterkte, de breukenergie en de maximale breuksnelheid. Hoewel numerieke simulatie met deze methode toelaat het breukgedrag van glasplaten redelijk goed te vatten in vergelijking met experimentele data blijft de element-erosie techniek sterk meshafhankelijk, wordt materiaal verwijderd uit de berekening en ontstaan er gaten in de mesh met de breedte van één element
Daarom worden twee alternatieve methodes geëvalueerd: de mesh-vrije partikel methode SPH en het gebruik van cohesieve elementen tussen alle glaselementen in. Echter, de SPH methode kan niet toegepast worden om glasbreuk onder impact met lage snelheid te modelleren, omdat de partikels aan elke zijde van een breuk in elkaars invloedsdomein blijven. Hierdoor vertoont de plaat een verminderde stijfheid en treedt geen fragmentatie op. Ook de benadering met intrinsieke cohesieve zones is niet geschikt, zelfs wanneer artificiële stijfheid vermeden kan worden door een kleine dikte aan de cohesieve elementen toe te kennen. In dat geval ontstaat een veelheid aan breuken simultaan, wat de buigstijfheid van de plaat ogenblikkelijk reduceert en verdere breukvorming in de weg staat.

De PVB tussenlaag voor gelamineerd glas vertoont zeer sterk niet-lineair viscoelastisch materiaalgedrag met een hoge gevoeligheid aan vervormingssnelheid en temperatuur. Temeer kunnen in het materiaal hoge rekken bereikt worden, tot meer dan 250% van de originele lengte. Ettelijke uniaxiale trektesten zijn uitgevoerd bij verschillende snelheden om het mechanisch gedrag te karakteriseren bij reksnelheden tussen $10^{-3}\,\mathrm{s}^{-1}$ en $100\,\mathrm{s}^{-1}$. Vervolgens is een numerieke methode ontworpen om een materiaalmodel voor PVB af te stemmen door simulatie van de trektesten bij verschillende testsnelheden. Het constitutief model dat hiervoor gebruikt wordt, bestaat uit de combinatie van viscoelasticiteit,

voorgesteld in een Prony-serie formulering, en een hyperelastische potentiaalfunctie die het ogenblikkelijke materiaalgedrag definiëert.

Delaminatie tussen glas en PVB kan gekarakteriseerd worden met verschillende experimentele methodes. Echter, met uitzondering van de adhesie-trektest voor het bepalen van de adhesiesterkte, laten deze methoden niet toe de adhesieve eigenschappen rechtstreeks te meten. M.b.v. numerieke simulatie van steady state delaminatie bij de peel en TCT testen kan ook de breukenergie bepaald worden. De simulaties tonen bovendien aan dat zeer weinig vereenvoudigingen aangenomen kunnen worden bij analyse van deze testen, in het bijzonder voor het materiaalgedrag van de tussenlaag.

Met de ontwikkelde materiaalmodellen kan de response van gelamineerd glas op transiënte belasting gesimuleerd worden. Een gestandaardiseerde test om impact van personen tegen vlakglas te beoordelen is beschreven in de norm EN 12600. Deze test houdt in dat een 50 kg zware slinger, bestaande uit een starre massa omringd door twee banden, gestoten wordt tegen een glaspaneel ingeklemd in een star frame. In de literatuur zijn verschillende numerieke benaderingen beschreven om deze test te simuleren. Het vereenvoudigde model van de impactor in deze werken is steeds zo afgesteld dat het overeenstemt met experimentele resultaten voor ijkingstesten. Dit geeft echter nog geen zekerheid dat zulk model ook algemener toegepast kan worden. Daarom is in dit werk een gedetailleerd model van de impactor opgesteld, waarin de fysische opbouw en eigenschappen van de banden zo nauwkeurig mogelijk nagevolgd zijn. Dit model kon gevalideerd worden voor quasi-statische compressie, impact bij verschillende valhoogte tegen een opstelling met druk- en krachtplaat, en voor impact tegen een dikke, monolithische glasplaat. De numerieke resultaten voor impact tegen gelamineerd glas zonder breuk zijn in goede overeenstemming met de efficiënte rekenmethode in SJ Mepla software.

Voor de simulatie van breuk met het 'crack delay' model kunnen gelamineerde glaspanelen van grotere afmetingen op verschillende manieren gediscretiseerd worden. De vergelijking met impact testen met een valgewicht tonen aan dat een configuratie met solid shell elementen voor het glas en solid elementen voor de tussenlaag het best de elastische respons, breuk en de verdere respons na breuk kunnen vatten voor gevallen met enkelzijdige en dubbelzijdige glasbreuk. Desondanks laat de element-erosie methode enkel vergelijking toe voor de globale respons, d.m.v. test data voor kracht en vervorming, en kwalitatieve vergelijking van het breukpatroon. Omwille van de inherente afhankelijkheid van de mesh en de elementgrootte kan het lokale gedrag in de gelamineerde glasplaat niet nauwkeurig gesimuleerd worden. Niettemin wordt in de numerieke resultaten wel een hoge rek bereikt in PVB-materiaal tussen de glasbreuken, voor die gevallen waarbij de tussenlaag scheuren vertoonde in de overeenkomstige experimenten. Indien de betrouwbaarheid van de voorspelling van zulke hoge rek bevestigd kan worden in verdere studie, zou dit uiteindelijk het nu-

meriek evalueren van falen door scheuren van de tussenlaag kunnen toelaten. Delaminatie kan meegerekend worden in het numeriek model met een cohesieve zone aan de interface tussen glas en PVB. Dit is uitgevoerd voor de simulatie van schokbuistesten waarbij testpanelen met een lagere adhesiegraad merkbaar minder faalden door scheuren. Evenwel vindt in de simulatie in zeer grote mate delaminatie plaats, wat waarschijnlijk te wijten is aan de elementgrootte en niet als realistisch toeschijnt.

Contents

Chapter 1

Introduction

Enkele woorden vooraf:
Autokerkhof, wijsgeer, banaan.

A few words:
Junkyard, sage, banana.

J.A. Deelder, Rotterdam, 2003.

1.1 Background

Brittle by nature, glass windows are among the most vulnerable components of buildings and vehicles, likely to break in the event of a crash or explosion. Although window failure would only in rare cases lead to the collapse of an entire structure, the projection of glass debris and penetration through crack openings are responsible for the majority of minor to moderate injuries, as reported in a.o. Refs. [1–4]. These medical studies from the turn of the century already point to the need for safer design of glazing in architecture, in particular for buildings at higher risk of being bombed (a recent example of the latter in Fig. 1.1). This becomes an even greater concern with the tendency towards ever larger glass surfaces in façades.

Figure 1.1: Shattered windows at Belgium National Airport after the attacks of March, 22nd, 2016. (©belga)

Safety may be provided by combining the glass with a transparent polymer film that adheres to the glass shards upon fracture. In a previous research project at Ghent University, De Pauw has investigated the mechanical behaviour under impact of glazing retrofitted with a thin safety window film [5]. For new constructions, the use of laminated glass is more performant at mitigating the blast load while ensuring the integrity of the broken glass panel in its frame. The analysis of the behaviour of laminated glass under dynamic, transient loading is the subject of the present study. Although the focus is on flat, architectural glazing, the developed methods and results of this work are also relevant for automotive windshield, where the same materials are being employed.

When the glass has fractured, the behaviour of the laminate is dominated by the polymer interlayer, which is most commonly polyvinyl-butyral (PVB). The interlayer material can be produced with different stiffness and adhesion pro-

perties. With a very soft interlayer, the PVB may too easily be torn, while a very stiff interlayer may cause the window to get blown out of its frame altogether. For the adhesion, it is known that ultimate failure by interlayer tearing is delayed when a lower bonding strength is used. But the interlayer should still be able to sufficiently adhere to the glass fragments. Consequently, an optimum may be found, as a combination of interlayer stiffness and adhesion grade. To enable an optimised design for impact and blast safety, the material's response should firstly be well understood for well-defined test conditions. Subsequently, a predictive calculation model may be conceived by thorough verification with the experimental observations.

Various approaches exist to simulate dynamic cracking of brittle materials within the framework of the finite element method, but only few appear capable of capturing the quick fracture with crack branching and intersection for large, thin-walled glass panels. In literature, the rather crude method of element deletion is most often employed, despite the lack of understanding of the implications on the analysis result of the numerical implementation. For the polymer interlayer, no verified material model can be found that describes the highly nonlinear, rate- and temperature-sensitive material at elongations up to tearing. Such material model is also necessary for proper characterisation of delamination behaviour, which has an important role in the ultimate failure of a laminated glass panel.

This thesis covers the conception and evaluation of finite element models to simulate the response up to failure of laminated glazing under impact and blast loading. Extensive experimental data is used for verification of the numerical results. The majority of experiments has been performed by Sam Van Dam [6] during his parallel research work at Ghent University. Well-controlled large-scale shock tube blast tests have been performed by Johannes Kuntsche [7] of Technische Universität Darmstadt, with whom a collaboration existed for the numerical modelling and validation of these tests. Additional support and test specimens have been provided by industrial partners Eastman Chemical Company and AGC Glass Europe.

1.2 Objectives

The main objective of this work is to investigate the possibility to reliably capture the post-fracture response and ultimate failure of laminated glazing under impact and blast loading with the finite element method. This may aid in the prediction of failure and of the loads transferred to the supporting structure. Eventually, this study may help structural engineers to improve the blast-safe design of window glazing.

Different numerical techniques to model the dynamic fracture of glass plates

are to be investigated. Especially the element deletion technique is widely used, but few publications discuss the accuracy and reliability that can be attained with this method. Moreover, different formulations of the damage model for element deletion are available. Understanding of the difference in correctness and numerical stability among these methods is limited. This thesis aims to address this gap by comparing the results of several numerical techniques for brittle fracture with experiments and to determine the best suited modelling approach for the cracking of glass panels.

The PVB interlayer used in safety glass shows highly nonlinear viscoelastic material behaviour, with a great sensitivity to temperature and deformation rate. Although various material models for PVB can be found in literature, few publications discuss the full range of its mechanical behaviour and none are found to describe a material model that is valid in a wide range of deformation rates and up to high elongations. Such material model is necessary for the numerical study of the post-fracture response in a dynamic event and therefore, a verified model for the used PVB interlayer will be developed.

It has already been mentioned that the interfacial adhesion is important in the safe performance of laminated glass under impact or blast loading. In scientific literature, various publications can be found that aim to characterise the debonding between glass and PVB. However, the results of these studies can be very different because of the many simplifications used in their analyses. To address this, the steady state debonding in the 90° peel test and the through-cracked tensile (TCT) test for laminated glass will be numerically modelled with the cohesive zone method. The objective is to closely model both delamination experiments, in order to identify the mixed-mode adhesive properties of laminated glass and the influential parameters in debonding.

The modelling techniques for the cracking and post-fracture response of laminated glass panels are to be studied in comparison with experimental test results for different cases of impact and blast loading. The aim of this study is to gain understanding both of the physical nature of the laminated glass response and of the influential parameters in the numerical analysis thereof. The loading itself should be numerically represented in a verified manner. Especially for the soft-body impact test described by the European standard EN 12600 [8], several numerical models of the impactor are described in literature, include several simplifications and appear to be tuned to fit test data, which may cast doubt over their general applicability.

1.3 Structure of the dissertation

The dissertation can be regarded as consisting of two major parts. In Chapters 2 to 4, the material constituents and adhesive properties of laminated glass

are characterised and material models are developed for further numerical analysis of dynamic, transient behaviour. In Chapters 5 to 7, different dynamic load cases are characterised and the proposed numerical modelling approach is evaluated for its ability to realistically capture the mechanical response of laminated glass up to its ultimate failure.

Chapter 2 discusses the numerical approaches to represent the cracking behaviour of annealed float glass, which is commonly used in construction. First, an overview of the theory and literature on the physical nature of glass strength and fracture is provided. Numerical methods are evaluated for the case of a small, monolithic glass specimen under drop weight impact. It is first ascertained that the elastic response can be captured well by proper definition of the load and boundary conditions. Subsequently, the accuracy and numerical implications of the element deletion technique for dynamic fragmentation are assessed by comparison of several damage models, among which a newly developed *crack delay* model for glass. As possible alternatives to element deletion, the meshfree method of Smoothed Particle Hydrodynamics (SPH) and the cohesive zone method with interface elements are investigated.

Chapter 3 describes the mechanical behaviour of PVB interlayer and the constitutive models by which the polymer can be represented under different load cases. Tensile experiments of Saflex® PVB are presented for a wide range of deformation rates and up to tearing of the specimens. Subsequently, a method to calibrate a hyper-viscoelastic material model for the interlayer by numerically simulating the tensile tests is developed. The resulting material models are valid up to the tearing strain of the interlayer and are accurate within a specified range of deformation rates and temperatures.

In Chapter 4, the characterisation of the adhesive properties at the PVB-glass interface is presented. Several test methods to measure quantities that are characteristic for the debonding of laminated glass are discussed, in particular the 90° peel test and the through-cracked tensile (TCT) test. A method to identify the energy expended in delamination is developed with use of the cohesive zone method, applied to simulation of the 90° peel test and the TCT test. This method enables to capture mixed-mode crack propagation in steady-state delamination. The results of the numerical analyses also allow to identify several influential factors in the debonding of laminated glass and enhance the interpretation of the experimental techniques.

In Chapter 5, the crack delay model for glass and hyper-viscoelastic material model for PVB interlayer are combined to simulate the response of a laminated glass panel under drop weight impact. Different element configurations to discretise the laminate are evaluated for their merits and shortcomings. Three different types of mechanical behaviour to the impact are discussed: the elastic response in the intact state of the glass, breakage of a single glass ply, and

fracture of both glass plies where the post-fracture response is dominated by the stiffness and deformation of the PVB interlayer material that bridges the cracks.

Chapter 6 presents the simulation of the pendulum impact test as described by the European standard EN 12600 [8], for which a detailed, numerical model of the impactor is conceived. This model aims to closely reproduce the physical behaviour of the tyres that are used in the test, and is validated for different drop heights of the impactor against a pressure and force plate setup. Further comparison is made for the elastic responses of monolithic and laminated glazing to impacts with varying intensity. Finally, simulation of the response of laminated glass panels beyond fracture is discussed and compared with experimental tests for thick and thin glass plates.

Chapter 7 discusses the simulation of laminated glass response to blast loading. First, the nature of blast wave propagation and reflection is characterised and numerical approaches to represent the blast loading of a surface are investigated. The simulated blast response of laminated glazing is evaluated for two experimental test cases: the open air blast of an explosive charge on small glass specimens, and the shock tube testing of larger glass panels, as described by the European standard EN 13541 [9]. Analysis results with the crack delay model for glass are compared with earlier numerical modelling of the shock tube tests, where a different damage model and interlayer material model have been used. The capability of the numerical models to capture delamination and tearing in the post-crack phase is evaluated.

Finally, the conclusions of this work are summarised in Chapter 8.

Chapter 2

Glass

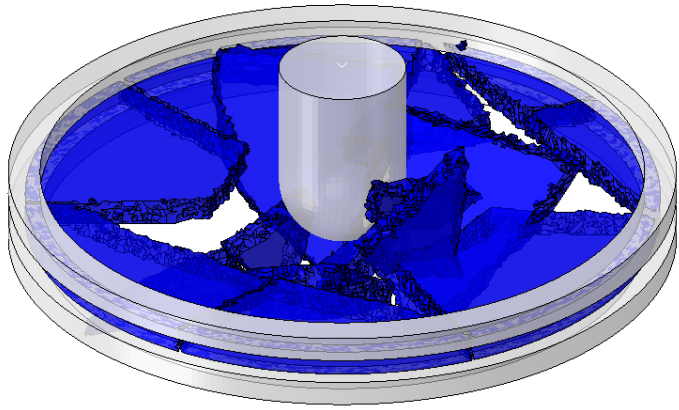

Simulated fragmentation of a monolithic glass disk under impact by a drop weight.

2.1 Introduction

From its first use in architecture in the ancient Rome, window glazing evolved greatly in composition and production methods. Especially the 20th century has seen a great rise in interest for the structural use of glass, because of the ability to reliably produce large window panes by the development of the glass drawing procedure (Belgium, 1910s) and later the float line process (UK, 1950s). Nowadays, soda-lime silicate glass is by far the most commonly used type of glass for structural applications. This composition of glass is favourable because of its hardness, cost of resources and production, and relatively low melting temperature which makes it more workable than other glass types. To a much lesser extent, borosilicate glass is used in construction as well. Because of its low thermal expansion coefficient, it is sometimes favoured for applications where resistance to thermal shocks is prioritised. Other frequently encountered types of glass for non-structural applications include: silicate glass for chemical lab recipients and lightning tubes, oxide glass for optical fibres and aluminosilicate glass for fibreglass and capacitive touch screens.

Many different processes can be used in the production of glass, but the main production steps are always similar: melting at 1600 - 1800 °C, forming at 800 - 1600 °C and cooling at 100 - 800 °C [10]. The great majority of flat soda-lime glass for structural use is produced in a float process. This production process is particularly advantageous because of the low production cost, the superior optical quality and the large sizes that can be reliably produced. Figure 2.1 schematically shows the float line, which is in reality a large production unit that operates continuously, 24 h per day. When the glass leaves the melting oven, it is poured at approximately 1000 °C on to a shallow pool of molten tin. Tin is chosen because of the large range of its liquid state (230 - 2300 °C), and because of its much higher density with respect to glass, i.e. 7360 kg/m^3 versus 2530 kg/m^3 for glass. The liquid glass then floats on the tin bath and spreads out to form a smooth surface at an equilibrium thickness of 6 to 7 mm. It is then cooled and drawn on to rollers before entering the annealing lehr, a long oven at around 600 °C. The glass thickness is controlled by the speed of the rollers. In a float line, flat glass thicknesses that can be produced are typically in the range of 2 to 25 mm. In the annealing lehr, the glass is slowly cooled in a precise and uniform manner to relieve residual stresses. Finally, the glass is cut to a typical size of 3.12 by 6 m.

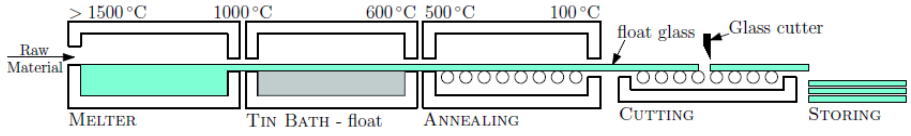

Figure 2.1: Production process for float glass (figure from Nielsen [11]).

As a consequence of this production process, the two sides of the glass are not identical. One side has been in contact with the tin bath whereby diffusion of an amount of tin at the glass surface could not be avoided. This surface is called the tin side; the other side is the air side.
A marginally lower bending strength has been reported for the tin side [12,13]. However, this is not due to the diffusion of tin atoms, but rather to the contact of the tin side with the rollers in the cooling phase. The rollers cause surface flaws at the tin surface that reduce the strength. Also, the tin side shows a notably smaller surface roughness which has an influence on the adhesive properties when glued [14]. Interlayer manufacturers therefore advise interlayer lamination to the air side.

In post-production the glass can be machined, bent in a hot or a cold forming process, thermally or chemically strengthened (see Sec. 2.2), laminated to a polymer interlayer (Sec. 3.1) and coated. Additional edge finishing may be provided, e.g. by grinding, polishing or acid etching.

The most important physical properties of soda-lime glass as used in construction are given in Table 2.1.

Table 2.1: Physical properties of soda-lime silicate glass (data from Ref. [10])

Density	ρ	$2500\,\mathrm{kg/m^3}$
Young's modulus	E	$70.0\,\mathrm{GPa}$
Poisson's ratio	ν	0.23
Knoop hardness	$HK_{0,1/20}$	$6\,\mathrm{GPa}$
Thermal expansion coefficient	α_T	$9 \cdot 10^{-6}\,\mathrm{K^{-1}}$
Specific thermal capacity	c_p	$720\,\mathrm{J\,kg^{-1}\,K^{-1}}$
Thermal conductivity	λ	$1\,\mathrm{W\,kg^{-1}K^{-1}}$
Dynamic viscosity	μ	$10^{20}\,\mathrm{Pa\,s}$

2.2 The strength of glass

2.2.1 The technical strength of glass

The technical strength is of great importance in the dimensioning of a structure and, in this work, to realistically capture the cracking and fragmentation of a glass panel. In general, the *strength of glass* alludes to its tensile strength because the compressive strength of glass is much higher and is usually not considered critical in design. However, it can be noted that some recent developments do rely on the compressive load-bearing capacity of glass, e.g. glass columns [15] and glass masonry [16].
The tensile strength of an elastic-brittle material such as glass is not a unique

value. The theoretical strength of glass, the stress needed to break its molecular bonds, is in the range of 5,000 to 10,000 MPa [17]. The technical strength measured for architectural soda-lime glass is many times lower, i.e. 15 to 200 MPa [18]. Because glass is not capable of plastic deformation on a macroscopic scale, it is highly sensitive to the flaws and inhomogeneities in its microstructure. Once the loading reaches the point where one *critical* flaw can extend, it grows quickly into a visible crack completely splitting the sample. These flaws were first analysed by Griffith [19], whose theory became the basis of the field of fracture mechanics. For glass, such flaws typically have a size in the order of 10 µm [20] and are available in large quantities at the surfaces and edges. Figures 2.2 and 2.3 show the atomic force microscopy (AFM) scans of surface and edge flaws of annealed float glass.

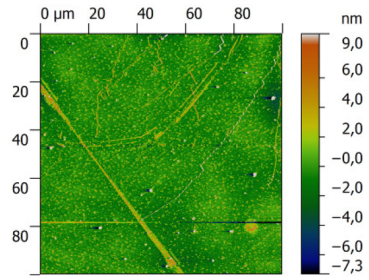

(a) 1 year after production

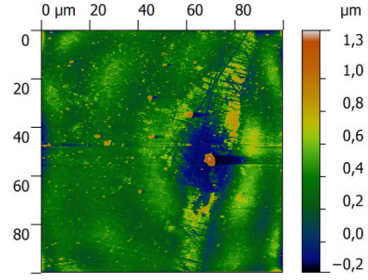

(b) 3 years after production

Figure 2.2: Atomic force microscopy scan of annealed float glass surface (figures from Molnar [21]).

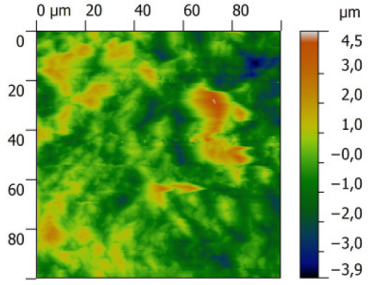

(a) Grinded edge

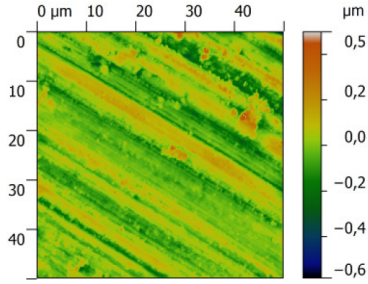

(b) Polished edge

Figure 2.3: Atomic force microscopy scan of annealed float glass edge (figures from Molnar [21]).

Much like Da Vinci's experiments on the strength of iron wires of different length, Griffith tested the strength of glass fibres with different diameter and

established the size effect in solids. He also observed that the maximum tensile stress in the corner of a crack is many times larger than the observed tensile strength of the specimen. The size effect can then be attributed to the observed, macroscopic strength being dependent on the size, shape and orientation of the flaws in the material. It is statistically more probable that the critical flaw leads to failure at a lower macroscopic stress for a large sample than for a small sample.

From Fig. 2.2 and Fig. 2.3 it is apparent that the flaws existing at the cut and machined edges of a float glass panel are much larger than on the very smooth glass surface. The edge flaws have a deteriorating effect on the measured glass strength, as evidenced by a.o. Vandebroek [22]. For this reason, international standards take account of edge effects for the testing of glass. ASTM E 1300-4 [23] clearly makes a distinction between the strength at and away from the edges, giving a tabular overview of allowable stresses for both cases depending on heat treatment and edge finish of the glass specimen. EN 1288-3 [24] and ASTM C 158 [25] describe a four-point bending test to determine the bending strength, where cracks may initiate from the edges. Where edge effects should be excluded, the coaxial double ring test is commonly used. Several setups for this test are described in EN 1288-2 and -5 [26, 27], and ASTM C1499-09 [28].

For practical design, the allowable limit of tensile stress for float glass is specified by DIN 1249-10 [29] as 45 MPa for annealed float glass. But when bending tests are performed on glass samples of the same size and under the same loading conditions, a high variability is found for the macroscopic failure stress. This can be explained on a mesoscopic level by linear elastic fracture mechanics. From the structural designer's point of view, a probabilistic approach allows to predict survivability without intimate knowledge of the critical flaw in a stressed component. The most widely used function for describing the failure probability is the Weibull distribution [30]. This distribution function is an appropriate mathematical expression of the weakest link principle and has in the past been reported to provide the best statistical representation of the strength of glass specimens [31]. The Weibull probability function $P_f(\sigma)$ is given by

$$P_f(\sigma) = 1 - exp\left(-k\,A\,\sigma^m\right), \tag{2.1}$$

where A is the glass surface area and k and m are interdependent strength parameters that can only be determined by experimental testing.
An overview of surface strength parameters for annealed glass which were published before 1995 has been compiled by Overend et al. [32]. Fig. 2.4 shows a Weibull plot, representative for as-received soda-lime glass samples that have been tested according to EN 1288-5 [27]. In this figure, the data points are clearly not on a straight line. Haldimann [33] examined the accuracy of the fit for the test results of as-received and artificially damaged glass specimens in

inert and in ambient conditions. He concluded that the Weibull representation is not satisfactory for assessment of the glass strength in ambient conditions, while a good fit can be confirmed for the inert conditions. Veer [34] noted earlier that the deviation from the Weibull distribution is most significant at the lower strengths, which are especially important in design. He further investigated alternative probabilistic representation for glass failure and identified several influential factors [35, 36]. Veer concluded that a multilinear Weibull distribution most accurately describes the probability of failure of glass components. Where edge effects cannot be excluded, a distinction should be made between the strength of the scored side and the other side, where the strength on the cut side is on average 20% weaker and shows greater scatter.

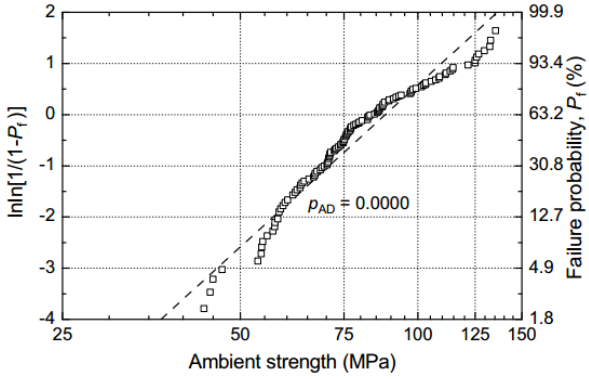

Figure 2.4: Experimental ambient strength data of as-received soda-lime glass specimens; Weibull plot (data from Fink [20], figure from Haldimann [33]).

Glass panels can be strengthened by tempering or by chemical treatment. Essentially, both treatments introduce compressive stresses on the outer surfaces which reduce the effective tensile stress and delay crack growth of the Griffith flaws. Tempering is a type of heat treatment in which the glass is heated above its glass transition temperature ($T_G = 525°\mathrm{C}$) and then quenched for fast cooling back to room temperature. At such elevated temperature, the glass is no longer regarded as an elastic solid, but behaves viscously as described by the Narayanaswamy model [37]. Fig. 2.5 shows the residual stress distribution in tempered glass, as calculated with finite elements by Nielsen [11]. After tempering, some glass panels may break spontaneously because of nickel-sulphide inclusions that expand during the phase change.

A different fracture pattern can be observed for annealed and tempered glass, as shown in Fig. 2.6. The fully tempered glass breaks into small, relatively harmless fragments of about $1\,\mathrm{cm}^2$. However, this also makes its post-fracture

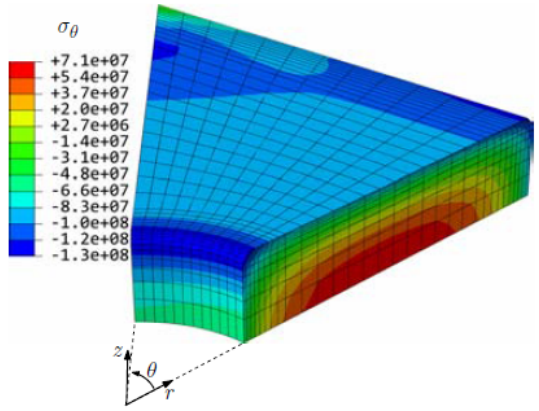

Figure 2.5: Residual stresses in a square glass panel with central hole, 1/16 symmetry calculated with FEM (figure from Nielsen [11]).

performance very poor. A compromise can be found in *heat-strengthened* glass, which is cooled at a slower rate than fully tempered glass. This provides fairly good structural performance and a sufficiently large fragmentation for good post-fracture performance [10]. Non-strengthened, annealed glass normally breaks into few large fragments. However, when exposed to high loads, the elastic energy stored in the material due to deformation can lead to a fracture pattern similar to that of heat-strengthened glass.

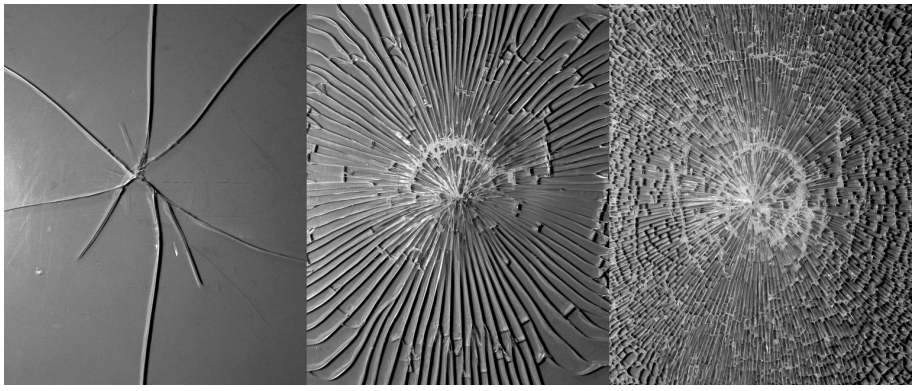

Figure 2.6: Fracture patterns for: annealed glass (left), heat-strengthened glass (middle) and fully tempered glass (right); (figure from Ref. [10]).

Glass can also be chemically strengthened by submersion in a potassium salt bath at 300°C. This causes sodium ions at the glass surface to be replaced by

potassium ions, which are larger and introduce high local compressive stress. Tensile stresses then exist in the core of the material as well, but they are negligible compared to those in tempered glass. Chemically strengthened glass is encountered frequently as touch screens, but is very rare in structural applications.

2.2.2 Fracture mechanics

The field of fracture mechanics provides quantitative description of stress concentrations around a crack tip. Figure 2.7 shows the three different fracture modes that can be distinguished: tensile opening (Mode I), in-plane shear (Mode II) and out-of-plane shear (Mode III). When a plate is loaded in bending, a crack (or flaw) at the outer surface is only loaded in Mode I. In general, this is the only fracture mode considered in the crack analysis of brittle materials.

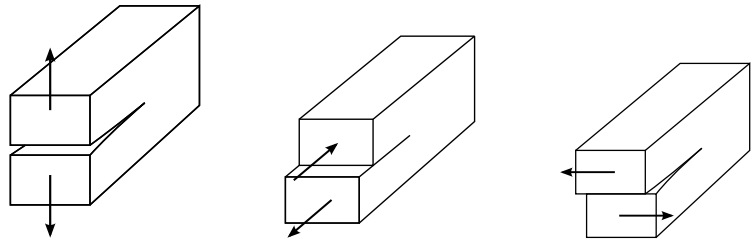

(a) Mode I **(b)** Mode II **(c)** Mode III

Figure 2.7: Fracture modes

2.2.2.1 Stress intensity factor

Fig. 2.8 schematically shows a crack loaded in Mode I, where it is assumed that the crack depth a is substantially smaller than the component size. The material is assumed as homogeneous, isotropic and linear elastic-brittle. When a crack tip is loaded, the stress components around the crack tip can be calculated with the Airy stress function method (when idealised as being linear). However, the sharp crack tip presents a singularity. To enable stress calculation, Irwin [38] introduced the stress intensity factor K_I, K_{II} and K_{III} for Mode I to III. With reference to Fig. 2.8, K_I is defined as the limit value of the 22-component of the crack tip stress:

$$K_I = \lim_{r \to 0} \left(\sqrt{2\pi r}\, \sigma_{22}(r, \theta)|_{\theta=0} \right) \tag{2.2}$$

The asymptotic stresses around the crack tip can then be described in function of K_I. Eqs. 2.3 give the stress field for a crack loaded under plane strain conditions. The description of the stress field under plane stress conditions or

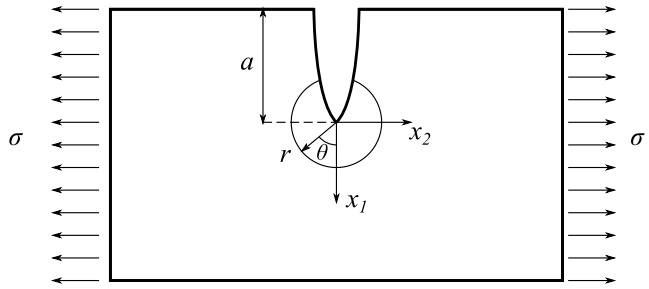

Figure 2.8: Schematic representation of general crack topology

for a 3D crack, in Mode I, II and III, as well as the derivation of all formulae can be found in various fracture mechanics handbooks, e.g. Refs. [39–41].

$$\begin{aligned}
\sigma_{11}(r,\theta) &= \frac{K_I}{\sqrt{2\pi r}}\cos(\theta/2)\,(1-\sin(\theta/2)\sin(3\theta/2)) \\
\sigma_{22}(r,\theta) &= \frac{K_I}{\sqrt{2\pi r}}\cos(\theta/2)\,(1+\sin(\theta/2)\sin(3\theta/2)) \\
\sigma_{12}(r,\theta) &= \frac{K_I}{\sqrt{2\pi r}}\cos(\theta/2)\,(\sin(\theta/2)\cos(3\theta/2)) \\
\sigma_{33}(r,\theta) &= \nu\,(\sigma_{11}(r,\theta)+\sigma_{22}(r,\theta))
\end{aligned} \tag{2.3}$$

The stress intensity factor is dependent of the geometry of the component, the size, shape and orientation of the observed crack, and of the applied loading. The general solution can be written as:

$$K_I = \sigma\, Y\, \sqrt{\pi a}, \tag{2.4}$$

where a is the crack size and Y is the geometry factor, which can be calculated (analytically or numerically) or determined by experiments. In the example of Fig. 2.8, the crack size a is small compared to the component's dimensions and σ is a uniform loading perpendicular to the crack. In that case, the geometry factor can be determined as $Y = 1.12$.

Irwin formulated a fracture criterion based on a critical value of the stress intensity factor K_{Ic}, also named the *fracture toughness*. Under quasi-static loading, crack growth initiates upon reaching K_{Ic}. For reference, the fracture toughness for typical ceramics is in the order of $1\,\mathrm{MPa\,m^{1/2}}$ [40] and in the order of $30 - 100\,\mathrm{MPa\,m^{1/2}}$ for ductile materials. For soda-lime silicate glass, the fracture toughness has been determined by different authors; an overview is given in Table 2.2.
Assuming a small crack size for the load case of Fig. 2.8, the following equation allows to estimate the magnitude of the critical stress:

Table 2.2: Fracture toughness of soda-lime glass

Author	K_{Ic}[MPa m$^{1/2}$]
Wiederhorn, 1967 [42]	0.82
Gehrke et al., 1987 [43, 44]	0.78
Atkins & Mai, 1988 [45]	0.82
Mencik, 1992 [46]	0.74 − 0.81
Ullner, 1993 [47]	0.76
Surdyka et al., 2014 [48]	0.77 (in water), 0.81 (in air, RH=40%)

$$\sigma_c = \frac{K_{Ic}}{1.12\sqrt{a\,\pi}} \tag{2.5}$$

For a fracture toughness $K_{Ic} \approx 0.8\,\mathrm{MPa\,m^{1/2}}$ and a crack size of $100\,\mu m$, a critical stress $\sigma = 40\,\mathrm{MPa}$ is expected to lead to failure.
For equal geometric proportions and loading conditions at the crack tip, the ratio of critical stresses depends on the ratio of crack sizes, given by Eq. 2.6. This provides an explanation why a much higher fracture strength is achieved for glass fibres, which have smaller surface flaws than structural glass.

$$\frac{\sigma_{2c}}{\sigma_{1c}} = \sqrt{\frac{a_1}{a_2}} \tag{2.6}$$

It should be noted that the surface flaws can grow by influence of the surrounding environment, even when the stress intensity factor is well below the fracture toughness. This is termed subcritical crack growth and is the mechanism behind the reduction of the technical strength of glass over time. In general, the surrounding medium is ambient air with up to 100% humidity. Particularly the presence of water, whether liquid or vapour, instigates crack growth. In two papers [42, 49], Wiederhorn measured crack velocities as a function of stress intensity on glass plates in air with varying humidity. He could distinguish three domains, which are shown in fig. 2.9. In Domain I, there exists a nearly linear relation between crack growth velocity and the stress intensity factor K_I. In this domain, the external parameters such as temperature, chemical enviroment and present stress state play a role of significance. In Domain II, crack growth is heavily influenced by chemical reactions, but is independent of the stress state. When the fracture toughness is exceeded in transition to Domain III, the crack velocity theoretically rises to the Rayleigh wave speed ($c_R = 3310\,\mathrm{m/s}$ for glass) [50]. Then the surrounding medium can no longer react with the surface flaws. Because of the high crack velocity, crack growth in Domain III is often described as unstable crack propagation. Experimentally found average values for the crack speed in this domain amount to $v_c \approx 1500\,\mathrm{m/s}$ [51], which is less than half of the theoretical value. Upon reaching the speed of 1500 m/s,

the crack velocity remains constant, even though the stress intensity factor may change substantially.

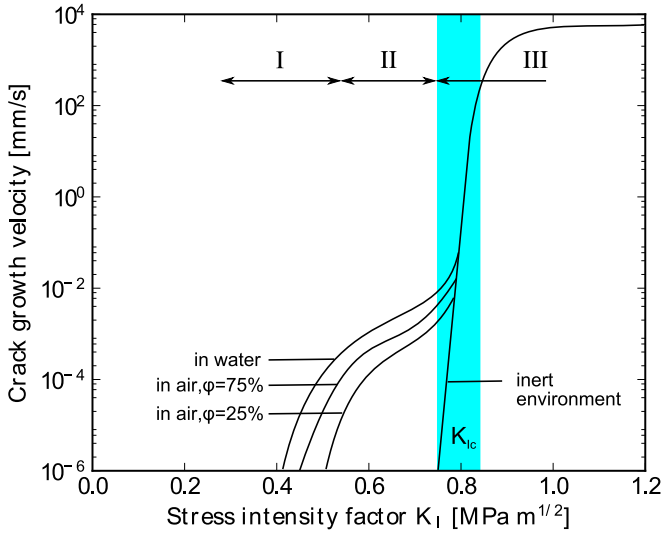

Figure 2.9: Relation between crack growth and stress intensity factor K_I for soda-lime glass (after Mencik [46]).

2.2.2.2 Energy release rate

A fracture criterion can also be formulated by considering the energy balance of the system. Griffith [19] already recognised that the macroscopic potential energy, consisting of the internal elastic energy U_i and the external energy U_e of the applied loads, vary with the crack. He also recognised that extension of the crack results in the creation of new cracked surface and concluded that a certain amount of work U_c must be expended at a microscopic level to create that area. The word "microscopic" implies that this work represents the area under the force-displacement curve that characterises the interaction between atoms or molecules from equilibrium to full separation, averaged over the surface area. Assuming linear elastic-brittle material under quasi-static conditions, the energy balance can be written as:

$$\frac{dU_e}{da} - \frac{dU_i}{da} = \frac{dU_c}{da}, \tag{2.7}$$

where a is the crack length. After division by the plate thickness t (out-of-plane thickness in Fig. 2.8), the left-hand side of Eq. 2.7 is named the *energy release rate* G and the right-hand side the *crack resistance force* G_c, which equals 2γ, where γ is the specific surface energy of the material.

$$G = \frac{1}{t}\left(\frac{dU_e}{da} - \frac{dU_i}{da}\right) \qquad [\mathrm{J/m^2}] \tag{2.8}$$

$$G_c = \frac{1}{t}\left(\frac{dU_c}{da}\right) = 2\gamma \qquad [\mathrm{J/m^2}] \tag{2.9}$$

The Griffith fracture criterion says that a crack will grow when the energy release rate equals the crack resistance force. This value is then also named the *critical energy release rate* or simply the *fracture energy* and is considered a material property. Moreover, it can be shown that a relation exists between the energy release rate and the stress intensity factor(s) for linear elastic materials [39–41]. In the pure Mode I case, a unique relation exists between G_I and K_I, given by Eq. 2.10. This relation also holds for the respective critical values. In Eq. 2.10, the function $A_I(v)$ expresses the dependency of the crack propagation velocity v.[1] For a stationary crack: $A_I(0) = 1$.

$$\begin{aligned} G_I &= A_I(v)\, K_I^2/E && \text{for plane stress} \\ G_I &= (1-\nu^2)\, A_I(v)\, K_I^2/E && \text{for plane strain} \end{aligned} \tag{2.10}$$

This formula allows to calculate the fracture energy for glass with knowledge of the fracture toughness. With $K_{Ic} = 0.8\,\mathrm{MPa\,m^{1/2}}$ and assumed plane strain conditions, this yields $G_{Ic} = 8.66\,\mathrm{J/m^2}$ for a stationary crack. However, various techniques have been used to determine the fracture energy. A selected overview is given in Table 2.3.

Table 2.3: Fracture energy of soda-lime glass (in ambient air)

Author	Test method	G_{Ic} [J/m^2]
Clif, 1957 [52]	Cone crack	7.4 − 8.6
Linger & Holloway, 1968 [53]	Double-cantilever cleavage	6.6 − 7.8
Wiederhorn, 1969 [54]	Double-cantilever cleavage	7.82
Inagaki et al., 1985 [55]	Chevron notch test	4.4
Yuan & Huang, 2012 [56]	Molecular dynamics sim.	11.72
Sharon & Fineberg, 1999 [57]	Notched sheet tensile test	30 − 40
Reich et al., 2014 [58]	Ball drop test	99.2 − 107.6

It is notable that the results of the last two references in Table 2.3 are much higher than other obtained values for the Mode I fracture energy of glass. They account for the fracture energy measured on a dynamically propagating crack. The energy balance concept has been generalised for dynamic fracture

[1] The function $A_I(v)$ relates the crack propagation velocity to the material's dilatational wave speed, shear wave speed and Poisson ratio. Formulae are given in 'Dynamic Fracture Mechanics' [50]. For a crack propagating in soda-lime glass at $v = 1500\,\mathrm{m/s}$, $A_I = 1.19$.

by Mott [59], to globally account for the kinetic energy that is released by a propagating crack. Mott's theory is used to locally describe an equation of motion for the crack, by equating the energy release rate G with the fracture energy G_c. To obtain such equation it is assumed that all of the dissipation in the system occurs within a small region surrounding the crack tip: the process zone. Thus, the fracture energy is not interpreted as strictly the energy required to break molecular bonds, but embodies all complex processes resulting from the stress field near the crack tip. The resulting equation of motion is given by [50]:

$$v/c_R = 1 - \frac{E\,G_c}{(1-\nu^2)\,{K_I}^2} \tag{2.11}$$

In practice, it is found that this theory holds for low crack velocities (up to $\sim 0.4\,c_R$) where a change in stress intensity results in an immediate change of the crack velocity [51]. This is no longer true for faster propagating cracks when a certain stability limit, $v = v_c$, is exceeded [57]. As the crack accelerates, many small *daughter crack* branches appear around the *mother crack* surface. The potential energy stored in the medium is channeled into creating new cracked surface. But the energy flowing into the crack tip is then divided between the crack branches, thus directing less energy into each crack which slows down the propagation velocity. The daughter cracks then arrest and the energy returns to the main crack tip causing it to accelerate and repeat the process. Sharon and Fineberg [57] concluded that the apparent increase in fracture energy at high crack velocity is simply explained as the energy required to create new fracture surface for both the main crack and its micro-scale branches.

In Table 2.3, the fracture energies measured by Reich et al. [58] are even higher than the results by Sharon and Fineberg [57], but here questions may arise over the accuracy of the experimental method. The ball drop test consisted of the standardised EN 356 setup [60], where the ball velocity before and after penetration of the glass is measured to compute the kinetic energy loss during the impact. Also the lengths of all cracks in the plate are measured and multiplied by the glass thickness (and a correction factor of 1.15) to determine the fracture surface.

2.2.2.3 Cohesive zone models

While the stress intensity factor and energy release rate belong to the field of linear elastic fracture mechanics (LEFM) and describe the state at the crack tip of a single material flaw, the cohesive zone approach has a wider field of applicability. In essence, the cohesive zone method models the fracture process zone by a line or a plane ahead of the crack tip subjected to cohesive traction, schematically represented in Fig. 2.10. The basic idea that originated in the work of Dugdale [61] and Barenblatt [62] is to consider fracture as a gradual process of separation that occurs in small regions of material adjacent to the

tip of a forming crack. The separation is resisted by tractions described by a traction-separation law (TSL). In contrast to damage approaches, the cohesive zone model defines accumulated damage as an effective behaviour of the fracture process zone, represented as a gradual degradation of the cohesive tractions. As such, the cohesive zone near the crack tip is a continuum representation of material degradation and failure at a microscopic level by many possible mechanisms.

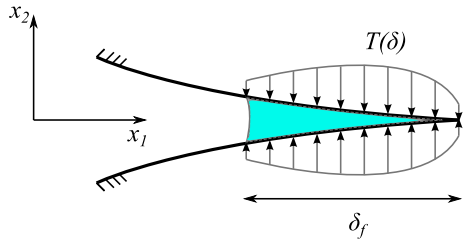

Figure 2.10: Cohesive zone ahead of the crack tip

With cohesive zones, crack formation in non-linear materials can be described and plasticity or viscous effects at the crack tip can be accounted for by the shape of the traction-separation law. Characteristic shapes for the TSL are shown in Fig. 2.11. The cohesive zone method allows to model delamination or debonding at the interface between two materials (see Chapter 4) and can also describe mixed mode crack propagation. For linear elastic-brittle materials such as glass, the cohesive zone method has the advantage of enabling the use of a macroscopic stress criterion for crack initiation, thus avoiding the need to have knowledge over each and every surface flaw.

The crack opening displacement is zero at the mathematical crack tip where $\delta = 0$. The opening increases with distance to the mathematical crack tip, and reaches a final value at the end of the cohesive zone where $\delta = \delta_f$. This is the physical crack tip and no cohesive tractions exist from here on: $T(\delta \geq \delta_f) = 0$. The work needed to reach full separation at δ_f for an infinitesimal area equals the fracture energy G_c:

$$\int_0^{\delta_f} T(\delta)\,\mathrm{d}\delta = G_c \tag{2.12}$$

2.2.3 Rate-dependency of glass strength under dynamic loading

The apparent increase of the strength of glass with loading rate has been observed early on by different authors [67–69]. Freund [50] explains this from the

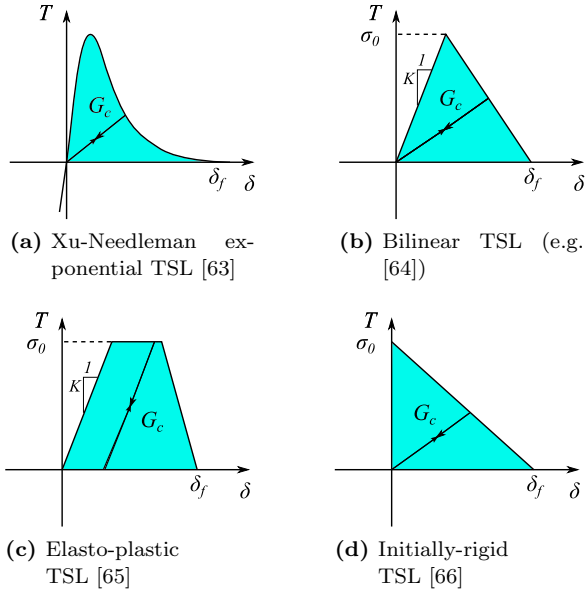

(a) Xu-Needleman exponential TSL [63]

(b) Bilinear TSL (e.g. [64])

(c) Elasto-plastic TSL [65]

(d) Initially-rigid TSL [66]

Figure 2.11: Commonly used shapes for traction-separation laws. Figures show Mode I behaviour only.

inability of glass, as a brittle material, to exhibit plastic deformation. Consider a specimen in a quasi-static bending test that is loaded slowly, but fast enough to exclude subcritical crack growth. The response up to fracture is insensitive to the rate of loading and the material deformation is elastic. Because glass is not capable of plastic deformation, it is highly sensitive to the flaws in its microstructure. Once the loading reaches the point where one critical flaw can extend, it grows quickly into a macroscopic crack completely splitting the specimen.

For intense pulse loading of a brittle material, the situation is quite different [50]. Suppose the material is deformed so rapidly that a stress level higher than that required to initiate growth of the most severe flaw is achieved in a short time. Once the critical stress level for that flaw is reached, a finite additional time can elapse before fracture begins. During this time, the stress level can rise as the deformation proceeds and the critical stress may be reached at many other flaws. The flaws then begin to grow as microcracks and as they become longer, the effective stiffness of the specimen diminishes and the stress rate decreases. Eventually, the microcracks grow into one or more macrocracks.

While this explanation is certainly correct for very high loading rates, the influence of the surrounding medium on the material strength cannot entirely be excluded for loading rates up to 10^6 MPa/s [43,44,70]. This is a loading rate

that can be expected for a glass test specimen under low velocity impact, which can be anywhere in the range of 10^4 to 10^7 MPa/s, depending on various factors, such as the impact speed, impactor material, clamping conditions, specimen thickness, etc. For example, in the drop weight impact presented in Section 2.3, the loading rate amounts to $\dot{\sigma} \approx 3.5 \cdot 10^5$ MPa/s. Fig. 2.12 shows the experimental results by Gehrke et al., where σ_s is the glass strength when it is unaffected by the surrounding medium.

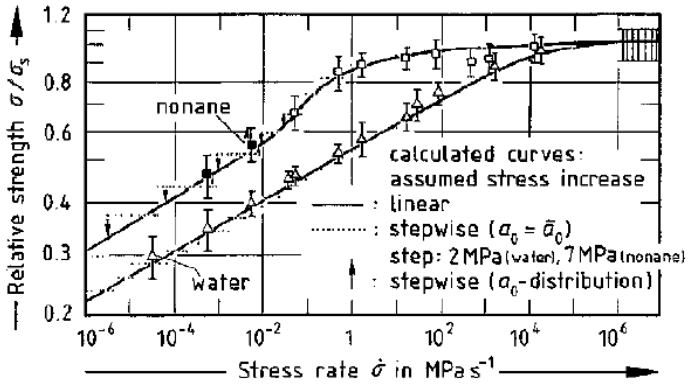

Figure 2.12: Dynamic fatigue curves of soda-lime glass under water and nonane, measured after initial crack generation (figure from Gehrke et al. [43])

To characterise the effect of the load duration on the strength of glass in ambient air, Beason and Morgan [71] presented the following relation, based on LEFM:

$$\sigma_{t_d} = \left[\frac{1}{t_d} \int_0^{t_d} \sigma(t)^n \, \mathrm{d}t \right]^{1/n}, \tag{2.13}$$

where t_d is the load duration and n is the crack growth parameter. The latter is usually taken to be $n = 16.0$ in an outside environment [72]. An overview of published values for n has been compiled by Overend et al. [73].

In a simplified form, Eq. 2.13 becomes:

$$\sigma_{60} = \sigma_{t_d} \left(\frac{t_d}{60} \right)^{1/16}, \tag{2.14}$$

where σ_{60} is the fracture strength corresponding with a load imposed for 60 seconds. This roughly corresponds to the strength measured in a standardised bending test at a loading rate of 2 MPa/s. Based on a measured average value $\sigma_{60} = 82.5$ MPa [74,75], the strength for a characteristic impact load duration of 10 ms would be 142 MPa. However, Beason and Morgan presented this formula

primarily for long-term loading, rather than dynamic, transient loading by impact or blast.

A number of authors have conducted research to establish the rate-dependent strength of glass under high velocity impact (HVI) [76–79]. For this load type, the impactor hits the glass plate at a speed $v_{imp} > 100\,\mathrm{m/s}$.
HVI is studied mostly for ballistic impact where the impactor is a light, but stiff projectile. Upon projectile impact, a compressive wave propagates ahead of the impacted area, thereby inducing hoop tensile stresses that nucleate pre-existing material flaws which grow into numerous microcracks [76, 80]. A circular crack front at speed $v_c = 1500\,\mathrm{m/s}$ then propagates from the contact area, consuming the kinetic energy lost by the projectile. When the glass is only a few millimeters thick, the projectile can pierce the plate and fly through. The fracture pattern for annealed glass consists of an intensely damaged zone in the immediate vicinity of the impact point. This failure regime is different from that found for the more common low velocity impacts (LVI) or for blast loading where fewer, but long cracks completely fragment the panel [81]. The rate-dependent behaviour of glass strength under LVI and blast is in a mid-range which is not fully described by either the time effect of sub-critical crack growth or by the cracking under HVI.

To experimentally assess the strength at high loading rates, the split Hopkinson pressure bar (SHPB) could be used [78, 79, 82]. With this method, a small specimen is compressively loaded with a very high strain rate ($\dot{\epsilon} \approx 1000\,\mathrm{s}^{-1}$ in [78], $\dot{\epsilon} > 100\,\mathrm{s}^{-1}$ in [83]). Tensile strength can be assessed by performing a split-tensile test, otherwise known as the Brazilian test [84]. However, in this test the tensile failure starts from within the volume of the specimen, rather than from the surface where the most significant material flaws are located. While the compressive strengths are increased up to 4 times at very high loading rates [79], the rate-effect is not confirmed so clearly for the split-tensile tests [78], as shown in Fig. 2.13.

Material models for the damage and failure of glass under HVI have been developed by Grujicic et al. [77, 81] and Holmquist et al. [85]. The latter included rate-dependency of the strength by the following relation:

$$\sigma_c = \sigma_{ref}\,(1.0 + C\,\ln(\dot{\epsilon}/\dot{\epsilon}_{ref}), \tag{2.15}$$

where σ_{ref} is the glass strength corresponding with a strain rate $\dot{\epsilon}_{ref}$ and C is a dimensionless constant. It is noted that Eq. 2.15 is not intended for glass or brittle materials in general, but is the same relation used in the Johnson-Cook plasticity model for ductile materials. According to Zhang et al. [79], $C = 0.035$ provides a good fit with experimentally obtained results for strain rates greater than $100\,\mathrm{s}^{-1}$.

Nie et al. used the SHPB to perform dynamic ring-on-ring bending tests on

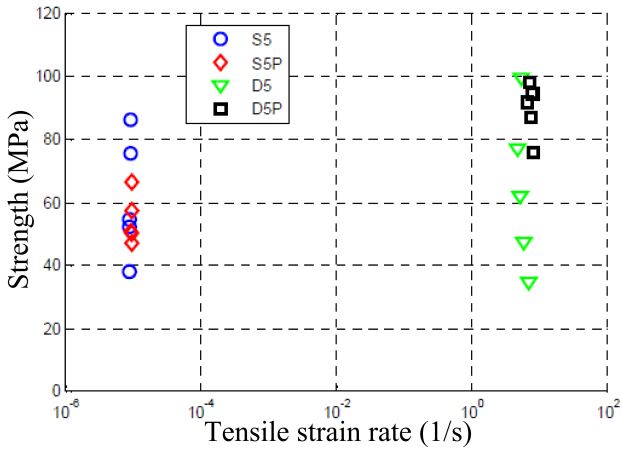

Figure 2.13: Tensile strength in split-tensile tests; suffix 'P' denotes the use of paper bearing strips (figure from Peroni et al. [78]).

circular samples of borosilacate glass with different surface roughness [70]. They found that the flexural strength increases with the loading rate for all surface conditions. This study's results for the flexural strength are given in Table 2.4, for which the examined loading rates cover the range that is expected for LVI and blast loading. When the relative strength increase in function of loading rate is compared for the three surface conditions, it is remarkable that the polished and ground samples follow a very similar trend. For all specimens, the increase of strength is less outspoken at the higher loading rates, which confirms Gehrke's experiments and that the surrounding medium still plays a significant role. An interpolated curve for the relative strength increase with loading rate is given in Fig. 2.14. However, the data do not conform to the Beason and Morgan relation for long-term strength. Also, the question remains whether a strength-rate relation derived from these data can be valid for soda-lime glass as well. The same trend is not confirmed by the ball-on-ring experiments of Bao et al. [86], although it is not clear from their article at which loading rates the samples were actually tested.

Table 2.4: Equibiaxial flexure strength of borosilicate glass under different loading rates and surface conditions; relative strengths with respect to the quasi-static bending strength are given between parenthesis (data from Nie et al. [70]).

Loading rate [MPa/s]	0.52	42	3500	$5 \cdot 10^6$
Acid etched [MPa]	357 (100%)	744 (208%)	1267 (354%)	1383 (387%)
Polished [MPa]	146 (100%)	180 (123%)	245 (168%)	255 (175%)
Ground [MPa]	46 (100%)	52 (113%)	77 (167%)	83 (180%)

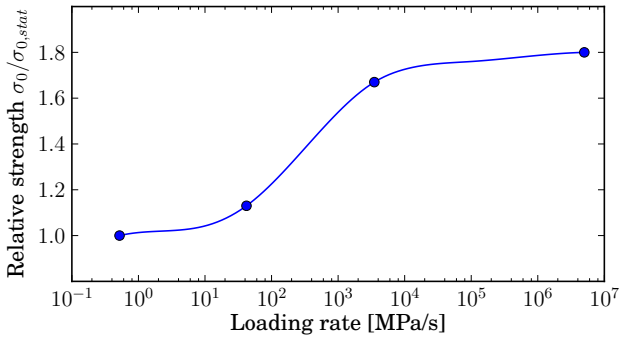

Figure 2.14: Strength increase with loading rate for borosilicate glass.

In conclusion, many studies have been conducted to identify the rate-dependent behaviour of glass strength, but few of them describe the range of loading rates that is of most interest in low velocity impact and air blast events. It appears that the growth of surface flaws under the influence of the surrounding medium is still of great importance in this regime, although it is no longer described by the long-term relation of Beason and Morgan. The work of Nie et al. confirms the general behaviour described earlier by Gehrke et al. and provides quantitative data. This may be used to calculate a rate-dependent strength of glass for LVI and blast if it can be assumed that soda-lime and borosilicate glass display the same behaviour.

2.3 Simulation of the elastic response to drop weight impact

This section introduces an in-house, well-instrumented drop weight test setup for controlled impact testing. Experiments on monolithic and laminated glass specimens were executed by De Pauw [5], Monserez [87] and Van Dam [6,88,89]. The experimental data obtained in the impact tests can be used to validate the simulation results of a numerical model and verify its accuracy. In this section, the numerical representation for the elastic response of a glass specimen under drop weight impact is studied. The purpose of this study is to establish which assumptions and simplifications in the model can be justified.

2.3.1 Experimental test setup

The small-scale drop weight setup consists of three major parts: an impactor striking the specimen, a steel rigid base support in which the specimens are clamped and guiding rails to guide the impactor. A photograph of the experimental facility is shown in Fig. 2.15.

Figure 2.15: Photograph of small-scale drop weight setup.

Fig. 2.16 shows the assembly drawings for the impactor and the base support that holds the test specimen. The impactor is mounted on guiding rails by its bearings. Several indentors can be mounted. Fig. 2.16a shows a hardened steel cylinder with a 10 mm radius ending in a spherical tip. Alternatively, a 28 mm rubber half sphere has been used by De Pauw [5], and a larger cylindrical silicon rubber indentor by Monserez [87]. The impactor is instrumented with a force sensor and accelerometer, placed as indicated on Fig. 2.16a. Additionally, magnetic sensors on the guiding rails measure the vertical displacement of the impactor.

The base support holds the test samples between two polypropylene rings and a bolted steel clamping ring. The polypropylene rings avoid direct hard contact between the stiff glass and steel parts while providing sufficiently rigid clamping conditions. Furthermore, a uniform clamping pressure is ensured by tightening the bolts in a certain sequence and by a specified force, which is explained in detail by De Pauw [5]. Various clamping rings are available for different specimen shapes and sizes. A polycarbonate cover plate and foam block with a cut-out slightly larger than the impactor diameter is placed above the clamping rings to brake the impactor, after the specimen has been hit and without interfering with the measurements of the impact event. A high-speed camera is set up to capture the impact from the bottom of the test specimen by means of a 45° tilted mirror.

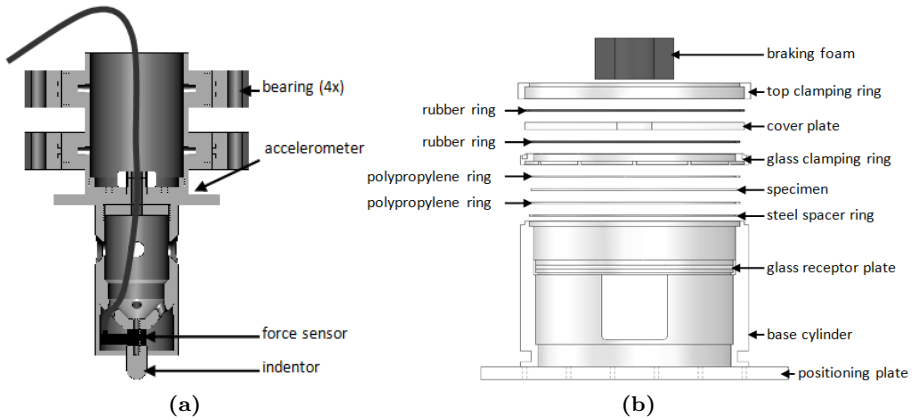

Figure 2.16: Assembly drawings for drop weight test setup components: (a) impactor, and (b) base support (figures from De Pauw [5]).

To characterise the elastic response of a monolithic glass plate under impact loading, a case study is made for the drop weight impact with the steel indentor tip on a ∅100 mm monolithic glass plate with a thickness of 4.0 mm, as measured. In this particular test, the impactor was released from a height of 200 mm. The measured impact velocity was 1.980 m/s, which corresponds well

with the theoretical free fall velocity: $\sqrt{2gh} = 1.981\,\mathrm{m/s}$. In the work of De Pauw, glass samples were tested with and without safety window film (SWF). It was evidenced that the addition of the safety window film has a negligible effect on the elastic response of the glass sample. As shown in Fig. 2.17, one sample (test 1) showed a very high strength. The measurement data for this sample can be used in validation of a numerical model of the elastic, intact response of a glass plate to the impact.

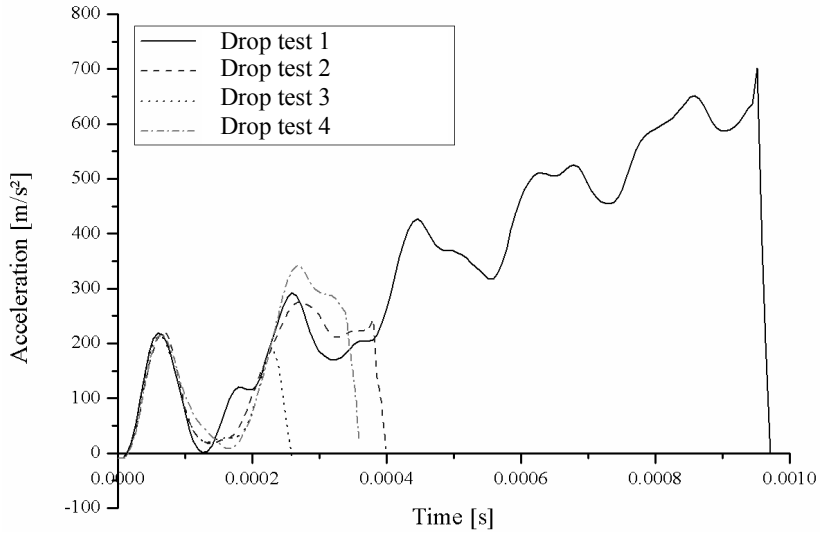

Figure 2.17: Accelerations for 200 mm free fall impact on ∅100 mm glass (figure from De Pauw [5]).

2.3.2 Simulation of the elastic response

Before simulating the fracture and failure of the glass component, it needs to be established that the forces, deformations and stresses in the intact phase of the impact can be reproduced to an acceptable degree of accuracy. This section examines which features of the actual setup need to be taken into account. This is done for the modelling of the impactor itself and for the clamping conditions of the glass sample. The base support is not taken into account, because it consists of thick steel components and is assumed sufficiently rigid.

Considering the available experimental data, the comparison of simulation results is made primarily with the axial force and acceleration measured on the impactor. These are the most sensitive signals that characterise the impact event. Impactor velocities and displacements can be calculated by integration of the accelerations. It can be noted that the force and acceleration measurements are equivalent, as $F = m_{imp} \cdot a$ where $m_{imp} = 7.38\,\mathrm{kg}$. However, their

curves are not perfectly equal, because the load cell and accelerometer are placed at different positions and have different characteristics. Fig. 2.18 shows both signals together for test 2 in Fig. 2.17.

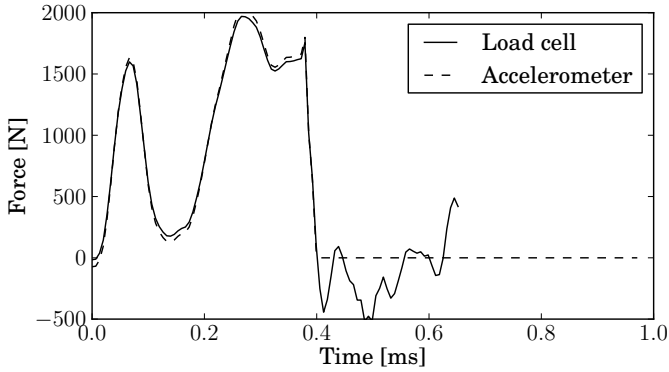

Figure 2.18: Force measurement as obtained by load cell and accelerometer on the impactor for drop height 200 mm on a $4 \times \varnothing 100$ mm glass plate (data from De Pauw [5]).

A first numerical analysis evaluates the boundary conditions (BCs) for the glass sample by use of an efficient axisymmetric model. In reality, the glass plate is held between polypropylene rings that are clamped by bolting of the surrounding steel plates, as indicated in Fig. 2.16b. Several options are available to represent this numerically. It may not be necessary to model all of the details. Three basic representations are examined: (a) fixed edge, (b) pinned bottom edge or 'simple support' conditions, and (c) held between deformable polypropylene rings. These three types of boundary conditions are shown schematically in Fig. 2.19.

The mechanical properties of all components are given in Table 2.5. The coefficient of friction between glass and steel is $\mu_f = 0.6$, and $\mu_f = 0.25$ between polypropylene and glass or steel [5]. In a first approach, the steel impactor and steel clamping rings are assumed as perfectly rigid. The indentor tip is in this case represented by a spherical surface and a total impactor weight of 7.38 kg.

Table 2.5: Mechanical properties of materials in drop weight impact

Material	density [kg/m^3]	Young's modulus [GPa]	Poisson's ratio [−]
Glass	2530	70.0	0.23
Polypropylene	900	1.3	0.42
Steel	7800	210	0.3

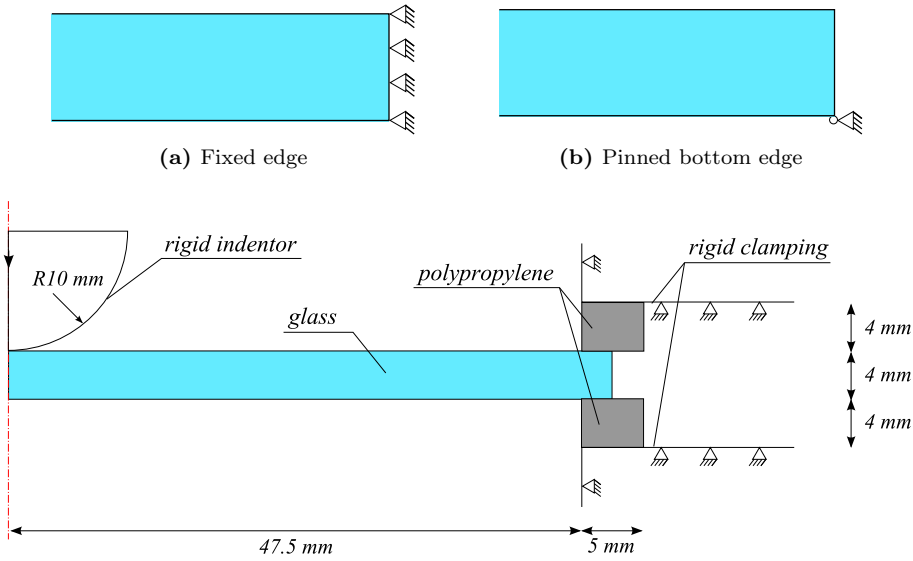

(a) Fixed edge

(b) Pinned bottom edge

(c) Clamped by polypropylene rings

Figure 2.19: Representation of boundary conditions for glass plate under drop weight impact.

Fig. 2.20 gives the resulting accelerations of the impactor in comparison with the experimental measurement (test 1 in Fig. 2.17). A characteristic element length $L_e = 0.25\,\text{mm}$ is used for the glass part in all three simulations in this figure. Also, the explicit solver for axisymmetric elements supports only linear elements with reduced integration.

A significant difference is seen in the impact behaviour with different boundary conditions. As can be expected, the fixed edge BCs result in a structurally stiffer response with overall higher forces and a higher frequency response. The more realistic representation with deformable propylene clamping rings already corresponds quite well with the experimentally obtained accelerations. Simulation with pinned bottom edge BCs comes close, but still overpredicts the plate stiffness in elastic response. To avoid early failure of glass elements by overprediction of the bending stresses in subsequent fracture analyses, it is therefore necessary to include the soft support provided by the polypropylene rings.

In the actual test setup, a clamping force is exerted on the glass sample and polypropylene rings by tightening of 12 M8 bolts. The clamping pressure and moment on the bolts is calculated in the thesis of Dekeukelaere [90]; the total axial clamping force on the assembly amounts to 5.5 kN. Abaqus allows to calculate the deformation and stress field due to the clamping in an implicit

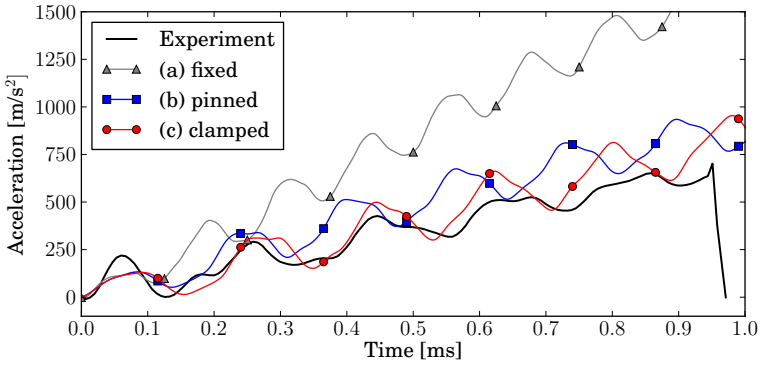

Figure 2.20: Comparison of simulation results for different boundary conditions to experimental accelerations in drop weight impact on a glass disk.

analysis, and import the result in subsequent explicit analysis. Fig. 2.21 shows the axial stress field calculated by a compressive force of 5.5 kN on the steel clamping rings. The resulting accelerations are given in Fig. 2.22. The pre-stressing of the glass and polypropylene components do not seem to have a great effect on the elastic response to the impact.

Figure 2.21: Axial stresses in glass and polypropylene due to bolt clamping.

Up to this point, only a characteristic element size $L_e = 0.25\,\text{mm}$ has been used for the efficient axisymmetric model. A higher computational effort is demanded for a full 3D model. Therefore, a mesh convergence study should demonstrate up to which element size consistent results are obtained for both the accelerations and bending stresses upon impact. These are shown in Figures 2.23 and 2.24, where the bending stress is evaluated at the bottom-most element in the center of the glass plate. Acceptable results are achieved for a mesh size up to $L_e = 1\,\text{mm}$, although the higher bending stresses are underestimated. However, at that point, an average glass specimen would have been broken already.

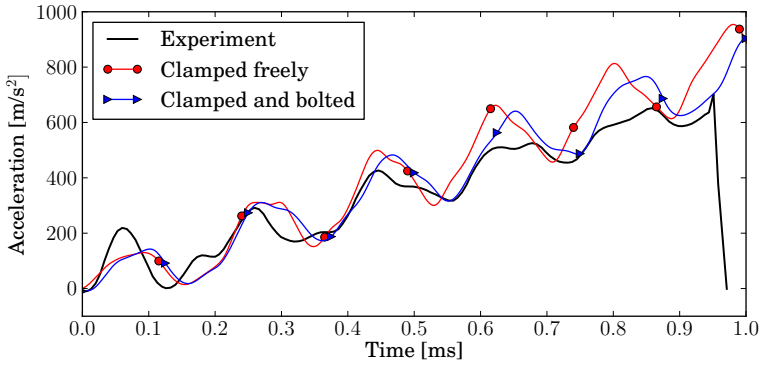

Figure 2.22: Comparison of simulation results for stressless and compressed conditions to experimental accelerations in drop weight impact on a glass disk.

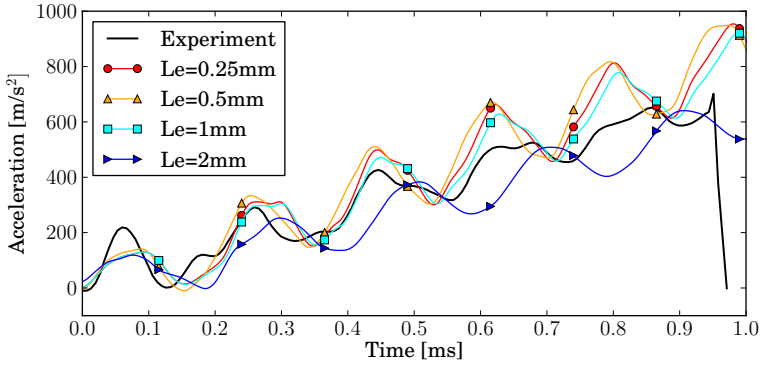

Figure 2.23: Comparison of simulation results for different mesh sizes to experimental accelerations in drop weight impact on a glass disk.

The impactor itself is not rigid, but a cylindrical, steel part with handles connected to a guiding rail. The material and structure of the impactor also respond to the impact event. Because strong vibrations are seen in the acceleration and force measurements, the question arises whether the impactor should be modelled as a deformable part, rather than as a rigid mass. A full 3D model is made for the impactor, as shown in Fig. 2.25, and its natural frequencies are evaluated in a modal analysis. The frequency content of the measurement data is obtained by Fast Fourier Transform (FFT). The frequencies are given in Table 2.6. The first mode frequency of the impactor is 2.6 times higher than the lowest frequency found in the impact accelerations and should not have led to resonance in the measurements. At higher modes, frequencies are found that

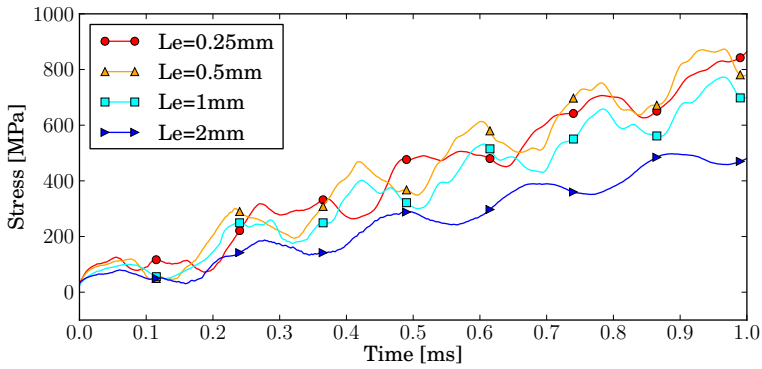

Figure 2.24: Comparison of simulated bending stresses for different mesh sizes in drop weight impact on a glass disk.

are close to the secondmost important frequency in the experiment. However, these are already very high and seem much less significant for the mechanical response.

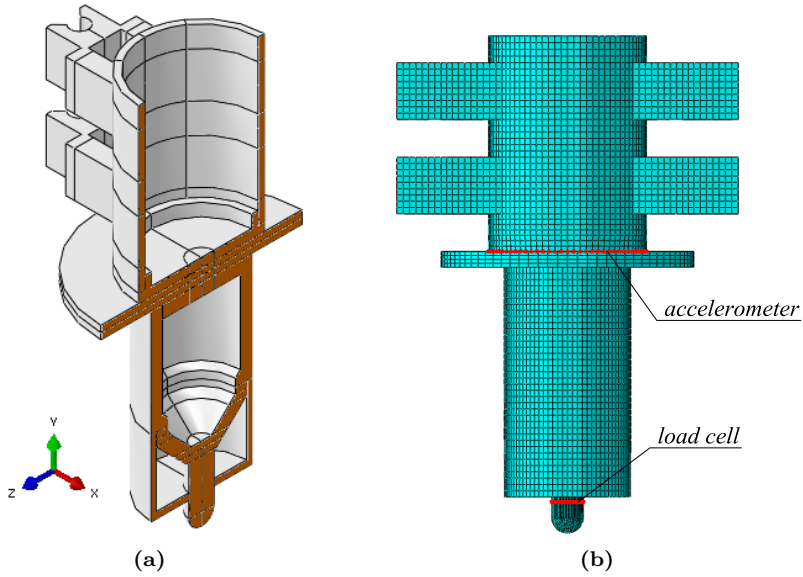

Figure 2.25: 3D model of steel impactor: (a) cut view, and (b) mesh (121k els.) with nodes for data collection.

A final evaluation is made by comparing the deformable and rigid impactor representations in a 3D model. The accelerations of the impactor are obtained

Table 2.6: Modal frequencies for drop weight impact test.

Mode	Acceleration measurement	Steel impactor
1	244 Hz	646 Hz
2	5860 Hz	835 Hz
3		2350 Hz
10 - 16		5538 – 6212 Hz

from the nodes at the locations of the accelerometer and the load cell in the actual setup. Because data obtained from one single node do not give a reliable result, a whole set of nodes is used, for which the accelerations are averaged and filtered. A Butterworth filter with cut-off frequency of 2.5 kHz is used. Fig. 2.26 shows the accelerations obtained at both locations, for the entire duration of the impact with a perfectly elastic glass plate (supposing no fracture occurs at all). The curve for the load cell, close to the impact, shows higher fluctuations, but both signals correspond well over the 5 ms duration. Results of two mesh sizes for the impactor are compared to those with the rigid indentor tip in Fig. 2.27, where the impactor accelerations are evaluated at the location of the accelerometer. Also here, the results show reasonable correspondence for the entire impact duration. However, averaging and filtering the acceleration data makes the curves of the deformable impactor model less reliable for detailed comparison. Because of this and the extra computational effort needed for the full model, the simplified representation as a rigid mass is preferred.

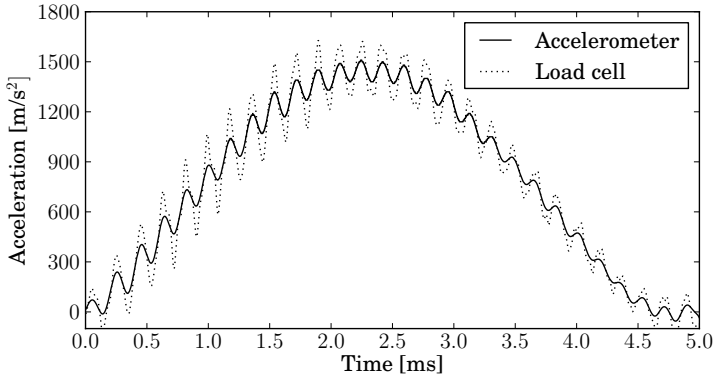

Figure 2.26: Accelerations at load cell and accelerometer locations for drop weight impact simulation with deformable impactor model.

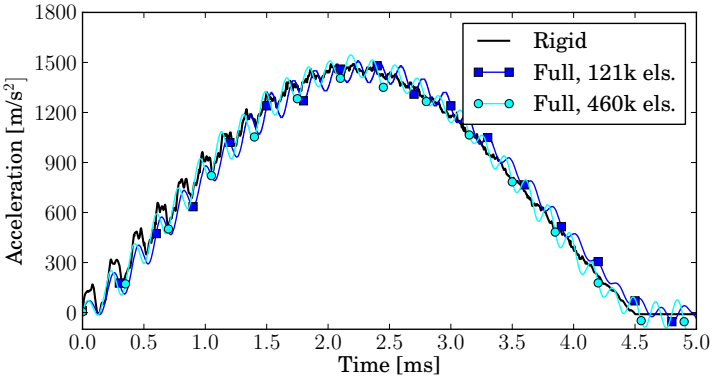

Figure 2.27: Accelerations for drop weight impact simulation with deformable and rigid impactor representation.

2.3.3 Conclusions

From the simulation of the intact response of a monolithic glass plate, it is seen that oversimplification of the problem by imposing direct constraints on the edges of the glass part leads to overestimation of forces on the impactor and stresses in the glass. It is necessary to model the boundary conditions more realistically, in this case by including the clamping between deformable, polypropylene rings with friction at the interface. More detail can be added by including the pre-stressed field that results from bolt tension, but this does not have a significant effect on the dynamic response.

The steel impactor may also be represented in a simplified manner as a rigid tip with added mass, rather than modelling the impactor in its entirety as a deformable part. It is shown that the resulting impact behaviour is equivalent, and that the influence of the impactor's eigenfrequencies on the acceleration and force measurements can be excluded. Also, the signal resulting from a rigid tip representation is more reliable than from the full impactor model, because the latter needs to be averaged and filtered to enable comparison with experimental data.

The next sections proceed with the failure modelling of the monolithic glass plate under the same impact conditions and use a rigid mass representation for the impactor, along with the clamping between deformable, polypropylene rings. The necessity of including the pre-stress field due to bolt tension is further investigated for the fracture response.

2.4 Crack simulation by element deletion

The numerical simulation of crack initiation and propagation in solids has been extensively studied over the years. Several approaches have been developed in order to describe the evolution of a crack, e.g. cohesive zone elements (CZM) [66, 91], extended finite element method (XFEM) [92], meshless [93] and particle conversion methods [94]. Despite these efforts, still many challenges remain, especially for coupled problems and for dynamic failure of thin-walled structures. A more simple and crude, but also versatile method is that of element deletion, in literature also referred to as *element erosion*, or the *kill element technique*. This technique is commonly used due to the simplicity of its numerical implementation and natural extension to 3D. Futhermore, it is possible to couple this method with any failure criterion or damage model without additional considerations. In engineering applications, the initiation of failure is commonly governed by a local strain or stress-based criterion. An often mentioned drawback is the removal of mass from the model, which conflicts with the conservation laws. However, most finite element codes do not actually delete the mass, but reduce the material stiffness of the element to zero. More serious are the very high degree of mesh dependency and occasional instabilities reported for this method. From the fracture mechanics point of view, element deletion is insensitive to the size effect of strength and the element meshes used in engineering applications are commonly too coarse to capture gradients near the crack tip which leads to an overestimation of the fracture energy. This makes the deletion of elements a rather crude technique to simulate fracture and fragmentation, and can lead to inaccurate failure prediction for some applications. It should therefore only be used to reproduce the global deformations, loads and energies of an experiment.

Despite its widespread use in failure analyses, very few publications discuss the numerical implications of element deletion for dynamic crack simulation. Unosson [95] encountered some of the aforementioned issues, as well as an increased sensitivity to hourglassing in the fracture zone. To address the size effect, he modelled the material imperfections by a probability density function and formulated the fracture criterion in terms of a critical principal stress which depends on the imperfection size [96, 97]. Furthermore, Unosson et al. developed an enhancement for the element deletion technique by introducing a scaling function for the strain rate at the elements around the crack tip [98]. In this way, a better prediction is made of the state at the crack-tip for crack propagation and the fracture energy absorption is no longer mesh dependent. However, the crack tip enhancement was validated only for the case of impact on a ductile material with a pre-crack and has only been included in an in-house FE code. Song et al. [99] compared element deletion, XFEM and CZM for the dynamic propagation and branching of a single crack in 2D. They reported a very strong mesh sensitivity for the element deletion method,

where a structured mesh could not at all model crack branching or deviation of the crack from its initial straight line. With an unstructured mesh, the crack path could be reproduced and branching could be modelled, but not as physically observed. XFEM and CZM achieved better results for these aspects, but none of the methods could accurately predict the crack propagation speed. Despite the lack of accuracy, the authors acknowledge that fracture simulation by element deletion may improve for very fine meshes, as indicated in the work of Bourdin et al. [100]. However, Song et al. did also experience spurious failure of elements which they ascribe to elastic wave reflections.

The criterion for element deletion can be formulated in many different ways. For crack simulation of glass as an elastic-brittle material, a Rankine criterion in tension is the most logical choice. This formulation defines a critical limit to the maximum principal stress. Upon reaching this limit, the element stiffness may be set to zero immediately or a damage phase may follow in which the stiffness is gradually reduced. When the element stiffness is zero, strains at its material points are no longer calculated and the element is excluded from visualisation in post-processing. Additionally, the failure criterion can be made rate-dependent, e.g. by deformation rate dependency of the stress limit as in the Johnson-Holmquist JH2 model [101], or dependent of the loading time such as formulated by the Tuler-Butcher criterion.

An overview of the failure criteria for glass used in literature is given in Table 2.7. Some authors define a critical limit for the maximum principal strain or the strain energy density. It should be noted that these are not equivalent to the Rankine criterion, as shown in Fig. 2.28.

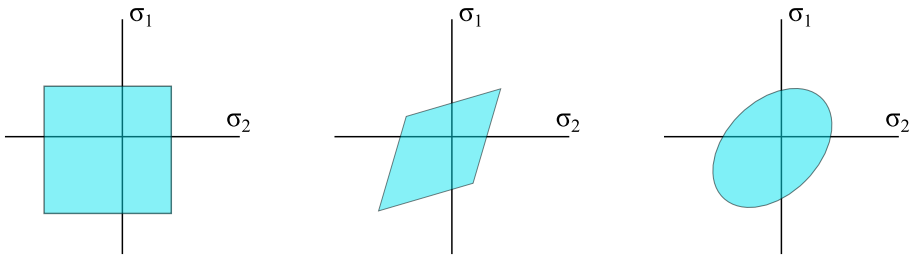

(a) Principal stress (Rankine)

(b) Principal strain (St. Venant)

(c) Strain energy density (Beltrami-Haigh)

Figure 2.28: Failure criteria for isotropic brittle materials.

The present work aims to investigate the possibility of simulating the fracture and fragmentation process of glass in a realistic manner. This implies the modelling of discrete crack formation with a credible crack path and sequence, which is necessary to later study the complex interaction between brit-

Table 2.7: Mechanical properties of materials in drop weight impact

Author(s)	Software and material model	Failure criterion
Dubois and Kolling, 2003 [102]	LS-DYNA: piecewise linear plasticity	$\epsilon_{Ic} = 1.0e-3$
Sun et al., 2005 [103]	ABAQUS: `VUMAT` for immediate deletion; LS-DYNA: modified piecewise linear plasticity	$\sigma_{Ic} = 65\,\text{MPa}$ (ABAQUS); $\epsilon_{Ic} = 9.0e-4$ (LS-DYNA)
Timmel et al., 2007 [104]	LS-DYNA: smeared laminated glass model	$\epsilon_{Ic} = 1.5e-3$
Larcher et al., 2008 [75, 105, 106]	EUROPLEXUS: self-defined failure models	$\epsilon_{Ic} = 1.2e-3$
Wu et al., 2010 [107]	LS-DYNA: JH2	constants from [101], $\sigma_{Ic} = 10-60\,\text{MPa}$
Pyttel et al., 2011 [108]	LS-DYNA: smeared cracking model	Threshold energy $E_c = 22.3\,\text{kNmm}$ in radius $R_c = 210\,\text{mm}$
Ivanov and Sadowski, 2011 [109]	ABAQUS: *Brittle Cracking	$\sigma_{Ic} = 40.8\,MPa$, $G_{Ic} = 104\,J/m^2$
Konrad and Gevers, 2010 [110, 111]	RADIOSS: self-defined failure model	biaxial tension (radial cracking): $\sigma_{Ic} = 300\,\text{MPa}$; uniaxial tension (concentric cracking): $\sigma_{Ic} = 50\,\text{MPa}$
Amadio and Bedon, 2012 [112–114]	ABAQUS: *Brittle Cracking	$\sigma_{Ic} = 120\,MPa$, $G_{Ic} = 100\,J/m^2$
Liu et al., 2012 [115]	LS-DYNA: modified piecewise linear plasticity	$\epsilon_{Ic} = 1.0e-3$
Peng et al., 2013 [116]	LS-DYNA: piecewise linear plasticity	$\epsilon_{Ic} = 1.0e-3$
Zhang et al., 2013 [117]	LS-DYNA: JH2	$\sigma_{Ic} = 150\,MPa$
Pelfrene et al., 2013 [118]	ABAQUS: *Brittle Cracking	$\sigma_{Ic} = 150\,MPa$, $G_{Ic} = 8.0\,J/m^2$
Pelfrene, Kuntsche et al., 2016 [119]	LS-DYNA: (a) elastic + erosion, (b) and (c) modified piecewise linear plasticity	(a) $\sigma_{Ic} = 81\,MPa$; (b) $\epsilon_{Ic} = 1.16e-3$; (c) $\sigma_{vm} = 81\,MPa$, $\epsilon_{pl,max} = 3e-4$

tle fracture and a polymer interlayer in laminated glass. For this reason, it is appropriate to use the Rankine failure criterion. In the following, several numerical approaches for element failure with this criterion are discussed and their performance is evaluated.

2.4.1 Hillerborg model: *Brittle Cracking in Abaqus

Hillerborg et al. [120] introduced a smeared crack model for concrete in finite elements by use of the cohesive zone concept. The smeared formulation denotes that a macro-crack is not represented explicitly, but rather that the model takes account of the effect of cracking in the form of an elastic stiffness reduction, or even elimination, at the integration points of an element. The traction-separation law used in this model is the initially-rigid law (see Fig. 2.11d), which is activated once the maximum principal stress at an integration point reaches the fracture strength σ_0. This is the Mode I, Rankine crack initiation criterion. Once a crack has initiated, the tensile stress perpendicular to the crack decreases with increasing crack width until the work performed on the element matches the fracture energy G_{Ic}. At that point, the element can no longer bear any tension in that direction. Compression can still be supported when the crack closes. The tensile softening is then halted until the crack grows again.

During the damage phase, also the shear stiffness $G_{\parallel}$ for shearing in the crack plane is reduced. In ABAQUS, a shear softening law may be defined in function of the Mode I crack opening u_c. $G_{\parallel}$ is reduced to zero at a crack displacement u_{cs}. Additionally, a crack opening displacement u_{cu} at ultimate failure of the element may be defined, at which point the element is deleted from the simulation. This may be before or after the stiffness across the original Mode I crack has been reduced to zero. Before u_{cu} is reached, additional cracks may initiate at the element's integration points, but only in a direction perpendicular to the original crack. Fig. 2.29 shows the material behaviour described by the Hillerborg model for the tensile stress perpendicular to the crack in function of the relative displacement of the nodes perpendicular to the crack. The initial stiffness is $K = E \cdot L_e$, where L_e is the undeformed distance between the nodes. When a crack initiates, the fracture energy consumes also the elastic strain energy contained in the element up to that point. The area under the triangle in Fig. 2.29, in units of [J/m^2], can be written as:

$$G_{Ic} = \frac{1}{2}\sigma_0(u_0 + u_{cf}) = \frac{1}{2}\sigma_0\, u_f \tag{2.16}$$

For the fracture energy to be consistent, the displacement at tensile failure should not be smaller than the displacement at crack initiation: $u_f \geq u_0$. This implies that:

$$\frac{1}{2}\sigma_0\, u_0 \leq G_{Ic}, \tag{2.17}$$

where $u_0 = L_e\, \sigma_0/E$. Thus, there exists a maximum allowable element size $L_{e,cr}$ for which the fracture energy can still be represented correctly:

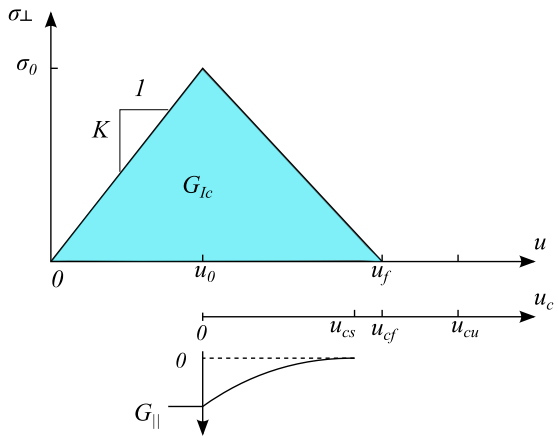

Figure 2.29: Tensile stress for Mode I cracking in function of relative nodal displacement and crack opening displacement; Shear stiffness reduction in function of crack opening displacement.

$$L_e \leq L_{e,cr} = \frac{2\,E\,G_{Ic}}{\sigma_0^2} \tag{2.18}$$

For a very brittle material such as glass, with a high stiffness and low fracture energy, this is quite a severe limit. Glass has an elastic modulus $E = 70\,\text{GPa}$ and fracture energy $G_{Ic} = 8\,\text{J/m}^2$. With an estimated strength of 80 MPa, the critical element size would be $L_{e,cr} = 0.175\,\text{mm}$. For the simulation of any realistically sized glass pane the calculation time would become unfeasibly high when such a fine mesh should be used. As such, the question becomes how and whether the *Brittle Cracking model in ABAQUS can be used when the critical element length is not respected.

2.4.1.1 Unit element

A simple model with a *unit element* is introduced to investigate how the material model performs when the element length criterion is satisfied and when it is not. The model, represented in Fig. 2.30, consists of a single solid element of size $1 \times 1 \times 1\,\text{mm}$. The element uses linear, reduced integration and consequently has one integration point at which the strains and stresses are evaluated. The material properties in this numerical example are chosen quite similar to those of glass and are listed in Table 2.8. With these properties, the element length criterion is satisfied when $G_{Ic} \geq 50\,\text{J/m}^2$. Three simulations are executed with different values for the fracture energy.
At this point, the intention is to evaluate the material model without taking into account dynamic effects in the elastic deformation. In an explicit calcu-

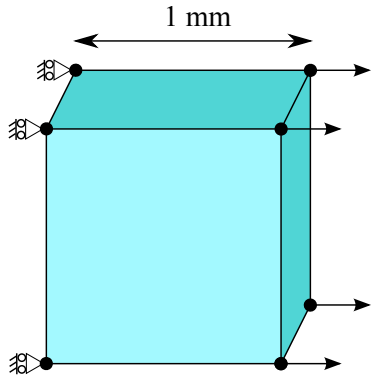

Figure 2.30: Unit element and boundary conditions.

Table 2.8: Material properties for unit element

Young's modulus	E	100 GPa
Poisson's ratio	ν	0.25
Fracture strength	σ_0	100 MPa
Fracture energy	G_{Ic}	100; 50; 10 J/m^2
Shear failure displacement	u_{cs}	1 µm
Ultimate failure displacement	u_{cf}	2 µm
Density	ρ	$2.5 \cdot 10^9$ kg/m^3

lation, this can be done in two different ways: either by loading the element very slowly or by artificially scaling the material density. In the first case the calculation time will be very high and requires a large data space. In the second case, the density is increased, which artificially slows down the wave speeds in the material and has the added advantage of increasing the time increment, so that the calculation is sped up. If the density is increased by a factor 10^6, the material wave speed decreases by 10^3 and the stable time increment increases by 10^3 according to the CFL condition.[2] Consequently, a high density of $2.5 \cdot 10^9$ kg/m^3 is chosen for the unit element.

The left side nodes of the element are constrained in horizontal direction while the right side nodes are imposed a horizontal displacement of 4 µm over the duration of 1 s. The fracture strength should be reached when the strain amounts to 0.1% in uniaxial tension, which occurs when the displacement of the right nodes is $u_0 = 1\,\mu$m.

[2]Courant-Friedrichs-Lewy condition for the stable time increment in explicit calculation: $\partial t = C_{CFL} \cdot \min_i \left(\frac{L_{e,i}}{c_i + |\boldsymbol{v}_i|} \right)$, where C_{CFL} is a predefined constant, $L_{e,i}$ is the shortest nodal distance for element i, c_i is the material wave speed in element i and $\boldsymbol{v}_i$ is the velocity vector at element i.

First, the case is considered where the element length criterion is fulfilled with some margin. The fracture energy is taken as $G_{Ic} = 100\,\mathrm{J/m^2}$. Then, the tensile stiffness across the crack is reduced to zero upon a displacement $u_f = 2u_0 = 2\,\mu\mathrm{m}$. This is seen also in the simulation results, presented in Fig. 2.31 and Fig. 2.32. The final value of the damage dissipation matches the fracture energy: $G_{Ic} \cdot A = (100\,\mathrm{J/m^2}) \cdot (1\,\mathrm{mm})^2 = 100\,\mu\mathrm{J}$.

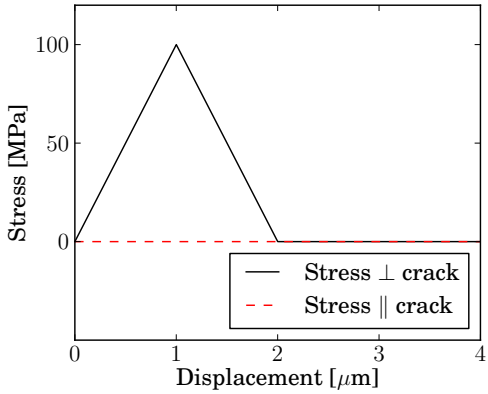

Figure 2.31: Stress in function of displacement for unit element using *Brittle Cracking with $G_{Ic} = 100\,\mathrm{J/m^2}$.

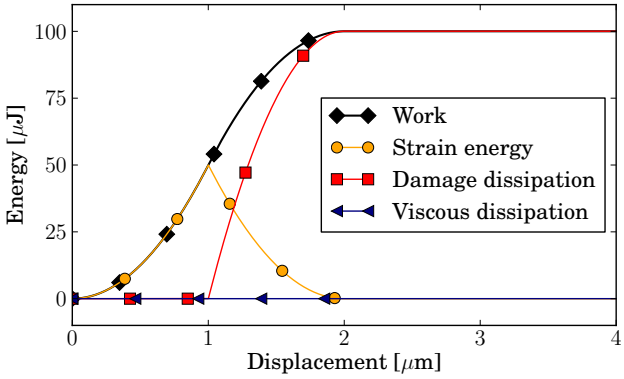

Figure 2.32: Energy balance in function of displacement for unit element using *Brittle Cracking with $G_{Ic} = 100\,\mathrm{J/m^2}$.

When the fracture energy is taken at the limit, i.e. $G_{Ic} = \sigma_0\, u_0\, /2 = 50\,\mathrm{J/m^2}$, it is expected that the stiffness in the direction of the maximum principal stress is set to zero immediately upon reaching the fracture strength. From

the simulation results in Figs. 2.33 and 2.34, this does appear to be the case. However, taking a closer look at the point of crack initiation in Fig. 2.33, the stiffness reduction does not take place at once, but a softening takes place over some 20 time increments. It is not explained in the ABAQUS manual [121] how this is implemented. Furthermore, it is seen that dynamic springback of the deformed element causes oscillations in all tensile stress components.

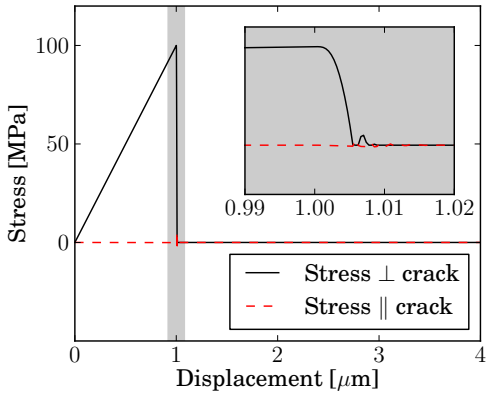

Figure 2.33: Stress in function of displacement for unit element using *Brittle Cracking with $G_{Ic} = 50\,\mathrm{J/m^2}$.

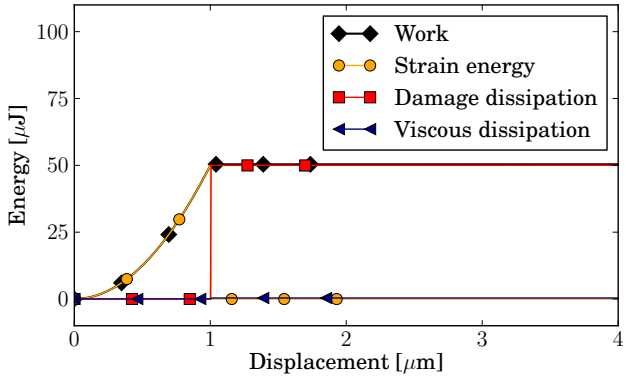

Figure 2.34: Energy balance in function of displacement for unit element using *Brittle Cracking with $G_{Ic} = 50\,\mathrm{J/m^2}$.

If the element length criterion is not respected, the *Brittle Cracking material model reacts quite differently. Simulation results for $G_{Ic} = 10\,\mathrm{J/m^2}$ are shown in Figs. 2.35 and 2.36. When the maximum principal stress reaches σ_0,

the crack opens without tensile softening, similar to linear elastic – perfectly plastic behaviour. The crack displacement increases until an additional work $\sigma_0\, u_f = 2\, G_{Ic}$ is consumed as damage energy. Then, the tensile stiffness across the crack is set to zero at once within one time increment. Such a sudden change in stiffness causes much larger oscillations in the remaining stress components, which are damped by the bulk viscosity. Damping of shock waves certainly occurs physically, but in explicit analysis the bulk viscosity, sometimes referred to as artificial viscosity, is primarily a numerical means to aid in regularising the mesh when high-amplitude waves propagate through the elements (see Ref. [122] for theoretical background). When the energy dissipation due to damping by bulk viscosity becomes too high, the simulation result is generally not acceptable.

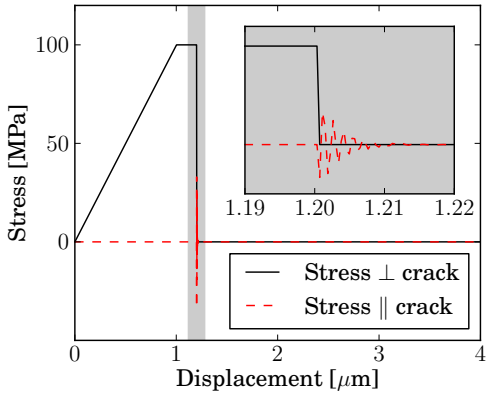

Figure 2.35: Stress in function of displacement for unit element using *Brittle Cracking with $G_{Ic} = 10\,\mathrm{J/m^2}$.

The response observed in this last example is not documented in the software manual [121] and the *Brittle Cracking model is clearly not intended to be used in this way. For a material such as concrete, which has much lower stiffness modulus and a higher fracture energy, there should not be any problems for the mesh size. Although the element size to satisfy the critical element length cannot practically be realised for the simulation of a glass panel, the penalty of an overestimation of the fracture energy and a small amount of viscous dissipation may still be acceptable for a larger model. From the previous examples, the most favourable situation would be where the fracture energy is chosen not as its physical value, but on the limit to fulfill the criterion with respect to the element lengths in the mesh. However, when a mesh with non-uniform element size is used, this is not practically feasible.

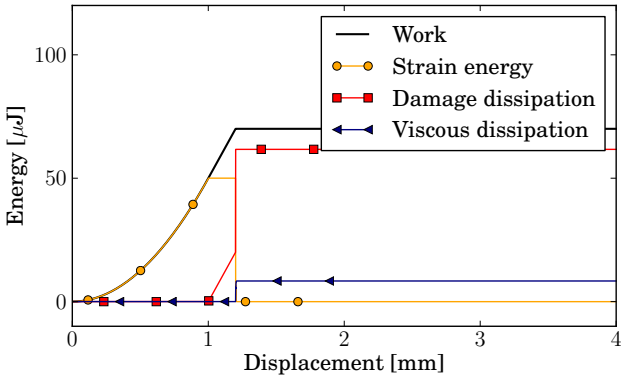

Figure 2.36: Energy balance in function of displacement for unit element using *Brittle Cracking with $G_{Ic} = 10\,\mathrm{J/m^2}$.

The elastic springback is felt not only in the cracking element itself, but much more in the surrounding elements. To assess the consequence of different settings for the *Brittle Cracking algorithm, and for other element deletion models, a model with three unit elements is used as shown in Fig. 2.37. The material properties for these elements are given in Table 2.8, except that cracking is only defined for the middle element. The prescribed displacement at the boundary is now 12 µm in 3 s.

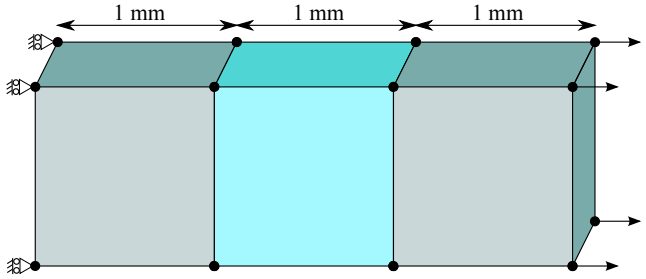

Figure 2.37: Model with three unit elements and boundary conditions; *Brittle Cracking is defined for the middle element.

A quantitative evaluation is enabled by comparing the amount of viscous dissipation at the end of the simulation, and is given in Table 2.9. It is seen that damping of stress oscillations is present for all used settings, except when the fracture energy is set sufficiently high to relieve the stresses of *all* elements in the model. This can be expected, as all the strain energy needs to be dissipated at the end of the simulation, when the middle element has fully failed.

For a high fracture energy, $G_{Ic} = 100\,\mathrm{J/m^2}$, a clear tension softening behaviour could be discerned in Fig. 2.31. Although the same tensile softening behaviour is retained within the cracking element, this occurs at a much faster rate when multiple elements are present. Because the stiffness in the middle element is reduced, its strain increases rapidly, while the strain of the surrounding elements is relieved. For fracture energies in the range of 50 - 150J/m^2, the stress across the crack is reduced to zero in 3 to 24 time increments. The resulting energy balance for three unit elements with $G_{Ic} = 100\,\mathrm{J/m^2}$ is shown in Fig. 2.38. The number of time increments used in softening of the tensile stiffness does seem to aid in reducing the level of stress oscillations and achieve a better numerical stability of the result.

Table 2.9: Work and viscous damping at end of simulation with 3 unit elements

Fracture energy G_{Ic} [J/m^2]	Work [µJ]	Viscous dissipation [µJ]	ratio
10	170	102	60%
50	150	93	62%
100	150	44	29%
150	151	1.5	1%
300	300	0.04	0%

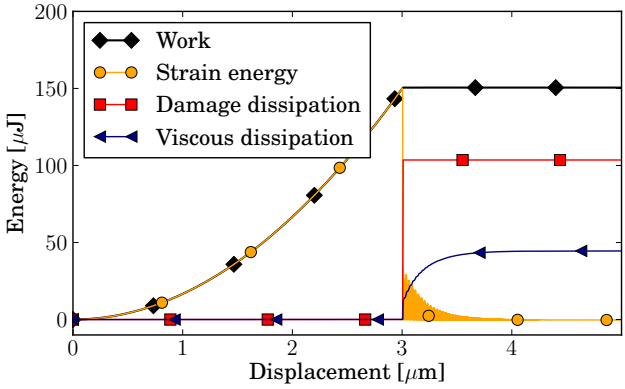

Figure 2.38: Energy balance in function of displacement for three unit elements using *Brittle Cracking with $G_{Ic} = 100\,\mathrm{J/m^2}$.

In conclusion, the *Brittle Cracking material model describes the tensile softening across a crack as a cohesive traction-separation as long as an element length criterion can be satisfied. For a material such as glass, this requires the use of tiny elements which is not practically feasible for simulating a realistically sized glass panel. In that case, a pseudo-plastic behaviour is observed instead

of tensile softening and the input values for damage behaviour somewhat lose their physical meaning. Moreover, at failure, the stiffness across the crack is reduced within one time increment, which may lead to additional instabilities in the analysis. In general, it is seen that allowing for the damage to develop over a longer period helps in reducing the level of stress oscillations in the surrounding elements.

2.4.1.2 Drop weight impact

The fracture and fragmentation of the small, monolithic glass plate under drop weight impact, introduced in Section 2.3, is simulated by use of the *Brittle Cracking model in Abaqus. Because the fracture pattern of a real glass plate does not only consist of perfectly concentric cracks, but foremost of radial cracks as seen in Fig. 2.39, axial symmetry can no longer be assumed.

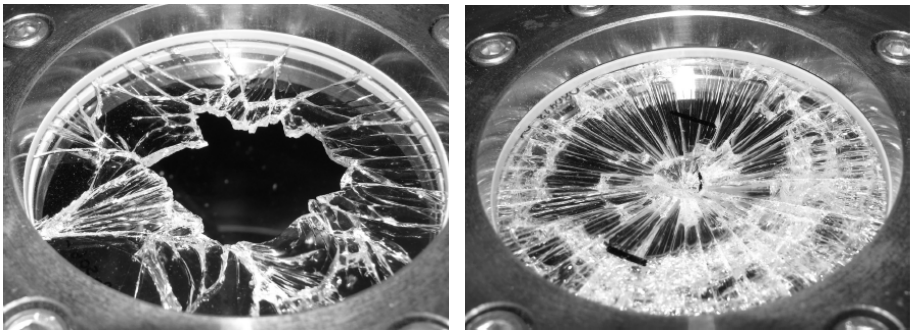

(a) **(b)**

Figure 2.39: Post-mortem photographs of $4 \times \varnothing 100$ mm samples under drop weight impact from 200 mm height: (a) glass only, and (b) glass fitted with safety window film (figure from De Pauw [5]).

A full 3D model is therefore built up in the same way as the axisymmetric model; with rigid impactor and steel clamping rings, 4 mm thick deformable propylene rings and the sample itself. For the fracture simulation by element deletion, great mesh dependence is expected. The mesh of the glass part can be built up in various ways. The importance of the element type and mesh topology is first investigated. Subsequently, the influence of the mesh size can be assessed.

Abaqus offers two algorithms to create a mesh with hexahedral elements: the *advancing front* algorithm generates an unstructured mesh for non-rectangular parts and the *medial axis* algorithm creates a structured mesh. However, both built-in algorithms result in the creation of locally tiny elements compared to the nominal element size. This is a significant disadvantage for explicit analysis, because the stable time increment decreases with decreasing element length as

described by the CFL condition. For this reason, a specialised meshing software is used, i.e. GMSH [123]. Four different mesh topologies with characteristic element length of 0.75 mm are shown in Figure 2.40: an unstructured mesh created with the standard Delaunay algorithm, a semi-structured mesh created with a frontal Delaunay algorithm, a structured mesh created by division into domains and a transfinite algorithm and a structured mesh generated by the medial axis algorithm in ABAQUS. Each mesh uses 4 elements through the thickness, which is the minimum for mesh convergence of the elastic response (see Sec. 2.3). While the minimum element length is characteristic for the stable time increment, the maximum element length is characteristic for the error in the fracture energy when an element fails. For both, the most extreme value of all meshes is found for the structured mesh created by ABAQUS.

The settings for the *Brittle Cracking material model are given in Table 2.10. At this point, the fracture energy is set at its physical value. The crack opening displacement u_{cf} at which the element is effectively deleted should be greater or equal to the crack opening displacement u_{c0} at which the stiffness across the crack is reduced to zero. When the element length criterion is not fulfilled, i.e. when $L_{e,max} > L_{e,cr}$, u_{c0} can be calculated as:

$$u_{c0} = 2\,G_{Ic}/\sigma_0 \tag{2.19}$$

Table 2.10: Settings for glass in *Brittle Cracking material model

Strength	σ_0	255 MPa
Fracture energy	G_{Ic}	7.8 J/m^2
Shear failure displacement	u_{cs}	$6.12 \cdot 10^{-8}$ m
Ultimate failure displacement	u_{cf}	$6.12 \cdot 10^{-8}$ m

The glass strength is the singlemost distinctive parameter for the cracking behaviour in the numerical simulation. However, to pin down a value for the strength is not self-evident because of the very high variability that is observed experimentally. The critical stress in Table 2.10 is motivated by the average strength measured in quasi-static testing, increased by influence of the loading rate. De Pauw [5] performed ball-on-ring tests for axisymmetric bending up to failure. The test specimens were of the same size and shape, and in fact of the same production batch as those used in the drop weight impact. The flexural strength in these tests was on average 150 MPa. The loading rate in the impact tests at a drop height of 0.2 m can be estimated from the slope of the increasing stress versus time, shown in Fig. 2.24, and is about $3.5 \cdot 10^5$ MPa/s. Interpolating between the relative strengths in the experiments of Nie et al., given in Table 2.4, a strength that is 70% higher than the quasi-static value may be expected at this loading rate. Indeed, in Fig. 2.17, three of the four test

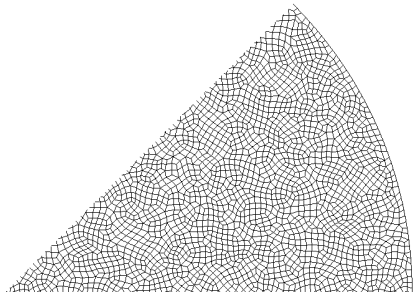

(a) Unstructured: 71k elements, $L_e = 0.53 - 1.07$mm

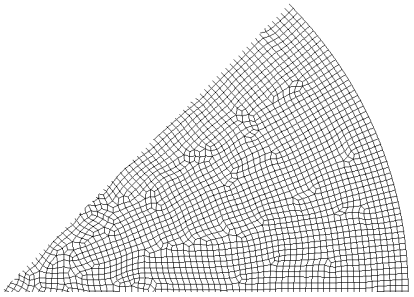

(b) Semi-structured: 62k elements, $L_e = 0.58 - 1.00$mm

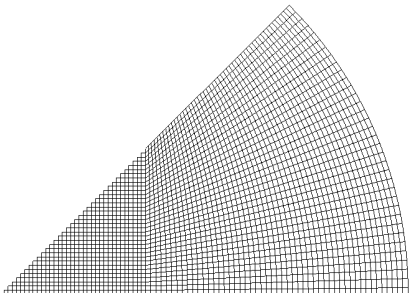

(c) Structured (transfinite): 74k elements, $L_e = 0.50 - 1.14$mm

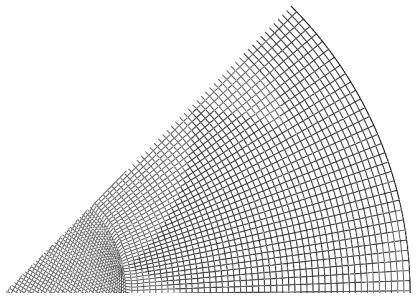

(d) Structured (medial axis): 64k elements, $L_e = 0.07 - 1.29$mm

Figure 2.40: Mesh topology for $4 \times \varnothing 100$ mm glass plate with hexahedral elements; 1/8 shown.

specimens fail around the second peak in the acceleration, which corresponds to a stress of about 250 MPa in Fig. 2.24.

First, the results for the structured mesh types are examined. The accelerations on the impactor in the simulated results are given in comparison with a representative specimen from experimental tests in Fig. 2.41. It is quickly seen that the accelerations in the simulation still attain high levels while in the experiment no forces act on the impactor after some 0.4 ms. In the experiment, complete fragmentation of the sample occurs very fast, the impactor then no longer experiences any resistance and simply drops through. This is not the case in the simulations where fragmentation requires some time. Moreover, Figs. 2.42 and 2.43 show that fewer cracks appear in the simulation than in the tested glass specimen: 4 to 8 radial cracks are formed in the simulations versus ca. 40 in the experiment.

The simulated glass plate first deforms elastically until the critical stress is reached somewhere in the mesh. For the GMSH-generated structured mesh, the point of crack initiation agrees well with the experiment. For the mesh

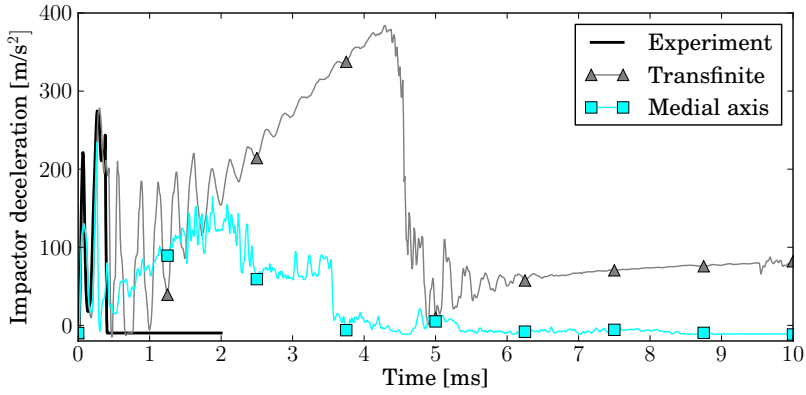

Figure 2.41: Comparison of simulation results for structured hexahedral mesh types to experimental accelerations in drop weight impact on a glass disk.

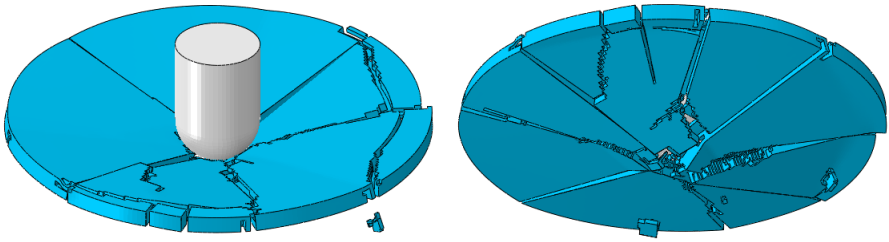

(a) Top view **(b)** Bottom view

Figure 2.42: Fragmentation of simulated 4 × ∅100 mm glass plate with *Brittle Cracking at $t = 10$ ms; structured mesh by transfinite algorithm.

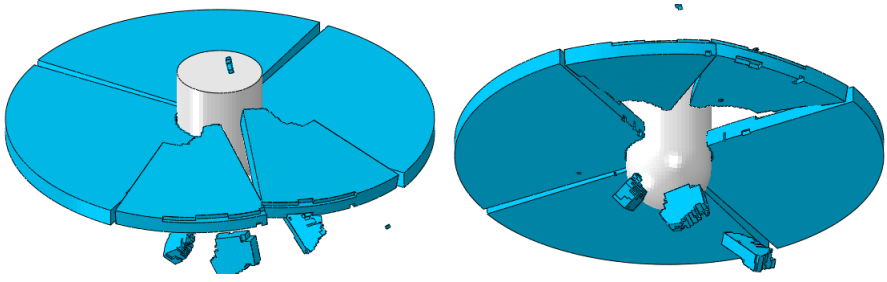

(a) Top view **(b)** Bottom view

Figure 2.43: Fragmentation of simulated 4 × ∅100 mm glass plate with *Brittle Cracking at $t = 10$ ms; structured mesh by medial axis algorithm.

created in ABAQUS, the first element failure occurs earlier and not on the bottom of the plate which is in tension, but directly underneath the impactor. The accelerations of this simulation also remain lower and decrease to the gravity constant sooner. However, this is attributed to gradual failure of top face elements in direct contact with the impactor, after which the contact definition is no longer valid and the impactor just seems to drop through the material, as shown in Fig. 2.44. This is not observed for a more uniform mesh size. But in that case, the force on the impactor is very high even after the first cracks appear. The acceleration is finally reduced at $t = 5\,\text{ms}$, when full fragmentation of the plate occurs in the simulation. The choice of mesh type is certainly important for element deletion and is further investigated.

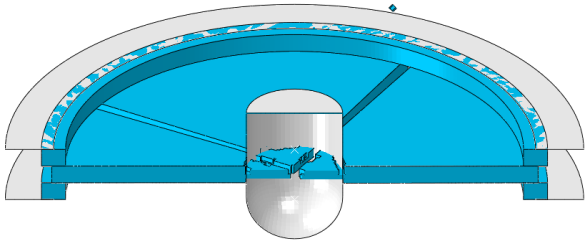

Figure 2.44: Local element failure and loss of contact for structured mesh by medial axis algorithm.

The results for the unstructured and semi-structured mesh topologies are presented in Figures 2.45, 2.46 and 2.47. The cracking behaviour is more similar for these simulations. Although the structured and semi-structured meshes favour the formation of radial and concentric cracks, realistic crack paths are also found with a more random, unstructured mesh. This is interesting for more complex crack patterns. Then it is not needed to construct the mesh to match the crack pattern in advance.
For all simulations, the accelerations are still significantly high long after the glass has fragmented in the experiment. Moreover, more cracks are seen at the bottom side of the simulated glass plates than at the top face. Both are a consequence of the meshing by solid, reduced integration, hexahedral elements. For all cracks, the elements at the tension side are deleted first. Subsequently, adjacent elements in thickness direction are deleted until only the elements at the compression side are left, as shown in Fig. 2.48. These element remain intact until the overall deformation finally becomes too high. The cause for this behaviour is the same as the reason for hourglassing in linear, reduced integration elements: when loaded in pure bending, the integration point where stresses are evaluated is located in the middle of the element, which is on the neutral line. The integration point simply does not experience any stress. In the impact simulation, the load case of these elements is more complicated than pure bending, but the tensile bending stress is still underestimated in the

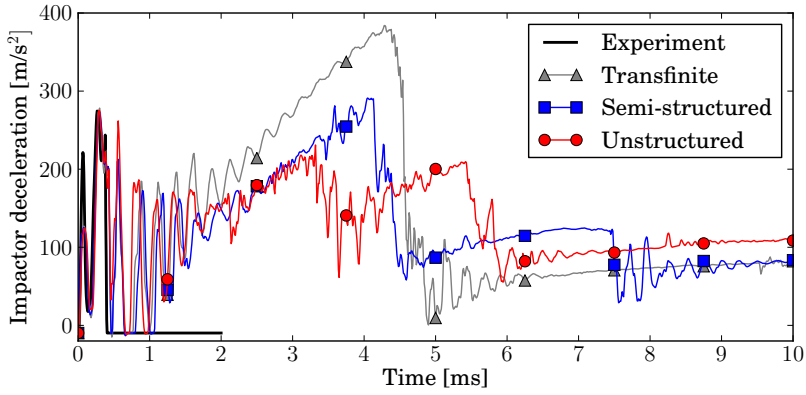

Figure 2.45: Comparison of simulation results for hexahedral mesh types to experimental accelerations in drop weight impact on a glass disk.

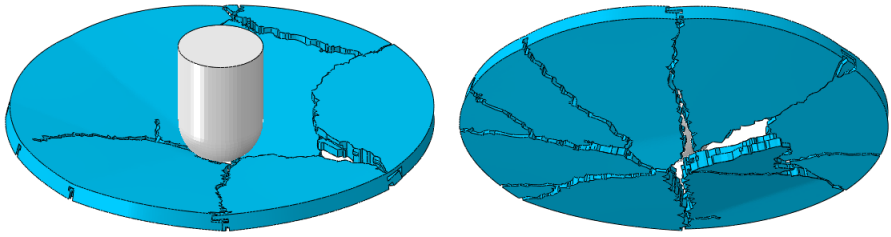

(a) Top view **(b)** Bottom view

Figure 2.46: Fragmentation of simulated 4 × ∅100 mm glass plate with *Brittle Cracking at $t = 10$ ms; unstructured mesh.

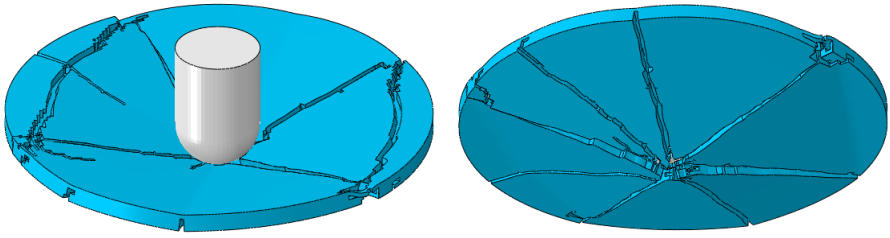

(a) Top view **(b)** Bottom view

Figure 2.47: Fragmentation of simulated 4 × ∅100 mm glass plate with *Brittle Cracking at $t = 10$ ms; semi-structured mesh.

calculation when only one element is present through the thickness. Unlike for a sharp crack in a solid continuum, the elements at the crack tip also do not experience stress intensity as described by LEFM.

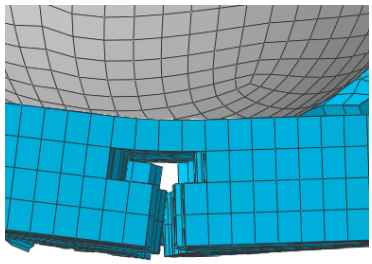

Figure 2.48: Crack arrest at last element in thickness direction for hexahedral elements with reduced integration.

This problem can be overcome in several manners; by using full integration elements, tetrahedral elements instead of hexahedrals or shell elements. The use of full integration elements results in purely local failure of the elements in contact with the impactor, without radial or concentric cracking. This punching-like behaviour is observed for every mesh type.

Meshing by linear tetrahedral elements does result in a more realistic cracking behaviour. The mesh used in this simulation is shown in Fig. 2.49 and has a randomised topology. The resulting crack pattern is given in Fig. 2.50.

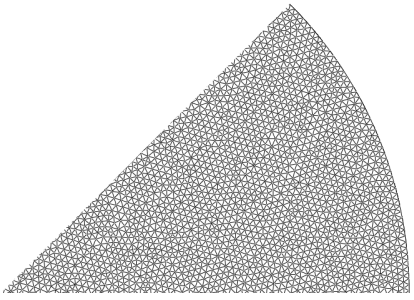

Figure 2.49: Mesh topology for $4 \times \varnothing 100\,\text{mm}$ glass plate with tetrahedral elements; 1/8 shown. 222k elements, $L_e = 0.68 - 1.73\text{mm}$.

For this type of mesh, radial cracks are formed directly through the thickness of the glass plate and propagate quickly from the center towards the edges. In the present simulation, 9 radial cracks are formed, which is still about 4 times

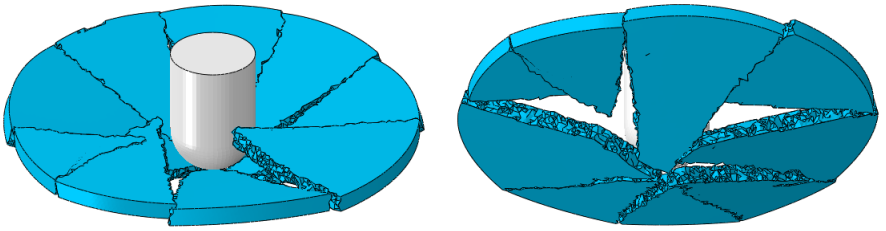

(a) Top view **(b)** Bottom view

Figure 2.50: Fragmentation of simulated $4 \times \varnothing 100\,\text{mm}$ glass plate with *Brittle Cracking at $t = 10\,\text{ms}$ for tetrahedral elements mesh.

less than in reality. Contrary to the experiment, no concentric cracks are being formed in the simulation and the fragments continue to exert a force on the impactor. It is also seen that, once fully broken, the glass fragments are not held fixed by the clamping rings, but are able to slide. This indicates that, although not needed for the elastic response, it may be required to include the bolting pressure in the boundary conditions for this type of simulation. Indeed, as shown in Fig. 2.51, this results in additional concentric cracking with propulsion of loose fragments, while sliding of fragments held between the clamping rings is more restricted.

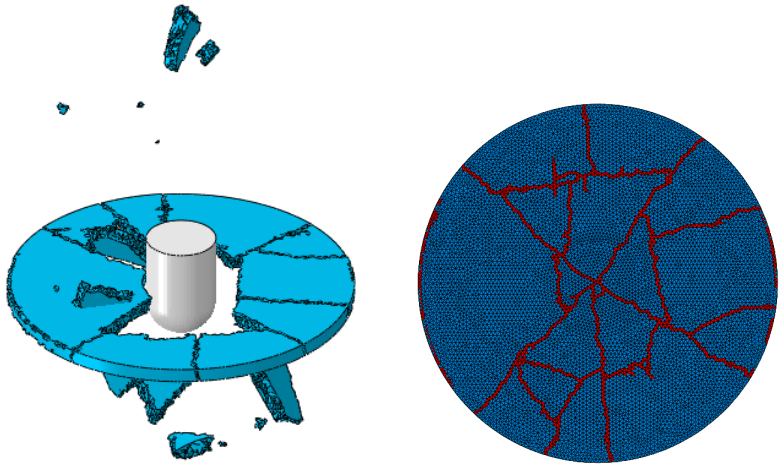

(a) **(b)**

Figure 2.51: Fracture of simulated $4 \times \varnothing 100\,\text{mm}$ glass plate with *Brittle Cracking at $t = 10\,\text{ms}$ for tetrahedral elements mesh with compressive clamping conditions: (a) fragmentation, and (b) failed elements.

The cracking pattern for the same simulation with a refined mesh is shown in Fig. 2.52, where the characteristic element length is $L_e = 0.75\,\text{mm}$. As this mesh already contains over 500,000 elements, further refinement is not considered because of computational efficiency. It should also be noted that true mesh convergence cannot be attained with an element deletion method.

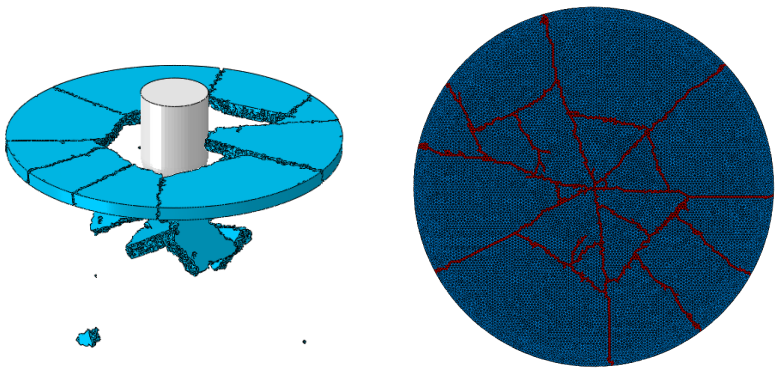

(a) **(b)**

Figure 2.52: Fracture of simulated $4 \times \varnothing 100\,\text{mm}$ glass plate with *Brittle Cracking at $t = 10\,\text{ms}$ for refined tetrahedral elements mesh with compressive clamping conditions: (a) fragmentation, and (b) failed elements.

Apart from a different crack topology, no major differences are noted in global behaviour of the refined model, which is also confirmed by the acceleration response in Fig. 2.53. In both simulations, the first radial cracks initiate at $t = 0.25\,\text{ms}$ with full fragmentation into 4 major shards appearing at $t = 0.6\,\text{ms}$. At this point in the experiment, the glass specimen is already fully broken and the impactor experiences no further resistance. In the simulation this occurs somewhat later, around $t = 2.0\,\text{ms}$ when further radial and concentric cracks quickly develop and the final fragmentation appears at $t = 2.5\,\text{ms}$. From then on, no force is exerted on the impactor any longer, or very little when it is still in contact with some of the glass debris.

It would have been expected that mesh refinement results in the formation of more radial and concentric cracks. This is not observed here, which is most likely due to the level of refinement not being significant enough.

The evolution of the energies for the drop weight impact simulation is shown in Fig. 2.54 for the tetrahedral mesh with $L_e = 1\,\text{mm}$. The kinetic energy lowers considerably in the first stage of the impact, corresponding with the deceleration of the impactor. The amount of viscous dissipation is due the damping of stress waves in the material that originate from the fast stress release in the cracked elements. The frictional dissipation results primarily

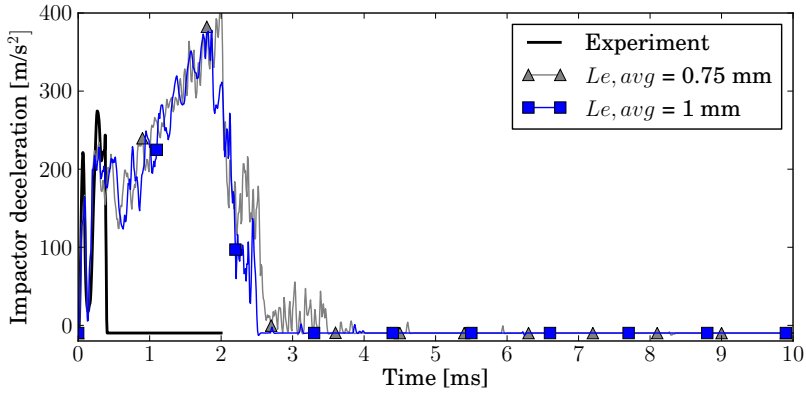

Figure 2.53: Comparison of simulation results for tetrahedral mesh type with compressive clamping conditions to experimental accelerations in drop weight impact on a glass disk.

from the glass fragments vibrating while being held between clamping rings. It would be expected that the elastic strain energy in the model goes back to zero when all cracks have been formed and the impactor experiences no further resistance of the glass. Instead, it is seen that the strain energy remains rather high, while damage dissipation is almost negligible. On closer inspection, the failed and deleted elements in the model show a constant, non-zero, and indeed quite high strain energy after they have failed. In that situation these elements are unable to carry stresses, which means that the remaining strain energy is not physical. This seems to be a bug in the built-in material model and it would be more logical to interpret this part of the strain energy as damage dissipation.

It would be interesting to look further into the *Brittle Cracking model by altering the set value for the fracture energy. As resulting from the analysis of unit elements, the most favourable setting would be where the fracture energy is chosen on the limit with respect to the element length. However, the glass disk cannot be meshed with a truly uniform element size. In this case, it is chosen to set the fracture energy that matches with the largest element length according to Eq. 2.18 in order to avoid a too small fracture energy for the entire mesh. Unfortunately, this causes excessive distortion during the damage phase for smaller elements upon which the analysis is disrupted and the simulation results become meaningless.

2.4.1.3 Conclusions

The Hillerborg fracture model, included in ABAQUS under the keyword *Brittle Cracking, has been investigated for its application in the simulation of glass

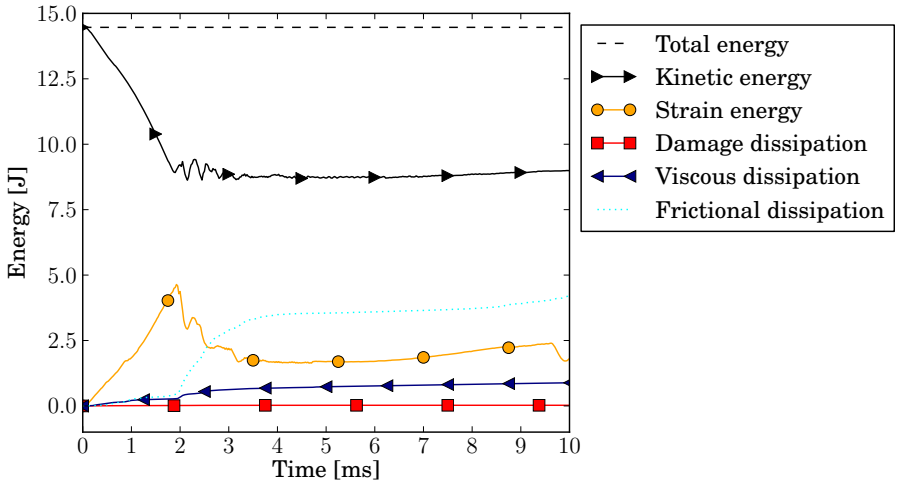

Figure 2.54: Energy balance for tetrahedrally meshed $4 \times \varnothing 100$ mm glass plate with compressive clamping conditions.

cracking. For correct representation of the fracture energy, a maximum allowable element length exists. For glass, having a high stiffness and strength in combination with a low fracture energy, this requires meshing by tiny elements which is not practically feasible for simulation of engineering problems. The behaviour of the damage model also changes when the element length criterion is not satisfied. Instead of elastic softening perpendicular to the crack, a pseudo-plastic phase exists during which an additional amount of energy is absorbed as damage and the stiffness across the crack is eventually set to zero within one time increment.

In simulation of the drop weight impact test on a small, monolithic glass plate, several mesh types with continuum elements have been evaluated for crack simulation with *Brittle Cracking. A more uniform element size is favourable in these analyses, both for achieving a larger stable time increment and for stability of the calculation with element deletion. Because mesh dependency is inherent to the element deletion technique, a mesh topology can be chosen to favour the crack formation. A structured mesh would in this case be ideal for radial and concentric crack propagation, but it is seen that a realistic cracking pattern comes forth from an unstructured mesh as well. However, when meshed by hexahedral solid elements, the simulated glass plate shows a delay in crack formation through the thickness. This originates from a zero-energy mode at the integration point of the last element to be cracked in the thickness direction. When loaded in bending, the corresponding stress is highly underestimated in the concerned integration point and does not reach the Rankine critical stress

until a much later time. Better fragmentation behaviour is achieved by a tetrahedral elements mesh, although much more tetrahedral elements are needed for convergence of the elastic response. Whereas the compressive clamping conditions on the specimen are not needed for simulation of the elastic response, this is required in fracture simulation. The firmer clamping prevents sliding of glass fragments when broken and is also important to correctly capture the subsequent bending of these fragments which facilitates the formation of concentric cracks.

The fracture energy in the simulations is overestimated compared to its physical value for glass, but it is seen that the total dissipation due to cracking is still negligible in comparison with the other energy quantities in the simulation.

2.4.2 Immediate element deletion

A different, very straightforward approach to crack simulation by element deletion consists of the direct removal the element upon reaching a failure criterion. This approach has been used by many authors, not only for the simulation of glass fracture, but for a great variety of problems. It can also be applied for highly deformed elements that are distorted in a way that they could endanger the stability of the calculation. In essence, all stress components of an element are set to zero within one time increment of reaching a failure criterion at one or more of its integration points. No damage or softening phase is included, nor is the directionality of the crack taken into account.
This type of element deletion is readily available in the commercial software package LS-Dyna for a number of different failure criteria. In Abaqus, this is not a standard option, but it can quite easily be implemented for a linear elastic-brittle material as a user-defined material model for explicit analysis by the `VUMAT` subroutine.

2.4.2.1 Unit element

The stresses and energies for the unit element with scaled density are given in Figures 2.55 and 2.56. All stress components are set to zero when the criterion is met and no stress oscillations can take place within the element. Therefore also no viscous dissipation is seen in the energy balance for the unit element. The elastic strain energy is entirely replaced by damage dissipation upon failure, with no dependencies on element size.
The situation is quite different for the simulation with three unit elements, as shown in Fig. 2.57. When the middle element is very suddenly deleted, that causes stress oscillations of large amplitude in the remaining elements. These stress waves decay under the influence of the bulk viscosity, but that requires a large amount of dissipation. Table 2.11 gives the dissipation for this model, in analogy with Table 2.9.

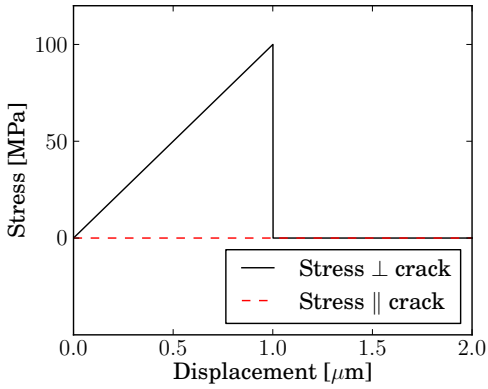

Figure 2.55: Stress in function of displacement for unit element using immediate deletion.

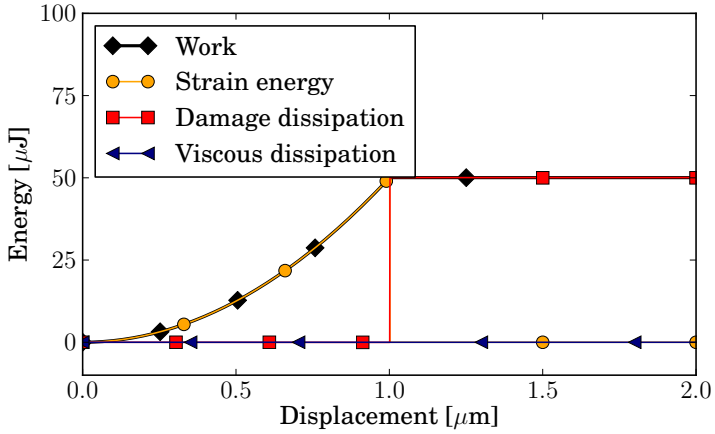

Figure 2.56: Energy balance in function of displacement for unit element using immediate deletion.

Table 2.11: Work and viscous damping at end of simulation with 3 unit elements

Fracture energy G_{Ic} [J/m^2]	Work [μJ]	Viscous dissipation [μJ]	ratio
N/A	150	100	67%

In the article by Song et al. [99], it is the reflection and interference of these stress waves that causes unexpected failure of elements away from the crack tip. This is shown in Fig. 2.58 for the case of dynamic crack growth in a notched steel plate after impact by a projectile.

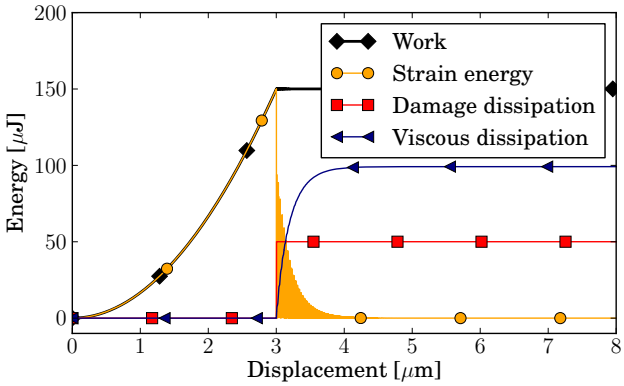

Figure 2.57: Energy balance in function of displacement for three unit elements and immediate deletion.

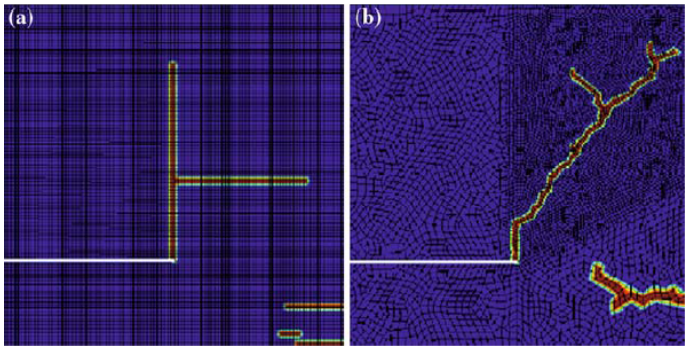

Figure 2.58: Crack paths for (a) structured and (b) unstructured mesh; spurious element failure in lower right corner (Figure from Song et al. [99]).

2.4.2.2 Drop weight impact

The drop weight impact on a ∅100 mm glass plate is simulated with immediate element deletion upon reaching the Rankine criterion: $\sigma_I \geq 255\,\text{MPa}$. Drawing from the conclusions in the previous section, a tetrahedral mesh (characteristic element size $L_e = 1.0\,\text{mm}$) is used and compressive clamping conditions are applied. From the deceleration of the impactor, given in Fig. 2.59, it appears that a much faster cracking is achieved than for the Hillerborg model, and the simulated result shows a better match with the experimental curve. However, Fig. 2.60 shows the glass fragmentation, from which it becomes clear that the technique of immediate element removal does not at all reproduce a realistic cracking behaviour. This most likely stems from the absence of a damage phase in which the crack direction is taken into account for softening of the elastic

stiffness.

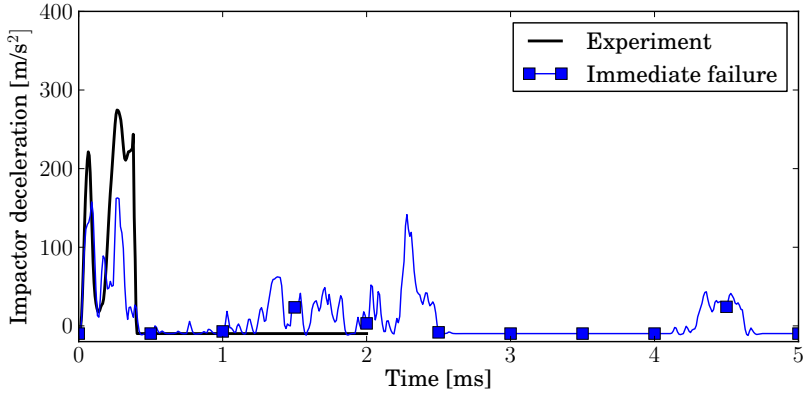

Figure 2.59: Comparison of simulation results for tetrahedral mesh type with immediate element deletion to experimental accelerations in drop weight impact on a glass disk.

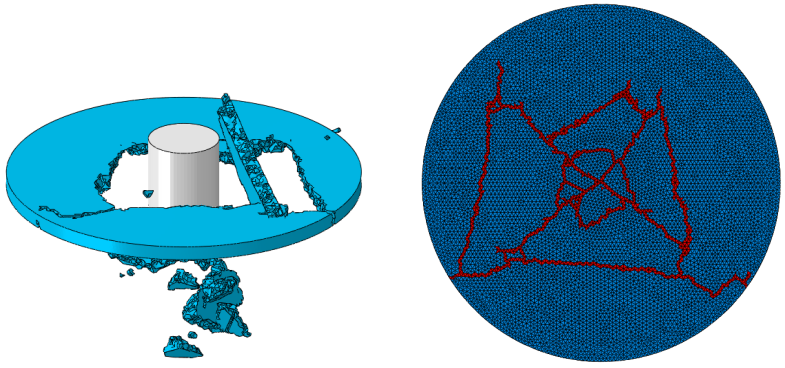

Figure 2.60: Fracture of simulated $4 \times \varnothing 100$ mm glass plate with immediate element deletion at $t = 10$ ms for tetrahedral elements mesh: (a) fragmentation, and (b) failed elements.

The energies for this simulation are given for completeness in Fig. 2.61. The very fast fragmentation does not decelerate the impactor much, so that the kinetic energy remains high and even rises above its original value because of gravity acting on the impactor and the glass debris. This energy balance would in fact better reflect the real behaviour in the experiment, but the crack formation unfortunately does not.

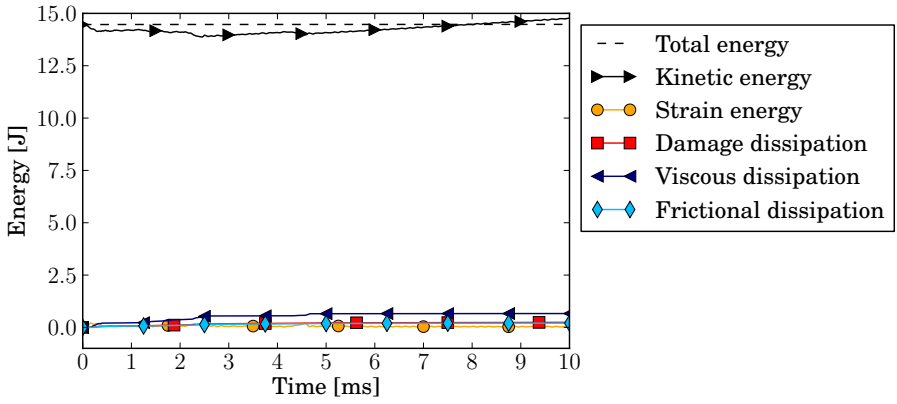

Figure 2.61: Energy balance for tetrahedrally meshed $4 \times \varnothing 100$ mm glass plate with immediate element deletion.

2.4.3 Crack delay model for glass cracking

It may be clear that the default implementations for element deletion in commercial FE software are flawed to model brittle fracture in glass. Alternative formulations can be developed to overcome the identified shortcomings. Moreover, a damage model may be designed to better capture the physical nature of glass fracture. Before discussing the implementation of a user-defined material model as `VUMAT` in Abaqus/Explicit, the desired characteristics of an element deletion cracking model for glass are listed:

- Brittle fracture should occur fast, but a damage softening phase of finite duration should be present in order to avoid instabilities. The stiffness across the crack should be monotonously decreasing during this damage phase.
- Directionality of the crack should be taken into account to achieve realistic crack propagation.
- The element length criterion in Eq. 2.18 applies to any element deletion model. Thus, the fracture energy will most likely be overestimated when using an element size that suits a practical engineering problem. As seen before, this can be acceptable when the share of damage dissipation remains low compared to other energy quantities in the numerical analysis.
- When a crack has initiated in an element, the subsequent constitutive behaviour should be independent of the element size as much as possible.

A possible cracking model that meets these requirements can be based on the concept of delay damage, as described for fibre reinforced plastics on the

mesoscale by Allix et al. [124]. The main assumptions for such damage model are that (i) the evolution of damage due to variations of forces is not instantaneous, and (ii) a maximum damage rate exists, just as a maximum crack propagation velocity exists.

Another key issue is the identification of energy dissipated during fracture. The fracture surface energy G_{Ic} for a stationary crack in glass under quasi-static loading is a quite well-known value (see Table 2.3). This is defined as the energy required to separate two newly created free surfaces and can be associated with a characteristic length u_{cf} in a cohesive traction-separation law:

$$G_{Ic} = \int_0^{u_{cf}} \sigma \, \mathrm{d}u_c, \tag{2.20}$$

where u_c is the crack opening width. At $u_c = u_{cf}$, the crack surfaces are fully separated and the traction σ should be nullified. The traction-separation law can be described by a single scalar damage parameter d, defined as the relative variation of the elastic modulus:

$$\sigma = E_0(1-d)\left\langle \epsilon \right\rangle_+ - E_0 \left\langle \epsilon \right\rangle_- , \tag{2.21}$$

where E_0 is the Young's modulus for undamaged material, and $\langle \cdot \rangle$ are Macaulay brackets, used to distinguish the behaviour in tension and in compression.

The damage function $d(u_c)$ for quasi-static behaviour should be monotonically increasing with the crack opening width, such that:

$$\begin{aligned} d(u_c < 0) &= 0 \\ d(u_c \geq u_{cf}) &= 1 \end{aligned} \tag{2.22}$$

Moreover, the damage is irreversible, i.e. the damage parameter d cannot decrease when the crack opening width decreases. Assuming linear behavior of the traction-separation relation, the damage increment can be written as:

$$\Delta d = \max(\Delta\epsilon_\perp / \epsilon_{cf}, 0), \tag{2.23}$$

where $\Delta\epsilon_\perp$ is the incremental strain in the direction perpendicular to the crack and $\epsilon_{cf} = u_{cf}/L_e$ with L_e being the characteristic size for the considered element. The crack opening width at failure u_{cf} can in turn be calculated as:

$$u_{cf} = \frac{2G_{Ic}}{\sigma_0}, \tag{2.24}$$

where σ_0 is the fracture strength of the material for a brittle failure mode defined by the Rankine criterion.

Under dynamic loading, the damage increment should be bounded by a maximum damage rate $\dot{d}_{max}$:

$$\Delta d \leq \dot{d}_{max}\, \Delta t \tag{2.25}$$

This maximum damage rate can be linked to the maximum crack velocity v_c which is a physical property for brittle materials. Suppose that a crack initiates at one edge of the element. Then the crack tip may not cross the element by a speed greater than v_c. Or otherwise stated, the damage may not increase at a rate faster than the crack can run through the element, i.e.:

$$\dot{d}_{max} = v_c / L_e \tag{2.26}$$

The described material behaviour is schematically represented in Fig. 2.62. The required input parameters to define the cracking behaviour for this material model are (i) the strength σ_0, (ii) the fracture energy G_{Ic} for a single crack under quasi-static loading , and (iii) the maximum crack velocity v_c. These are all physical material properties and are valid regardless of the element size.

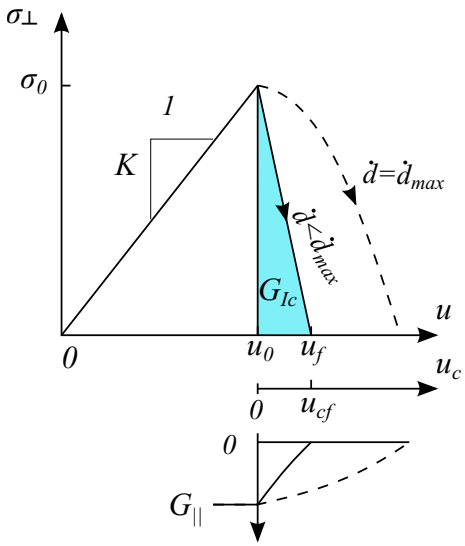

Figure 2.62: Tensile stress for Mode I cracking with crack delay in function of relative nodal displacement; shear stiffness reduction in function of crack opening displacement.

A few notes can be made regarding the physical interpretation of this damage model:

- The fracture energy G_{Ic} used as input parameter is defined as the energy needed to create two free surfaces by cracking and is given by Eq. 2.20.

In the material model, an opening crack is not modelled explicitly (for this would require element enrichment such as in XFEM), but rather its effect on the element stiffness is taken into account. In the simulation output, damage dissipation is defined as the difference between the work performed on the element and the strain energy. For the quasi-static case, this means that the dissipated energy by fracture of an element amounts to G_{Ic} added with the strain energy that is present in the element prior to cracking.

- In the dynamic case, the damage rate is bounded by the crack propagation velocity. Then it is possible that $\Delta d < \Delta\epsilon_{\perp}/\epsilon_{cf}$. Consequently, the effective fracture energy can also be greater than G_{Ic}. As shown by Sharon and Fineberg [57], the experimentally measured fracture energy of a crack propagating at $v = v_c$ also appears greater than G_{Ic}, because at this stability limit many micro-crack branches are created which increase the effective fracture surface.

- The maximum crack propagation velocity cannot be enforced on the mesh scale. It is possible that damage increases for several adjacent elements simultaneously, such that the propagation velocity of the simulated crack is greater than v_c. This will not likely be the case for a realistic engineering problem, but it is not prohibited by the current finite element formulation either.

The stress calculation in the damage phase takes account of the direction of the crack. A rotated Cartesian coordinate system is used in which one direction is perpendicular to the crack face and the two other directions are parallel with the crack. The rotation matrix $\mathbf{R}$ is composed of the direction cosines of the eigenvectors associated with the stress state in the element at the moment of reaching the Rankine breakage criterion. For the plane stress state (by which shell elements are calculated), the stresses in the damage phase are calculated as given by Equations 2.27a to 2.27c. The stress calculation for 3D solids follows the same principle.

$$\sigma_{\perp} = \frac{(1-d)\,E_0}{1-\nu^2}\epsilon_{\perp} + \frac{\nu\,E_0}{1-\nu^2}\epsilon_{\parallel} \tag{2.27a}$$

$$\sigma_{\parallel} = \frac{\nu\,(1-d)\,E_0}{1-\nu^2}\epsilon_{\perp} + \frac{E_0}{1-\nu^2}\epsilon_{\parallel} \tag{2.27b}$$

$$\sigma_{\perp\parallel} = \frac{(1-d)\,E_0}{1+\nu}\epsilon_{\perp\parallel} \tag{2.27c}$$

In analogy with the previous sections, this material model is evaluated for a unit element and for drop weight impact on a circular glass plate.

2.4.3.1 Unit element

Firstly, the single unit element of Fig. 2.30 is considered. The material properties used as input parameters for the `VUMAT` are given in Table 2.12.

Table 2.12: Material properties for unit element.

Young's modulus	E	$100\,\mathrm{GPa}$
Poisson's ratio	ν	0.25
Fracture strength	σ_0	$100\,\mathrm{MPa}$
Fracture energy	G_{Ic}	$10\,\mathrm{J/m^2}$
Max. crack velocity	v_c	2.0; $0.01\,\mathrm{m/s}$
Density	ρ	$2.5 \cdot 10^9\,\mathrm{kg/m^3}$

The choice of the crack velocity is based on the ratio of crack velocity to dilatational wave speed for glass: $\frac{1500\,\mathrm{m/s}}{5697\,\mathrm{m/s}} = 0.26$. For the unit element, the dilatational wave speed is $c_d = 6.93\,\mathrm{m/s}$; then $v_c/c_d = 0.28$ when $v_c = 2.0\,\mathrm{m/s}$. However, the unit element is slowly strained by predefined displacement of its nodes. This implies that the damage rate will not be surpassed in this example, unless a much smaller v_c is used. Hence the second value $v_c = 0.01\,\mathrm{m/s}$ for which the material model is evaluated as well.

Fig. 2.63 shows the evolution of the stress orthogonal to the developing crack. The stress components parallel to the crack faces are zero for this quasi-static case.

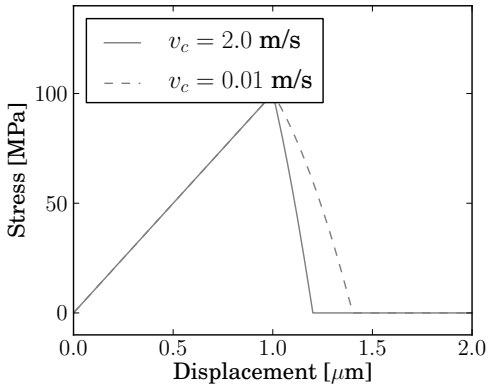

Figure 2.63: Stress orthogonal to the crack for unit element using a crack delay model with $G_{Ic} = 10\,\mathrm{J/m^2}$.

This figure demonstrates the delay effect for the damage evolution. For $v_c = 2.0\,\mathrm{m/s}$, the material model behaves as defined for the static case, where the

stress is reduced to zero at the predefined cracking strain. When $v_c = 0.01\,\mathrm{m/s}$, the damage is delayed and the stress in the element only becomes zero at a higher strain. This is reflected in the energy balance, where the dissipated energy is larger when the delay effect is active, as shown in Fig. 2.64.

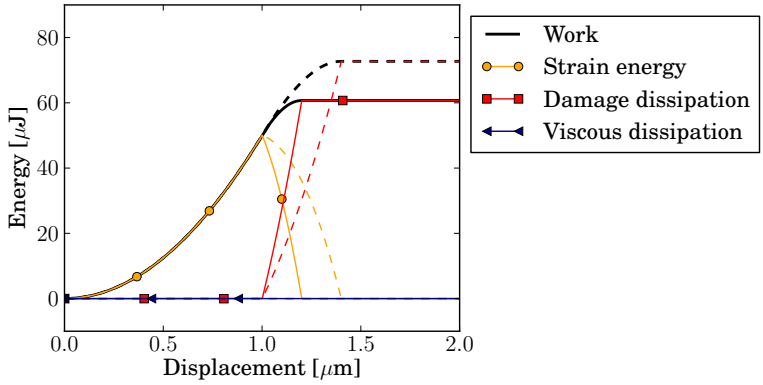

Figure 2.64: Energy balance for unit element using a crack delay model with $G_{Ic} = 10\,\mathrm{J/m^2}$; solid and dashed lines for $v_c = 2.0\,\mathrm{m/s}$ and $v_c = 0.01\,\mathrm{m/s}$ respectively.

The influence of the crack delay becomes clear when the failing element is surrounded by other elements whose elastic springback in response to the damage poses a dynamic load. Therefore, the controlled problem with three unit elements of Fig. 2.37 is revisited. An assessment is made for several settings of the crack velocity around 2.0 m/s, and for the case where the fracture energy is set to a small value. A special case is found when the crack velocity is set greater than the ratio of the element size L_e to the stable time increment Δt. Then, the damage rate in the model can never reach the limiting damage rate $\dot{d}_{max}$ as defined by Eq. 2.26. With a stable time increment $\Delta t = 1.243 \cdot 10^{-4}\,\mathrm{s}$, the ratio $L_e/\Delta t = 8.05\,\mathrm{m/s}$.

The stress decay in the damage phase is given in Fig. 2.65 for different settings of v_c and G_{Ic}. For all given cases, the stiffness is reduced to zero quickly over a few time increments. The delay of the damage evolution becomes active where $v_c < L_e/\Delta t$, in which case the stress decay takes place less abruptly with smaller values for $\dot{d}_{max}$. A smaller fracture energy, on the other hand, implies a steeper gradient in the traction-separation law schematically given by Fig. 2.62, and thus a more aggressive damage behaviour.

Table 2.13 gives the work and viscous dissipation at the end of the simulation for the different settings of v_c and G_{Ic}. A full energy balance is given for the case where $v_c = 2\,\mathrm{m/s}$ and for $v_c = 10\,\mathrm{m/s}$, where the damage rate is not limited, in Fig. 2.66 and 2.67 respectively. The comparison of both these figures

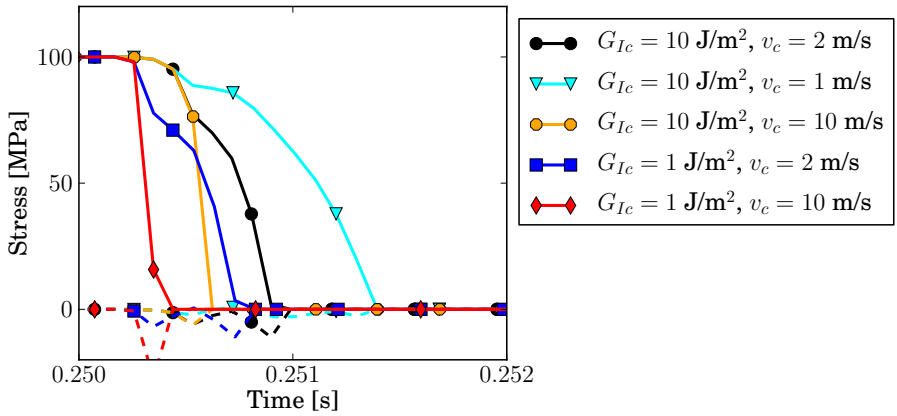

Figure 2.65: Stress decay of failing element for model with three unit elements using a crack delay model; solid and dashed lines for stress components orthogonal and parallel to the crack face respectively.

shows that the delay effect aids in reducing stress oscillations upon failure of an element. However, this comes at the price of a higher damage dissipation, which can be interpreted as an overestimation of the effective fracture energy.

Table 2.13: Work and viscous damping at end of simulation with 3 unit elements

G_{Ic} [J/m^2]	v_c [m/s]	Work [µJ]	Viscous dissipation [µJ]	ratio
10	1	151.2	17.2	11%
10	2	150.8	37.9	25%
10	10	150.6	88.3	59%
1	2	150.6	36.5	24%
1	10	150.3	95.5	64%

2.4.3.2 Drop weight impact

The `VUMAT` is evaluated in the simulation of a glass specimen in the drop weight experiment. The cracking behaviour of the crack delay model is governed by σ_0, G_{Ic} and v_c. In the Rankine fracture criterion, again $\sigma_0 = 255\,\text{MPa}$ for this model. The fracture energy of a stationary crack and the maximum crack velocity are physical constants for soda-lime glass and amount to $G_{Ic} = 7.8\,\text{J/m}^2$ (see Table 2.3) and $v_c = 1500\,\text{m/s}$. The latter is less than three times smaller than the dilatational wave speed in glass ($c_d = 5697\,\text{m/s}$). Taking account of the CFL condition used, it can be noted that a minimum of 4 time increments are needed for the stress decay of the smallest element when the damage rate is limited. A slightly longer duration is needed for larger elements

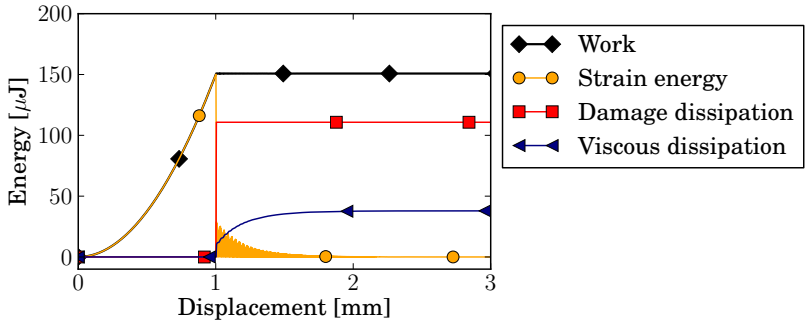

Figure 2.66: Energy balance in function of displacement for three unit elements and crack delay with $v_c = 2\,\mathrm{m/s}$ and $G_{Ic} = 10\,\mathrm{J/m^2}$.

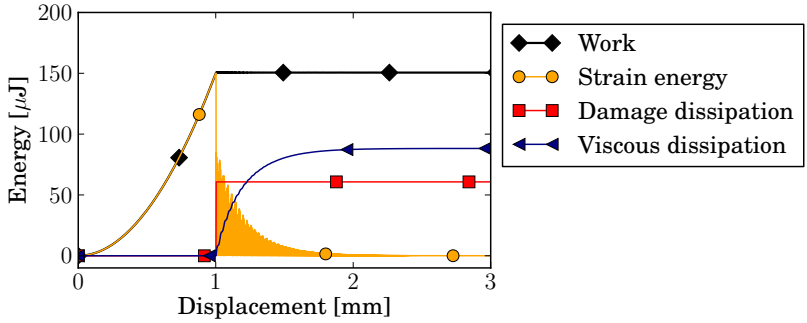

Figure 2.67: Energy balance in function of displacement for three unit elements and crack delay with $v_c = 10\,\mathrm{m/s}$ and $G_{Ic} = 10\,\mathrm{J/m^2}$.

in failure. Thus, also for this damage model, it is recommended to mesh the glass with a more uniform element size.

As in the previous sections, the compressive clamping condition by tightening of the bolts on the clamping rings is taken into account by a static step that precedes the dynamic analysis. Fig. 2.68 shows the simulated cracks and fragmentation that follow from the `VUMAT`. Great similarity with the built-in *Brittle Cracking model is seen, both in the number of cracks and the size of the fragments. For this reason, the deceleration of the impactor in the simulation is given in comparison with the result from the analysis using *Brittle Cracking in Fig. 2.69. This figure shows that cracking and full fragmentation of the simulated specimen occurs quicker with the crack delay model and that the impactor is slowed down less than for the *Brittle Cracking model. This is an improvement, although the crack formation is still not as quick as in the experiment.

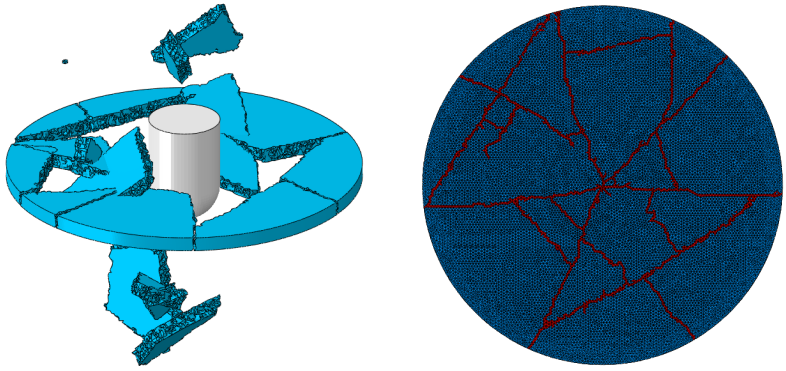

(a) (b)

Figure 2.68: Fracture of simulated $4 \times \varnothing 100\,\text{mm}$ glass plate with crack delay model at $t = 10\,\text{ms}$ for tetrahedral elements mesh: (a) fragmentation, and (b) failed elements.

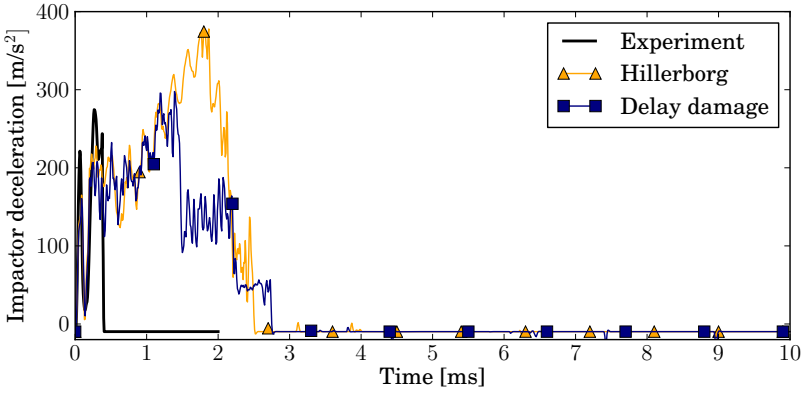

Figure 2.69: Comparison of simulation results for tetrahedral mesh type to experimental accelerations in drop weight impact on a glass disk.

The energy balance is given in Fig. 2.70. In comparison with the *Brittle cracking model (see Fig. 2.54), the impactor keeps more of its kinetic energy, which is consistent with the trend of the decelerations. The viscous dissipation is smaller, which indicates that the damage delay effectively reduces stress oscillations. However, the damage dissipation is no longer negligible in this simulation.

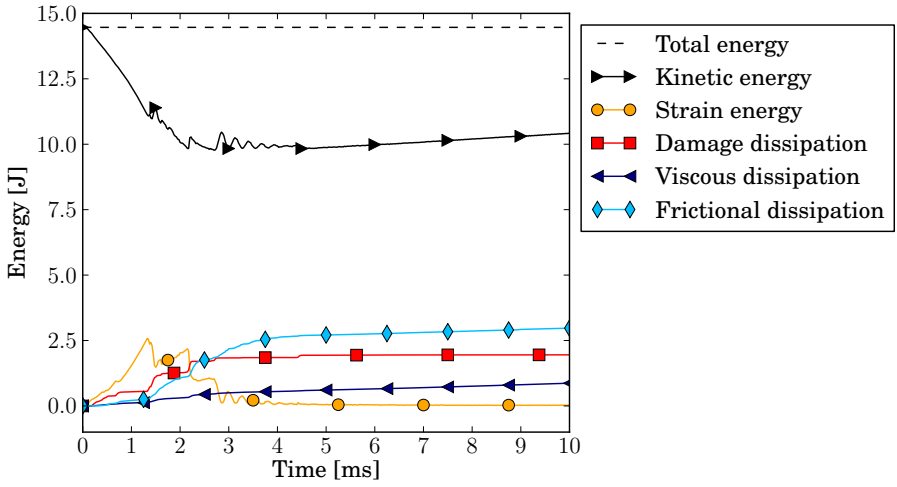

Figure 2.70: Energy balance for tetrahedrally meshed $4 \times \varnothing 100$ mm glass plate with crack delay model.

2.4.3.3 Conclusions

A user-defined material model based on the crack delay concept has been developed to bypass the shortcomings experienced with other element deletion models. The major idea is that cracking does not occur instantaneously and a maximum damage rate exists. The material model is implemented as a `VUMAT` for Abaqus/Explicit and is designed with glass in mind, using only input parameters that are physical constants for that specific class of elastic-brittle materials. In comparison with the built-in *Brittle Cracking model in Abaqus, the crack delay model is a more theoretically correct implementation. Moreover, its behaviour is designed to be independent of the element length, although it is still recommended to use a more uniform element size. It is seen that the delay effect becomes active under dynamic loads and, as a side effect, lowers the stress oscillations in the surrounding elements which is beneficial for the stability of the simulation. In an impact simulation, a credible cracking pattern can be simulated which is in part achieved by taking account of the crack directionality. In the damage dissipation, the fracture energy of glass is, once again, overestimated. But here, the damage dissipation in the impact simulation is no longer negligible. This is not detrimental for the accuracy of the model when compared with other solutions, but should be followed up with caution in further numerical investigations on laminated glass in Ch. 5.

2.5 Smoothed Particle Hydrodynamics for crack simulation

As indicated before, alternatives to element deletion exist that would allow for more advanced modelling of the fracture and post-failure behaviour of brittle materials under dynamic loads. The applicability of two particularly attractive modelling techniques is investigated for the case of a monolithic glass plate under low velocity impact. The present section addresses the meshfree method of Smoothed Particle Hydrodynamics (SPH), while Sec. 2.6 regards the use of cohesive zone elements for dynamic fracture.

SPH was developed as one of the earliest meshfree particle methods by Monaghan and Gingold [125]. The method was originally aimed to model problems in astrophysics, and has since been adapted into a number of fields. Being a Lagrangian, meshfree method, SPH uses a set of discrete particles without fixed connectivity as the computational framework on which the governing equations are solved. When large deformations are likely to be present, a meshfree method can be favoured over a meshed grid-based method to eliminate the mesh tangling that can lead to instability in classical FEM. The SPH method is nowadays most commonly used for fluid flow problems, e.g. the breaking of free surface waves, water impact and sediment flow. The behaviour of solid materials can be similar to fluids under extreme situations such as high velocity impact. In general, the SPH method can be considered as a suitable candidate for the numerical modelling of large deformation and fragmentation problems where other methods might fail.

2.5.1 SPH formulation

The governing equations for SPH with material behaviour are the conservation equations of continuum mechanics:

$$\frac{D\rho}{Dt} = -\rho \frac{\partial \boldsymbol{v}^\beta}{\partial \boldsymbol{x}^\beta} \tag{2.28a}$$

$$\frac{D\boldsymbol{v}^\alpha}{Dt} = \frac{1}{\rho} \frac{\partial \sigma^{\alpha\beta}}{\partial \boldsymbol{x}^\beta} \tag{2.28b}$$

$$\frac{De}{Dt} = \frac{\sigma^{\alpha\beta}}{\rho} \frac{\partial \boldsymbol{v}^\alpha}{\partial \boldsymbol{x}^\beta} \tag{2.28c}$$

The total stress tensor $\sigma^{\alpha\beta}$ consists of the hydrostatic and deviatoric stress components, as in Eq. 2.29. For an elastic solid, the deviatoric stress is a function of the strain through the shear modulus G, as described by Eq. 2.30.

$$\sigma^{\alpha\beta} = -p\,\partial^{\alpha\beta} + \tau^{\alpha\beta} \tag{2.29}$$

$$\tau^{\alpha\beta} \;=\; G\left(\epsilon^{\alpha\beta} \;-\; \frac{1}{3}\partial^{\alpha\beta}\epsilon^{\gamma\gamma}\right) \tag{2.30}$$

The hydrostatic pressure is related to energy and volume by an equation of state (EOS). Many formulations can be used; a common choice is the Mie-Gruneisen EOS for solid materials. Whereas it is common practice in SPH fluids modelling to reduce the computational cost by decreasing the speed of sound in the fluid, this cannot be done when modelling solid material, since speed of sound is closely related to material properties that are essential to the deformation behaviour under a load.

The SPH formulation can be divided in two key steps: (i) the integral representation or kernel approximation of field functions and (ii) the particle approximation.

The integral representation of a field function (Eq. 2.31) is given by the integral of the multiplication of an arbitrary function and the smoothing kernel function (also named smoothing function, kernel function or simply kernel) $W(\boldsymbol{x}-\boldsymbol{x}', h)$ over the domain Ω:

$$f(\boldsymbol{x}) = \int_{\Omega} f(\boldsymbol{x}')\, W(\boldsymbol{x}-\boldsymbol{x}', h)\, \mathrm{d}\boldsymbol{x}', \tag{2.31}$$

where h is the smoothing length defining the influence area of the smoothing function W. Figure 2.71 shows a concept image of the smoothing kernel and support domain.

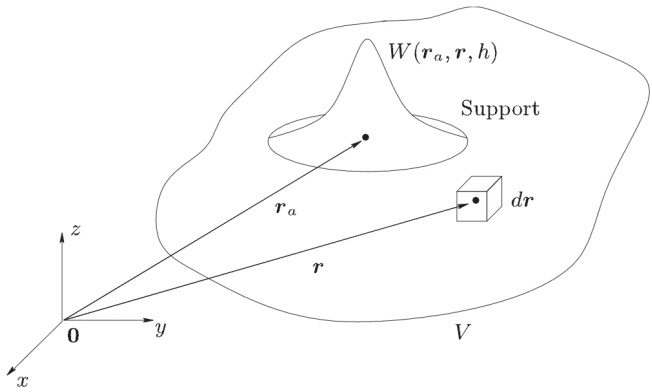

Figure 2.71: Representation of the smoothing kernel and support domain. While the support domain is shown here as a circle, it is in fact a sphere in 3 dimensions. (Figure from Vaughan [126]).

The smoothing function plays a very important role in SPH approximations, as it determines the accuracy of the function representation and efficiency of the computation. The kernel function can be constructed taking in account a number of conditions, as described in Ref. [127]. Many different smoothing functions can be constructed. Some frequently used functions are: the Gaussian kernel, the cubic, quartic and quintic spline kernels, and the quadratic kernel function (Johnson, 1996 [128]; used for simulation of high velocity impact).

The second key step in SPH formulation is the particle approximation, which enables the system to be represented by a finite number of particles that carry an individual mass and occupy an individual space. The continuous integral representations can be transformed into discrete form as a summation over all particles in the support domain with radius κh. The particle approximation for a particle i can be written as:

$$f(\boldsymbol{x}_i) = \sum_{j=1}^{N} \frac{m_j}{\rho_j} f(\boldsymbol{x}_j) \cdot W_{ij}, \tag{2.32}$$

where $W_{ij} = W(\boldsymbol{x}_i - \boldsymbol{x}_j, h)$ is the smoothing function centered on particle i and evaluated at particle j. The value of a particle i is approximated using the weighted average of function values at all the particles within its support domain. The particle approximation for the spatial derivative of the function is:

$$\nabla \cdot f(\boldsymbol{x}_i) = -\sum_{j=1}^{N} \frac{m_j}{\rho_j} f(\boldsymbol{x}_j) \cdot \nabla W_{ij}, \tag{2.33}$$

where:

$$\nabla W_{ij} = \frac{\boldsymbol{x}_i - \boldsymbol{x}_j}{r_{ij}} \frac{\partial W_{ij}}{\partial r_{ij}} \tag{2.34}$$

Thus, the SPH method uses particles to represent material and as a computational frame. There is no need for predefined connectivity between these particles.

The smoothing kernel and particle approximation can be used for discretisation of partial differential equations (PDE's). The SPH formulation is derived by discretising the conservation equations spatially, thus leading to a set of ODE's which can be solved via time integration.

The derivative of density of particle i may be solved from the continuity equation, as in equation 2.35.

$$\frac{D\rho_i}{Dt} = \sum_{j=1}^{N} m_j (\boldsymbol{x}_i^{\beta} - \boldsymbol{x}_j^{\beta}) \cdot \frac{\partial W_{ij}}{\partial \boldsymbol{x}_i^{\beta}} \tag{2.35}$$

The updated velocity may be obtained from the discretisation of the momentum equation, which can be formulated in a number of ways. With a symmetric kernel function, such as the cubic B-spline kernel, the most commonly used formulation is given by:

$$\frac{D\boldsymbol{v}_i^\alpha}{Dt} = \sum_{j=1}^{N} m_j \left(\frac{\sigma_i^{\alpha\beta}}{\rho_i^2} + \frac{\sigma_j^{\alpha\beta}}{\rho_j^2} + \Pi_{ij} \right) \cdot \frac{\partial W_{ij}}{\partial \boldsymbol{x}_i^\beta} \tag{2.36}$$

The particle approximation of the energy equation can be formulated as:

$$\frac{De_i}{Dt} = \frac{1}{2} \sum_{j=1}^{N} m_j (\frac{p_i}{\rho_i^2} + \frac{p_j}{\rho_j^2} + \Pi_{ij})(\boldsymbol{v}_i - \boldsymbol{v}_j) \cdot \frac{\partial W_{ij}}{\partial \boldsymbol{x}_i^\beta} + \frac{1}{\rho_i} \tau_i^{\alpha\beta} \epsilon_i^{\alpha\beta} \tag{2.37}$$

The term Π_{ij} denotes the Monaghan artificial viscosity term [129], which is similar to the bulk viscosity in explicit FEM. This term is added to the physical pressure to allow shocks to be simulated. If not, the simulation will result in unphysical oscillations around the shocked region. The role of the artificial viscosity is to smoothen the shock over several particles and to allow the simulation of viscous dissipation. Also, it prevents unphysical penetration of particles approaching each other.

2.5.2 Fracture and fragmentation with SPH

One of the first studies to use SPH for brittle fracture simulation was performed by Benz and Asphaug [130]. In their work on the collision of comets and planetesimals, they modelled laboratory experiments of basalt spheres, impacted at $\pm 3\,\mathrm{km/s}$. Two damage models were used for the SPH particles: an elastic-perfectly plastic relation for stresses above the Hugoniot elastic limit (HEL) and the Grady-Kipp model for brittle failure at lower stresses. The latter accounts for the size effect of brittle materials by the statistical flaw distribution. They demonstrated that SPH can represent the rupture of bonds and formation of new surfaces, resulting from spallation and brittle crack growth.

Michel et al. [131] simulated the high velocity impact (HVI) of 0.5 mm steel spheres on 5 mm thick fused silica glass disks at impact speeds ranging from 0.5 to 5 km/s. They have identified the material properties of glass for the Johnson-Holmquist (JH-2) ceramic model and were able to validate these in 2D SPH simulation. The simulation results were able to represent spallation and fragmentation above the HEL.

Fracture simulations at low loading rates were performed by Das and Cleary [132] and Ma et al. [133]. Both studies considered a cylindric rock under a quasi-static, axial compression load. In the SPH analysis, Das and Cleary used the Grady-Kipp damage model while Ma et al. used an elasto-plastic damage

model. Fracture and fragmentation could be realistically simulated and also the obtained crack patterns were very similar for the two damage models.

In all the referenced studies, it was stated that cracking occurs naturally with SPH and there is no need for special treatment of the particles positioning. This is contradicted by Gupta et al. [134] who showed that the crack path depends heavily on the topology of the SPH particles when an Eulerian kernel is used. The SPH kernel is Eulerian when expressed in terms of spatial coordinates, whereas a Lagrangian kernel uses a fixed set of particle neighbours. With a Lagrangian kernel, particles can be released from each other's influence upon reaching a fracture criterion, which would more accurately represent the formation of crack paths and crack branching.

2.5.3 2D high velocity impact of a glass disk

The first case considered is an example in 2D, modelled after a simulation by Das and Cleary [132] of a circular rock shape that impacts a straight surface at 70 m/s. The same case is simulated except the material of the disk is now given the properties of glass. The disk has a diameter of 200 mm and is discretised by 31,428 particles with a spacing of 1 mm. The default settings for the SPH formulation are used in LS-Dyna, where the only available kernel function is the cubic smoothing kernel. Because 70 m/s is a relatively high impact speed, the Johnson-Holmquist material model can be used. The JH-2 parameters for glass are used as given by Holmquist et al. [135].

This simulation shows that the SPH technique can simulate fast, dynamic fracture and full fragmentation, as evidenced by the simulation output in Fig. 2.73. When contact is made between the disk and the rigid surface, a compressive stress wave initiates and travels radially through the glass material at a velocity slightly higher than the dilatational wave speed, $c_d = 5440\,\mathrm{m/s}$. Fig. 2.72 shows a pressure plot at the moment of incipient crack propagation. Cracks initiate immediately upon impact in the contact zone, but only really start to propagate as macro-cracks at $t = 10.7\,\mu\mathrm{s}$. The crack tip velocity in the simulation cannot be determined exactly from the SPH particles, but is seen to be in the range of 1500 to 2000 m/s. Tensile failure of a particle occurs as the damage accumulates, leading to full fragmentation and propulsion of glass fragments in Fig. 2.73.

In this process, SPH does not suffer from mesh tangling, shear lock or hourglassing, and there is no removal of particles from the analysis to represent the cracks. Because the SPH solver relies on interpolation, discretisation with good resolution is of great importance for finding sufficient neighbours in each particle's kernel influence domain. However, there is a limit to the number of neighbours that could be used, imposed by the 'pairing instability' explained by Price [136]. In this simulation the mean neighbour number is $N_n = 20$,

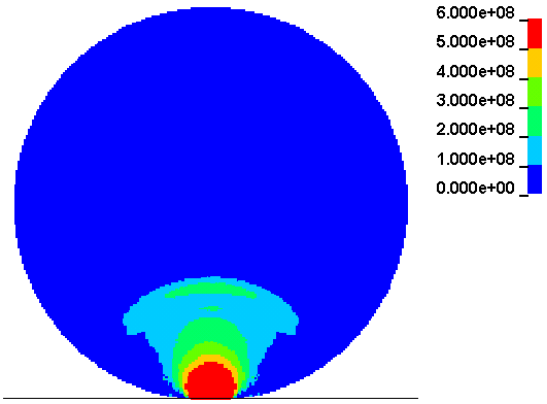

Figure 2.72: Pressures [Pa] at $t = 10.7\,\mu s$ for 2D SPH simulation of impacting glass disk.

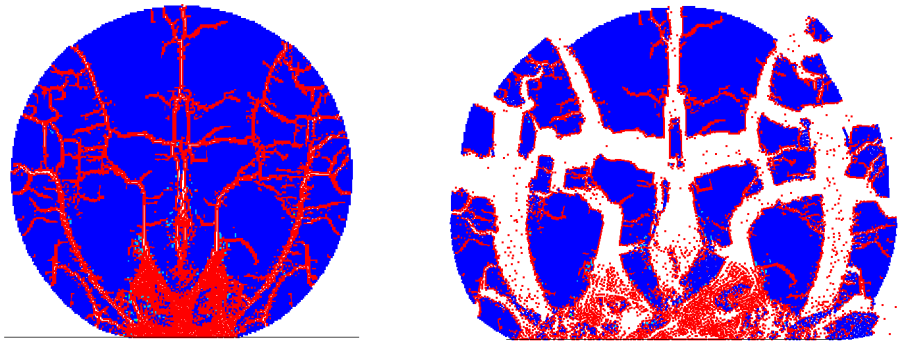

(a) $t = 100\,\mu s$ **(b)** $t = 1.0\,ms$

Figure 2.73: Damage contours and fragmentation for 2D SPH simulation of impacting glass disk.

which is a common choice for 2D calculation with the cubic smoothing kernel. For the 3D case, $N_n = 50$ to 60 would be a sensible choice.[3]

For SPH with material properties, the *tensile instability* is a common issue. This occurs when the second derivative of the smoothing function changes sign within its support domain. When the net pressure is negative, the net force between the closest particles becomes attractive, which can cause particles to unphysically clump together. A different kernel function can be chosen to avoid tensile instability, e.g. Johnson's quadratic smoothing kernel. However,

[3]No mathematic rule exists to determine the smoothing length or number of neighbours, nor has any rule of thumb been formulated. The numbers stated here are based on what is commonly seen in literature and on our own experience.

the presented simulation does not show any particle clustering and the cubic kernel can further be used.

2.5.4 Drop weight impact on monolithic glass

The SPH method is used to model a three-dimensional glass plate under realistic impact loading, i.e. the drop weight impact introduced in Section 2.3. The glass part is discretised by ca. 850,000 particles with a particle spacing of 0.33 mm. The initial particle grid has 12 particles through the thickness of the glass, which is a minimum to properly model the glass stiffness, considering the interpolation over the kernel domain. The *Brittle Cracking model in ABAQUS is used for the glass material. Instead of deleting a particle, it is simply flagged as 'cracked' when full damage is reached. In that state, it can no longer support tensile stresses in any direction, but does retain its stiffness in compression.

The numerical analysis is performed with ABAQUS/Explicit, using the cubic kernel function with an adaptive smoothing length and a maximum of 75 particle neighbours. The initial stress state by compressive clamping is not taken into account here, because SPH is an explicit method only and therefore results cannot be imported from ABAQUS/Standard.

A plot of the damage status of the particles at the end of the simulation is given in Fig. 2.74. Even though few radial cracks have developed, no concentric cracks are formed, nor does fragmentation of the specimen occur. From the decelerations of the impactor, given in Fig. 2.75, it appears as if the SPH part is acting as a softer, but coherent material, rather than a shattered piece of glass. To show that this is not merely a consequence of the material model, or even the solver, a similar plot is given in Fig. 2.76, which is generated in LS-Dyna using the JH-2 material model.

The observed behaviour can be explained from the kernel interpolation that is at the basis of the SPH method. Particles in the vicinity of a crack are still in the influence domain of the smoothing kernel for particles at the other side of the crack. This means that particles across the crack are still taken into account in the calculation of forces and impulse, albeit with a smaller weighting factor. When their respective velocity vectors do not differ much, particles on both sides of the crack do not move away from each other and remain within each other's influence domain for a longer period. This explains the different behaviour for high velocity impact and low velocity impact. Because of the reduced stiffness of damaged particles and the smaller weight factor in interpolation for particles across the crack, the SPH particles in the vicinity of the crack effectively behave as a softer material.

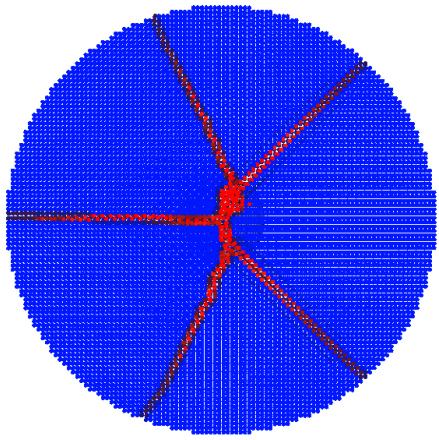

Figure 2.74: Damage contours for glass with delay damage material model in SPH simulation of drop weight impact. Bottom view of glass part at $t = 10\,\text{ms}$.

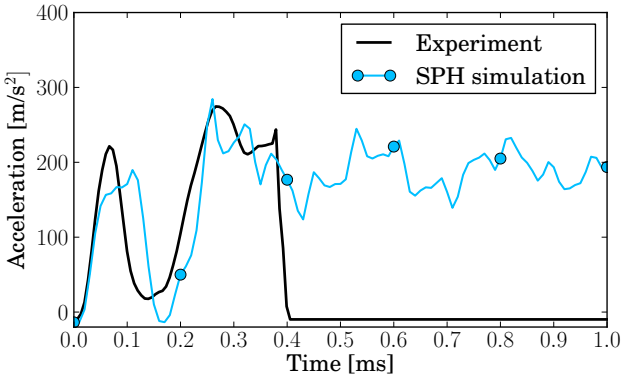

Figure 2.75: Comparison of SPH simulation results to experimental accelerations in drop weight impact on a glass disk.

2.5.5 Conclusions

The SPH method has been evaluated for the failure behaviour of monolithic glass specimens. It is shown that this meshless simulation technique enables the modelling of brittle fracture with crack branching and intersection, subsequent fragmentation and propulsion of fragments. However, the SPH formulation used in this study appears to be applicable only for more extreme load cases, such as a glass disk falling on a rigid floor at high speed. For impact at lower speeds, which are relevant in this work, it is seen that radial cracks in the glass do develop, but no further cracks are formed and the SPH part behaves as a

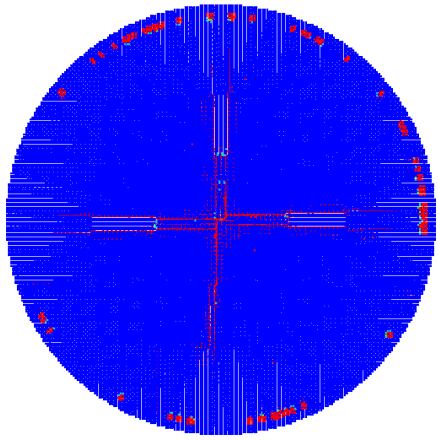

Figure 2.76: Damage contours for glass with JH-2 material model in SPH simulation of drop weight impact. Bottom view of glass part at $t = 10\,\text{ms}$.

softer material. This is explained by the kernel formulation, for which particles on one side of the crack can still belong to the influence domain of particles across the crack when their velocity vectors remain similar after fracture has occurred. This may be resolved by the use of a Lagrangian kernel, which uses a fixed set of particle neighbours. With this method, particles can be excluded from each other's influence domain when they are on the other side of a crack. However, such kernel formulation is not readily available in ABAQUS or LS-DYNA.

Because it is also apparent that the resolution needed for particle methods in simulation of a realistically sized window glass would increase the calculation time immensely, the SPH method is not further considered.

2.6 Cohesive zone elements for crack simulation

The simulation of brittle fracture in finite element analyses can be categorised into two classes: those based on a continuum approach and those based on a discrete approach [137]. The element deletion method and SPH with an Eulerian smoothing kernel both belong to the continuum approach, which homogenises the cracked solid and finds its response by locally degrading the elasticity of the material. The shortcomings of this approach lie in the difficulties to include the small-scale response of the material: the stress intensity at the crack tip is not recognised, the size of a crack highly depends on the size of the elements, etc. In the discrete approach, a crack is treated as a separate entity, which can nucleate, propagate and coalesce during the deformation process. In this respect, the cohesive zone method (CZM) can provide a powerful modelling

technique. In its implementation via interface elements, made mature by Xu and Needleman [138] and Camacho and Ortiz [66], a crack opening is represented as a displacement jump at the interelement boundaries. When the stress at a node surpasses a critical level, a crack initiates by splitting the node and propagates along the element boundary while opening further nodes. The obvious shortcoming is that the crack path is constrained to the element edges. This has been addressed by various methods, most notably the extended Finite Element Method (XFEM) [92]. However, this method would be less applicable for problems such as the dynamic fracture of impacted glass; for each possible crack, the nucleation point must be defined in advance, along with the enriched zone (level set) in which the crack can propagate. In most FE codes, XFEM allows only one crack per level set and no branching.

An excellent overview of the history, theory and advances in cohesive zone modelling of dynamic fracture is given by Seagraves and Radovitsky [91]. In this section, the main concepts of this simulation method are shortly introduced before discussing our own efforts within ABAQUS.

2.6.1 Cohesive elements

The cohesive zone, introduced in Section 2.2.2, models the crack face separation as a displacement jump δ across an initially coincident surface. The separation process is resisted by macroscopic forces acting on the crack faces: cohesive tractions T. The traction decays to zero when new crack surface is being formed at some critical amount of separation δ_f ahead of the crack tip.

A cohesive element, shown in Fig. 2.77, can be inserted at the interface between two continuum elements. It consists of nodes at the bottom and top surface, coincident with the crack faces. Integration points exist only at the midsurface, at which the normal (through-thickness) and transverse shear tractions are computed. The element has no membrane stiffness. Thus, the constitutive response of a cohesive element is defined entirely by its traction-separation law $T(\delta)$.
Several formulations can be used for the traction-separation law, some of which are given schematically in Fig. 2.11 for normal (Mode I) separation. The work performed in the cohesive zone up to the critical separation equals the fracture energy G_c.

Two fundamentally different classes of traction separation laws exist, distinguished by their behaviour prior to the onset of fracture. Fig. 2.78a shows the *intrinsic* approach, which models the cohesive zone as having reversible, elastic response before the critical stress is reached. The *extrinsic* approach, shown in Fig. 2.78b, is characterised by initially rigid behaviour.

Intrinsic cohesive laws were initially developed for modelling delamination at

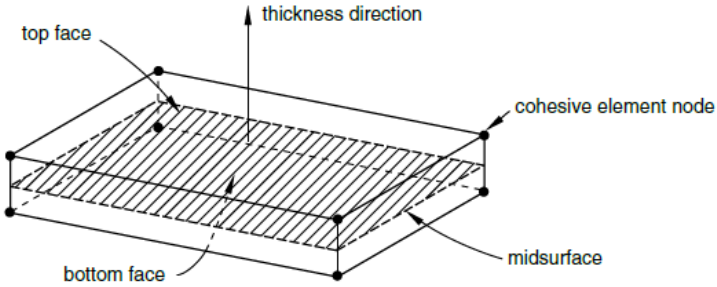

Figure 2.77: Spatial representation of a three-dimensional cohesive element (Figure from ABAQUS manual [121]).

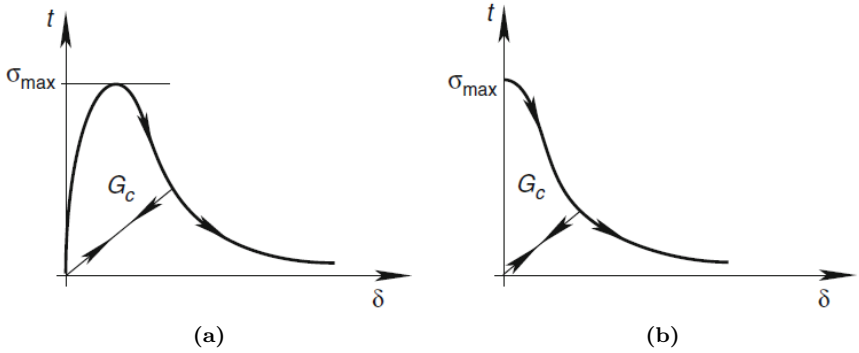

Figure 2.78: Schematic of the traction-separation laws used in (a) the intrinsic approach, and (b) the extrinsic approach (figure from Ref. [91]).

material interfaces by Needleman [139] and Tvergaard [65]. In interface problems, the crack path is well known and cohesive elements need only be present at those locations of the finite element mesh. When the cohesive elements are intrinsically present from the start of the analysis, it is required that their traction-separation law has an elastic response, as well as an intrinsic fracture criterion beyond which the response is irreversible and dissipative. Problems with arbitrary crack initiation and propagation thus require the inclusion of cohesive elements at all interelement boundaries of the mesh when using the intrinsic approach.

Contrarily, in the extrinsic approach, developed by Pandolfi and Ortiz [140,141] for the simulation of brittle fracture, initial elastic response is not required. Only after a fracture criterion has been satisfied, cohesive elements are dynamically inserted where the crack propagates in between the continuum elements. This provokes topological changes in the mesh, requiring an adaptive procedure. Both approaches are known to have some specific, numerical issues:

- Mesh-dependency of the crack path is a common point of attention. Cracks can only run along interelement boundaries and their possible propagation directions are severely limited. Moreover, the crack initiation point must always coincide with a node. This could be treated by adaptive remeshing, although such procedure is computationally expensive.

- Artificial compliance is a major issue for the intrinsic approach. In finite element modelling of elastic solids, consistency is guaranteed by enforcing interelement continuity. However, when the mesh is embedded with cohesive elements (usually with zero thickness), discontinuities occur from the start of the calculation. The displacement jumps give rise to an artificial stiffness, lowering the overall stiffness of the body and introducing artificial anisotropy as well. A bilinear traction-separation law allows to control the initial slope, which can serve as a penalty parameter that can be made so high that the effect of artificial compliance is negligible [142]. However, very stiff cohesive elements can severely reduce the stable time increment.

- Xu and Needleman noted that intrinsic cohesive zones can also suffer from 'lift-off' under high, dynamic loading [138]. This occurs when a sudden load is imposed on a crack for which a high degree of separation is already reached along the length of the crack path, causing all cohesive elements to fail very quickly, with a crack velocity higher than the Rayleigh speed. This is particularly seen when the crack is confined to a straight path, e.g. in dynamic delamination problems.

- The main difficulty with the extrinsic method is the need for a complex adaptive meshing scheme for the cohesive zones, which inevitably reduces the computational efficiency as well.

The current state of the art in cohesive zone modelling is dominated by implementations in the discontinuous Galerkin framework, first introduced by Mergheim et al. [143]. The main feature of this approach is that it takes into account discontinuities of the unknown field in the interior domain. The interelement compatibility is ensured by boundary integrals, which are similar to the interelement term in cohesive elements and can be implemented as interface elements. Put simply, when a crack appears, the behaviour of the involved interface element changes from boundary condition to (extrinsic) traction-separation. This entirely avoids the artificial compliance and lift-off experienced for the intrinsic CZM approach, along with the complex element insertion needed with the extrinsic approach. Interestingly, the discontinuous galerkin method can be applied to thin bodies, discretised by shell elements. This is successfully demonstrated in the recent work of Becker and Noels [144, 145].

2.6.2 Embedding cohesive elements in Abaqus

An evaluation is made only for the intrinsic approach for the cohesive zone method. Cohesive interface elements with an intrinsic traction-separation behaviour are available from the Abaqus elements library for both the implicit and explicit solvers. Only the meshing with zero-thickness cohesive elements in between the bulk elements during pre-processing needs to be implemented by a user-specified program.

Implementation of the extrinsic approach does not seem possible in Abaqus without access to the source code. While the initially rigid traction-separation law can be included in a `UMAT` or `VUMAT` subroutine, there is no option to program the adaptive insertion of cohesive elements in either Abaqus/Standard or Explicit. The subroutine `UMESHMOTION` allows to define constraints for the relocation of nodes in the mesh, but provides no manner to specify the element that is to be inserted.

For the discontinuous Galerkin approach, Nguyen [146] argues that it should be possible to implement this in Abaqus. The cohesive behaviour can be programmed as a user-defined element (`UEL`), by modification of the code for an intrinsic cohesive interface element as developed by a.o. Scheider [147]. This element depends not only on its own nodes, but also on the neighbouring bulk elements. Data from those elements can be extracted during the analysis by use of the `UVARM` subroutine, which is unique to Abaqus/Standard. By this method, it might also be possible to use the cohesive zone method for shell elements within Abaqus. Although a promising method for fracture simulation, it is obvious that such implementation takes quite an effort to program and validate. Moreover, it cannot be formulated for Abaqus/Explicit without access to the source code.

A program to insert cohesive elements at all interelement boundaries of an existing continuum mesh is developed by the author as a standalone Python program. The required inputs are a list with all node numbers and their respective coordinates, and a list of element numbers and their nodal connectivity. As such, the program can be used for meshes created by multiple sources and works by the following algorithm:

1. Read the nodes: node numbers are stored as integers in a list; coordinates are stored as a single string for each node.

2. Read the elements: element numbers are stored as integers in one list. Distinction is made between hexahedral, pentahedral and tetrahedral elements (or rectangular and triangular in 2D) in that order. The nodes they are connected to are stored as integers in one single list for all elements.

3. Search interelement faces: every face of an element is connected to either 3 or 4 nodes, which have a certain position in the list of nodes connected

to each element. For a face, a list is made of all the node numbers in the list of points that are the same as those composing the face. If more than two points belong to the same element, the connected element is found.

4. Find the nodes for the cohesive element: if two connected elements are found, the positions of their shared nodes in the points list are stored in an order that is consistent to compose a cohesive element, i.e. bottom and top face of the cohesive element should be coincident with the faces of the adjacent bulk elements.

5. A sum of the nodal positions in the connectivity of an element is unique to each face of that element. In this way, it can be determined for which face of the second element a match has been found.

6. Write new mesh: the 'points' are the new nodes. Their coordinates can be found from the original node numbers. Bulk elements remain the same, but are connected to an array of successive points/nodes. The newly created cohesive elements are connected to the point numbers as stored.

By this algorithm, cohesive elements can be embedded in the mesh for any mesh topology. The Python program is also rather efficient: for a 3D solid mesh originally containing 98,000 hexahedral elements, it takes 16 s to insert cohesive elements at 278,000 locations.[4][5]

The intrinsic cohesive zone method in ABAQUS is evaluated for a validation test case, i.e. the wedge splitting of a pre-notched concrete block. Experimental data for this test are available from Trunk [150]. The same problem has been modelled by Areias and Belytschko [151] with XFEM and by Su et al. [148] with a similar implementation of intrinsic CZM. The dimensions and boundary conditions of the test setup are given in Fig. 2.79.

The concrete has an elastic modulus of 28.3 GPa, Poisson ratio of 0.2 and density 2500 kg/m^3. The Mode I tensile strength is $\sigma_I = 1.59$ MPa and the fracture energy amounts to 196 N/m [151]. The mesh for the concrete part, with zero-thickness cohesive elements, is shown in Fig. 2.80. This mesh is constructed in analogy with Su et al. [148], having a refined region of pentahedral elements where cracking is expected. The intrinsinc cohesive elements have a bilinear traction-separation law. Their initial stiffness is chosen as very high in order to have quasi-rigid behaviour before the fracture criterion is reached; for Mode I and II: $K_I = K_{II} = 10^{13}$ N/m^3.

Opposite horizontal displacements are imposed on the vertical sides of the cutout section at the top of the concrete block. The force vs. opening displace-

[4] Compared to 30 minutes for 46,800 solid elements in the similar MATLAB code by Su et al. [148].

[5] Note: this program was developed two years prior to publication of Nguyen's article [149] about an open-source code with similar functionality.

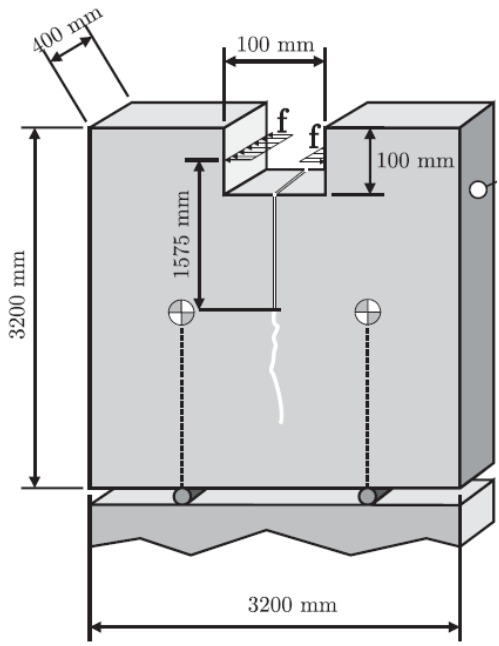

Figure 2.79: Wedge splitting test case: dimensions and boundary conditions (figure from Areias and Belytschko [151]).

ment can be compared with the experimental measurement. Su et al. indicate that the implicit solver tends to diverge for the intrinsic CZM once the crack propagates. This is confirmed for our own implementation as well. Therefore, it is recommended to use an explicit solver with a total simulated time that is long enough to ensure negligible kinetic energy in the analysis. Without the need to apply mass scaling, this time is $t_{tot} = 100\,\text{ms}$ to reach a final opening displacement of 4.0 mm. Results are given in Fig. 2.81 for both the coarse mesh and a refined mesh containing 17,000 bulk elements and 42,500 cohesive elements.

The numerical result can correctly reproduce the maximum force that can be exerted on the concrete block. In comparison with the simulations by Areias and Belytschko, and Su et al., also the post-fracture behaviour is captured reasonably well. The crack path, however, is dependent of the mesh topology. While the crack propagates almost straight and central in the concrete block for the coarser mesh, the crack path shows a deviation for the refined mesh, as shown in Fig. 2.81b. Nonetheless, it can be concluded that the intrinsic cohesive zone method can be used for fracture simulation in Abaqus/Explicit.

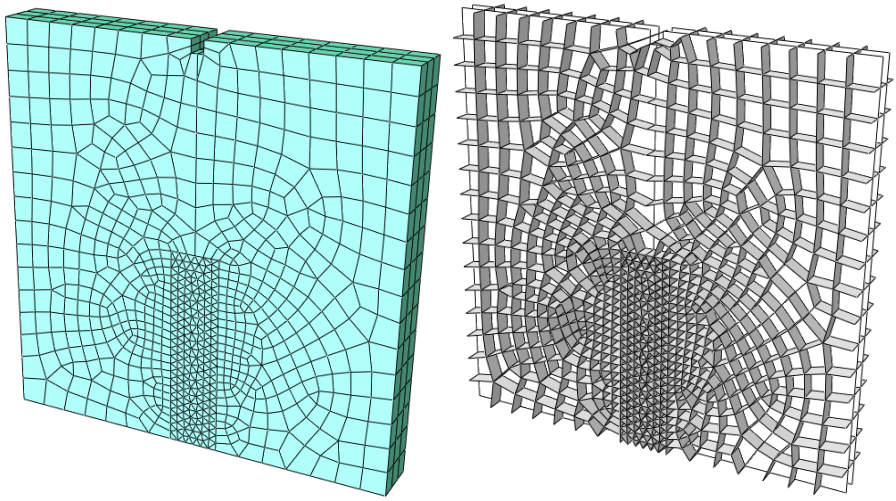

(a) (b)

Figure 2.80: Coarse mesh for concrete block in wedge splitting test: (a) 2,700 bulk continuum elements, (b) 10,000 zero-thickness cohesive interface elements.

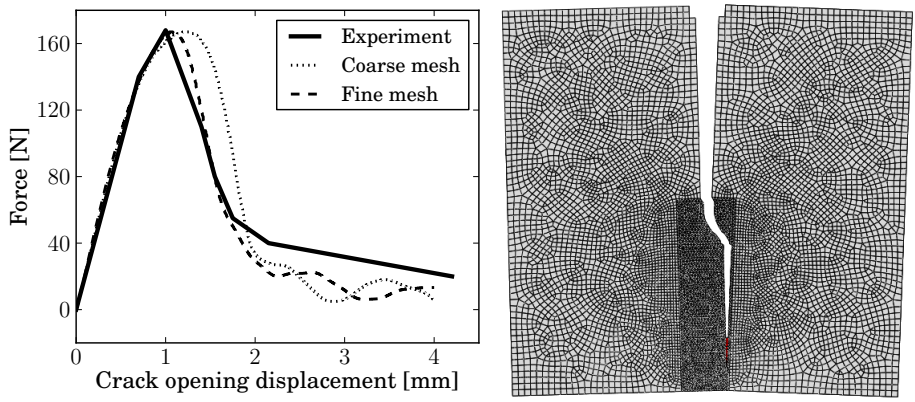

(a) (b)

Figure 2.81: Results for wedge splitting of concrete block: (a) Force vs. opening displacement, (b) Crack formed at 4 mm opening, for fine mesh (deformation scale factor = 50).

2.6.3 Drop weight impact on monolithic glass

Contrary to the wedge splitting test case, the drop weight impact test is a transient load case and the dynamic response is indispensible for the simula-

tion. Therefore, the elastic behaviour without cracking is first considered to determine at which slope in the traction-separation law, the effect of artificial compliance can become negligible. Because the technique allows to simulate very thin cracks, the meshing of the bulk continuum elements does not have to be as fine as for the element deletion method. Fig. 2.82 shows the mesh for a $4 \times \varnothing 100\,\text{mm}$ monolithic glass plate.

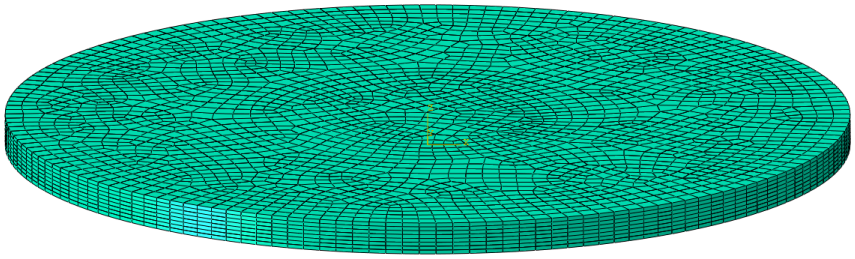

Figure 2.82: Mesh for $4 \times \varnothing 100\,\text{mm}$ glass plate containing 19,400 full integration hexahedral solid elements and 55,200 cohesive elements.

In analogy with Section 2.3, Fig. 2.83 shows the deceleration of the impactor in simulations with varying initial slope of the elastic part in the cohesive law. It is seen that for a low cohesive stiffness K_I, the stiffness of the glass plate as a whole is seriously underestimated because of artificial compliance. A much higher cohesive stiffness can be enforced, although this reduces the stable time increment: $\Delta t = 5 \cdot 10^{-9}\,\text{s}$ for $K_I = 10^{15}\,\text{N/m}^3$, while $\Delta t = 2 \cdot 10^{-8}\,\text{s}$ for the solid mesh in Fig. 2.49. Moreover, the simulated decelerations do not converge to the result obtained with a regular, solid mesh of the same topology when the cohesive stiffness is increased. Therefore, the intrinsic CZM approach with zero-thickness interface elements must be abandoned.
Alternatively, the cohesive elements can be given a small, finite thickness. This allows to adjust the cohesive stiffness so that it matches the material stiffness of the bulk elements. An additional Python program is developed to modify the mesh by displacing the bottom and top face nodes of each cohesive element along the normal direction to the respective faces. The element length criterion of Eq. 2.18 now also applies to the thickness of the cohesive elements. For $\sigma_0 = 255\,\text{MPa}$ and $G_{Ic} = 8\,\text{J/m}^2$, the thickness should be smaller than the ultimate crack separation $u_f = 17.9\,\mu\text{m}$. The cohesive elements are assigned a thickness of $10\,\mu\text{m}$ and cohesive stiffnesses $K_I = 7.0 \cdot 10^{15}\,\text{N/m}^3$ and $K_{II} = 2.85 \cdot 10^{15}\,\text{N/m}^3$. Only Mode I fracture is considered for glass; the Mode II strength is set to a very high value in the analysis input.

It should be mentioned that this technique leaves small gaps around the nodes, as shown in Fig. 2.84. However, this does not have a significant effect on the elastic response, which does match the experimentally measured impactor

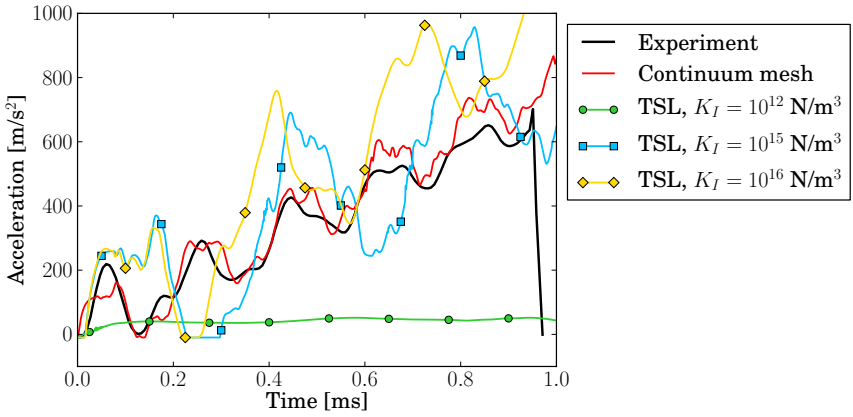

Figure 2.83: Comparison of simulation results for mesh with intrinsic cohesive elements to experimental accelerations in drop weight impact on a glass disk.

deceleration quite well. However, the simulation takes about 10 times longer to complete than an equivalent simulation using the element deletion method with the same computational resources.

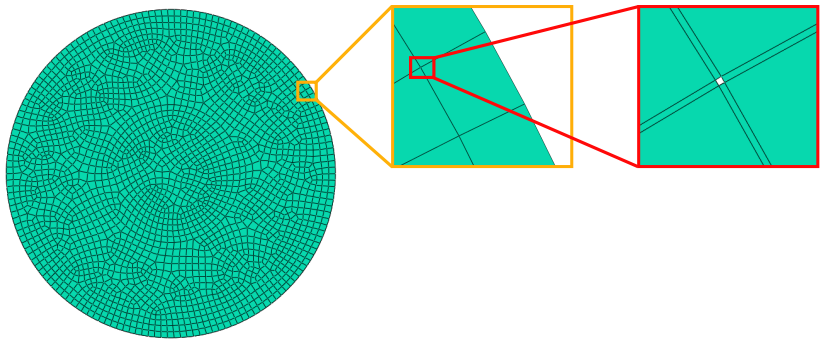

Figure 2.84: Voids in the mesh for intrinsic CZM approach with finite thickness cohesive interface elements.

The formation of cracks in the simulated glass plate is shown in Fig. 2.85. The first cracks appear around $t = 0.25\,\text{ms}$, which is slightly earlier than in the simulations with element deletion. Afterwards, radial cracks are seen to develop, but no full fragmentation of the specimen occurs. It appears that all radially oriented cohesive elements *simultaneously* develop some degree of degradation. This has a significantly reducing effect on the global stiffness of the glass part. At the majority of the cohesive elements, the degradation is

halted before reaching the failure displacement δ_f, upon which they spring back elastically with lowered stiffness. This leads to conclude that also this method is not suitable for the simulation of dynamic glass fracture.

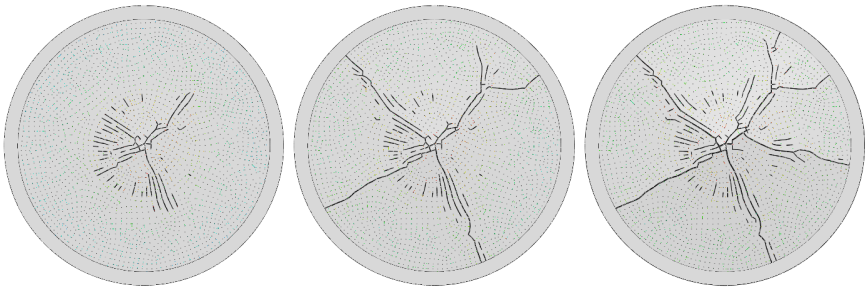

(a) $t = 0.25\,\mathrm{ms}$ **(b)** $t = 0.5\,\mathrm{ms}$ **(c)** $t = 1.0\,\mathrm{ms}$

Figure 2.85: Simulated cracking of glass plate under drop weight impact by use of intrinsic CZM approach with finite thickness cohesive interface elements: bottom view.

Yet another variation on the intrinsic CZM approach can be thought of. Instead of inserting cohesive interface elements, regular elements with a small, finite thickness can be inserted in the same way. Only these elements are allowed to fracture by element deletion, while the bulk elements are not. Because regular elements have membrane and transverse shear stiffness, the void gaps in the mesh can be filled as well. Also, this technique is not restricted to continuum elements only, but can be used for shell elements too, which is an important advantage for simulating large-scale components. Unfortunately, also this approach lacks applicability, because the aspect ratio of the inserted elements is now too large to enable correct stress calculation. In elastic response, the stresses in the plate are far from continuous, and the dynamic result is particularly noisy.

But when the thickness of the inserted elements is increased to e.g. 5% of the size of the bulk elements, a decent stress calculation can be obtained for the inserted elements. The simulation of brittle fracture seems credible, as shown in Fig. 2.86, where the thin elements in blue are the inserted elements that can represent crack formation by element deletion. However, the inserted shell elements do not fulfill the element length criterion; they are larger than the maximum element length (in this case: $17.9\,\mu\mathrm{m}$) for which the fracture energy can correctly be modelled. Although initial results seem promising, further investigation is needed to verify this approach. However, it is more likely that the discontinuous Galerkin approach to cohesive zones will be useable in the near future, and allowing to capture the traction-separation response correctly.

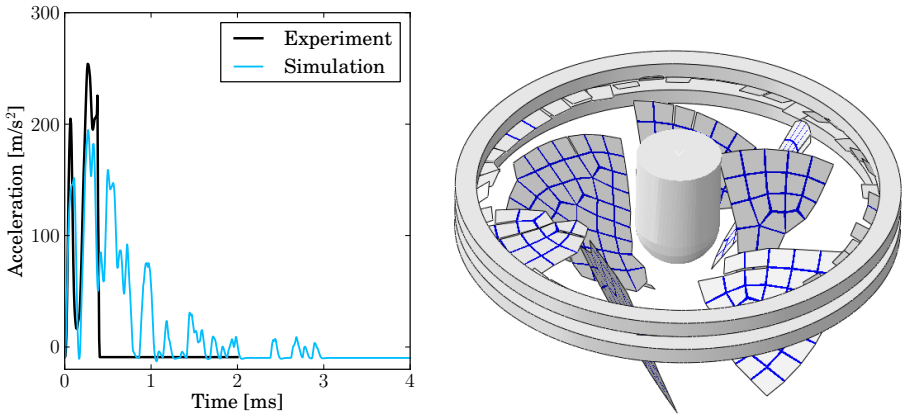

Figure 2.86: Simulated cracking of glass plate under drop weight impact for element deletion of inserted shell elements with small thickness: (a) accelerations, and (b) fragmentation at $t = 10\,\text{ms}$.

2.6.4 Conclusions

By introducing a cohesive zone at the interelement boundaries of a finite elements mesh, a crack can be treated as a separate entity within the simulation. This enables the simulation of very thin cracks with less sensitivity to the size of the bulk elements. The propagation of a crack is still mesh sensitive in the sense that its path is constrained to the element edges.
Different approaches exist to the implementation of the cohesive zone method for crack modelling. For dynamic fracture simulation in ABAQUS/Explicit, only the intrinsic approach can be used, which requires the embedding of cohesive elements at all interelement boundaries prior to execution of the numerical analysis. An efficient program has been written to insert cohesive elements accordingly.

Simulation of a quasi-static case, the wedge splitting of a large concrete block, shows that the intrinsic cohesive elements approach can be used to simulate crack initiation and propagation, and is able to produce realistic results. However, the method does suffer from artificial compliance, which becomes clear for the dynamic simulation of an impacted glass disk. As a result, the glass part as a whole acts softer in the simulation. Increasing the initial stiffness of the traction-separation law dramatically reduces the stable time increment and does not seem to solve the problem either. Assigning a small, finite thickness to the cohesive interface elements allows to match the stiffness modulus of the bulk elements and simulate the elastic response correctly. But when cracks initiate, they initiate at so many different locations that the glass part shows a globally lowered stiffness rather than fragmenting by a few discrete cracks.

Most of the cohesive elements where a crack has initiated do not reach their ultimate failure separation, but linger with degradation. As such, this technique is not quite fit for the analysis of large glass components under dynamic loading.

A hybrid approach could be presented, in which small-sized continuum elements replace the finite thickness cohesive interface elements. The replacing elements may fail by element deletion with the crack delay model, while the larger bulk elements behave only linear elastic without damage or failure. This approach can also be applied to shell elements and seems to produce acceptable results, although it should further be verified for other cases. On the other hand, the discontinuous Galerkin approach to the cohesive zone method is a more mature and widely valid method that can be included in commercial software in the near future.

2.7 Summary and conlusions

In the present chapter, several methods to numerically represent the fracture and fragmentation of structural glass have been assessed. While the physical properties of soda-lime silicate glass are well known for the intact state, the fracture strength is a less obvious quantity. Griffith flaws at the surface cause great variability of the observed, technical strength of glass, which can only be described statistically. Furthermore, the overall strength seems to increase with the loading rate for long and short load duration, but no clearly defined law for impact loading can be found in literature. Based on test data from Nie et al. [70], the relative strength increase with loading rate can be estimated and used to numerically evaluate dynamic glass response. However, a validated relation obtained by controlled testing would be most valuable in the future. Other characteristics of glass fracture are known with more certainty: fracture toughness, fracture energy and maximum crack propagation velocity.

In numerical analysis, the onset of fracture can only be predicted correctly when the model captures the elastic response well. The boundary conditions have a major influence on the accuracy and the validity of simplified representation should be evaluated on case by case basis. The drop weight impact on a small, circular glass specimen has been introduced; in this case, elastic response only agrees with the experiment when the deformable clamping rings are modelled as such. Subsequent fracture simulations show that fragmentation of the modelled glass part requires the stress field due to bolt clamping to be taken into account as well.

The most encountered simulation technique for the cracking of structural and automotive glass panels is that of element deletion. This technique is relatively easy to implement, but far from perfect; it shows tremendous mesh sensitivity,

leaves cracks as wide as an element's length and is unable to capture gradients near the crack tip. But the element deletion method can be used for thin-walled structures under dynamic loading and does allow crack branching and coalescence, as opposed to most other numerical methods. Many different formulations for the fracture criterion and damage evolution are possible. Three approaches are evaluated for unit elements and for drop weight impact on a glass disk:

- Immediate deletion with no damage evolution (implemented as `VUMAT`): this approach is often used in literature, although it is characterised by an aggressive failure which causes high stress waves in the surrounding elements, occasionally resulting in instabilities. The direction of a crack is not taken into account and the fracture of glass cannot be properly modelled with this method.
- Hillerborg model (built-in material model in ABAQUS): an element length criterion exists for this model to properly represent the fracture energy. When this is not satisfied, which is usually not the case for glass, the material model switches to pseudo-plastic behaviour with a sudden change of stress at ultimate failure. While the fracture pattern is simulated reasonably well, it is seen that components in the energy balance result from instabilities and have no physical meaning.
- Crack delay model (implemented as `VUMAT`): this material model is designed to overcome issues experienced with other approaches and is intended specifically for glass cracking. It is based on the fact that the evolution of damage is not instantaneous. The limiting damage rate is derived from the maximum crack propagation velocity, and aids in preventing overly high stress oscillations in the simulated glass fragments. Furthermore, crack directionality is taken into account and only physical constants are used as input for the material model.

Generally, the crack pattern resulting from the element deletion depends on the mesh topology. A mesh can be built to favour the formation of certain cracks, but an unstructured, random mesh type allows cracks to propagate more naturally, which is generally preferred.

Alternative, more advanced methods to simulate fracture exist as well. Not all such methods can be used (yet) for dynamic fracture with crack branching, intersection and fragmentation; e.g. XFEM and discrete elements method. The meshfree SPH method has been evaluated for both high and low velocity fracture. Although performing well for high velocity impact, under low velocity impact the glass disk behaves with a globally softened stiffness upon cracking instead of fragmenting. This is due to the smoothing kernel formulation by which particles on either side of a crack are still within each other's influence domain when their velocities do not drive them apart rapidly.

Also the use of cohesive zone elements has been considered for dynamic fracture. Different approaches exist for the implementation in FE software, of which only the intrinsic approach can be used in ABAQUS without access to the source code. This approach requires the insertion of interface elements at all interelement boundaries, for which an efficient program has been developed. However, the cohesive zone, initially with zero thickness, has an additional stiffness that distorts the elastic response to an impact loading. This can be solved by assigning the interface elements a small, finite thickness. Upon fracture, cracks initiate at many locations, rather than a few propagating cracks. Subsequently, the damage in the cohesive zone does not reach its ultimate separation at most of the cohesive elements, which further act with reduced stiffness and fragmentation no longer occurs.

In further modelling of the fracture response of larger, laminated glazing, the element deletion technique is used with the crack delay model that has been introduced in this chapter.

Chapter 3

PVB Interlayer

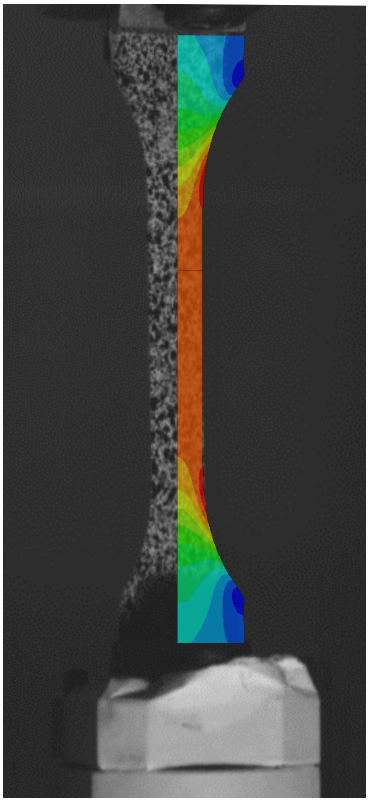

Uniaxial test of PVB interlayer: experiment and simulation.

3.1 Introduction

Two or more glass plies can be laminated with transparent, polymer interlayer to form a layered material with enhanced characteristics. In construction and for automotive windshield, laminated glass is used mainly for safety purposes. In essence, the interlayer foil will retain glass fragments when the window is fractured. By proper selection of the interlayer material, laminated glass may also be used for reasons other than mechanical. These include acoustic insulation, fire resistance, altering transparency and appearance, blocking of UV light and lamination to photovoltaic cells.

The polymers that are used in structural glass are mainly amorphous thermoplastics and elastomers whose properties can be fine-tuned by various chemical additives and plasticisers. For safety and security purposes, the thermoplastic polyvinyl butyral (PVB) is by far the most used interlayer material. PVB products are manufactured by various companies, notably Eastman™ (Saflex®) and Kuraray™ (Trosifol®, Butacite®). PVB interlayer can be produced with mechanical and adhesive properties as desired. For laminated safety glass, the most common PVB interlayers, Saflex® R-series and Trosifol® BG-series, have a glass transition temperature T_G around room temperature and are relatively flexible [152] (see Fig. 3.1). When stiffer post-fracture behaviour is required, e.g. for glass floors and balustrades, a PVB product with higher T_G or an ionomeric interlayer may be used. An example of the latter is Kuraray™'s SentryGlas®, which is a modified polyethylene with strong adhesion to glass surfaces.

Interlayer materials that are less frequently used for safety purposes are the elastomeric ethylene vinyl acetate (EVA) and thermoplastic polyurethane (TPU), which do not require the use of an autoclave for lamination. EVA has low moisture sensitivity and good durability, and is therefore often used as an interlayer in the photovoltaic sector. TPU can be preferred for its good adhesion to polycarbonate, which is used in protective glazing with resistance to burglary and ballistic impact. Also thermosetting Cast-In-Place (CIP) resins may be used for safety purposes, although this product is less commonly applied. Glazing laminated with CIP resin requires a higher manufacturing cost and has poorer low temperature impact performance compared to PVB laminates [153].

In this work, only polyvinyl butyral interlayers are considered, as they constitute the vast majority of interlayers used in laminated safety glass and their performance has proven to be effective under low velocity impact and blast. PVB interlayer is produced from PVB resin, which is too stiff in film form to be used as interlayer directly [14]. Plasticisers are added to the resin to make the end product more flexible, as well as decrease the cold-crack temperature. When cured in an autoclave process, the PVB material adheres to glass through hydrogen bridges [154]. The adhesive properties of PVB to glass

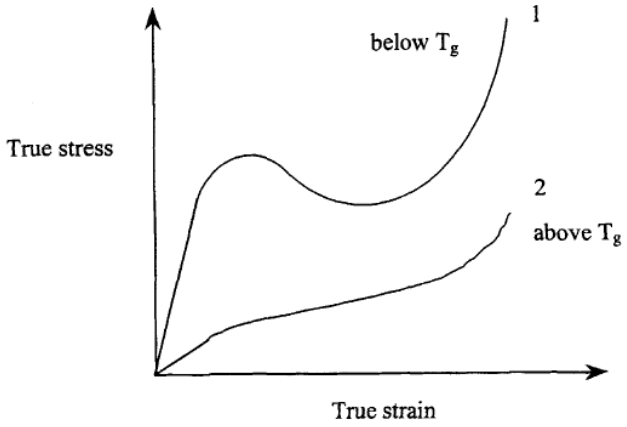

Figure 3.1: Typical stress-strain relation of amorphous polymers (Figure from Juang et al. [152]).

can be controlled by salt additives that are mixed with the resin. Before lamination, the glass surfaces should also be cleaned from mineral residues that interfere with the bonding of PVB to glass and reduce the overall quality of the adhesion. Subsequently, the glass-film assembly is de-aired in a nip-roll or vacuum process and finally laminated in an autoclave.

When the glass breaks in an impact event, the function of the interlayer exceeds the mere adhesion of glass fragments to avoid propulsion. The PVB foil can absorb a large portion of the impact energy. This takes place by various mechanisms: elastic deformation and material damping, viscous relaxation, and local delamination. The elastic stiffness of the interlayer has a major influence on the forces exerted on the impactor in the post-fractured state. This impactor may in the worst case be a pedestrian in a vehicle crash, for whom the experienced accelerations can be lethal above a critical level. In such case, a softer interlayer may prevent severe injury or worse. Furthermore, an object or air blast wave can penetrate the window when the PVB tears. This can be avoided to some extent by using a relatively soft PVB with lower adhesion grade.

The objective of this chapter is to describe the mechanical behaviour of PVB interlayer by a material law that can be used in FEM analysis. This is a key step to finally enable prediction of forces, energies and ultimate failure of a broken laminated glass panel under a given impact or blast load. Section 3.2 presents a description of concepts in the constitutive modelling of polymers. This is followed by a review of the characterisation of PVB in scientific literature. In Section 3.4, results are given for uniaxial tensile tests of Saflex® R-series PVB interlayer and Section 3.5 discusses the fitting of a material model to the test results.

3.2 Constitutive modelling

As indicated by Fig. 3.1, PVB interlayer with its glass transition temperature $T_G \approx 30°\text{C}$ is highly dependent of temperature and loading rate, and may reach very high strains (200% and more) during the impact event. However, various sources (a.o. Refs. [155–157]) report that PVB does not show permanent deformation, but returns to its original shape after some time. This is confirmed by our own observations, except for experiments at an elevated temperature of 60°C. Therefore, plasticity is not taken into account for the constitutive modelling of PVB interlayer.

This section introduces the terms and principles for constitutive laws that can be used to describe the behaviour of PVB interlayer. When only small deformations are considered, the time-dependent material behaviour for creep and relaxation, as well as the temperature-dependency can be described by linear viscoelasticity. For large deformation under constant temperature and quasi-constant deformation rate, the stress-strain curve for PVB may well be approached by a hyperelastic law for a nearly incompressible material. A more generally valid material law can be obtained by the combination of both these material models, or by a different, more direct approach.

3.2.1 Linear Viscoelasticity

In solid mechanics, the classical Hooke's law describes the stress as directly proportional to the strain, but independent of the strain rate. The classical theory of hydrodynamics considers Newtonian fluids, for which the viscous stress is directly proportional to the rate of deformation, but independent of the strain itself. In a viscoelastic medium, which can be either solid or fluid, stresses are dependent of both strain and time. The theory of viscoelasticity is explained in various handbooks, most notably Ref. [158].

Many materials display some form of viscoelastic behaviour, e.g. polymers, concrete, ice, biological materials, etc. They have the following properties in common:

1. The relation between the stress and deformation is causal: the strain at time t_1 can only influence the stress at t_2 if $t_1 \leq t_2$.

2. The relation between stress and strain is local.

3. The stress is dependent of the strain history. As a consequence, no direct relation exists between $\epsilon_{ij}(\boldsymbol{x}_1, t_1)$ and $\sigma_{ij}(\boldsymbol{x}_1, t_1)$.

4. If the stress in a point describes a closed cycle, the strain does not necessarily go through a closed cycle as well during this time. This means

that the work exerted by the stress during this cycle is not necessarily zero, but can be positive: energy can be dissipated in the process.

$$\oint \sigma_{ij}\dot{\epsilon}_{ij}\mathrm{d}t \geq 0 \tag{3.1}$$

For the sake of clarity, the basics of linear viscoelasticity are explained here for the 1-dimensional case. More complete theory may be found in textbooks on viscoelasticity, such as by Ferry [158] and Bergström [159].

3.2.1.1 Relaxation and creep

Given the strain evolution $\epsilon(t)$, an increase $\dot{\epsilon}(\tau)\Delta\tau$ at a time $\tau \leq t$ has an influence on the stress $\sigma(t)$:

$$\sigma(t) = G\dot{\epsilon}(\tau)\Delta\tau \tag{3.2}$$

As τ goes further in history, its influence on the current state diminishes. Thus, the shear modulus must be a monotonously decreasing function of $t - \tau$, i.e. $G(t - \tau)$. Moreover, according to Boltzmann's superposition principle, the effects of sequential changes in strain are additive. Assuming that no stress or deformation is present at $t = 0$, this results in the following constitutive law for relaxation behaviour of a viscoelastic solid:

$$\sigma(t) = \int_0^t G(t-\tau)\dot{\epsilon}(\tau)\mathrm{d}\tau \tag{3.3}$$

Which can also be written as:

$$\sigma(t) = G(0)\epsilon(t) + \int_0^t \dot{G}(t-\tau)\epsilon(\tau)\mathrm{d}\tau \tag{3.4}$$

The function $G(t - \tau)$ can be experimentally determined in a relaxation test.

Similarly, a constitutive law can be defined for creep behaviour:

$$\epsilon(t) = J(0)\sigma(t) + \int_0^t \dot{J}(t-\tau)\sigma(\tau)\mathrm{d}\tau, \tag{3.5}$$

where the compliance function $J(t - \tau)$ can be determined experimentally in a creep test.
Using the Laplace transform, it can be established that the descriptions of the deformation process for relaxation and creep are equivalent.

3.2.1.2 Complex modulus

If the viscoelastic material is harmonically excited by imposing a strain $\epsilon(t) = \epsilon_1 \sin(\omega t)$, the stress responds with the same frequency in steady state. There exists a frequency range in which the stress lags behind on the strain with a phase difference $\delta(\omega)$, as shown in Fig. 3.2. Also the amplitude of the stress varies with the excitation frequency.
Application of the Fourier transform on Eq. 3.4 results in:

$$\begin{aligned} \mathcal{F}(\sigma(t)) &= G(0)\mathcal{F}(\epsilon(t)) + \mathcal{F}\left(\dot{G}(t)\right)\mathcal{F}(\epsilon(t)) \\ &= \left[E_r(\omega) + E_i(\omega)\right]\mathcal{F}(\epsilon(t)), \end{aligned} \tag{3.6}$$

where:

$$E_r(\omega) = G(0) + \mathrm{Re}\left[\mathcal{F}\left(\dot{G}(t)\right)\right] \tag{3.7}$$

$$E_i(\omega) = \mathrm{Im}\left[\mathcal{F}\left(\dot{G}(t)\right)\right] \tag{3.8}$$

When the material is harmonically excited with a strain function $\epsilon(t) = \epsilon_1 e^{(i\omega t)}$, the amplitude $\sigma_1(\omega)$ and phase angle $\delta(\omega)$ can be determined as:

$$\sigma_1 = \epsilon_1 \sqrt{E_r^2 + E_i^2} \tag{3.9}$$

$$\tan\delta = E_i / E_r \tag{3.10}$$

The functions $E_r(\omega)$ and $E_i(\omega)$ are termed the *storage* and *loss modulus*. The typical behaviour of a viscoelastic material is given for the frequency domain in Fig. 3.2. Three different regimes can be discerned: at very low frequencies (or low strain rates), the material behaves *rubbery* with a low stiffness that is not very sensitive to changes in the deformation rate. The stiffness is much smaller than the bulk modulus, which is more or less independent of the deformation rate. In this regime, the stress responds in phase with the strain. At very high frequencies, a similar behaviour is seen but with a much higher stiffness. This is the *glassy* state. If the difference between this stiffness and the bulk modulus is not very large, incompressibility of the material may no longer be assumed. The transition between both states is where the material behaves very rate-sensitive. It is also the region where the loss modulus is important and where a considerable portion of the strain energy can be viscously dissipated. The strain energy density is expressed as the work per cycle for harmonic excitation:

$$\frac{\mathrm{dU}}{\mathrm{dV}} = -\omega E_r \epsilon^2 \int_0^{2\pi/\omega} \sin(\omega t)\cos(\omega t)\mathrm{d}t + \omega E_i \epsilon^2 \int_0^{2\pi/\omega} \sin^2(\omega t)\mathrm{d}t, \tag{3.11}$$

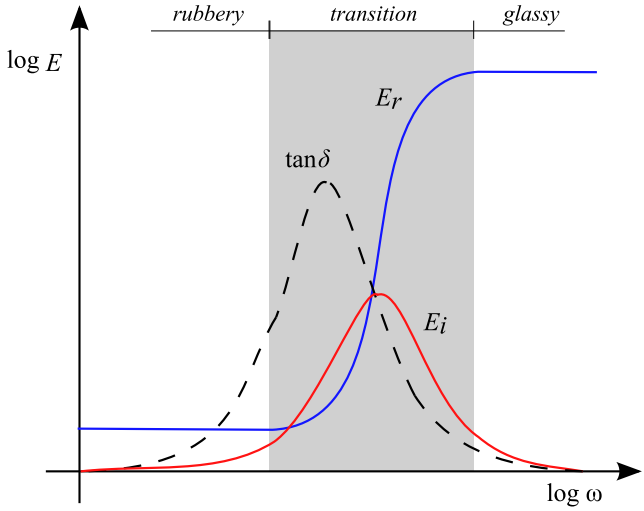

Figure 3.2: Storage and loss modulus of a viscoelastic material in function of excitation frequency.

where the term proportional to the loss modulus is the viscoelastic energy dissipation per cycle.

Temperature has a similar, but opposite effect on the viscoelastic modulus. At low temperatures, the modulus is high and the losses are small; at high temperature, the modulus is low and the losses are also small. The *time-temperature superposition principle* states that the functions of the loss and storage moduli can be shifted by a certain factor in the frequency or time domain when evaluated at a different temperature. This is schematically shown in Fig. 3.3 for the time domain. The shift factor α_T is a function of temperature, relative to a reference temperature at which $\alpha_T = 1$.

3.2.1.3 Generalised Maxwell model

Viscoelastic material behaviour can be represented by a network of elastic springs and viscous dashpot elements. Historically important models are the Maxwell model, consisting of a single spring and dashpot in series, and the Kelvin-Voight model where they are in parallel. The most general representation is the generalised Maxwell model, shown in Fig. 3.4. This viscoelastic material model is included in most commercial FE codes.

The relaxation spectrum is formed by all couples (G_k, η_k). The relaxation time for each Maxwell element is given by $\tau_k = \eta_k / G_k$. The stress is equal to the sum of contributions from all Maxwell elements, while the strain is equal for every element. For $n + 1$ elements, the relaxation modulus is given by:

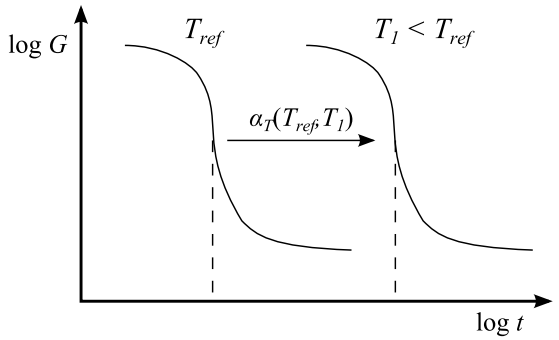

Figure 3.3: Shift of relaxation curve in accordance with temperature-rate superposition principle.

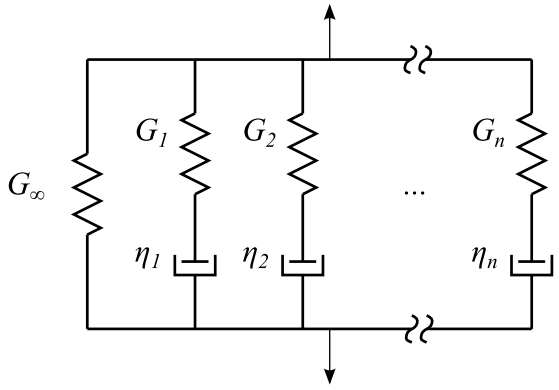

Figure 3.4: Generalised Maxwell model.

$$G(t) = G_\infty + \sum_{k=1}^{n} G_k e^{(-t/\tau_k)}, \tag{3.12}$$

where G_∞ is the modulus for long-term load duration. Similarly, the instantaneous modulus G_0 is defined as the sum of all spring constants G_k. For use in finite element calculation, the dimensionless relaxation modulus $g(t) = G(t)/G_0$ is developed as a *Prony series*:

$$g(t) = 1 - \sum_{k=1}^{n} g_k \left[1 - e^{(-t/\tau_k)}\right] \tag{3.13}$$

By substitution in Eq. 3.4:

$$\sigma(t) = G_0 \left[\epsilon(t) - \sum_{k=1}^{n} \epsilon_k(t)\right], \tag{3.14}$$

where:

$$\epsilon_k(t) = \frac{g_k}{\tau_k} \int_0^t e^{-\tau/\tau_k} \epsilon(t-\tau) \mathrm{d}\tau \tag{3.15}$$

Alternative model representations exist for viscoelastic materials. An overview is given by Potvin [160], who also developed a fractional Kelvin-Voight model. However, she concluded that the formulation by Prony series is accurate and efficient in finite element analysis. Only when little experimental data is available, other methods may be preferred.

3.2.2 Hyperelasticity

The elastic deformation of rubber-like materials can no longer be described by Hooke's law for the following reasons:

1. The strain can become very large.
2. The material is nearly incompressible; the bulk modulus K is much greater than the shear modulus G.
3. At large strains, the stress is no longer directly proportional to the strain, but it is reversible.

The first item is dealt with by using the finite Green-Lagrange strain tensor ϵ_{ij}, which accounts for geometric non-linearity, and the second Piola-Kirchhoff stress tensor S_{kl}. If the stress is a function of the strain, the strain energy density can be written as:

$$\frac{\mathrm{d}U}{\mathrm{d}V} = \int_0^t S_{kl}(\epsilon_{ij}) \dot{\epsilon_{kl}} \mathrm{d}t \tag{3.16}$$

Then it can be stated that the elastic energy density is only dependent of the deformation, i.e.:

$$\frac{\mathrm{d}U}{\mathrm{d}V} = W(\epsilon_{kl}), \tag{3.17}$$

where $W(\epsilon_{kl})$ is a positive definite function and is termed the *strain energy potential*. Consequently:

$$S_{kl} = \frac{\partial W}{\partial \epsilon_{kl}} \tag{3.18}$$

Thus, a suitable expression should be found for the function W to describe the material behaviour. For an isotropic material, a certain strain ϵ_{kl} that is applied in one coordinate system should result in the same strain energy as when the same deformation is applied in another coordinate system. This is

only possible when the function W is an invariant and, as such, a function of the three invariants of the Green deformation tensor $\mathbf{C}$: $W = W(J_1, J_2, J_3)$, where in terms of the principal stretch ratios:

$$\begin{aligned} J_1 &= tr(\mathbf{C}) && = \lambda_I^2 + \lambda_{II}^2 + \lambda_{III}^2 \\ J_2 &= \frac{1}{2}\left[tr(\mathbf{C})^2 - tr(\mathbf{C}^2)\right] && = \lambda_I^2\lambda_{II}^2 + \lambda_{II}^2\lambda_{III}^2 + \lambda_{III}^2\lambda_I^2 \\ J_3 &= det(\mathbf{C}) && = \lambda_I^2\lambda_{II}^2\lambda_{III}^2 \end{aligned} \tag{3.19}$$

The third invariant is related to the volume change: $J_3 = (V/V_0)^2$. If the material can be idealised as incompressible, J_3 is no longer a variable.

A common expression for the strain energy potential function is the polynomial formulation:

$$W(J_1, J_2) = \sum_{i+j=1}^{N} C_{ij}(J_1 - 3)^i(J_2 - 3)^j \tag{3.20}$$

Certain strain energy potential functions are commonly known under a different name, depending on their non-zero coefficients as given in Table 3.1. Many strain energy density functions other than the polynomial form can be defined. A notable alternative is the Ogden strain energy potential, for which the variables are the principal stretches, rather than the invariants of the deformation tensor. The Ogden function can more accurately describe rubber materials at higher strains, but requires extensive experimental data for more than one deformation mode. Many other hyperelastic functions can be formulated; an extensive overview is given by Hoss and Marczak [161].

Table 3.1: Strain energy potential functions of polynomial form.

	Non-zero coefficients
Neo-Hookean	C_{10}
Mooney-Rivlin	C_{10}, C_{01}
Haines and Wilson	C_{10}, C_{01}, C_{20},C_{11},C_{02}, C_{30}
Yeoh	C_{10}, C_{20}, C_{30}
Reduced Polynomial	C_{i0}

In his seminal paper, Yeoh [162] examined the best suiting formulation for a strain energy density function when only uniaxial test data is available. Based on his observations for filled rubbers, he noted that for small strains $\partial W/\partial J_1$ and $\partial W/\partial J_2$ vary considerably with J_1 and J_2, but for larger strains $\partial W/\partial J_1$ tends to become relatively much larger than $\partial W/\partial J_2$ and independent of J_2. Moreover, a simple relation seems to exist between stress-strain data obtained in uniaxial tension, uniaxial compression and simple shear. The stress terms

plotted against the invariant $(J_1 - 3)$ give a single curve for data in these three deformation modes. Therefore, Yeoh proposed a strain energy density function in reduced polynomial form of third order or higher. Such function has a varying shear modulus, as opposed to the Neo-Hooke and Mooney-Rivlin functions, and can describe the rise of the modulus at high strains due to the limiting chain extensibility. This point of view is followed by Arruda and Boyce [163], and Gent [164] who proposed sophisticated models that require less material constants to be determined, but are also less generally applicable than the (higher order) Yeoh function. While Arruda and Boyce merely reduce the number of material constants to be defined for a 5th-order reduced polynomial form that approaches the behaviour of a rubber with limiting extensibility, Gent proposed a logarithmic function that more naturally describes this behaviour. The Gent function is given by:

$$W(J_1) = -\frac{\mu J_m}{2} \ln\left(1 - \frac{J_1 - 3}{J_m}\right), \tag{3.21}$$

where μ is the shear modulus when $J_1 = 0$, and J_m is the extensibility limit of the material. The typical shape of this function is shown in Fig. 3.5. The function reverts to Neo-Hookean behaviour (a constant shear modulus) when $J_m \to \infty$.

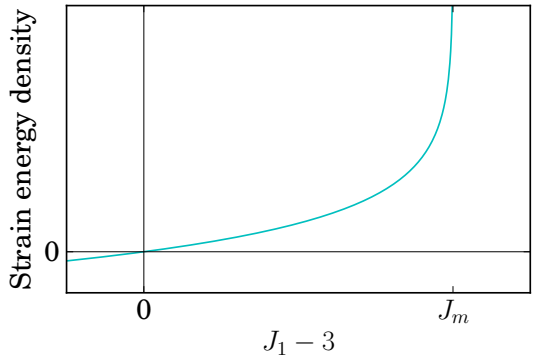

Figure 3.5: The Gent strain energy potential.

3.2.3 Rate-dependency at finite strains

Real rubbers, polymers and biomaterials show rate-dependency of the stress-strain behaviour, stress relaxation and hysteresis in cyclic loading, also for strains that are no longer regarded as small. These aspects of material behaviour have basically common sources: reorientation and uncoiling of molecular chains, readjustment of kinks, etc. Macromechanically, this behaviour can

be described in a number of ways. They differ in the formulation of the physical behaviour of the material and the accuracy by which this is represented.

A phenomenological formulation for hyperelasticity with rate effects has been proposed by Kolling et al. [165]. It requires only test data from uniaxial tensile tests at different, but constant, strain rates. Subsequently, the test data is transformed into an Ogden functional not by parameter fitting, but as a tabulated formulation. Rate-dependency of the model is established by interpolation between the different Ogden functions at constant strain rate, without considering the viscoelasticity of the material.

Another approach is to combine hyperelasticity and the Prony series representation into a hyper-viscoelastic constitutive model. In this case, it is assumed that the effects of deformation and time are separated:

$$\sigma(\epsilon) = \sigma_0(\epsilon)g(t), \tag{3.22}$$

where the dimensionless function $g(t)$ is represented by Prony series. Thus, for a given load duration and temperature, the instantaneous stress-strain relation $\sigma(\epsilon)$ is scaled in magnitude, but its shape remains the same. Dalrymple et al. [166] note that this constitutive model is able to represent elastomer strain rate dependency accurately and can effectively be used to simulate also dynamic peak load conditions. However, the Prony series do not replicate the material's hysteresis loop during loading and unloading well. Consequently, it will not necessarily capture the energy dissipated by loading and unloading correctly.

For many polymers, it is not experimentally observed that their stress-strain behaviour simply scales with the loading rate. To overcome this, a more general function $g(\epsilon, t)$ could be defined. Khajehsaeid et al. [167] propose a function in which the spring elements of the generalised Maxwell model (see Fig. 3.4) are made dependent of the strain: $g_k(\epsilon)$ in Eq. 3.13 as a function derived from a strain energy potential. Additionally, nonlinear viscous behaviour can be modelled by dashpot elements that are dependent of the strain rate. In the model of Khajehsaeid et al., this is achieved by a function $\eta(\dot{\epsilon})$.

The Parallel Rheological Framework (PRF) in Abaqus has been specifically designed for modelling the nonlinear viscoelasticity of polymers and rubbers [168]. This is a Parallel Network model (see Bergström [159]) which allows for an arbitrary number of parallel networks where each network consists of an elastic component and an optional flow component. Only the instantaneous behaviour is defined by a hyperelastic law and not each spring separately. Nonlinear viscous behaviour is defined for each dashpot element separately by a flow rule for the creep strain rate. Such viscoplasticity model can capture the rheological response of almost any polymer, but requires extensive experimental data for different deformation modes and for cyclic loading.

3.3 Characterisation of mechanical properties of PVB in literature

The mechanical behaviour of laminated glass has been a major concern among glass researchers and designers since its first usage. Before 1990, most efforts went into describing a layered-plate model for the laminate as a whole. Experimental research to this end has been conducted by a.o. Behr et al. [169] and Vallabhan et al. [170]. Later, Vallabhan et al. [171] characterised the PVB interlayer separately by experiments for simple shear at a very low strain rate and room temperature ($21 - 23°C$). For these conditions, they observed that the shear modulus is less than 1.0 MPa for small strains and ascends with increasing strain until remaining constant for shear strains greater than 1.5. Upon removal of the load, all specimens returned back to their original state without permanent set.

Juang et al. [152] studied the viscoelastic behaviour of PVB interlayer near and above the glass transition temperature in order to better understand how the material undergoes processing. They proposed a hyper-viscoelastic material model, valid for low strain rates and around a reference temperature of 65°C. For the normal operation temperature, i.e. around 20°C, several authors have performed Dynamic Mechanical Analysis (DMA) tests to characterise the small-strain linear viscoelasticity. By this method, described in detail by Ferry [158], they have obtained material constants for a Prony series representation, along with the temperature shift function. These models are shown graphically in Fig. 3.6. It is important to note that the interlayers that were tested by the different authors were not all of the same type. They do all have the same function in laminated safety glass, which is to absorb energy during an impact and have a glass transition temperature of around 30°C. The interlayer products for acoustical damping and the high-stiffness variant are not considered. Bennison et al. [172] worked with Butacite® interlayer, while D'haene and Savineau [173], and later Hooper [156], tested Saflex® R-series PVB. Barredo et al. did not state which type of PVB they have used in DMA-testing. Kuntsche [7] has tested the Trosifol® BG-series interlayer. Interestingly, Kuntsche has also performed DMA tests for other interlayer types, such as EVA, TPU and ionomers.

It is apparent that the material models by D'haene and Savineau, and Hooper differ substantially from each other even though the tested material and the method are the same. The temperature dependency of Saflex R-series PVB, also used in this work, has been characterised alternatively by Van Dam [6] with the resonalyser method, for which the results are in good agreement with the model of D'haene and Savineau.

The small-strain viscoelasticity is sufficient to characterise the interlayer's be-

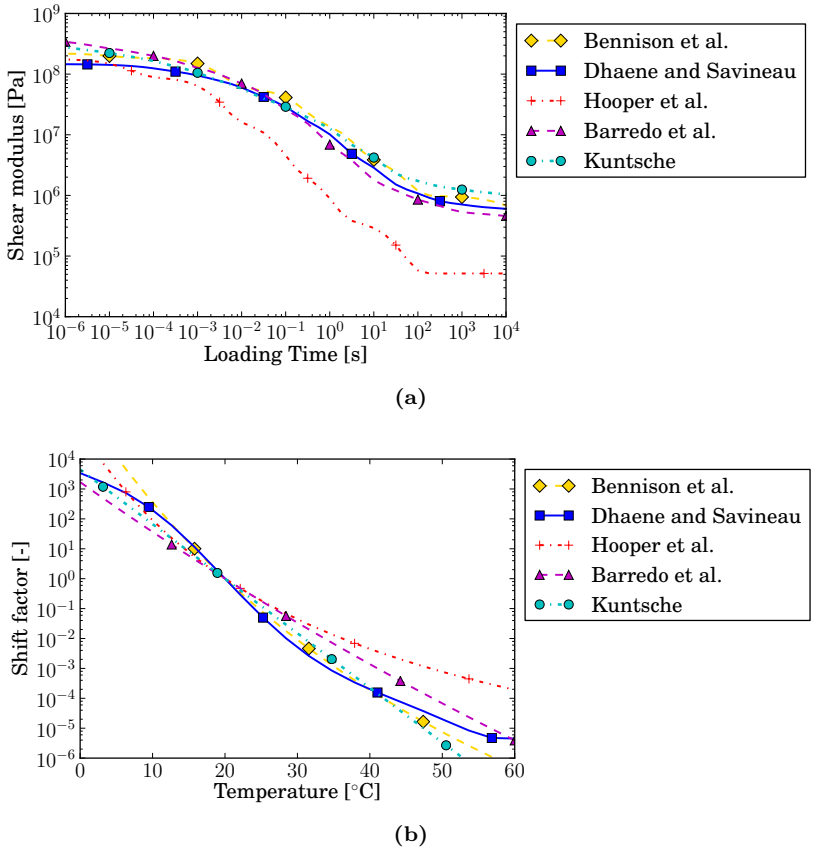

Figure 3.6: Relaxation stiffness of PVB in literature: (a) shear modulus at reference temperature $T = 20°\mathrm{C}$, and (b) temperature-time shift factor.

haviour for intact laminated glazing, under both static and transient loading. However, when the glass breaks, the PVB material may rapidly reach a state of high deformation. Very high strains are particularly found in the immediate vicinity of the narrow glass cracks. If the strain becomes too large, the interlayer may locally tear, which can quickly lead to failure of the entire panel. Therefore, in order to conceive a predictive numerical model, it is highly important to also understand the PVB response at moderate and large strains, and over a representative range of deformation rates. Morison et al. [155] have performed uniaxial tensile tests on Saflex® R-series PVB at strain rates between 9.4 and 74.2 s^{-1}. The tests were performed for both cured and uncured samples, but no notable difference was observed between their measured responses (which is later confirmed by Van Dam for similar specimens at low tensile loading rates). At all extension rates, the force-displacement results were observed to approach a bilinear relation with a distinguishable stiffness

at the low strain range and another, about twenty times lower, for strains of 20% and upwards. Iwasaki et al. [174] observed a similar bilinear relation in the stress-strain curve for Sekisui S-LEC™ PVB, tested in uniaxial extension at a nominal strain rate of $118\,\mathrm{s}^{-1}$. Despite no permanent set being observed, Morison et al. initially modelled the material as elasto-plastic, but noted high local concentrations of plastic strain, distorting the numerical result. For this reason, they recommend a non-linear viscoelastic constitutive model.

Hooper et al. [156] also performed uniaxial tensile tests on Saflex® R-series PVB. They described the material behaviour empirically by expressing the small-strain modulus E_0, the large strain modulus $E_{20\%}$ and the ultimate tearing strain ϵ_f as a function of the strain rate. This model is given by Eqs. 3.23 and provides a good fit to the experimental data for strain rates between 0.2 and $60\,\mathrm{s}^{-1}$. For a reference strain rate $\dot{\epsilon}_0 = 1\,\mathrm{s}^{-1}$, the small strain modulus is $E_{0,0} = 51\,\mathrm{MPa}$ and the failure strain $\epsilon_{f,0} = 2.2$. It should be noted that Hooper derived these relations from the nominal stress vs. nominal strain relation, which was directly obtained from the force-displacement data.

$$\begin{aligned} E_0 &= E_{0,0} \left(\frac{\dot{\epsilon}}{\dot{\epsilon}_0} \right)^{1/2} \\ E_{20\%} &= 9\,\mathrm{MPa} \\ \epsilon_f &= -0.05 \log \left(\frac{\dot{\epsilon}}{\dot{\epsilon}_0} \right) + \epsilon_{f,0} \end{aligned} \tag{3.23}$$

Similar tests on Trosifol® BG-series PVB were performed by Kuntsche et al. [7, 157] for both low and high pulling speeds. Kuntsche et al. made use of the Digital Image Correlation technique (DIC) to obtain the true strains and stresses. Using this technique, they also note that the strain rate during the test is not a constant value. Consequently, they have used an interpolation technique to calculate the behaviour at constant strain rates. For these curves, shown in Fig. 3.7 the stress-strain relations no longer appear as approximately bilinear. The data from Fig. 3.7 can be used directly as input for the constitutive model by Kolling et al. [165], which has been done for the finite element simulations in Ref. [119].

Finally, a selected overview of material models for PVB interlayer used in the numerical simulation of laminated glass under dynamic loading is given in Table 3.2.

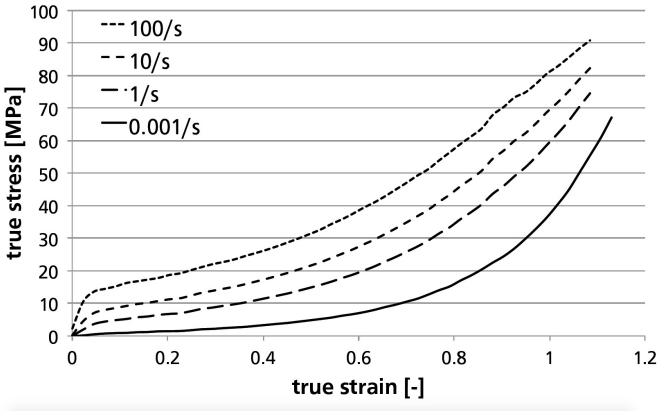

Figure 3.7: Uniaxial tensile tests on PVB at 22°C by Schneider et al. [157]: true stress vs. true strain at constant strain rates (Fig. from Schneider et al. [157]).

Table 3.2: Material models for PVB for impact simulation of laminated glass in literature.

Author(s)	Constitutive model	Material constants
Dubois and Kolling, 2003 [102]	hyperelasticity (Mooney-Rivlin)	$C_{10} = 1.60\,\text{MPa}$, $C_{01} = 0.06\,\text{MPa}$
Sun et al., 2005 [103]	linear elasticity	$E = 9\,\text{MPa}$
Timmel et al., 2007 [104]	elasto-plasticity (smeared)	$E_{mod} = 15260\,\text{MPa}$
Larcher et al., 2008 [75]	elasto-plasticity	$E = 220\,\text{MPa}$, $\sigma_y = 11\,\text{MPa}$
Amadio and Bedon, 2012 [112, 113]	elasto-plasticity	$E = 500\,\text{MPa}$, $\sigma_y = 11\,\text{MPa}$
Pelfrene, Kuntsche et al., 2016 [119]	rate-dependent hyperelasticity	from test data (Fig. 3.7)

3.4 Tensile testing of PVB

Considering the differences in material properties for PVB interlayer products by different manufacturers and the strong influence of temperature, it is appropriate to perform additional experiments for the response at large extension of the interlayer considered in this work, Saflex® R-series PVB. The small-strain rheological behaviour for this material is deemed to be sufficiently known by

both the DMA experiments by D'haene [173] and the resonalyser technique used by Van Dam [6].

Uniaxial tensile tests are performed for PVB specimens with dimensions as given in Fig. 3.8. The checkered areas in this figure are glued to cardboard strips of the same size, by which the sample is clamped between machine grips.

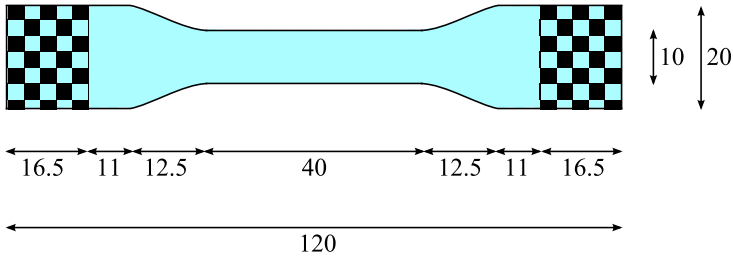

Figure 3.8: Dimensions in [mm] of PVB specimens for uniaxial tensile testing; thickness of the specimen is 0.76 mm.

The specimens are stored at room temperature in the laboratory where they are tested. The temperature is measured on the mounted specimen at the start of each test with a Fluke 561 infrared thermometer.

The material is tested for both low and high deformation rates. The low-speed tests are performed on an Instron 5800R tensile testing machine at predefined crosshead speeds of 0.33 and 3.33 mm/s. For the high-speed tests, an Instron IST Hydropuls tensile testing machine has been used, which is capable of reaching speeds up to 20 m/s. With this machine, tests have been performed at nominal crosshead speeds of 0.1, 0.33, 0.5, 3.0 and 10.0 m/s. Both machines record the loading force and displacement of the crosshead. No additional strain measurement has been performed.[1] This is also not strictly necessary for the numerical approach in Section 3.5.

For testing at high speeds, it is common to install a lost-motion device to allow acceleration of the crosshead up to its predefined velocity. However, for the PVB samples, the weight of the lost motion device already poses a high load by which it begins to extend before any measurement can take place. An alternative solution is found in positioning the machine clamps a mere 37 mm apart prior to the test, as opposed to the 87 mm distance between the checkered areas in Fig. 3.8. In that position, the flexible interlayer specimen is curled up and experiences no force until it is straightened by a 50 mm downward motion of the crosshead.

[1] Initially, DIC technique was used for precise strain measurement, but this required the use of strongly powered lamps which heated up the specimen to temperatures over 40°C. Taking account of the time-temperature superposition principle, testing speeds beyond the capability of the machine would be required to capture the rate effect on the material.

The force-displacement measurements for the low-speed tensile tests are given in Fig. 3.9.

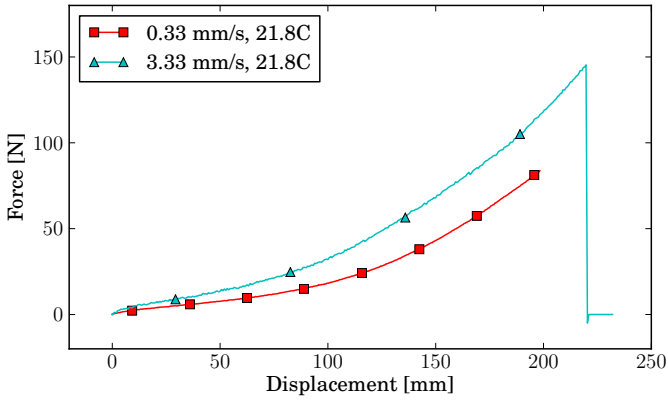

Figure 3.9: Tensile test results for PVB specimens at low speeds.

For the high-speed tests, five specimens were used at each speed. In Fig. 3.10, the results are shown for the specimens that have been tested at 333 mm/s. The time and displacement are set to zero on the moment that the specimen is straightened and begins to extend. For 100, 333 and 500 mm/s, the crosshead has at this point reached its nominal speed, which remains approximately constant thereafter. The force-displacement curves for all high-speed tests approach a bilinear behaviour, even more clearly than for tests of the same PVB product by Morison [155] and Hooper et al. [156]. For one specimen in Fig. 3.10, that was tested at a slightly higher temperature, the measured forces are a bit, yet noticeably, smaller than for the others. This again demonstrates the material's sensitivity to temperature in the transition zone between its glassy and rubbery state.

Similar curves are shown in Fig. 3.11 for the highest testing speed, 10 m/s. It is seen that the crosshead has not accelerated to its nominal velocity yet when the specimen starts to extend. Neither does the crosshead speed remain constant for the short duration in which the specimen is strained and tears. This should be taken into account when numerically simulating the tensile test.

The results of the tensile tests are well reproducible; force vs. displacement curves for samples tested at the same speed and temperature are as good as coincident. The median of force-displacement responses at every testing speed is shown in Fig. 3.12. The raw force data has been processed by a 2nd-order Butterworth filter with cutoff frequency of 2.3 kHz, 7.6 kHz, 11.5 kHz, 69 kHz and 93 kHz for lowest to highest speed respectively.

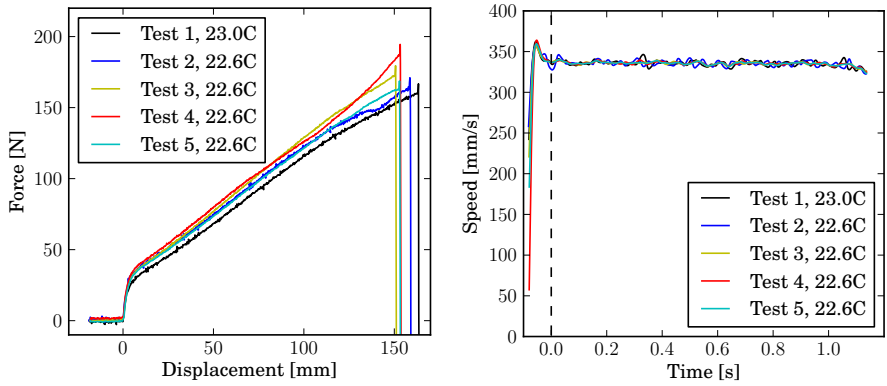

Figure 3.10: Uniaxial tensile tests of PVB at 333mm/s: measured forces (a), and recorded speed (b).

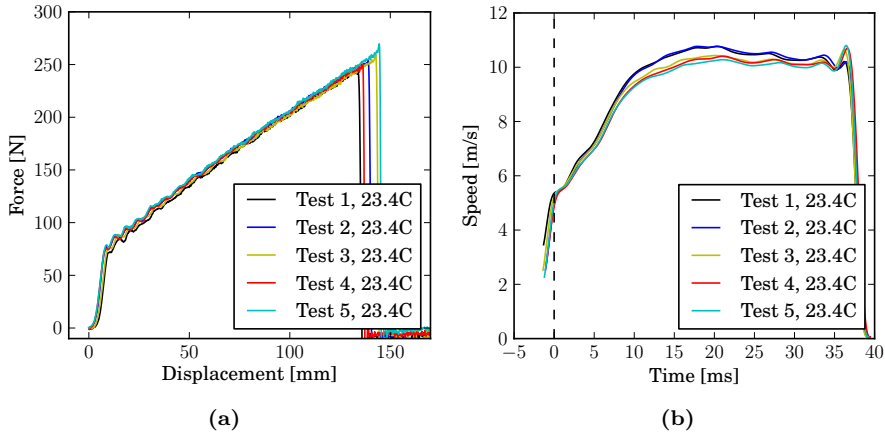

Figure 3.11: Uniaxial tensile tests of PVB at 10m/s: measured forces (a), and recorded speed (b).

As expected, the material acts stiffer with higher rate of deformation. Contrary to Hooper's empirical material model (see Eq. 3.23), the large strain stiffness also seems to increase with the deformation rate as seen in Fig. 3.7 from the work of Schneider et al. [157] as well. Another trend can be observed for the extension at failure, which decreases with the testing speed.

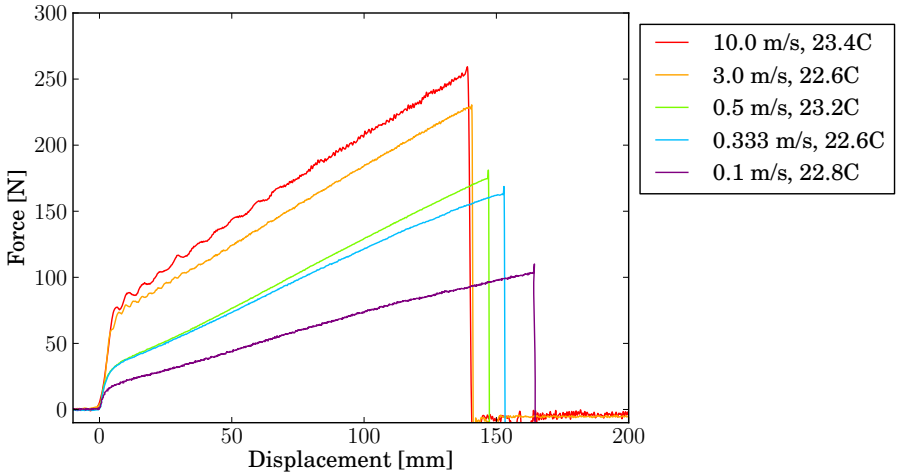

Figure 3.12: Uniaxial tensile tests of PVB at various crosshead speeds: force vs. displacement.

3.5 A material model for PVB

The small strain behaviour of the Saflex® R-series PVB used has been characterised by D'haene and Savineau [173] and described by a Prony series representation and a time-temperature shift function. The latter could be confirmed by Van Dam [6] by resonalyser tests on laminated glass samples. The small-strain material model can be extended for finite strains by fitting the material model to the uniaxial tensile tests at different speeds. As explained in Sec. 3.2, several approaches exist for constitutive modelling. A choice can be made, based on the following observations:

1. At normal operation temperatures, the PVB interlayer shows no permanent deformation. This has been reported in literature and was observed for all experiments in Sec. 3.4.

2. The force vs. displacement curves on Fig. 3.12 show the same general shape and appear to be scalable for different testing speeds.

3. No experimental data is available for the unloading at finite strains.

As such, it would not be required to use the powerful, but more complex, viscoplastic parallel network models, nor could such model be properly validated by lack of data on the biaxial and hysteretic behaviour of the material. The latter is not indispensable because, during an impact, the loading of the material is far more important than the unloading. As the tensile tests

show similar response at different speeds, not all spring elements in the generalised Maxwell model should be assigned nonlinear stiffness as in Khajehsaeid's model. Rather, a single hyperelastic strain energy potential to characterise the instantaneous material behaviour can be coupled with the viscoelastic model. Of course, the small-strain modulus for hyperelasticity should be equal to the instantaneous shear modulus of D'haene and Savineau's viscoelastic model, i.e. $G_0 = 146.12\,\mathrm{MPa}$.

First, a suitable strain energy density function is sought to properly represent the instantaneous material behaviour. Subsequently, the material constants for this strain energy potential can be found by iterative simulation of the uniaxial tensile test at one testing speed. The found material model is further evaluated for the tensile tests at the other tested rates.

3.5.1 Choice of strain energy density function

Yeoh [162] has shown that the strain energy potential for many rubbers and polymers may be expressed in terms of a single variable, i.e. the first invariant of the Green deformation tensor. This is especially advised when only uniaxial tensile test data is available, which is the case here.

As seen in the previous section, the force vs. displacement curves for tensile tested Saflex® PVB approach a bilinear relation. It can be expected that this will be roughly the same for the stress vs. strain behaviour. In order to determine which expression for the strain energy potential is best suited, several functions are evaluated in an example. Because the hyperelastic curve should eventually describe the instantaneous stiffness, it is most logical to pick the test data obtained at the highest test speed, 10 m/s, for this example. The nominal stress and nominal strain are calculated from the force and displacement as by Eq. 3.24 and 3.25. It should be noted that this is only a rough approximation, because the specimens do not have a uniform section over their entire length between the grips.

$$\sigma_N = \frac{F}{w\,t}, \tag{3.24}$$

$$\epsilon_N = \frac{u_{cr}}{l_{cc}}, \tag{3.25}$$

where the width of the specimen is $w = 10\,\mathrm{mm}$, thickness $t = 0.76\,\mathrm{mm}$ and the length between the grips $l_{cc} = 87\,\mathrm{mm}$. The strain energy density $W(\epsilon_N)$ is calculated by simply integrating the nominal stress by the nominal strain. The resulting stress and strain energy density are given as function of the nominal strain in Fig. 3.13.

The invariants of the deformation tensor are given by Eq. 3.19. A simplification can be made for uniaxial tension. Supposing that tension is applied in the

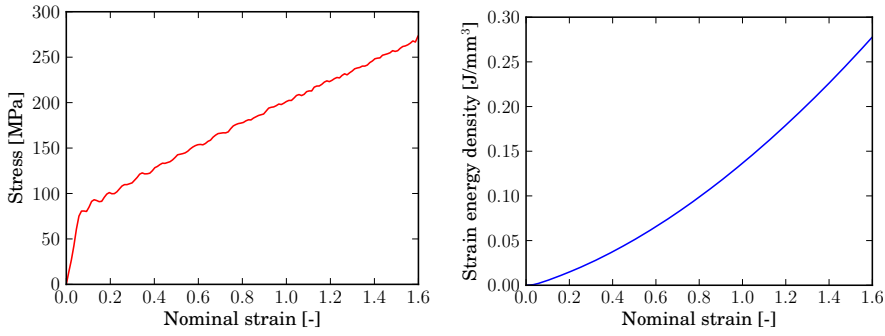

Figure 3.13: Estimation for uniaxial tensile test of Saflex® PVB at 10m/s: a) Nominal stress, b) Strain energy density.

I-direction and the material is incompressible, then $J_3 = 1$ and consequently $\lambda_{II}^2 = \lambda_{III}^2 = 1/\lambda_I$. With $\lambda_I = \lambda$, the first invariant can be written as:

$$J_1 = \lambda^2 + \frac{2}{\lambda}, \tag{3.26}$$

where $\lambda = 1 + \epsilon_N$. Table 3.3 gives corresponding values for the first invariant and the nominal strain.

Table 3.3: First invariant of Green deformation tensor for uniaxial tension: corresponding values for nominal strain.

ϵ_N	$J_1 - 3$
1.0%	0.0003
5.0%	0.0073
10.0%	0.028
20.0%	0.11
40.0%	0.39

The strain energy density can be expressed as a function of the invariant J_1, for which the curve is shown in Fig. 3.14. It is remarkable that this function shows a nearly constant shear modulus at large strains. This curve can be approximated by a reduced polynomial function of at least third order, as proposed by Yeoh. For such function, μ_0 is the shear modulus at infinitesimal strain. In combination with viscoelasticity, this value is known for D'haene and Savineau's material model. In the present example, the small-strain shear stiffness in Fig. 3.13a, $\mu_0 = 403.11\,\text{MPa}$, is used as a direct input. The coefficients for the higher order terms are found by use of the curve fitting module

in SciPy.[2] It should be kept in mind that the fitted function should most accurately approximate the experimental values for small strains. Considering that the first invariant, J_I, changes very quickly with the strain in this range, the fitted function should foremost capture the initial bend in Fig. 3.14.

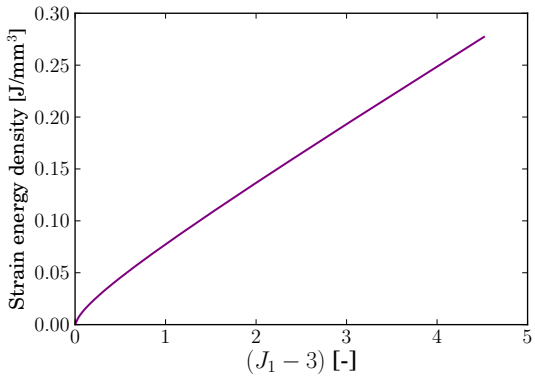

Figure 3.14: Strain energy density in fuction of first invariant for uniaxial tensile test of Saflex® PVB at 10m/s.

In Fig. 3.15, the resulting fitted curves are shown for reduced polynomial strain energy potentials of 3rd order (Yeoh's function), 6th order (the maximum order for the built-in hyperelastic model in Abaqus) and 10th order. It is notable that the 3rd order fit shows large oscillations and is not monotonously ascending. The 6th order approximation does not capture the small strain behaviour accurately. This is only the case for a polynomial function of 10th order and higher. A hyperelastic law of that order is not allowed by the built-in material models in Abaqus, but can be implemented through the `VUANISOHYPER_INV` subroutine, which allows for combination with viscoelasticity.
It should be noted that a polynomial fit is only valid in the range of strains for which it has been calibrated. There is no guarantee over the behaviour beyond these limits. For example, the 10th order fit in Fig. 3.15 does behave stable in compression, but shows a drastic decrease in stiffness for nominal strains higher than 150%.

Other strain energy potential functions can be designed to more naturally describe PVB behaviour with less material constants to be determined. Similar to the Gent function or the Exp-Ln function by Khajehsaeid et al. [175], a function can be found which has a constant shear modulus at large strains. A function

[2]SciPy is an open source Python library for scientific computing. Combined with NumPy and matplotlib libraries, it provides a powerful alternative for MatLab. And importantly here: all libraries can be used directly within the Abaqus Scripting Interface.

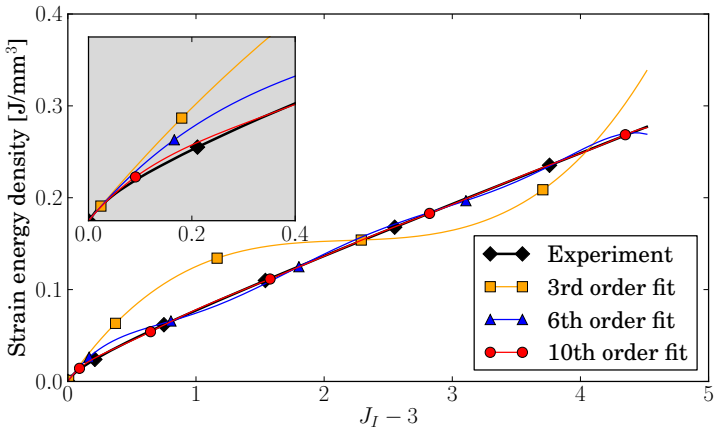

Figure 3.15: Fitted reduced polynomial strain energy potential functions for uniaxial tensile test of Saflex® PVB at 10m/s.

proposed here is given by Eq. 3.27, which is named the Petitzon-Pelfrene strain energy potential for further reference.[3]

$$W(J_1) = C_1 \frac{J_1 - 3}{2} - C_2 \ln \frac{1 + \exp\left(\frac{J_1 - 3}{J_m}\right)}{2}, \tag{3.27}$$

where C_1, C_2 and J_m are material constants, of which J_m controls the curvature for small to moderate strains. The shear moduli for infinitesimal and large (towards infinite) strains are:

$$\begin{aligned} \mu_0 &= C_1 - C_2/J_m \\ \mu_\infty &= C_1 - 2C_2/J_m \end{aligned} \tag{3.28}$$

Using SciPy, a fitted curve can be found also for this function. The result is shown in Fig. 3.16, in comparison with the 10th order polynomial fit. It is seen that with only three material constants already a rather good approximation of the experimental results is achieved. At strains between 5 and 40%, the solution deviates somewhat more than for the 10th order polynomial fit. But in comparison, the function of Eq. 3.27 is smooth without ripples and hyperelastic behaviour does not become unstable in compression or at high strains.
This function is also implemented for Abaqus by use of the `VUANISOHYPER_INV` subroutine, and combined with Prony series for viscoelastic behaviour. However, for values of J_m smaller than 0.8, the Abaqus computation becomes unstable. In fact, a similar instability can be noted for the Gent function for small values of J_m. For the function of Eq. 3.27, this is most likely due to a

[3] With regards to Felix and Marius Petitzon-Pelfrene who hinted to this solution.

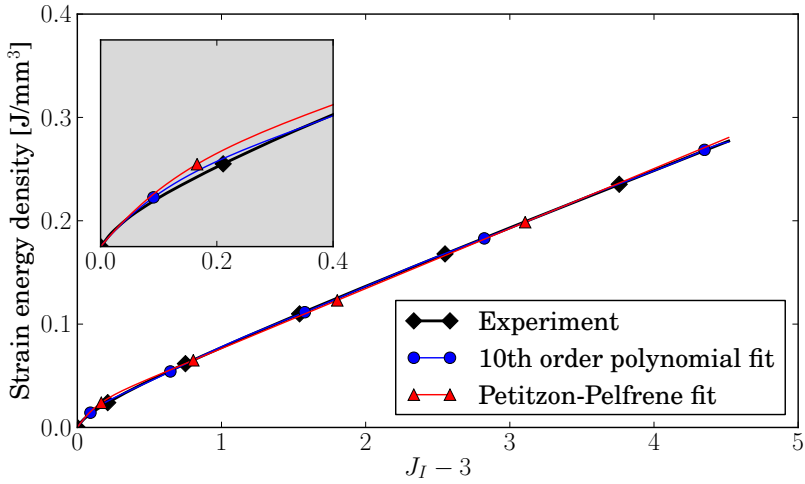

Figure 3.16: Fitted Petitzon-Pelfrene strain energy potential function for uniaxial tensile test of Saflex® PVB at 10m/s.

steep minimum in the second derivative of $W(J_1-3)$ at infinitesimal strain. Alternative functions can be designed, but also show steep gradients in their first or second derivative that appear too difficult to handle for Abaqus/Explicit. This is not the case for the higher order polynomial functions, which will further be used.

3.5.2 Simulation of the uniaxial tensile test

The method described in the previous section is very similar to the *Evaluate* step in Abaqus to find material constants for a hyperelastic strain energy density function [121]. However, this method can only be considered as an estimation because it is not entirely consistent with the theory: the strain energy density is calculated from the nominal stresses and strains, and the deformation tensor invariant is formulated for idealised uniaxial tension and calculated from an averaged strain rather than a locally measured one. To find the material constants that better represent the PVB, the uniaxial tensile experiment can be simulated and its material properties iteratively adjusted until a satisfying match with the force-displacement measurement is found.

Direct simulation of the PVB interlayer allows for the use of a constitutive model that combines hyperelasticity with viscoelasticity. The latter is known and implemented as D'haene and Savineau's model. Consequently, only a hyperelastic law for the instantaneous behaviour should be found. In theory, curve fitting at every testing speed should yield the same strain energy potential. In practice, a best fit is obtained only for the testing speed at which an optimised

solution is created; for other strain rates, the result can be expected to deviate from the actual material behaviour.

The steps taken in the iterative procedure are given schematically by the diagram in Fig. 3.17.

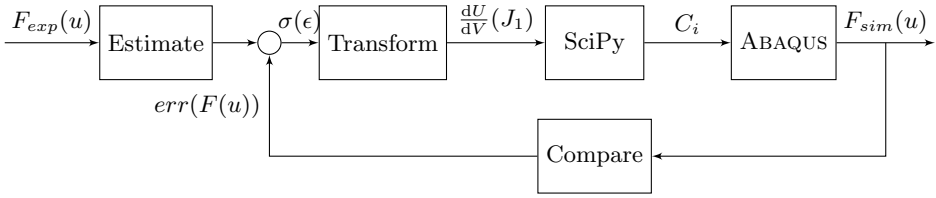

Figure 3.17: Iterative scheme to find material law for PVB interlayer in uniaxial tensile test.

Estimate: An initial estimation for the stress-strain behaviour is made by deriving the nominal stress and nominal strain directly from the experimentally measured force and displacement. Because hyperelasticity is coupled with a generalised Maxwell model, the nominal stress is scaled such that the small-strain shear modulus equals the instantaneous shear modulus for D'haene and Savineau's viscoelastic model: $\mu_0 = G_0 = 146.12\,\text{MPa}$.

Transform: The strain energy density, $\frac{dU}{dV}$, and the first invariant, J_1, of the deformation tensor are calculated as in Sec. 3.5.1. It has been remarked that a polynomial strain energy potential is only valid for the range of strains to which it has been fitted. In order to avoid instability of the numerical simulation in which locally higher strains may be reached, an extension is made by following the trend of the estimated strain energy density at high elongations. A 3rd order polynomial function is fitted to the last quarter of data points. Extra data points are created for higher values of the first invariant, up to $J_1 - 3 = 12.0$ which corresponds to a nominal strain of 280%.

SciPy: The curve fitting module in SciPy is used to find matching material constants C_i for an N-th order polynomial strain energy density function as described by:

$$W(J_1) = \sum_{i=1}^{N} C_i (J_1 - 3)^i \tag{3.29}$$

ABAQUS: The material constants for the instantaneous behaviour are used in a finite element model of the uniaxial tensile test. The numerical model consists of a 2D plane stress representation of a quarter of the PVB specimen, as shown in Fig. 3.18. The material clamped between the machine grips is not

modelled (i.e. the checkered area in Fig. 3.8). The displacement is imposed on the edge nodes of the sample. In perfect clamping, these nodes are not allowed any lateral movement. However, in reality, the PVB does give way, being separated from direct contact with the rigid grips by a layer of glue and strips of cardboard. In the numerical model, the choice is made to allow free lateral movement of the edge nodes at the clamps. The displacement they are imposed in longitudinal direction is not at constant, nominal velocity, but is interpolated between the crosshead displacements recorded during the experiment, where $t = 0$ is the instant at which the PVB sample is straightened.

The constitutive model for the PVB consists of the combination of a reduced polynomial strain energy potential (implemented through the `VUANISOHYPER_INV` subroutine for an order higher than 6th) with a Prony series formulation of viscoelastic behaviour (D'haene and Savineau's model [173]). The time-temperature shift factor is taken into account for all simulations.

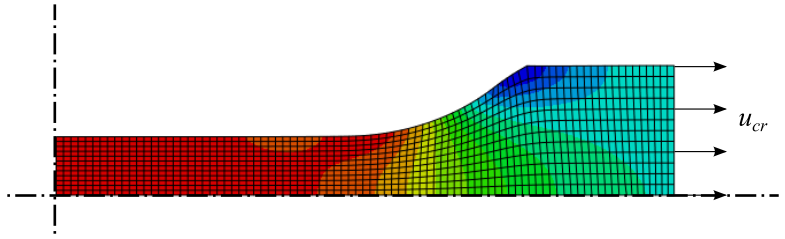

Figure 3.18: Mesh and boundary conditions for uniaxial tensile test model of PVB specimen; contours of longitudinal stress at 10 mm elongation.

The explicit solver is used because equilibrium is not always reached for the higher strains when using the rather complex material model with the implicit solver. Also, the material model will be primarily used in impact simulations, which commonly make use of the explicit solver. Mass scaling can be used to increase the stable time increment. This is not done for the two highest testing speeds, 3.0 and 10.0 m/s, where dynamic effects could be expected.
Upon completion of the analysis, output is written for: the reaction force at the boundaries, the longitudinal (true) stress, local strain (both nominal and logarithmic) and strain rate in the middle section of the specimen. Because of mass scaling in the simulation, a check is also made for the kinetic energy and the artificial dissipations.

Compare: The force-displacement curves of the experiment and the simulation are compared. Error factors are calculated for the forces of the simulated result as in Eq. 3.30.

$$err(F(u_k)) = \frac{F_{exp}(u_k) - F_{sim}(u_k)}{F_{exp}(u_k)} \tag{3.30}$$

The error factors are used to adjust the estimated stress-strain behaviour of the present iteration by simply scaling the corresponding stress value. The new estimation is fed back into the loop. This is repeated until a satisfying match with the measured force-displacement is achieved.

The system of Fig. 3.17 is implemented as a single Python script, which can be run in ABAQUS/CAE. The required input consists of the experimentally recorded time, displacement and measured forces. 5 to 10 iterations are sufficient to find an acceptable solution for the material model. This purpose-built method is highly efficient compared to optimisation schemes in specialised software such as iSight which fill in material constants directly in the ABAQUS model and easily require over 100 iterations.

3.5.3 Resulting material law for Saflex PVB

Before coming to a material model by which the experimental results could be reproduced numerically, two deviations from the original idea had to be taken:

1. In SciPy, the first-order constant can be set as $C_1 = \mu_0/2 = G_0/2$, such that the small-strain modulus equals that of D'haene and Savineau's viscoelastic model. However, it is seen after the curve fitting that this creates a high overshoot of the stress at the turning point in the stress-strain curve. Simulations quickly become unstable when strains past this point are reached. Therefore, the constant C_1 is left as a parameter in the curve fitting procedure. This alleviates the stability issues and enables a better matching fit with the experimental curve, but the solution is no longer truly consistent with D'haene and Savineau's viscoelastic model for infinitesimal strains.

2. In Section 3.5.1, a 10th order polynomial has been proposed to provide a good fit with the estimate for the strain energy density. When simulating the tensile test in ABAQUS, it appears that there is a significant ripple on the resulting force and in local stress, which eventually leads to excessive element distortion. An example of such force-displacement response is shown in Fig. 3.19. Thus, the 10th-order polynomial fit is still not sufficiently smooth. A 20th-order fit will further be used.

With this approach, hyperelastic material constants can be found at every testing speed that provide a good fit with the experimental force-displacement response. The strain rates of most interest in an impact situation are in the order of 0.1 to $10\,\mathrm{s}^{-1}$. These strain rates are found for the testing speeds of 100 to 500 mm/s. In a first approach, the 500 mm/s test is used to calibrate the material model.

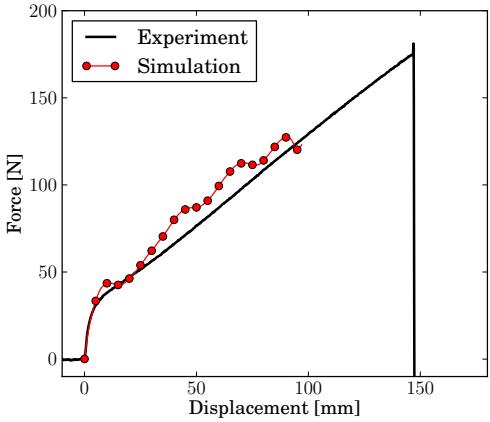

Figure 3.19: Force vs. displacement for uniaxial tensile test at 0.5 m/s and 23.2°C; simulation using 10th-order reduced polynomial hyperelastic law and viscoelasticity.

A decent fit is obtained after 8 iterations. The resulting forces are shown in Fig. 3.20 in comparison with the experimental measurement at 500 mm/s and 23.2°C. The simulated true stress vs. true strain and the strain rate at the middle of the specimen are given in Fig. 3.21. As opposed to the nominal stress-strain behaviour, the true stress vs. true strain does not approach a bilinear curve. The strain rate at the middle section is not constant during the test, contrary to what is often assumed, but slightly descending. Both these aspects correspond with the experimental observations by Schneider et al. [7, 157].
As seen from the simulations, the ultimate, logarithmic (true) strain at tearing is between 1.0 and 1.2, and decreases with the deformation rate.

The same material model resulting from the fit at 500 mm/s is used to simulate the other testing speeds. The force vs. displacement responses are shown together with the experimental measurements in Fig. 3.22. While the measured forces can be reproduced rather well for testing speeds 0.1 and 0.33 m/s, the results for the highest speeds do not show good correspondence. Thus, the assumption that the material stiffness can be scaled by a linear viscoelasticity model also at large strains is not valid for the entire range of deformation rates. A more generally valid material description may be found by introducing non-linearity for the dashpot elements in the generalised Maxwell model. Calibration of such material model does require more extensive test data; more specifically for cyclic loading at a higher strain level, as described by Bergström [159].

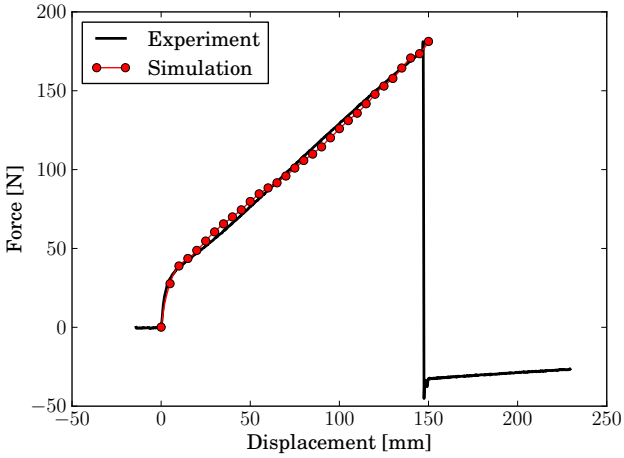

Figure 3.20: Force vs. displacement for uniaxial tensile test at 0.5 m/s and 23.2°C; fitted result for 20th-order reduced polynomial hyperelastic law and viscoelasticity.

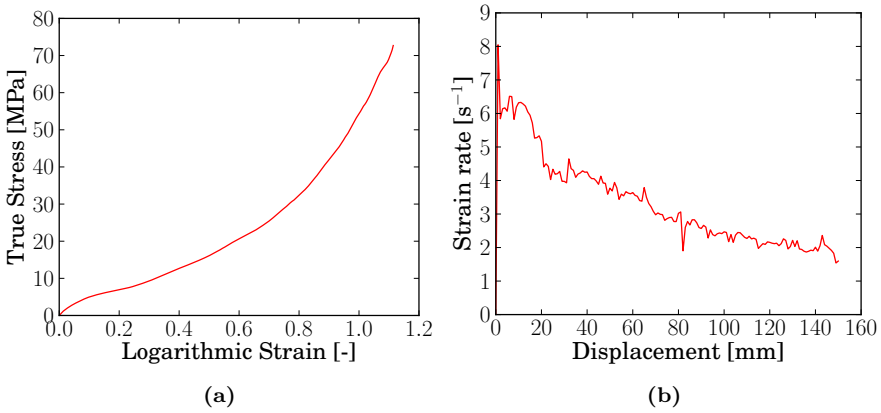

Figure 3.21: Stress vs. strain (a) and strain rate (b) for simulation of uniaxial tensile test at 0.5 m/s and 23.2°C.

An additional calibration of the material model is made for the highest testing speed, 10 m/s. The resulting forces for all dynamic tests are shown in Fig. 3.23. While achieving more or less acceptable correspondence for the 3.0 m/s test, the material constants should not be used for simulation at lower deformation rates. Remarkably, some overshoot of the force is seen around the kink in each force-displacement curve. This could not be resolved with the polynomial fit, but also does not lead to instability of the simulation.

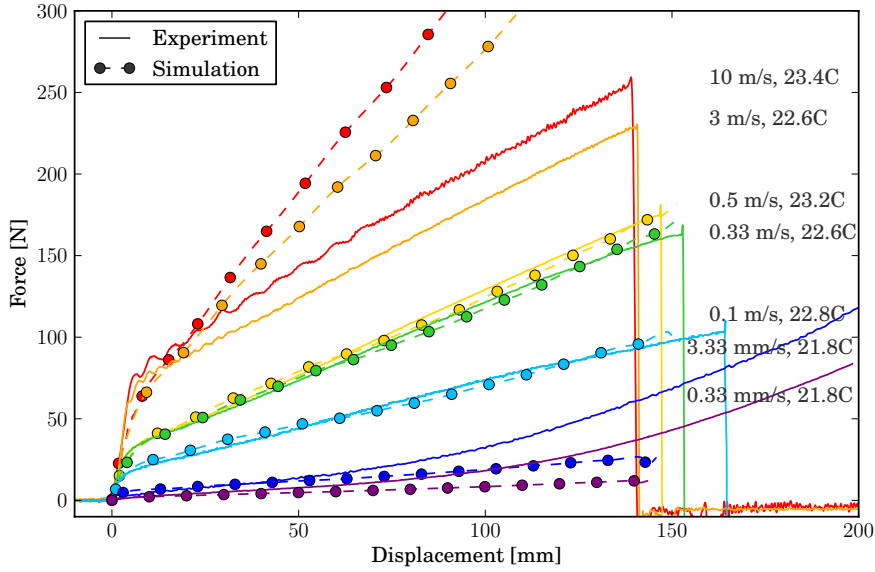

Figure 3.22: Force vs. displacement for uniaxial tensile tests; simulated results for material model calibrated at 0.5 m/s and 23.2°C.

Finally, the material model calibrated for 500 mm/s will further be used for the simulation of dynamic events with glass breakage. The material constants for the instantaneous, hyperelastic behaviour are given in Table 3.4. The constants for the Prony series of D'haene and Savineau's viscoelastic model [173] are given in Table 3.5, and coefficients for the time-temperature shift factor α_T of the general form of Eq. 3.31 are given in Table 3.6. The user-defined time-temperature shift function is implemented in ABAQUS via the `VUTRS` subroutine.

$$\log_{10} \alpha_T = \sum_{i=0}^{6} a_i \, T^i \tag{3.31}$$

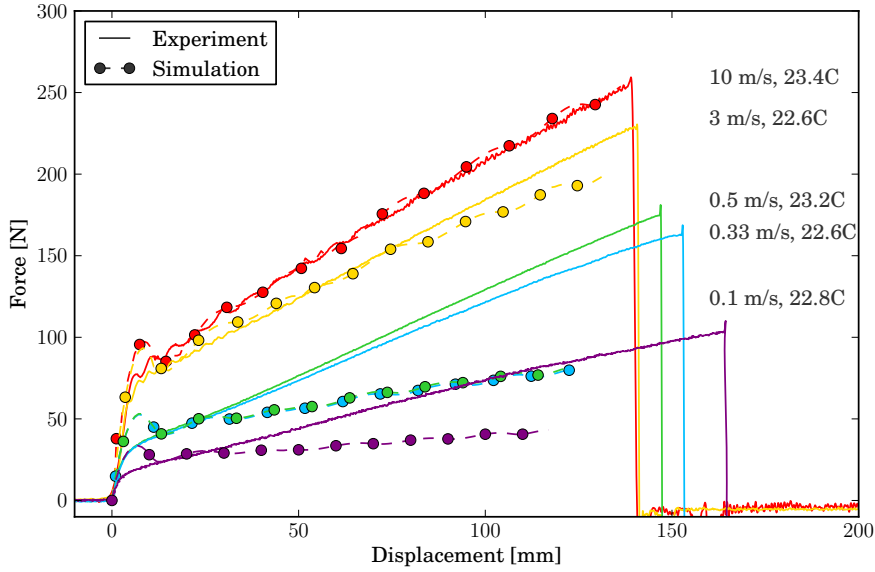

Figure 3.23: Force vs. displacement for uniaxial tensile tests; simulated results for material model calibrated at 10.0 m/s and 23.2°C.

Table 3.4: Constants for 20th order reduced polynomial strain energy density function for instantaneous behaviour of Saflex® PVB.

C_i	[MPa]	C_i	[MPa]
C_1	28.52	C_{11}	-0.46
C_2	-44.32	C_{12}	0.14
C_3	134.36	C_{13}	$-26.18 \cdot 10^{-3}$
C_4	-226.46	C_{14}	$3.58 \cdot 10^{-3}$
C_5	240.24	C_{15}	$-0.36 \cdot 10^{-3}$
C_6	-168.26	C_{16}	$25.95 \cdot 10^{-6}$
C_7	78.68	C_{17}	$-1.34 \cdot 10^{-6}$
C_8	-23.41	C_{18}	$0.05 \cdot 10^{-6}$
C_9	3.28	C_{19}	$0.99 \cdot 10^{-9}$
C_{10}	0.57	C_{20}	$9.57 \cdot 10^{-12}$

Table 3.5: Constants for Prony series of viscoelastic model for Saflex® PVB by D'haene and Savineau [173] at reference temperature of 20°C.

τ_k [s]	g_k [-]	τ_k [s]	g_k [-]
10^{-5}	0.0155	10^{2}	0.00508
10^{-4}	0.1727	10^{3}	0.00114
10^{-3}	0.2111	10^{4}	$0.485 \cdot 10^{-3}$
10^{-2}	0.2684	10^{5}	$0.554 \cdot 10^{-3}$
10^{-1}	0.1988	10^{6}	$0.752 \cdot 10^{-3}$
10^{0}	0.0974	10^{7}	$0.70 \cdot 10^{-3}$
10^{1}	0.0254	10^{8}	$0.985 \cdot 10^{-3}$

Table 3.6: Constants for time-temperature shift function of viscoelastic model for Saflex® PVB by D'haene and Savineau [173].

a_0	3.531
a_1	-0.106
a_2	$5.525 \cdot 10^{-3}$
a_3	$1.113 \cdot 10^{-3}$
a_4	$46.33 \cdot 10^{-6}$
a_5	$-0.751 \cdot 10^{-6}$
a_6	$4.317 \cdot 10^{-9}$

3.6 Summary and conclusions

PVB interlayer is by far the most common interlayer for laminated safety glass. It is an amourphous thermoplast that adheres to glass through hydrogen bonding. Mechanically, PVB interlayer is nearly incompressible, can reach very high strains before tearing and does not show permanent deformation. It is also characterised by very high sensitivity towards temperature and deformation rate.

While showing rather complex mechanical behaviour, several simplifications can be made in constitutive modelling, depending on the considered load case. The small-strain behaviour of PVB is well captured by linear viscoelasticity, for which the time-temperature superposition principle applies. When the glass breaks under impact or blast, the PVB can locally reach large strains. In that case, the material can be modelled by rate-dependent hyperelasticity, a combination of hyper- and viscoelasticity or the more general viscoplasticity. The first is an engineering solution which allows to calculate forces during the loading stage, but ignores much of the material's physical nature. The latter allows to model any type of polymer behaviour, but requires a great amount of test data for different deformation modes. The combination of a hyperelastic strain energy potential with Prony series for viscoelastic behaviour is used here, under the assumption that the stress-strain behaviour at finite strains can be scaled for different deformation rates by the same generalised Maxwell model as for the small strains.

Uniaxial tensile tests of Saflex® R-series interlayer at low to high pulling speeds provide experimental data to calibrate the material model. Remarkably, the dynamic tests all show a similar, nominal stress-strain reponse which approaches a bilinear relation. The tearing strain slightly decreases with the deformation rate.

A strain energy potential that can capture the instantaneous stress-strain curve of the PVB is to be found. As shown by Yeoh [162], the strain energy density depends foremost on the first invariant of the Green deformation tensor and the strain energy potential may best be written as a function of this variable only. A polynomial fit is a common approach, but a high order is needed to provide a good match with the quick changes in stiffness that the material shows at small strains. An even higher order is needed to enhance the smoothness of the solution in order to avoid instability in numerical analysis.

Specially tailored strain energy density functions, such as Eq. 3.27, can be formulated as well. Such solution provides a smooth curve with controlled behaviour at elongations beyond the range of the test data. In Abaqus, it is possible to implement user-defined hyperelastic functions, but the analysis runs into stability issues when large gradients in the first or second derivative

are present. This is inevitably the case here and it is preferred to continue with a 20th order polynomial function, implemented for ABAQUS/Explicit through the `VUANISOHYPER_INV` subroutine.

An iterative simulation procedure has been developed to find the material constants for which a good fit with the experimental results can be established. However, a proper match can only be found when the small-strain modulus of the 20th order polynomial function is allowed to deviate from the instantaneous modulus of D'haene's linear viscoelastic model, to which it is coupled. Also, it appears that the simulated behaviour at large strains only provides a good fit with the test data for a limited range of deformation rates. This indicates that it would be more correct to include rate-dependency of the viscous component in the material behaviour.

Finally, a PVB material model is proposed for use in numerical analysis of dynamic events with glass breakage. This material model is calibrated for a mid-range of strain rates, i.e. 0.1 to $10\,\mathrm{s}^{-1}$. The material constants are given in Tables 3.4, 3.5 and 3.6.

Chapter 4

Glass-PVB adhesion

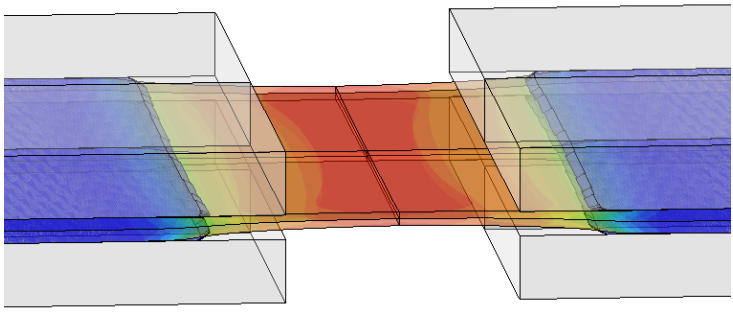

Simulation of delamination in a Through-Cracked Tensile test for laminated glass.

4.1 Introduction

It stands without doubt that good adhesion between a transparent interlayer and the glass is key for any laminate. For laminated safety glass, the main purpose of the interlayer is to retain glass fragments upon fracture. Because requirements can differ in terms of glass retention or penetration, PVB products with the same mechanical properties are marketed with varying adhesion grades, e.g. Saflex® RA, RB and RC, and Trosifol® BG R20, BG R15 and BG R10, from high to low adhesion respectively. Under impact or blast loading, safety is better provided when a lower adhesion level is installed, rather than maximum adhesion to prevent injury from the propulsion of shards [176, 177]. When the adhesive bond is very strong, a fine stretch of interlayer material that bridges the crack may be forced into rapid and large deformation. This can lead to early tearing of the polymer, causing the loss of integrity of the panel. A lower level of adhesion allows for some delamination around the crack, thus softening the deformation of the interlayer at this location to prevent it from tearing. The difference between high and low adhesion is shown in Fig 4.1 where the strain $\epsilon_1 > \epsilon_2$ for the same crack opening width. For this reason, interlayer manufacturers advise low to medium adhesion levels for best favourable results in impact and blast. Use of products with higher adhesion level may require a thicker interlayer or thicker glass to achieve a similar performance [178].

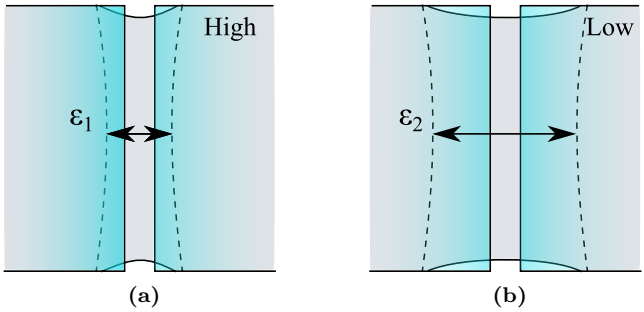

Figure 4.1: Delamination of interlayer from glass around a crack with given opening width: (a) high adhesion grade, and (b) low adhesion grade.

Simultaneously, delamination and post-fracture viscoelastic deformation can contribute greatly to the kinetic energy absorption in an impact, and thus provide protection to humans inside a building or vehicle.

4.1.1 Experimental methods for glass-interlayer adhesion

Several methods are available to evaluate the interfacial adhesion of a laminated glass. These methods have not been standardised and they are mainly being

used for in-house quality control by interlayer manufacturing companies. The adhesive and elastic properties of the interlayer will therefore be different for every PVB product and manufacturer. The most often used test methods can be categorised as follows: pummel test, compressive shear test, 90° peel test and through-cracked tensile test (TCT).

The pummel test relates the level of adhesion to the amount of glass detached from frozen laminate by repeated pummeling with a one-pound hammer. The laminate is then assigned an adhesion number on a scale from 0 to 10 by visual comparison to reference pummeled specimens. However, test results may vary from operator to operator, thus compromising the overall objectiveness [154]. Nonetheless, the pummel test does give an idea of the relative adhesion quality of different interlayer products. Table 4.1 gives pummel values for common Saflex® and Trosifol® PVB interlayers.

Table 4.1: Pummel values for Saflex® and Trosifol® PVB interlayers (Data from Eastman™ and Franz [179]).

Saflex®		Trosifol®	
RA	8-9	BG R20	8-9
RB	7-8	BG R15	4-6
RC	5	BG R10	3-4

In compressive shear testing (CST), a vertical load is applied to the laminate with compressive and shear components at 45°. When force is increased, deformation and stress in the laminate increase up to a critical value at which the laminate fails under shear at one of the interfaces. This critical value of stress is taken as the Mode II adhesion strength. In an article by Aguilar et al. [180], the critical shear stress for Butacite® is specified as $10 \pm 1\,\mathrm{MPa}$.

In a peel test for laminated glass, the adherent is peeled off of a glass substrate at constant speed, while measuring the needed force. The test is performed on specimens of PVB laminated between a layer of glass and a layer of foil backing, as described in the international standard ISO 8510-1 [181]. Using this test setup, Butchart et al. [177] have demonstrated sensitivity of PVB interlayer's adhesive properties to moisture: specimens kept in especially moist conditions require only half the force needed to disassemble specimens stored under normal room conditions.

The TCT test, first introduced by Sha et al. [182], consists of a pre-cracked laminated glass sample subjected to uniaxial tensile load perpendicular to the crack face. As the interlayer stretches to bridge the gap, adhesion fails at the interface by a combined Mode I and Mode II failure mechanism. Seshadri et al. [183] report that, at constant crosshead speed, delamination propagates

under constant force until the interlayer finally tears. This is confirmed by Butchart et al. [184] and Franz and Schneider [179, 185], who also investigated the rate-dependency of glass-PVB adhesion by TCT testing. They observed that the PVB acts stiffer at higher rates, leading to an overall higher stress level and a reduction of the ability to delaminate. In Franz's tests, interlayers with a high adhesion grade are seen to no longer delaminate, but tear immediately in a fast TCT test. PVB with a lower adhesion level does still show delamination at high rates.

The through-cracked bending (TCB) test, pioneered by Franz [179], is an interesting variation on the TCT test. The same type of samples is tested in four-point bending. The intention is to approach the load case of a broken laminated glass panel that is pushed into higher deflection.

In the industry, the results of these tests are commonly being compared against each other or a benchmark, rather than measuring a direct value characteristic for the adhesion. This impedes determining the energy absorption related to delaminated surface on a test specimen, or including delamination in numerical analyses. For an analytical derivation of these quantities, many assumptions have to be made about the specimen and the testing process as a whole. Using numerical simulation, it is attempted to overcome this by appropriately characterising materials, boundary conditions and application of loads to accurately compute local strains and stresses.

4.1.2 Calculation of adhesive properties

An early numerical study on the effects of delamination upon fracture of laminated glass subjected to impact was published by Flocker and Dharani [186]. Adhesive properties for the interface between PVB and glass were estimated for a peel test by deriving fracture energy G_{Ic} according to the method described by Kaelble [187, 188]. These values, along with others found in literature, are given in Table 4.2. From the impact simulations, Flocker and Dharani conclude that the effects of delamination are negligible and advise that the adhesion be produced as strong as possible. However, recent experimental studies by Hooper et al. [189] and Kuntsche and Schneider [190] have demonstrated the importance of interlayer delamination upon glass breakage, indicating that the conclusions by Flocker and Dharani may have been untimely and more profound investigation of the interfacial adhesion in laminated glass is needed.

A number of publications have reported on the quantification of adhesion at the glass-PVB interface. An overview of published values that are characteristic for the interfacial adhesion in laminated glass is given in Table 4.2, where $\sigma_{I,0}$ and $\sigma_{II,0}$ are the interfacial strengths, and G_{Ic} and G_{IIc} the fracture energies for Mode I and Mode II delamination.

Sha et al. [182] were the first to use numerical analysis for this purpose, by use of cohesive zone elements. In a cohesive zone, all damage mechanisms around the crack tip are projected onto the interface, resulting in a constitutive relation in the form of a traction-separation law. Such law can be formulated independently of the bulk constitutive behaviour, enabling this technique to be used to study cases not so easily treated by fracture mechanics, e.g. where large deformation and material non-linearity are present. Sha et al. have used the cohesive zone method numerically to calculate the energy required for interfacial debonding in a TCT test by calibrating the numerical model to correspond with experiments. In these models, the TCT specimen is represented in 2D (plane strain) and a linear elastic material law is assumed for the interlayer. Results for low, medium and high adhesion level are given in Table 4.2. Seshadri et al. continued this approach for analysis of TCT tests and have formulated a nonlinear viscoelastic constitutive law for PVB interlayer, valid at finite strains [191]. Since these early results, the numerical study of the TCT test for laminated glass by cohesive zone method has been further explored by Bati [192], Nhamoinesu [193], Bernard [194] and Franz [179].

Rahul-kumar et al. have implemented cohesive interface elements by the `UEL` subroutine in Abaqus and demonstrated their use to simulate the compressive shear test, where unstable Mode II debonding occurs through a dynamic crack pop-in [197]. A Neo-Hookean, incompressible and rate-independent material law was used to model the interlayer polymer. This work was further elaborated by Jagota et al. [195] with the combination of hyperelasticity and viscoelasticity as a constitutive law for the PVB interlayer. Rate-dependency of the cohesive law governing the failure process was ignored in these models, although recognised to be present.

In this chapter, a study is made on the quantification of interfacial adhesion in laminated glass by a numerical cohesive zone approach. In Section 4.2, a first analysis is conceived for the peel test, which is a well-controlled test that has been used for many years by the industry for quality control. Subsequently, pull-off tests have been performed to characterise the Mode I strength for different adhesion levels of the PVB. In Section 4.4, a numerical framework for the TCT test is presented. Finally, the combined analysis of peel test and TCT gives information about the mixed-mode debonding energy.

Table 4.2: Published glass-PVB interfacial adhesion values

Author(s)	**Test**[(a)]	$\sigma_{I,0}$ [MPa]	G_{Ic}[J/m^2]	$\sigma_{II,0}$[MPa]	G_{IIc}[J/m^2]
Sha et al. [182]	TCT	1.24; 1.688; 1.723 [(b)]		1.22; 1.929; 1.929 [(b)]	104; 154; 295 [(b)]
Flocker and Dharani [186]	Peel	126		1.67	
Seshadri et al. [183]	TCT				280 – 930
Jagota et al. [195]	CST				50 – 200
Iwasaki [174]	TCT				20 – 110
Bati et al. [192]	POT + TCT	5.62	600	1.40	600
Aguilar et al. [180]	CST			10.0	
Butchart and Overend [184]	TCT				255 – 660
Franz and Schneider [196]	POT + DST	4.13 – 6.45		2.60 – 6.11	
Franz [179]	POT,	9.20;		7.36; 6.97;	400; 400;
6 mm/min	DST, TCT	10.84; 12.54 [(b)]		12.69 [(b)]	1200 [(b)]
600 mm/min		8.68; 8.36; 16.75 [(b)]		9.39; 9.94; 16.50 [(b)]	1400; 1500; 2700 [(b)]

Note: measurements for publications in this table were performed on a variety of PVB interlayer from different manufacturers

(a) CST = compressive shear test; TCT = through-cracked tensile test; POT = pull-off test; DST= direct shear test

(b) values are given for low, medium and high adhesion levels respectively

4.2 Peel test

4.2.1 Experimental setup

The experimental setup for the peel test is installed at the Eastman™ production plant where it is used daily for quality control of the produced Saflex® interlayers. Experimental results, and the subsequent numerical study, are presented for PVB interlayers commonly used in construction, i.e. standard Saflex® PVB with medium (RB) and low adhesion level (RC).

The test specimens consist of PVB laminated on one side to the glass substrate. A thin layer of the soft aluminium alloy AL1145-O is glued to the free surface of the PVB. The aluminium acts as a stiff backing foil to avoid large longitudinal stretching and attain steady state. A crack is made along the width of the glass to clamp the peel arm between the grips of a Instron 5564 tensile test machine, as in Fig. 4.2. The substrate is held fixed to a trolley on the testing device.

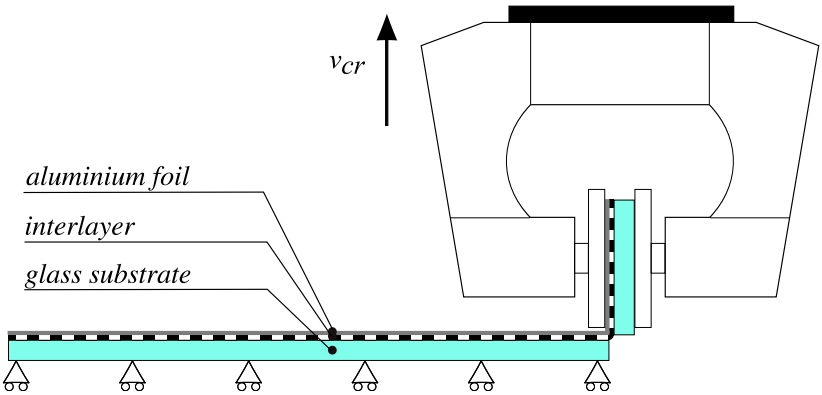

Figure 4.2: Concept drawing of the peel test experimental setup.

Because PVB is highly sensitive to environmental conditions, the test room is kept at a temperature of $23 \pm 2°C$ and humidity in the room is controlled. During the test, the peel arm is moved upwards at constant crosshead speed $v_{cr} = 127\,\text{mm/min}$ while the trolley makes a horizontal movement accordingly as the adherend is peeled off. Meanwhile, the pulling force is measured.

The dimensions of the substrate are $40 \times 115\,\text{mm}$. The thickness for each layer is: 2 mm for the glass, 0.76 mm (30 mil) for the PVB and 0.13 mm (5 mil) for the aluminium. The measured peel forces for low and medium adhesion PVB foils are $2650 \pm 50\,\text{N/m}$ and $3575 \pm 70\,\text{N/m}$ in steady state peeling.

4.2.2 Numerical model

A two-dimensional model of the 90° peel test is developed in Abaqus. As shown in Figure 4.3, some alterations have been applied in the numerical representation.
The peel arm is initially in a stressless state, thus undeformed and not yet bent to 90°. The initial peel arm is modelled longer (40 mm) than in the experiment, to smoothly introduce bending stresses, both elastic and plastic. The length of the glass substrate is taken as 60 mm. Since only a small portion of the PVB will be peeled off in the analysis (enough to reach steady state), it is deemed unnecessary to model the entire length of the sample. Moreover, the material

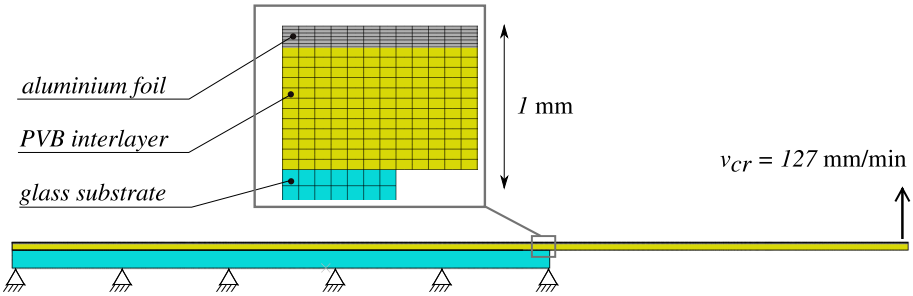

Figure 4.3: Geometry and boundary conditions of the numerical model; a zero-thickness cohesive zone exists at the interface between glass and PVB.

between the testing device clamps is omitted. Instead, the free end of the peel arm is moved upwards with constant velocity.

The adhesive bonding and subsequent failure of the PVB-to-glass interface is included in the model by a cohesive zone. The interfacial adhesion by hydrogen bonds is represented by zero-thickness cohesive elements, placed between the glass and PVB parts and connected by tie constraints for the nodes at the respective surfaces.

The materials involved in the peel test are characterised as follows:

- **Glass:** The elastic behaviour before breakage is characterised by a linear elastic modulus $E = 70\,\text{GPa}$ and a Poisson's ratio $\nu = 0.23$. The glass substrate does not deform much during the peel test. In fact, strains in the glass remain sufficiently low ($\epsilon < 0.03\%$) to assume rigid body conditions.
- **PVB:** Because of the much stiffer backing foil, it is expected that strains in the PVB remain small. Therefore, the linear viscoelastic model by D'haene and Savineau [173] is assigned to the PVB elements in order to capture the change in shear stiffness with varying deformation rate. The volumetric modulus is assumed constant, as is the case for most dense polymers; $K = 2.0\,\text{GPa}$ as measured by van Duser et al. [198]. A temperature shift factor of $\alpha_T = 0.175$ has been taken into account in the model, since experiments are performed at constant temperature of 23°C.
- **Aluminium:** Figure 4.4 presents the results of a tensile test, performed on the aluminium cover sheet. It is seen that the initial, elastic, stage is characterised by a Young's modulus $E = 69\,\text{GPa}$, common for all aluminium alloys. At a stress of 30 MPa, a clear yielding point is observed, initiating the plastic hardening phase. This plastic behaviour is implemented as a material model for the backing foil in Abaqus.

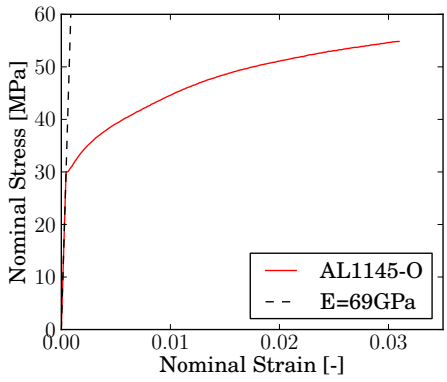

Figure 4.4: Stress-strain curve of AL1145-O, obtained by tensile test on cover sheet sample

The adhesive bonding at the glass-PVB interface is represented by zero-thickness cohesive elements, whose mechanical and damage behaviour is described by a traction-separation law. The intrinsic, bilinear traction-separation law is used to represent the zero-thickness chemical bond between PVB and glass. This cohesive zone law is shown in Fig. 4.5 and is characterised by a reversible elastic phase until reaching the debonding strength σ_0, and the ultimate separation δ_f when fully damaged. The fracture energy G_c is the energy required to separate a unit area of the adhesive bond.

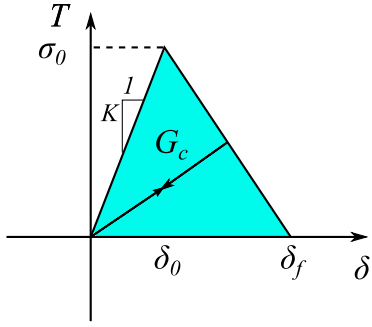

Figure 4.5: Bilinear traction-separation law for cohesive zone

The cohesive stiffness and fracture energy can be formulated respectively as:

$$K = \sigma_0/\delta_0 \ [\mathrm{N/m^3}] \tag{4.1}$$

$$G_c = \frac{1}{2}\sigma_0\,\delta_f \ [\mathrm{J/m^2}] \tag{4.2}$$

This traction separation law is valid in Mode I and Mode II. The debonding behaviour can be calculated either as the result of separated fracture modes or as coupled, mixed modes. Because the peel test serves as a Mode I adhesion test, no mixed mode behaviour is taken into account. For input in ABAQUS, the Mode II cohesive stiffness, strength and fracture energy are assumed to be the same as in Mode I.

Diehl [199] has shown that the cohesive zone model is relatively insensitive to the choice of the damage initiation ratio, δ_0/δ_f, for a 180° peel test simulation. Therefore, a favourable ratio is chosen with respect to numerical stability: $\delta_0/\delta_f = 0.5$.

Glass manufacturer Saint Gobain specifies that adhesive failure in a compressive shear test should occur when reaching a maximum shear stress of $10 \pm 1\,\mathrm{MPa}$ [180].

With these assumptions, the Mode I fracture energy G_c is the only parameter left for calibrating the traction-separation law to match the resulting steady state peel force. An initial estimation of the fracture energy, $G_c = 600\,J/m^2$, is made for both low and medium adhesion level PVB. A matching result can be found iteratively.

For a reliable simulation of the peel test, the mesh needs to be sufficiently fine, especially in and around the crack process zone. To establish this, mesh convergence is studied by comparison of the simulated peel force for 4 different mesh refinements. The results are given in Fig. 4.6, where forces have been normalised to the steady state force of the finest mesh, i.e. Mesh 1. The element types used in all models are linear 4-node, plane strain elements for the glass part and quadratic 8-node, plane strain elements for both the PVB and aluminium parts, where large shear deformation and curvature are expected. A hybrid formulation to avoid volumetric locking is used for the PVB interlayer elements, because PVB can be regarded as a nearly incompressible polymer at low deformation rates. Table 4.3 gives the mesh sizes that are considered in a mesh convergence study. In analogy with Diehl [199], the cohesive overmeshing factor is defined as the average number of cohesive elements tied to one bulk element.

In Fig. 4.6, it is seen that the simulated peel forces for Mesh 1 and Mesh 2 correspond very well. Also, the force curves show oscillations, which originate from the successive failure of cohesive elements. Further mesh refinement has the only effect of reducing the oscillations in the reaction force. Therefore, the configuration of Mesh 2 is used in all further simulations.

Table 4.3: Specifications of meshes in convergence study for peel test simulation.

	Mesh 1	Mesh 2	Mesh 3	Mesh 4
Horizontal element length	50 µm	100 µm	100 µm	200 µm
Glass els. through thickness	4	4	4	4
PVB els. through thickness	12	12	12	8
Aluminium els. through thickness	6	6	6	4
Cohesive els. overmeshing	4	4	2	4

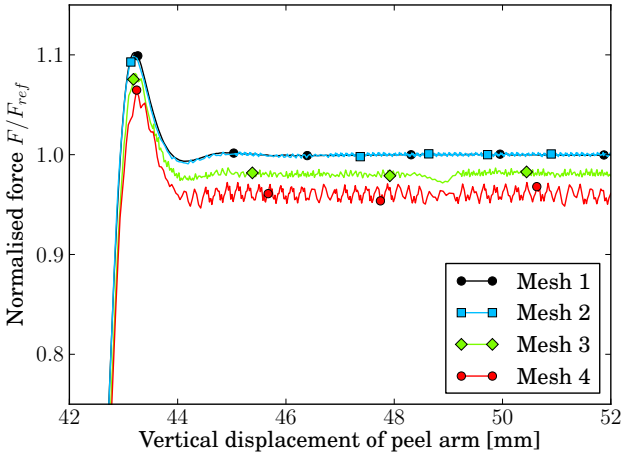

Figure 4.6: Mesh convergence study for peel test simulation of glass-PVB interface. Forces are normalised to the steady state peel force (F_{ref}) of the finest mesh, i.e. Mesh 1.

4.2.3 Simulation results

The fracture energy G_c in the cohesive zone is iteratively adjusted to match the experimental peel force. The resulting traction-separation law constants for medium and low adhesion, found after four iterations, are given in Table 4.4. Figure 4.7 shows when steady state peeling is reached in the simulation. The resulting Mode I fracture energies are in line with the estimation made by Bati et al. [192]. The corresponding length of the crack process zone in the peel test simulations is ca. 0.4 mm, for both low and medium adhesion levels. Table 4.5 gives the influence on the simulation results when the aluminium foil has been modelled differently. It is sometimes assumed that the thin backing foil acts more like a membrane with no bending stiffness, e.g. by Flocker and Dharani [186] and Rahul-Kumar et al. [200], or as a linear elastic material without plasticity, as by Williams et al. [201]. These two approaches have been tried for the case of low adhesion level PVB interlayer, and a clear difference

Table 4.4: Simulation results for calibrated peel test model of standard Saflex® PVB

PVB	σ_0 [MPa]	G_c [J/m^2]	δ_f [µm]	P_{sim} [N/m]	P_{exp} [N/m]
Saflex® RC	10.0	452	90	2647 ± 4	2650 ± 50
Saflex® RB	10.0	795	159	3572 ± 2	3575 ± 70

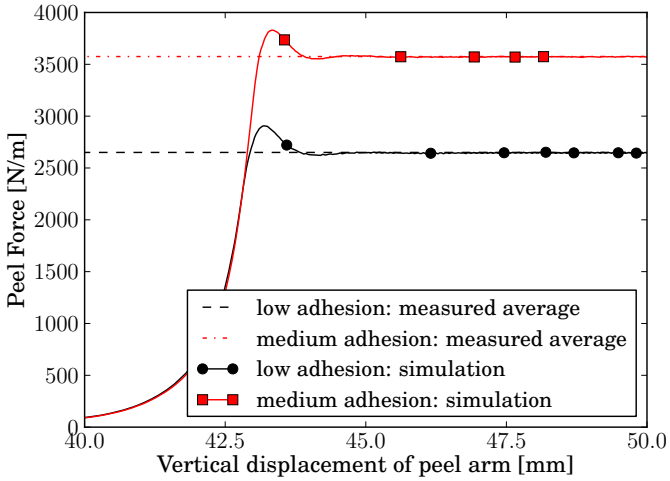

Figure 4.7: Simulation results for calibrated peel test model of standard Saflex® PVB, for low (Saflex® RC) and medium adhesion (Saflex® RB) levels.

is observed, because the yield stress is exceeded in the zone of the crack tip. A linear elastic cover sheet, with or without bending stiffness, predicts a much higher fracture energy for the same peel force. Also, the plastic deformation accounts for an additional energy dissipation, which should not be neglected.

Table 4.5: Calibrated peel test model of low adhesion Saflex® RC: material law for aluminium

Aluminium material law	σ_0 [MPa]	G_c [J/m^2]	P_{sim} [N/m]	R_{tip} [mm]
Elasto-plastic (see Fig. 4.4)	10.0	452	2647 ± 4	1.5
Linear elastic	10.0	1310	2642 ± 5	5.2
Linear elastic (membrane)	10.0	1004	2651 ± 8	1.2

An additional note can be made on the radius of curvature R_{tip} at the 90° turn around the crack tip. This radius could not be measured directly in the experiment, but is seen to be about 1 mm. The radius being larger in the

models is an indication that the interlayer material behaves stiffer in the model than it does in reality. This could be explained by the linear viscoelastic law being used in this analysis. D'haene's material model is intended to describe small-strain behaviour, while (eng.) strains up to 65% and strain rates up to $3.5\,\mathrm{s}^{-1}$ are observed locally in the peel test simulation. At large strains, the material in the model is acting overly stiff. Therefore, a visco-hyperelastic material model could be more appropriate for simulation of the peel test as well. However, before abandoning the present numerical model, the sensitivity of the cohesive zone towards various parameters can further be studied.

Because the adopted value for the critical stress ($\sigma_0 = 10\,\mathrm{MPa}$) is based on an initial estimation, additional simulations are performed for a range of 5 to 15 MPa. The results of these simulations are presented in Fig. 4.8. The crack release energy corresponding to low and medium adhesion level PVB interlayer varies greatly with the assumed interface strength.

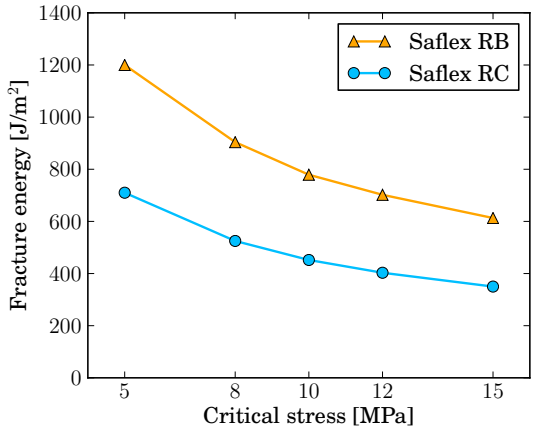

Figure 4.8: Simulation results for calibrated peel test model of low (Saflex® RC) and medium (Saflex® RB) adhesion PVB interlayer: fail stress - fracture energy relation.

According to Diehl [199], the influence of the damage initiation ratio δ_0/δ_f, and with it the stiffness of the cohesive element, is limited. Additional simulations for adhesion level RC, with $\delta_0/\delta_f = 1/4$ and $3/4$ can confirm this. In Fig. 4.9, it is seen that the steady state peel force for all three damage initiation ratios converges around $2650\,\mathrm{N/m}$ when $\sigma_0 = 10\,\mathrm{MPa}$ and $G_c = 452\,\mathrm{J/m}^2$ in the traction-separation law.

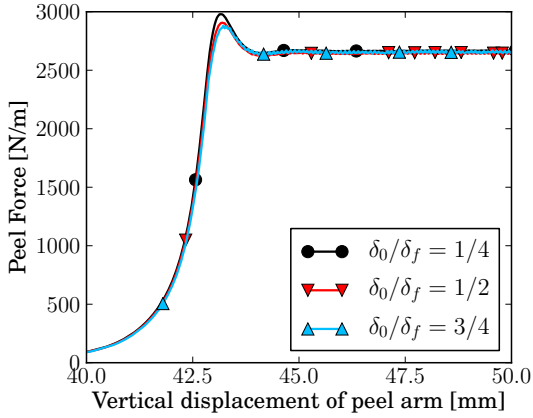

Figure 4.9: Simulation results for calibrated peel test model of standard Saflex® PVB: influence of damage initiation ratio δ_0/δ_f when $\sigma_0 = 10\,\text{MPa}$ and $G_c = 452\,\text{J/m}^2$.

Fig. 4.10 gives the energy balance at the onset of steady state peel-off for the Saflex® RC model with $\sigma_0 = 10\,\text{MPa}$ and $G_c = 452\,\text{J/m}^2$.

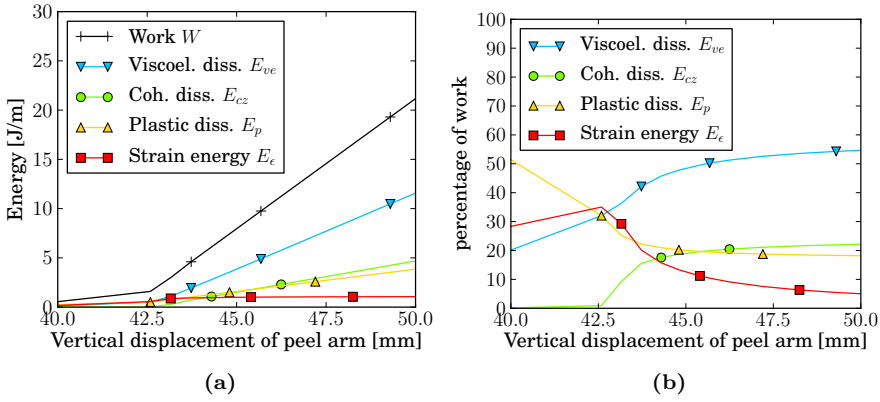

Figure 4.10: Energy balance for simulation of 90° peel test for laminated glass, at onset of peel-off: (a) absolute, and (b) relative to work input.

The energy balance can be written as:

$$\mathrm{d}W = \mathrm{d}E_\epsilon + \mathrm{d}E_p + \mathrm{d}E_{ve} + \mathrm{d}E_{cz}, \tag{4.3}$$

where W is the work input, which can be calculated by the peel force $\vec{P}$ and the displacement at the end of the peel arm $\mathrm{d}\vec{u}_a$, of which y_a is the vertical component.:

$$\mathrm{d}W = \vec{P} \cdot \mathrm{d}\vec{u_a} = P\,\mathrm{d}y_a \tag{4.4}$$

E_ϵ is the reversible strain energy and the other terms on the right hand side of Eq. 4.3 are dissipations: E_p is the plastic dissipation in the aluminium backing foil; E_{ve} is the viscoelastic dissipation by relaxation or creep of the polymer interlayer, and E_{cz} is the energy dissipated in the cohesive zone, i.e. the energy required to debond a unit area at the PVB-glass interface. Under the assumption that peeling occurs in Mode I only, this term can be explained as:

$$\mathrm{d}E_{cz} = G_c\,\mathrm{d}\tilde{A} = G_c\,b\,\mathrm{d}\tilde{x}, \tag{4.5}$$

where $\tilde{A}$ is the debonded surface and $\tilde{x}$ the corresponding peeled-off distance, while b is the specimen width.

When steady state has been fully reached, $\mathrm{d}y_a = \mathrm{d}\tilde{x}$. Then work input and energy dissipations accumulate at a constant rate. Fig. 4.10b presents the ratio of these dissipations to the work input. This shows that for steady state peeling, the plastic, viscous and debonding dissipations all approach a certain, constant percentage of the work input, i.e. of the total energy contained in the model. With plastic dissipation approaching 19% of the total energy, it is again confirmed that the deformation of the backing foil should not be overlooked.

From the energy balance in Fig. 4.10, it can be seen that the damage dissipation in the cohesive zone is higher than only the Mode I fracture energy: at $635\,\mathrm{J/m^2}$, E_{cz} is 40% higher than G_c. This is ascribed to the Mode II contribution. It can be concluded that the assumption of a purely Mode I delamination is incorrect for the 90°peel test and a mixed-mode traction-separation law should be used.

The contribution of viscoelastic dissipation in the numerical simulation is predicted at some 55% of the total work input, which is surprisingly high. It is possible that this is an overestimation due to the small-strain, linear viscoelastic description of the PVB interlayer. The zone where this energy is dissipated is located around the crack tip where high strain rates are present, as shown in Fig. 4.11. There, the material behaviour changes from the rubbery to the glassy state, and back to the rubbery state.

In Fig. 4.12, a plot is shown of the accumulated viscoelastic dissipation by element during a period of 0.2 s in steady state. This gives an idea of the size and location of the viscoelastic zones in peel-off, as described by Rahulkumar [200] (see Fig. 4.13). As expected, this zone is in the curved part of the material. The most energy is dissipated at the bottom edge just after the material is released from the cohesive zone and returns from its glassy state. This is in accordance with the observations by Knauss [202] for tearing of

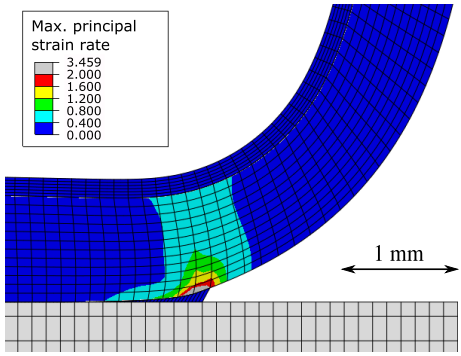

Figure 4.11: Simulation result showing strain rates around crack process zone at steady staty peeling.

elastomeric materials; bulk energy is dissipated in a small region ahead of the crack tip. Comparing Figs. 4.11 and 4.12 shows that the glassy state is already reached for a small amount of interlayer material in the peel test: the highest strain rates are located directly above the crack process zone. Thus, viscous dissipation accumulates in the relaxation phase, after the material has passed through the crack zone.

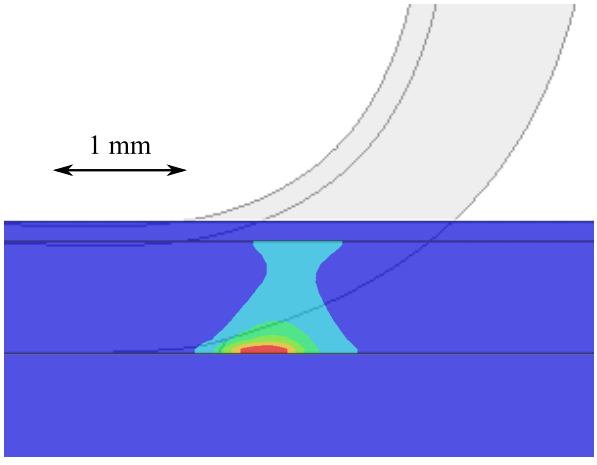

Figure 4.12: Simulation result showing location of viscoelastic dissipation in PVB, accumulated over 0.2 s (corresponding with 0.42 mm) of steady state peeling.

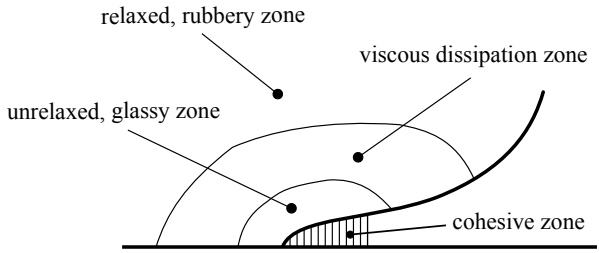

Figure 4.13: Schematic drawing depicting different zones around a crack propagating with constant velocity in a viscoelastic material (after Rahul-Kumar et al. [200]).

4.2.4 Conclusions

A numerical framework for identification of adhesive properties from a 90° peel test for PVB-laminated glass has been developed. The results show that a steady state is reached where the numerically calculated peel force can be fitted to the experimentally measured force value. The cohesive zone fracture energy is identified as the energy required to separate a unit area at the glass-PVB interface. However, the simulation results presented in this section are preliminary in that more experimental knowledge of the interface is needed. Nonetheless, important conclusions can be drawn for the continuation of this study:

1. Stiffness in bending and plastic deformation of the aluminium backing foil need to be taken into account in the calculation. It has been demonstrated that the interfacial debonding energy is greatly overestimated when aluminium bending stiffness and plasticity are neglected.

2. A bilinear traction-separation law has been used in the cohesive zone. It was shown that the damage initiation ratio δ_0/δ_f has negligible influence on the numerical results. This leaves only the critical stress σ_0 and the fracture energy G_c as the quantities that define delamination.

3. A linear viscoelastic law has been used to characterise the constitutive behaviour of PVB interlayer. But strains up to 65% and strain rates up to $3.5\,\mathrm{s}^{-1}$ are observed in the region of the crack tip. It is necessary to switch to a non-linear viscoelastic law for the interlayer, as the stiffness at high strains is tremendously overestimated with a linear viscoelastic model.

4. The critical stress σ_0 is needed as an input for simulation of the peel test. Its value has been estimated in the range of 5 to 15 MPa. In this range, the critical stress greatly influences the numerical result. Specific tests should be performed to measure the adhesion strength directly.

5. Unlike the double cantilever beam test, debonding in the 90° peel test is not purely Mode I. The share of energy dissipation in Mode II is considerable; in these simulations around 40%. Subsequent calculations should take account of a mixed-mode formulation for the cohesive zone.

These conclusions stand also for the numerical analysis of the through-cracked tensile test for PVB-laminated glass. Together, analysis of the 90° peel and TCT tests by the cohesive zone method allow to characterise the Mode I and II debonding of PVB and glass. Before continuing with the simulation of the TCT and peel tests, experiments are conducted to determine the critical stress at which the interfacial adhesion starts to fail.

4.3 Pull-off adhesion tests

4.3.1 Specimens and setup

To determine the Mode I bonding strength, tensile pull-off tests are performed. In a pull-off test, a laminated glass specimen is glued to metal stubs, named *dollies*, and pulled apart by which the glass-PVB interface should be separated. The specimens are cylindrical with a nominal diameter of 30 mm and are composed of two plies of 6 mm thick glass and a 0.76 mm interlayer. To avoid debonding at the interface between the metal dollies and the glass, a strong adhesive has been selected: the 2-component epoxy glue 3M Scotch Weld 9323 B/A.

A first test series with specimens drilled from a larger plate showed high scatter in the results. This could mostly be attributed to glass dust attached to the PVB around the edges. Therefore, test specimens have been produced by waterjet cutting of a laminated glass plate, which does provide clean and smooth edges. The diameter of these specimens is slightly smaller than its nominal value: 29.25 ± 0.25 mm. For each specimen, the measured diameter is taken into account for calculation of the critical stress. Test results with drilled specimens are not included in this section.

Experiments are performed with a Instron 8801 hydraulic tensile testing machine, equipped with a 50 kN load cell. The crosshead speed is 0.05 mm/min for all tests. The laboratory has a controlled temperature of 23°C and the relative humidity varies between 29 and 33%. As pointed out by Allaer et al. [203], the stress state at the interface in a pull-off test is very sensitive to the alignment of the specimen and non-axiality of the loading. Already, a small offset angle of 1° results in peeling behaviour rather than an even stress distribution. Thus, great care was taken in the positioning of each specimen and its axial alignment was checked with a laser level.

4.3.2 Test results and discussion

Typical force vs. displacement curves for this test are given in Fig. 4.14. A linear loading phase up to a maximum load at which the interface debonds can clearly be discerned.

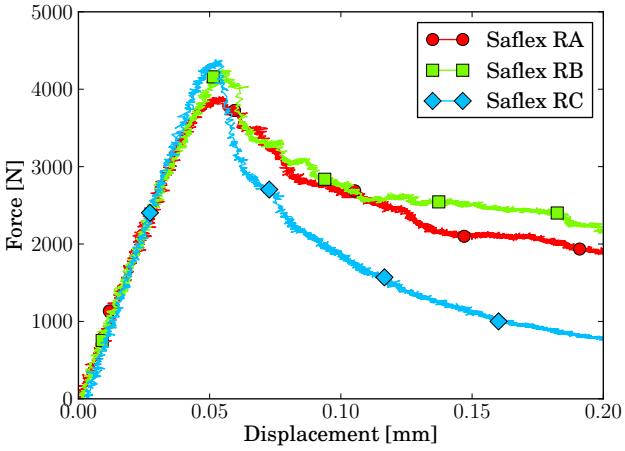

Figure 4.14: Representative force measurements for three different Saflex® PVB adhesion levels in a dolly pull-off test.

Subsequent delamination does not occur instantaneously for any of the specimens, but stress is still transferred over the bond until fully separated. This happens faster for the Saflex® RC interlayer, which would be expected because of its lower fracture energy. It would be possible to derive the Mode I traction-separation law directly from the second part of these curves if the delamination takes place ideally with uniform stress distribution throughout the whole process. In reality this is not the case. Two different failure modes are observed: either two-sided delamination in which a peeling-type debonding dominates, or single-sided delamination. Both types are shown in Fig. 4.15.

Intuitively, a single-sided delamination would better approach the desired uniform pull-off failure. However, shortly after the test the debonded surface appears as spotty. This looks very similar to the wavy type of debonding that is often seen for confined elastomeric layers between stiff adherends, for which the conditions and expected undulation spacing are described by Mukherjee et al. [204] using the cohesive zone method. For a simpler case, Mukherjee et al. found that the dominant wavelength is close to three times the thickness of the confined layer. The size and spacing of spots on the tested specimens are indeed in this order of magnitude. It is, however, not clear which effect this behaviour can have on the relation between the measured maximum force

(a) (b)

Figure 4.15: Photographs of debonding in dolly pull-off test: (a) one-sided failure, (b) two-sided failure.

and the physical Mode I strength of the PVB-glass interface. For now, it can only be assumed that the maximum force is a direct measure for the strength, which can be computed as force divided by sectional area.

The strengths calculated in this way are presented for all tested specimens in Fig. 4.16. Distinction is made between the two failure modes. It is notable that all specimens with high adhesion level fail two-sidedly, while most specimens with low adhesion level show one-sided failure. Moreover, for low and medium adhesion level, it appears that the two-sided failure mode is generally weaker. A possible explanation is that two-sided failure originates from particularly weak spots in the interface adhesion. Such weak spots can be present for various reasons, e.g. washing of the glass (moisture, residual minerals) or the distribution of salts in the PVB foil. Debonding commences at one location, instigating a bending moment and subsequent peeling. The force decreases slowly instead of the faster downfall seen for one-sided failure. This also implies that the maximum force for two-sided failure is not representative for the entire interface area, but only for the strength at its weakest point. Naturally, an interlayer with inherently higher adhesion strength is more likely to fail by two-sided debonding.

Because further analysis of the peel and TCT tests requires a single value for the Mode I strength, only one-sided failure is taken into account. The average strength for Saflex® RC interlayer is 6.41 MPa, and 6.36 MPa for Saflex® RB interlayer.

In general, the results of the pull-off tests differ notably from those obtained by Franz [179] in similar experiments with Trosifol® interlayer. In his case,

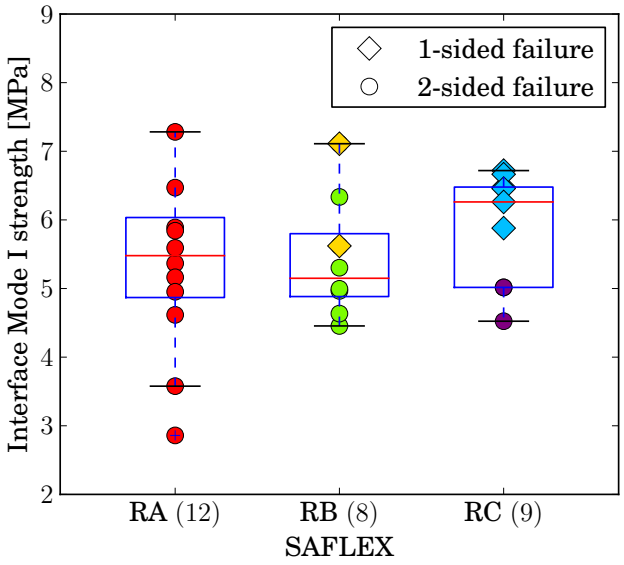

Figure 4.16: Interfacial Mode I strength for Saflex® PVB in a dolly pull-off test; number of tests between brackets for each adhesion level.

higher adhesion levels clearly show higher Mode I strength. Also the scatter on the strength is smaller, even though one- and two-sided failure modes are observed as well. Franz's specimens consist of a circular PVB interlayer laminated between two larger square glass plies. This is done so to avoid edge effects from the glass and, considering the consistency of the results, might be the better approach. It can also be mentioned that Franz's tests were conceived at higher speeds, and the interfacial adhesion strength does increase with the loading rate. The results in Fig. 4.16 were obtained for a rather low testing velocity. Higher test speeds were not possible because fracture occurs at a very low displacement (± 0.05 mm) and forces would no longer be measured precisely with a load cell for static testing.

Alternatively, to ensure one-sided failure, it could be interesting to produce specimens similar to those for the peel test, i.e. glued on one side to an aluminium layer. In this way, peeling behaviour would be prohibited under uniform tensile loading and generally higher forces are to be expected.

4.3.3 Mode II strength tests

Although not performed during the term of this study, tests may be designed to measure the Mode II interfacial strength for laminated glass. The compressive shear test is often used to this end by the laminated glass industry. However,

the measurement of Mode II strength seems to be influenced by the application of compressive force, as Franz [179] measured 40% to 50% lower strength for the same material in a simple shear test. Alternatively, a torsional shear method can be applied, in which the test setup is very similar to that for the dolly tests, except an axial moment is applied on the specimen instead of axial force.

In the work of Franz, large test series are conducted to determine both the Mode I and Mode II strength, at different loading rates and for different PVB adhesion grades. These tests showed that for every adhesion level, the Mode II strength is quite close to the Mode I strength. For further use in FE analysis, it can be assumed, by reasonable approximation, that the Mode II strength has the same value as the Mode I strength.

4.4 Through-Cracked Tensile test

Like the peel test, the TCT test provides a means to measure and compare the interfacial adhesion strength and the energy dissipated in debonding. Moreover, the loading state of the interlayer and the interface is closer to the loading of a broken laminated glass window than for other adhesion tests. The rectangular laminated glass specimens are cracked on both sides in the middle, as shown in Fig. 4.17, and loaded under remote tension at a constant displacement rate.

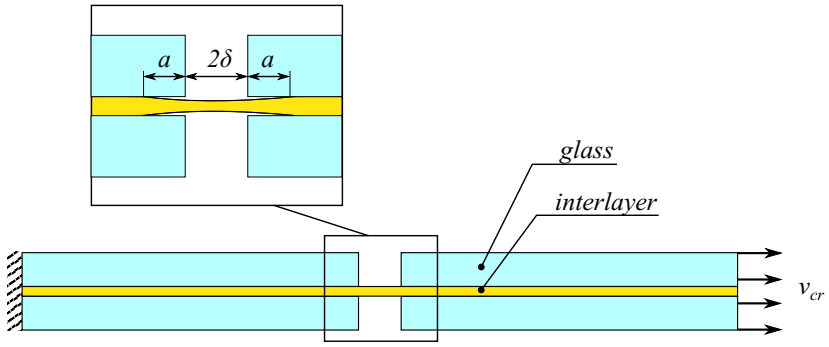

Figure 4.17: Schematic representation of the Through-Cracked Tensile test.

As first noted by Sha et al. [182], a steady state equilibrium can arise between the deformation of the interlayer and delamination from the glass. In this state, the force measured at the grips remains constant: P_{ss}. Also the delamination progresses at a constant rate $\mathrm{d}a/\mathrm{d}t$, and consequently the nominal longitudinal strain over the delaminated part of the interlayer $\epsilon = \delta/a$ remains constant as well.

For tests with similar specimens, higher variability is found on the steady state force than in the case of the peel test. It can be understood that the existence

of an equilibrium between deformation and delamination is more sensitive to imperfections at the interface, how well the specimens were cut, etc. than in the ongoing, forced delamination of the peel test. However, the mean values do show a clear trend when comparing different adhesion grades and testing speeds [6, 179, 182], and can be used for further (numerical) analysis of the interfacial adhesion.

4.4.1 TCT experiments

A series of TCT experiments with Saflex® PVB interlayer were performed by Van Dam. For a detailed description of these tests and thorough discussion of the experimental results, the reader is referred to Van Dam's dissertation [6]. Here, a short summary of the experiments is given, along with the main results, which are to be used in subsequent characterisation of the cohesive zone at the interface by numerical techniques.

The considered specimens have been produced at the Eastman™ quality control lab and are 250 mm long by 50 mm wide. The glass plies have a thickness of 3.8 mm and are laminated to a PVB interlayer of either 0.76 mm or 1.52 mm. Two different adhesion grades were tested, Saflex® RA and RC, at three deformation rates: 5, 25 and 125 mm/min. The cracks at the middle of the glass plies were applied by first scoring the surface and subsequently tapping gently with a rubber hammer. The experiments were performed on a Instron 5800R electromechanical tensile testing machine, at room temperature between 20 and 22°C and relative humidity around 32%.

Fig. 4.18 shows force measurements for specimens with a thick, low adhesion interlayer loaded at 25 mm/min. All force vs. displacement curves in this figure reach a steady state at some point for which constant force is measured before ultimately tearing. This is not always the case. At the lowest testing speed, only 1 out of a total 27 tested specimens showed a steadily increasing delamination at a constant force. The other force measurements at this speed show no consistent behaviour; some are descending or ascending, others show unstable oscillations of the force. Steady state behaviour is reached for the majority of TCT tests at the higher speeds, and most constistently where a thicker interlayer has been used. The results for the steady state of test series at 25 and 125 mm/min are given in Table 4.6. Apart from the steady state force, also the nominal strain and delamination speed $\mathrm{d}a/\mathrm{d}t$ are given. The latter has been determined by analysis of photographic images: a MATLAB routine, based on the work of Delincé et al. [205], is used to identify and track the delamination front. The delamination length a is thereby calculated as the median of the delamination front. Fig. 4.19 shows a specimen with a symmetric, steady delamination front and a specimen with an irregular delamination front.

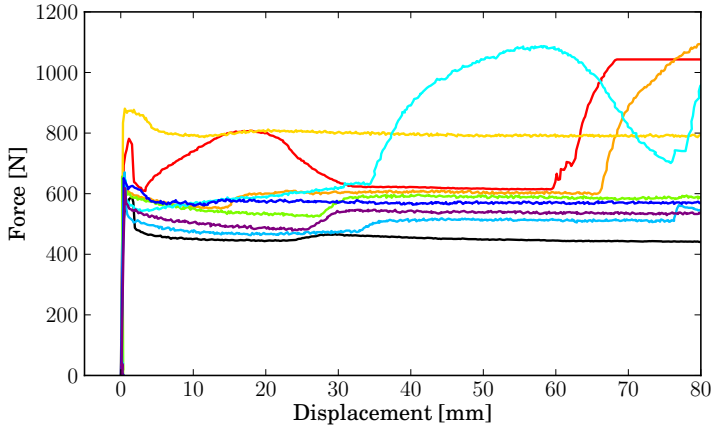

Figure 4.18: Force vs. displacement for TCT test with 1.52mm Saflex® RC interlayer at pulling rate of 25 mm/min (see also Van Dam [6]).

Table 4.6: Results for steady state in TCT tests on laminated glass with Saflex® PVB interlayer (See also Van Dam [6]). First column, between brackets: number of specimens showing steady state delamination.

Saflex®	t_{PVB} [mm]	v_{cr} [mm/ min]	P_{ss} [N]	ϵ_{ss} [-]	$\frac{\mathrm{d}a}{\mathrm{d}t}\big\vert_{ss}$ [mm/ min]
RA (2)	0.76	25	419 ± 48	1.11 ± 0.13	7.5 ± 0.5
RA (2)	0.76	125	441 ± 16	1.22 ± 0.06	44 ± 2
RA (3)	1.52	25	571 ± 113	1.09 ± 0.01	8.0 ± 2.0
RA (6)	1.52	125	718 ± 61	1.24 ± 0.02	45 ± 3
RC (1)	0.76	25	394	1.12	10.0
RC (4)	0.76	125	415 ± 30	1.10 ± 0.06	54 ± 12
RC (9)	1.52	25	570 ± 102	0.97 ± 0.03	9.5 ± 3.0
RC (8)	1.52	125	715 ± 130	1.04 ± 0.03	62 ± 9

The work performed in the TCT test can be decomposed as the sum of elastic strain energy and dissipation by debonding, as in Eq. 4.6. The dissipation by viscoelastic relaxation is commonly assumed to be negligible as the strain in the material only increases and strain rates remain relatively low.

$$\mathrm{d}W = \mathrm{d}E_{\epsilon} + \mathrm{d}E_{cz} \tag{4.6}$$

During steady state debonding:

$$P_{ss}\mathrm{d}\delta = \mathrm{d}E_{\epsilon} + bG_T\mathrm{d}a, \tag{4.7}$$

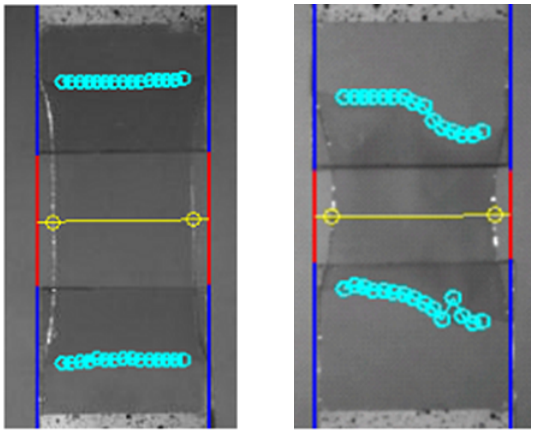

(a) (b)

Figure 4.19: Detection of delamination front in TCT test: processed image of (a) symmetric, regular delamination, (b) irregular delamination (See also Van Dam [6]).

where G_T is the total fracture energy required to release a unit surface by a combination of Mode I and Mode II debonding.

If also the elastic strain energy can be determined, it is possible to derive the energy dissipated in delamination directly. Several authors have calculated the strain energy for the TCT test analytically by assuming a simplified material law for the interlayer: linear elastic (Sha et al. [182], Iwasaki [174], Bati et al. [192], Ferretti et al. [206]), linear viscoelastic (Jagota et al. [195], Butchart et al. [184]) or rate-independent hyperelastic (Seshadri et al. [183]). In these calculations, it is furthermore assumed that the strain is uniform and constant over the entire delaminated interlayer volume, which is also not the case in reality. In view of the mechanical characterisation of PVB interlayer in Ch. 3, it may be clear that simplified representation of the PVB material law at such high strain is a very crude approximation and is bound to give false results. This is reflected in the widely varying values found for the fracture energy in Table 4.2. Seshadri [191], and later Franz [179], have acknowledged this as well and have made efforts to solve the problem via a numerical approach using a nonlinear material model for the interlayer. In the following sections, a numerical framework to extract the Mode I and II fracture energies in TCT testing is proposed. The analysis of mixed-mode debonding is coupled to results from the pull-off tests and peel tests, and is performed for the low adhesion Saflex® RC interlayer.

4.4.2 Numerical representation

In the TCT experiments, substantial contraction is seen at the middle of the bridging interlayer and the delamination front mostly appears as slightly curved, with a larger delamination length at the edges than at the center. Considering this, a choice is made to conceive the numerical model in three dimensions, rather than a plane strain representation. Regarding symmetry, only an eighth of the entire specimen needs to be modelled. The boundary conditions of the model consist of symmetry conditions on all three principal planes and imposed displacement at constant rate at the back edge of the glass part.

The constitutive model for the interlayer is a combination of hyperelasticity for instantaneous behaviour coupled with viscoelasticity by Prony series, as described in Ch. 3. The deformation rates expected for the TCT test are much lower than for a laminated glass under impact or blast. The material behaviour is closer to the quasi-static tensile tests in Fig. 3.9, which are less accurately described by the material model calibrated for strain rates between 0.1 and $10\,\mathrm{s}^{-1}$ (see Fig. 3.22). The force vs. displacement curves for these tensile tests deviate from the bilinear shape seen at higher deformation rates. In fact, they are well described by a simple Yeoh law. The material model for PVB is again calibrated to fit the quasi-static tensile tests. This gives following constants for instantaneous hyperelastic behaviour with the Yeoh strain energy potential: $C_{10} = 34.58\,\mathrm{MPa}$, $C_{20} = 6.68\,\mathrm{MPa}$, $C_{30} = 0.110\,\mathrm{MPa}$. The Prony series are given in Table 3.5 and the temperature shift function in Table 3.6. Fig. 4.20 shows the simulation results for this material law in uniaxial tensile tests at 200 and 20 mm/min. The strain rates in these tests range between 0.001 and $0.05\,\mathrm{s}^{-1}$.

The glass can either be modelled as linear elastic or as rigid. A preliminary analysis of the TCT test does show bending stresses in the glass up to 10 MPa. However, the strains in the glass are still very low and are negligible in comparison with the deformation of the interlayer and the cohesive elements. Therefore, the glass can be modelled as rigid.

A layer of zero-thickness cohesive elements is inserted at all interfaces between glass and interlayer elements. The traction-separation law is again bilinear, but uses mixed-mode definitions for crack initiation and critical energy release rate. The crack initiation criterion is given by a quadratic relation:

$$\left(\frac{\sigma_I}{\sigma_{I,0}}\right)^2 + \left(\frac{\sigma_{II}}{\sigma_{II,0}}\right)^2 = 1, \tag{4.8}$$

where $\sigma_{I,0}$ and $\sigma_{II,0}$ are the critical stresses in Mode I and Mode II. For Saflex® RC interlayer, both amount to 6.4 MPa, as resulting from the pull-off tests

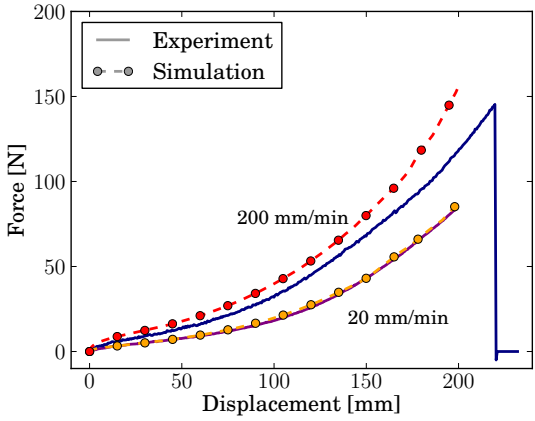

Figure 4.20: Force vs. displacement for uniaxial tensile tests; simulated results for material model calibrated at 20 mm/min and 21.8°C.

in Sec. 4.3. The mixed-mode fracture energy G_{Tc} can be described by the Benzeggagh-Kenane law [207], which is given by:

$$G_{Tc} = G_{Ic} + (G_{IIc} - G_{Ic}) \left(\frac{G_{II}}{G_T} \right)^{\eta}, \tag{4.9}$$

where G_{II}/G_T is the modal ratio, which is 0 for pure Mode I debonding and 1 for pure Mode II. The parameter η is specific to the interlayer. A common value is $\eta = 2.6$, which is used here as well. Fig. 4.21 shows the influence of η on the mixed-mode fracture energy.

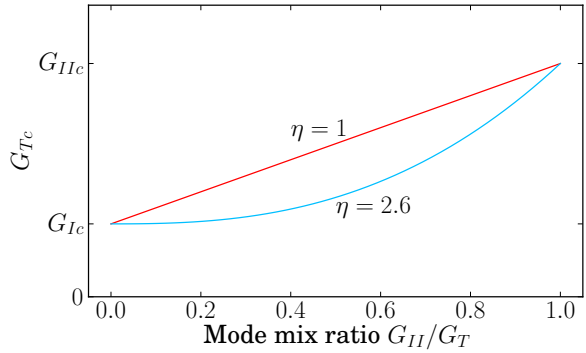

Figure 4.21: Mixed-mode critical energy release rate by Benzeggagh-Kenane law.

A regular, hexahedral mesh is used for the TCT specimen, with zero-thickness cohesive elements inserted at the interface. The mesh is divided in three zones

of refinement: the quarter 31.25 mm closest to the symmetry plane where the debonding initiates, the second quarter and the second half. For the cohesive zone, an overmeshing factor of 2 is used in the length direction: two cohesive elements are created for each bulk PVB element at the interface. A mesh convergence study, shown in Fig. 4.22, demonstrates that a mesh with 400 elements in the length direction, 60 in the width direction and 5 elements through the thickness for the interlayer produces consistent results. The characteristic element length for this mesh is $L_e = 0.078$ mm.

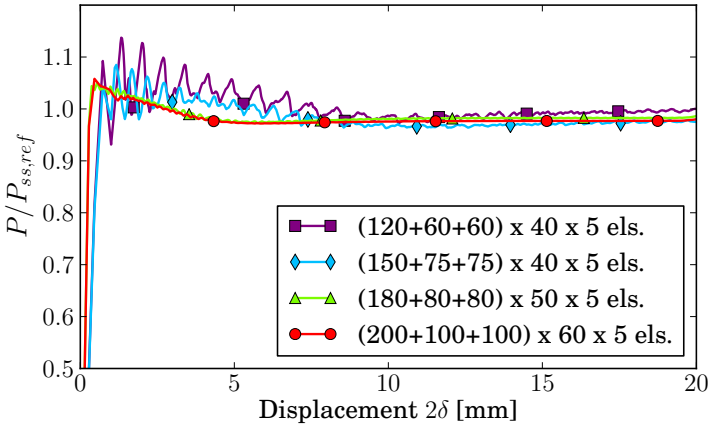

Figure 4.22: Mesh convergence study for TCT test; force normalised to steady state force of finest mesh.

The combination of a highly nonlinear material law with the simulation of crack propagation proves to be challenging for the ABAQUS implicit solver. Although no instabilities are reported, a single simulation with the finest mesh takes up to two weeks to complete. Computational efficiency can be enhanced by using the explicit solver for a quasi-static analysis, whereby the stable time increment is artificially increased by mass scaling. With this procedure, care should be taken to avoid dynamic effects that distort the analysis result. Fig. 4.23 shows that the stable time increment can be increased up to 5 µs for a TCT test at 25 mm/min, and produce the same results as the implicit calculation without loss of accuracy. The figure furthermore shows that the scalability is excellent for the explicit analysis, which is not an obvious trait for fracture simulations. The explicit simulation of a 20 mm opening displacement in the TCT test takes around 75 hours with 6 CPU's[1].

[1]Using a workstation with 2 Intel Xeon Processor E5-2667 and 128 GB RAM

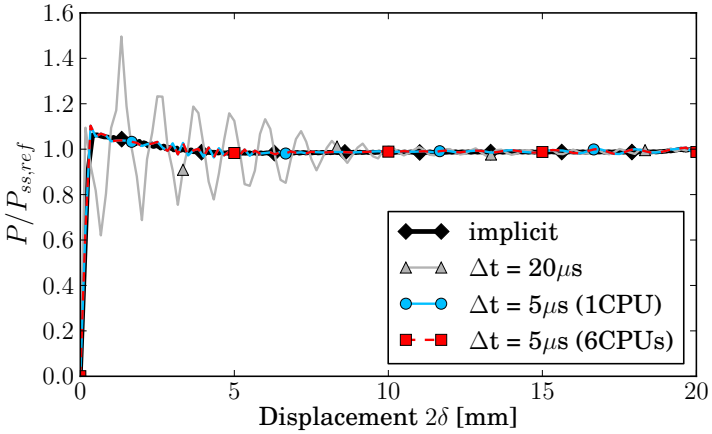

Figure 4.23: Mass scaling for TCT test at 25 mm/min; force normalised to steady state force of implicit calculation.

4.4.3 Simulation results and discussion

The numerical analyses for the TCT test and the peel test for Saflex® RC interlayer are solved simultaneously and iteratively in order to find the parameters for the cohesive zone that provide the best approximation to the experimental observations. The resulting constants for the traction-separation law are given in Table 4.7. The steady state characteristics of the experiments and simulations with this traction-separation law are compared in Table 4.8 for the peel test, and in Table 4.9 for the TCT test.

Table 4.7: Constants of traction-separation law for Saflex® RC interlayer.

	σ_0 [MPa]	G_c [J/m^2]
Mode I	6.4	1035
Mode II	6.4	2700

Table 4.8: Characteristics of steady state in 90° peel test for Saflex® RC interlayer.

	Force P_{ss} [N]	Radius R_{tip} [mm]	Mode mix ratio G_{II}/G_T
Experiment	2650 ± 50	< 1	
Simulation	2644 ± 4	1.13	38%

Table 4.9: Characteristics of steady state in TCT test for 1.52 mm Saflex® RC interlayer.

Test speed		P_{ss} [N]	$\frac{da}{dt}\Big\|_{ss}$ [mm/ min]	G_{II}/G_T
25 mm/min	Experiment	570 ± 102	9.5 ± 3	
	3D Simulation	592	8.93	$63\%^{(c)}$, $94\%^{(s)}$
	2D Simulation	612	8.33	63%
125 mm/min	Experiment	715 ± 130	62 ± 9	
	3D Simulation	793	75	$63\%^{(c)}$, $95\%^{(s)}$

(c) at the center of the delamination front
(s) at the sides of the delamination front

The cohesive law is calibrated primarily to match the steady state forces of the peel test and the TCT test with a 1.52 mm interlayer at 25 mm/min. When the TCT test is simulated at 125 mm/min, the steady state force is greater than the mean measured force, but still within bounds. The simulated delamination speeds are quite close to the experimental averages as well, for both crosshead speeds. Fig. 4.24 shows the evolution of the delaminated distances at the center and sides, which become parallel and maintain a constant delamination speed in steady state.

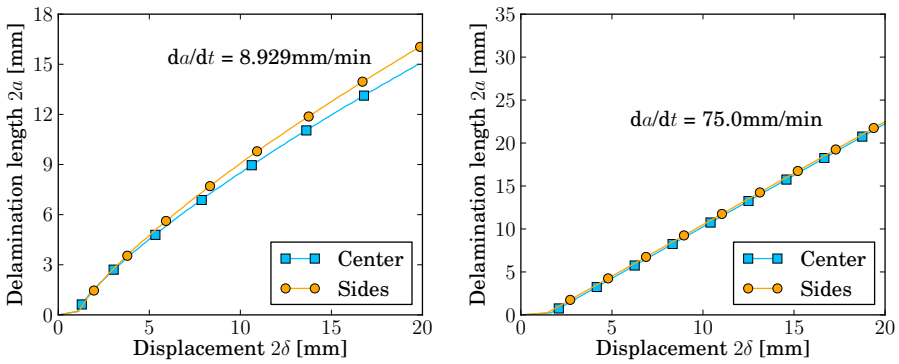

Figure 4.24: Delaminated distance for simulated TCT tests with 1.52 mm Saflex® RC at (a) 25 mm/min and (b) 125 mm/min.

The strain state for the PVB in the TCT test is shown in Fig. 4.25. In the steady state, the strain at the middle section remains nearly constant at ca. 170% engineering strain. Therefore, the strain rate in the delaminated interlayer is very low, as can be seen in Fig. 4.26. This is also why the material model for large strain behaviour of PVB has been calibrated for the lowest

uniaxial testing speed to simulate the TCT test (see Fig. 4.20). The strain rate only becomes higher in and around the cohesive zone, but never greater than $0.1\,\mathrm{s}^{-1}$ at a crosshead speed of 25 mm/min and $0.3\,\mathrm{s}^{-1}$ at 125 mmmin. For the repeated simulation of the peel test, the max. strain and strain rate are found in close vicinity of the crack tip and amount to 42% eng. strain and $1.6\,\mathrm{s}^{-1}$ respectively.

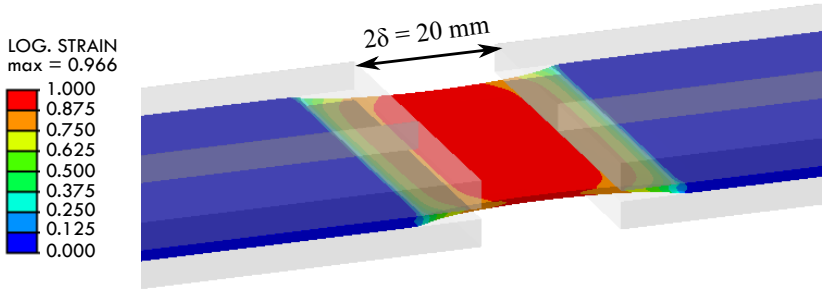

Figure 4.25: Contours of logarithmic strain in length direction for TCT numerical model at crosshead speed of 25 mm/min.

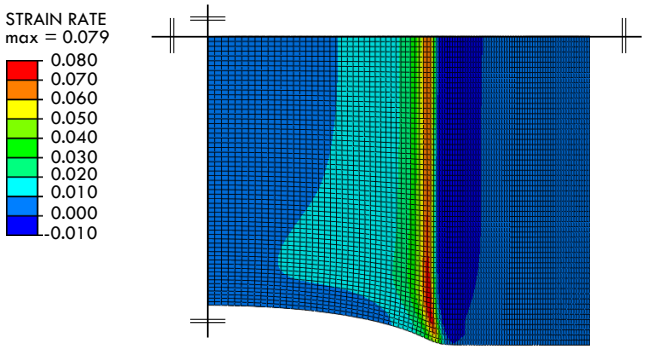

Figure 4.26: Contours of strain rate in length direction for TCT numerical model at crosshead speed of 25 mm/min.

In Tables 4.8 and 4.9, the mode mix ratio is given for the simulations in the same way as it is defined in the ABAQUS software and manual, i.e. as the Mode II contribution to the total energy dissipation in a cohesive element. Contrary to common assumptions, both the peel test and the TCT test show important mixed mode behaviour. For the TCT test, the mixed mode ratio is between 60 and 70% at most of the delamination front, but increases sharply to over 90% at the side edges. The peel test has a Mode II contribution of about 40%, which is consistent with earlier results.

In Fig. 4.27, the energy balance is given for both adhesion tests. In the updated energy balance for the peel test, the share of the viscoelastic dissipation has decreased with the switch to a non-linear viscoelastic material law for the PVB. Also the max. strain rate in the model is smaller, at $1.21\,\mathrm{s}^{-1}$ (in comparison with Fig. 4.11). The strain energy also increases as delamination progresses. It should be mentioned that the strain energy also includes the contribution of viscoelastic dissipation, because ABAQUS/Explicit does not distinguish between both when a nonlinear viscoelastic material model is used. The shares of the strain energy and damage dissipation in the energy breakdown eventually approach a constant value. In steady state, about 22% of the work is dissipated by delamination at the glass-PVB interface.

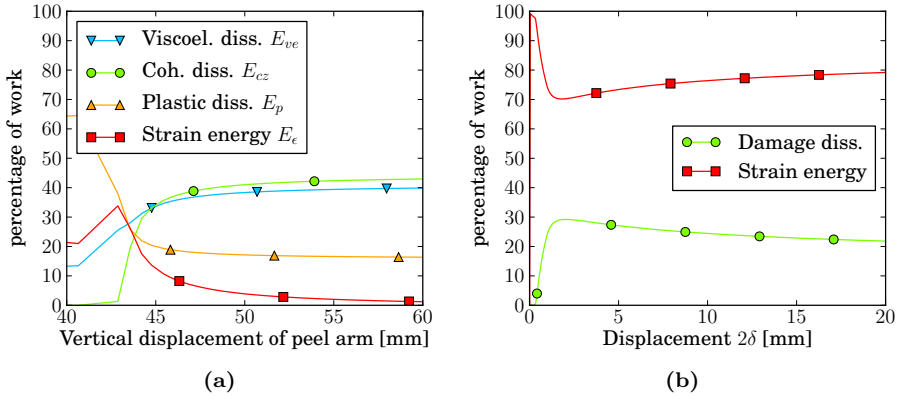

Figure 4.27: Energy division as share of total work: (a) simulation of the 90° peel test; (b) simulation of the TCT test with 1.52 mm Saflex® RC at 25 mm/min.

In a further remark on the peel test, the radius of the 90° turn is smaller than with the linear viscoelastic PVB model in Section 4.2. However, at 1.13 mm, this radius is still slightly larger than the visually estimated 1 mm for the experiment.

Finally, the TCT test has been simulated with finite elements before by Seshadri et al. [183], Nhamoinesu et al. [193] and Franz [179]. These authors have all modelled the test as a plane strain 2D problem, despite clear contraction of the interlayer upon elongation and a curved delamination front. To compare with the results for the 3D model, the TCT test with 1.52 mm Saflex® RC interlayer at 25 mm/min has been simulated in 2D as well. The material model for the PVB interlayer and the traction-separation law are the same as described above. The resulting steady state force amounts to 612 N, while the delamination speed $\mathrm{d}a/\mathrm{d}t$ reaches a constant 8.33 mm/min. Thus, the force is overestimated and the delamination speed underestimated in the 2D model. This behaviour could

be expected, because the 3D model also shows that the delamination is tougher at the center of the specimen. Unless the specimen is very wide, it would not be correct to simplify the TCT test as a 2D problem. Also, a 2D model requires a finer mesh before convergence of the steady state force is reached. Where a characteristic element length of 0.08 mm can be used for the 3D model, this is 0.04 mm in 2D. Presumably, mesh convergence is reached easier in 3D because an entire delamination front is simulated, which makes the model less sensitive to minor changes in the mesh.

4.5 Conclusions

Several experimental test methods to determine the adhesive properties between glass and PVB interlayer have been used and analysed. Neither the 90° peel test, nor the through-cracked tensile test allow to quantify the interfacial strength and energy dissipated by delamination directly from the experiment. For the peel test, the complicating causes are the plastic deformation of the aluminium backing foil and the rapidly changing strain state of the viscoelastic interlayer around the crack tip. In the case of the TCT test, high strains are reached in the delaminated PVB. This material behaves highly nonlinear and rate-dependent, yet is key to the balance between elongation and delamination and therefore the force measured in steady state. Oversimplification of the interlayer constitutive behaviour for analytical calculation cannot be justified. However, the finite element method provides a framework to solve both problems.

In preliminary numerical analysis of the peel test, it is seen that the interfacial adhesion, represented as a cohesive zone, is characterised by its strength and fracture energy. The actual shape of the traction-separation law has negligible influence. However, the strength and fracture energy should be determined for both fracture modes, as delamination in the peel test is a mixed-mode process. It is seen that different combinations of these constants can yield the same steady state peel force.

Pull-off tests have been performed to measure the Mode I strength. Two failure modes could be discerned: sudden debonding at one of the glass-PVB interfaces, or a slower mixed-mode debonding of both interfaces simultaneously. In subsequent numerical modelling only results for the one-sided failure mode have been taken into account because this answers to the desired Mode I debonding behaviour and the measured strengths are generally higher than for two-sided failure.

The analysis of the peel test is repeated alongside simulations for the TCT test in order to determine a single traction-separation law that characterises the adhesion between soda-lime glass and Saflex® RC interlayer. The cohesive

law takes account of mixed-mode behaviour and the interlayer is modelled as a nonlinear viscoelastic material. The latter is required for simulation of the TCT test where high strains are being reached at low, but locally varying strain rates. But it is also necessary for the peel test where a linear viscoelastic material model overpredicts the radius of the peel arm at the crack tip and the viscoelastic energy dissipation in the model.

The resulting strengths and fracture energies in the traction-separation law are given in Table 4.7. A few critical remarks can be made with regards to the precision of the numerical models for the peel and TCT tests:

- The Mode II strength has been assumed to be the same as the Mode I strength. This would be a reasonable approximation considering the values given in literature. However, direct measurement is preferred.
- The Mode I strengths measured in dolly tests are lower than those for comparable PVB products tested by Franz [179] and show much greater scatter. It would be recommended to reconsider the laminated glass specimens with extra attention to the edges of the interface.
- Both Seshadri [183] and Franz [179] have stated that the interfacial adhesion is rate-dependent. In the present analyses, a rate-independent traction-separation has been used and evaluated at two different speeds for the TCT test. The simulations do not allow to exclude inherent rate-dependency of the interfacial adhesion entirely, but the results do show that rate-dependency in these tests stems mostly from the viscoelastic nature of the interlayer.
- The nonlinear viscoelastic material law for the interlayer can be calibrated to a uniaxial tensile test at a single speed and serves as an approximation for other speeds (or strain rates). It is seen that this approximation is less accurate at higher strains.
- The Benzeggagh-Kenane law is used to describe mixed mode behaviour in the cohesive zone. A shape factor $\eta = 2.6$ has been assumed as a common value, but could not be verified for this particular laminate.

Nonetheless, the resulting cohesive zone model can be used in subsequent analysis. And more generally, the method presented in this chapter can be applied to analyse the debonding behaviour of any laminated glass product.

Chapter 5

Numerical simulation of laminated glass

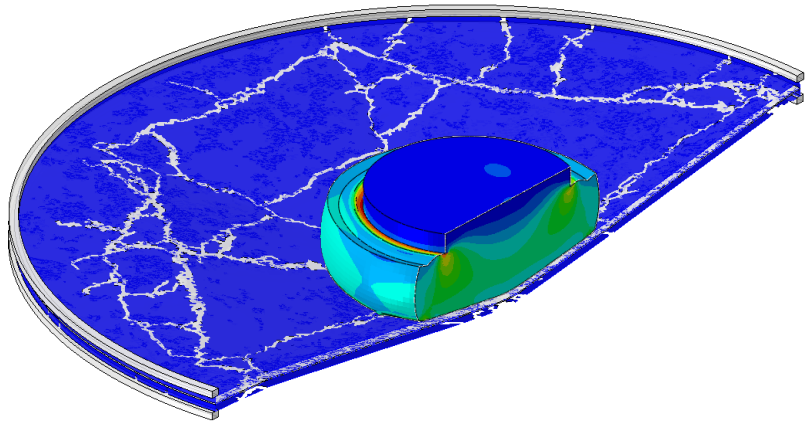

Cut view of breakage in simulated soft-body impact on laminated glass disk.

5.1 Introduction

Chapters 2–4 concern the separate components that constitute laminated glass: materials and interfacial adhesion have been characterised and the numerical representation has been discussed. The present chapter investigates how to combine these elements in a numerical model that allows for the analysis of laminated glass into the post-fractured state during an impact or blast event. Several approaches to this end are documented in literature, although their intention can differ.

In general, the cracking of laminated glass is characterised by several stages, as sketched in Fig. 5.1:

1. Intact, elastic deformation of the panel.
2. Fracture of the first glass ply in tension. The other glass ply is still intact and there is no damage to the interlayer.
3. The second glass ply fails. In many cases, this occurs almost simultaneously with the cracking of the first glass ply.
4. Membrane-like deformation of the interlayer with delamination occurring around the cracked edges of glass fragments.
5. Tearing of the interlayer by reaching its ultimate failure strain, or by cutting from splinters.

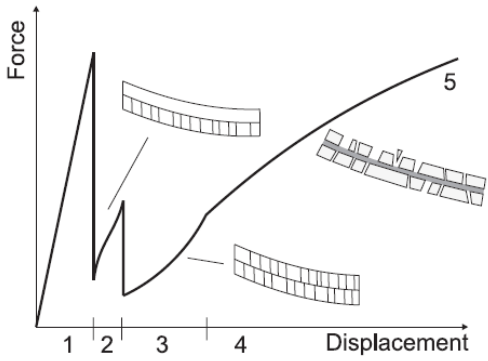

Figure 5.1: Schematic representation of laminated glass failure (figure from Larcher et al. [75]).

Early simulations of laminated glass fracture were performed by Flocker and Dharani [186,208], in which they modelled the cone cracking through the thickness of the glass following an impact by a small spherical missile. As they considered only local behaviour, the model consisted of a small, two-dimensional

domain of plane strain solid elements. In an illustrative example, they also included the delamination process by setting all stress components to zero for those PVB elements at the interface where a critical shear stress or critical tensile cleavage stress is reached. This is essentially an element deletion method which takes no account of the energy absorbed in debonding.

Du Bois et al. [102] have presented 3D models for windshields under impact and crushing, where the laminated glass is discretised by coincident shell and membrane elements. The shell elements, representing the glass, can fail by element deletion. When this occurs, the underlying membrane element is left to represent the interlayer. With this configuration, it is assumed that the intact laminate behaves as one monolithic glass ply of the same thickness, which can be justified for high loading rates, as noted by Norville et al. [209], Kutterer [210], and Kuntsche and Schneider [211, 212]. The approach of Sun et al. [103] consists of three element layers: shell–solid–shell as shown in Fig. 5.2. In this way, the transfer of shear forces between both glass plies can be preserved. The shell elements share nodes with the solid element. A drawback of this method is that the nodal surface of a shell element has a full offset from the mid-surface, which may lead to less accurate stress calculation and is more difficult to handle in contact.

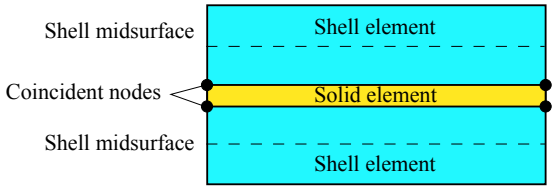

Figure 5.2: Layer structure of the finite element model for laminated safety glass (after Sun et al. [103]).

Wagner and Müller [213] modelled the response of laminated glass to blast loading using layered shell elements. In this approach, the integration points through the thickness of a shell element are assigned distinct material behaviour. Upon glass fracture, the stress components perpendicular to the crack are set to zero for the integration points associated with glass behaviour. When also the interlayer tears, the shell element can be deleted entirely. Although allowing to capture the global deformation of very large windows reasonably well, this approach severely limits the accuracy by which the interlayer can be modelled; it is simplified as linear elastic. The same technique has been used by Konrad and Gevers [110], who concluded that a decoupled approach, such as by Sun et al. [103] is preferable. Similar limitations are experienced by Timmel et al. [104], who used a smeared modelling technique, consisting of two coincident shell elements of the same thickness. One of the elements represents

the inner glass ply and interlayer, while the outer represents the outer glass ply, which is expected to break first. Consequently, this technique requires the use of a corrected thickness, modified densities and modified moduli for both shell elements. Notwithstanding all the modifications to the material behaviour, simulation results do show a realistic fracture pattern and good correspondence to measured forces.

Fig. 5.3 shows the different element configurations for the representation of laminated glass that were evaluated by Peng et al. [116]. They observed that the best correspondence with the experimentally measured forces and fracture pattern could be achieved with the two-layered G-P-T configuration. Unfortunately, no reasoning is given why the meshes with shared and tied nodes produce different results or why the triple layered representation would be less suited.

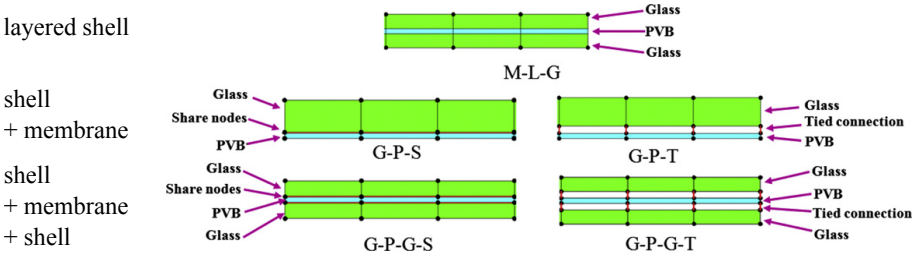

Figure 5.3: Five element configurations for windshield laminated glass in LS-Dyna investigated by Peng et al. [116].

A generally shared finding in many of the aforementioned publications is that a rectangular, structured mesh topology is less capable of realistically representing the cracking pattern of laminated glass. Rather, a mesh can be carefully designed to suit the considered case, or an unstructured mesh can be used which allows a more natural crack propagation. Moreover, none of the authors have used a verified material model for the PVB interlayer, but they did conclude that a material law that is valid at large strains and able to capture the strong rate-dependency of the polymer is requisite.

With the developments presented in the previous chapters, an investigation can be made on how to discretise the laminated glass in a way that is efficient and able to capture the material response during a dynamic event. An evaluation is made for the elastic response in Sec. 5.2 and for crack formation and the post-fractured response in Sec. 5.3. Three different element configurations are considered, as shown in Fig. 5.4. The LG2 and LG3 configurations are most commonly encountered in literature. The LG1 configuration is added as an interesting option, which preserves the modelling of shear transfer by the

interlayer and uses continuum shell elements which do not require any offsets from the mid-plane and deal more naturally with contact at the outer surfaces. When no delamination is considered, the nodes of the PVB and glass elements are shared. Otherwise, they are connected by a cohesive zone, which can be implemented either by the use of cohesive elements or as a contact condition. For the LG3 configuration, only Mode II debonding can be modelled at the interface and an additional tie constraint in normal direction is required for the shell and membrane elements.

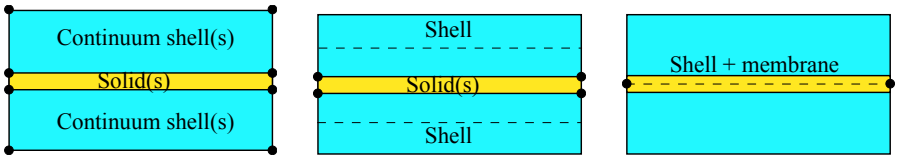

(a) LG1 **(b)** LG2 **(c)** LG3

Figure 5.4: Element configurations for laminated glass considered for evaluation

5.2 Simulation of the elastic response to drop weight impact

5.2.1 Experiments

The drop weight test setup introduced in Section 2.3 has been used for impact experiments on laminated glass plates by Van Dam [6]. Instead of the hard, steel indentor used on the small, monolithic specimens, a soft, rubberlike indentor is used for impact testing of laminated glass. This indentor exerts a more distributed load, rather than local hard contact which would provoke spalling on the impacted glass surface of a laminate. Also human body impact and blast, studied in the next chapters, pose a distributed load for the glass surface. The soft indentor, shown in Fig. 5.5, is moulded from Zhermack ZA22 silicon rubber and weighs 0.90 kg.The total mass of the impactor is 8.3 kg.

The material properties for the ZA22 silicon rubber are not known from the datasheet. Therefore, the indentor is submitted to a compression test. A hyperelastic material law can be found by simulation of the same test with finite elements. The experiment is performed with the aluminium back plate of the indentor placed flat on the test bench and a flat steel plate connected to the load cell that presses on the silicon part. The resulting force-displacement curve is given in Fig. 5.6.

An axisymmetric model of the compression test is created for implicit analysis. The aluminium plate is assumed to be rigid and is not included in this model as

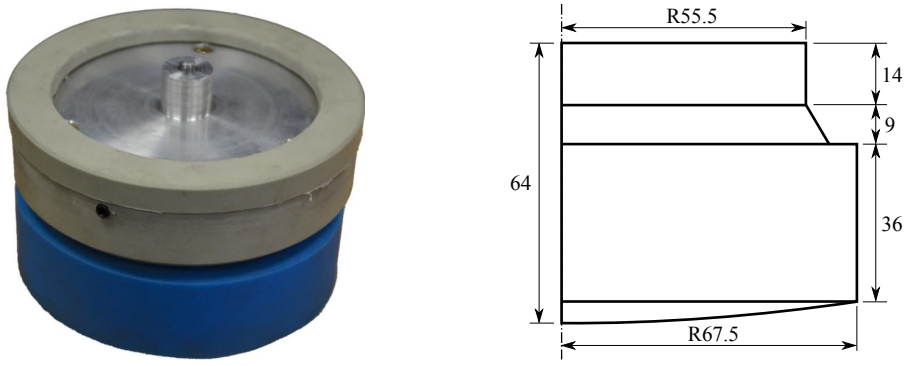

Figure 5.5: Soft indentor for small-scale drop weight test setup: a) photograph, and b) dimensions (in mm) of silicon rubber part.

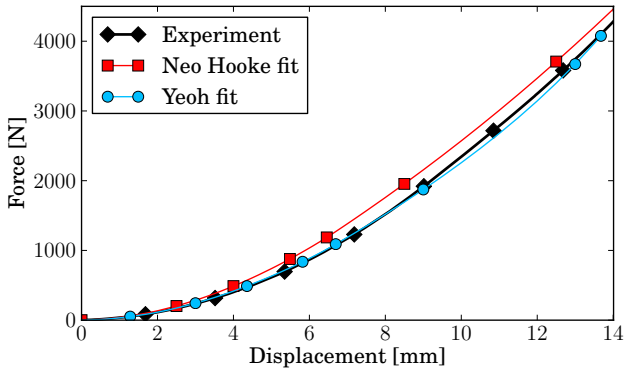

Figure 5.6: Force-displacement curves for compression test and simulations.

it is sufficient to impose boundary conditions on the top surface of the silicon part. The steel plate is modelled as a rigid surface that is fixed in space. The silicon rubber is a nearly incompressible material which is best described by a hyperelastic constitutive law. To avoid volumetric locking, the silicon part is meshed by linear elements in a hybrid formulation in ABAQUS [121]. For the silicon rubber, a bulk modulus of 2.0 GPa is assumed, which is a realistic value for this type of material [214]. Because the test does not measure the shear behaviour of the material, no strain energy potential involving the second invariant of the strain tensor should be used, as recommended by Yeoh [162]. First, a Neo-Hookean material law has been used to find a good fit with the small-strain behaviour of the material. Subsequently, the Yeoh material law is used to find a better fit also at higher deformation. The hyperelastic constants are first estimated and then iteratively evaluated to match the experimental

force-displacement curve. The resulting compressive behaviour is shown in Fig. 5.6 and the elastic constants are given in Table 5.1.

Table 5.1: Hyperelastic constants for silicon rubber ZA22

Material law	C10 [kPa]	C20 [kPa]	C30 [kPa]
Neo-Hooke	110		
Yeoh	94	0	16

5.2.2 Setup of the numerical model

For simulation of the intact laminated glass plate, the axisymmetric representation would be most efficient. However, the LG1 element configuration requires the use of continuum shell elements, which are not available for axisymmetric analysis in Abaqus. Therefore, a three-dimensional model is constructed, similar to the model for smaller monolithic specimens described in Sec. 2.4. The circular test specimens have a diameter of 470 mm; the thicknesses of the glass plies and the Saflex® RB interlayer are 3.9 mm (as measured) and 0.76 mm. The glass is clamped between 3.0 mm thick polypropylene rings with an inner diameter of 460 mm. The numerical model is shown in Fig. 5.7.

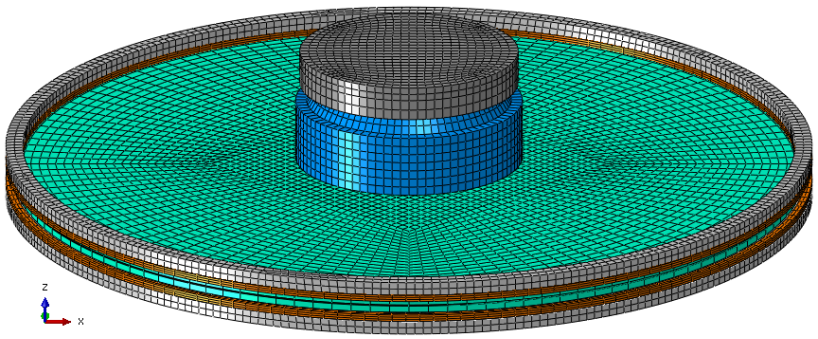

Figure 5.7: Numerical model for drop weight impact on ∅470 mm laminated glass.

The mesh of the laminated glass part is first created in Gmsh for a 2D circle. The different layers of the 3D mesh are then generated with a Python script for all three configurations of Fig. 5.4. For the simulation of elastic, intact response, a structured mesh with a characteristic element length of 5.2 mm is constructed with the transfinite algorithm in Gmsh (similar to the mesh in Fig. 2.40c). No delamination is considered for the intact state, and therefore no cohesive zone is inserted at the interface between glass and PVB. For the configurations LG1 and LG2, two layers of solid elements are used for

the interlayer. The strain in the interlayer material remains small throughout the impact when no breakage occurs. Therefore, the PVB is modelled as linear viscoelastic with the generalised Maxwell model obtained by D'haene and Savineau [173]. The room temperature of 21°C at the time of testing is taken into account by a temperature shift factor $\alpha_T = 0.56$.

The impact is simulated for different drop heights. The impact velocity, as measured for each considered drop height, is given in Table 5.2. Gravity is included as a body load with an acceleration constant of $9.81\,\mathrm{m/s^2}$.

Table 5.2: Impact velocity corresponding with drop height for drop weight impact test on ∅470 mm laminated glass..

Drop height [mm]	Impact velocity [m/s]
250	1.99
350	2.28
450	2.60
550	2.85
650	3.10
1200	4.75

5.2.3 Results and discussion

The simulation results can be compared to the experimentally recorded impactor displacement, deceleration measured by an accelerometer and force measured by the load cell between the indentor and the steel part of the impactor. The deceleration of the impactor is preferred for verification of the model, because it is a measure for the global behaviour of the laminated glass plate and a more sensitive signal than the displacement. Moreover, the deceleration is equal to the force divided by the mass of the 'rigid' part of the impactor, i.e. 7.41 kg. The signals from the accelerometer and load cell are shown in Fig. 5.8. Because the accelerometer signal contains much noise, the accelerations derived from the load cell are used for further comparison.

Also the simulated deceleration of the impactor shows considerable noise, as shown in Fig. 5.9. Therefore, the data is processed by a Butterworth low-pass filter with cutoff frequency of 1.0 kHz.

Fig. 5.10 shows the decelerations for all three element configurations for a drop height of 550 mm. It is immediately apparent that the results of the different mesh configurations produce equivalent results for the elastic response to the impact. In the configuration LG3, the glass is modelled as an equivalent monolithic ply with the thickness of the total laminate, i.e. 8.56 mm. The interlayer membrane has no effect on the response of the laminate when no fracture is

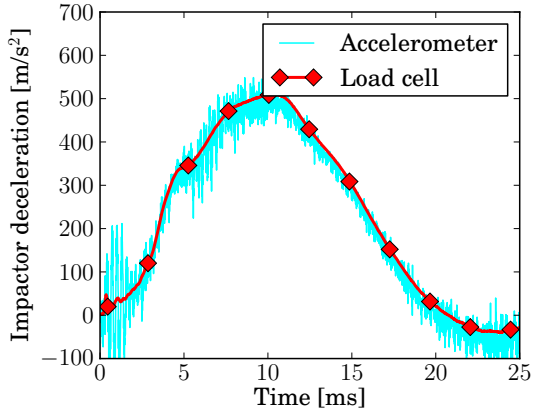

Figure 5.8: Impactor decelerations as measured by accelerometer and load cell for drop height of 550 mm.

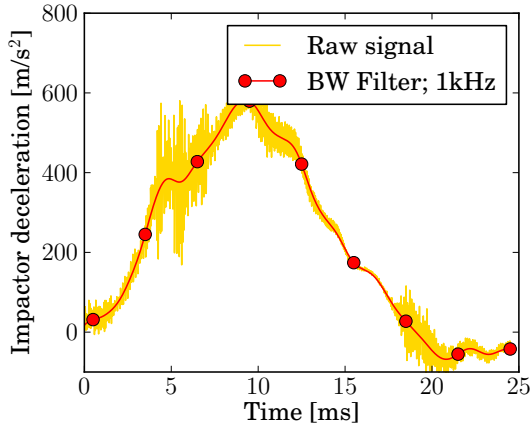

Figure 5.9: Filtering of simulated impactor deceleration signal; curves for LG1 mesh configuration and drop height of 550 mm.

being modelled. Because the responses of the other two configurations (nearly) coincide with that of the LG3 mesh, it can be concluded that the interlayer does act stiff enough under impact at ambient temperatures to consider the laminate as a monolithic glass of the same thickness.
The decelerations for the LG1 mesh are given in comparison with their experimental counterpart at all tested drop heights in Fig. 5.11.

In comparison with the experimental data, the simulated specimens act slightly stiffer: the peak acceleration is higher and the acceleration of the impactor in

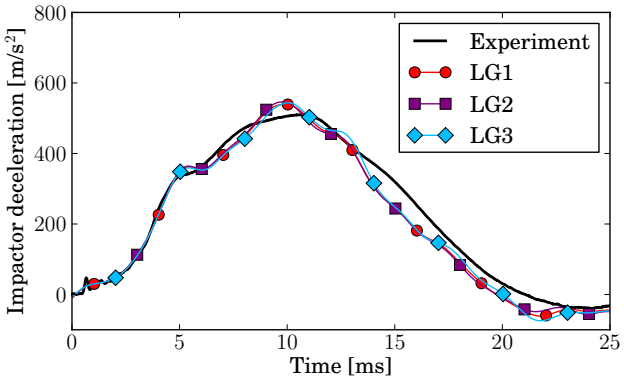

Figure 5.10: Comparison of impactor decelerations for different mesh configurations in drop weight impact for drop height of 550 mm.

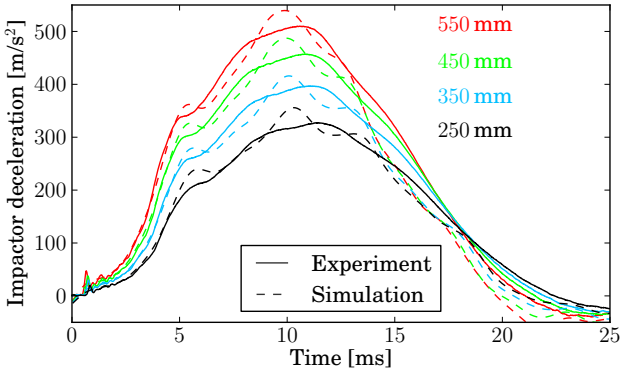

Figure 5.11: Comparison of measured and simulated impactor decelerations for different drop heights in drop weight impact on laminated glass.

the rebound takes place earlier. It can be noted that a high speed camera was used to film the test, requiring the use of high-powered lamps which heat up the specimens as well. The exact temperature of the specimens is not known for these tests, but would have been around 40°C, judging from similar tests. This has its effect on the interlayer stiffness. The difference in deceleration response is shown in Fig. 5.12 for mesh configuration LG1, where the curve at higher temperature better matches the experimental data for the peak acceleration, time of rebound and the first peak at 4.5 ms. The same result is obtained for the LG2 configuration at 40°C, but not for the LG3 mesh which does not capture the influence of the interlayer on the elastic response.

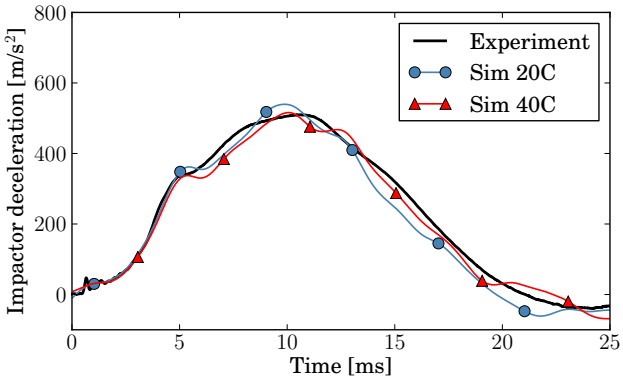

Figure 5.12: Comparison of impactor decelerations for mesh configuration LG1 in drop weight impact for drop height of 550 mm: influence of temperature.

5.3 Simulation of laminated glass fracture

The circular laminated glass plate considered in the previous section remained intact in consecutive impact tests up to a drop height of 550 mm. At a drop height of 650 mm the glass plate on the tension side broke, with a cracking pattern as shown in Fig. 5.13. When the glass breaks, a great number of radial cracks develop very quickly. At a later stage, the central zone of the plate further breaks into tiny fragments.

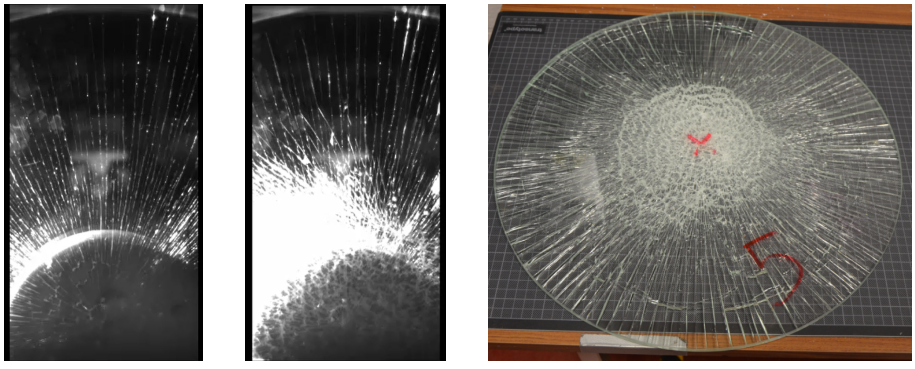

(a) **(b)** **(c)**

Figure 5.13: Cracking of circular laminated glass plate under drop weight impact: (a) & (b) high speed images of crack development (approx. 3 ms between (a) and (b)); (c) photograph taken after test.

Four other test specimens have been impacted from a drop height of 1.20 m, at which both glass plies are broken. The global acceleration response for these panels is shown in Fig. 5.14.

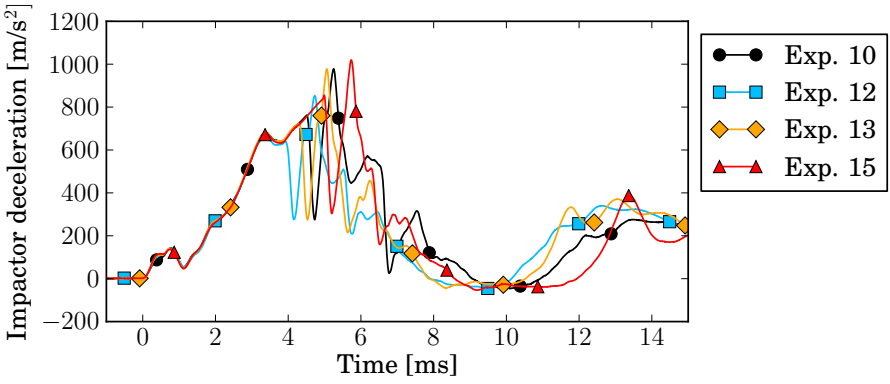

Figure 5.14: Impactor decelerations measured for test specimens under impact from a drop height of 1.20 m.

Unfortunately, no post-mortem image of these test specimens remains available. However, the difference in cracking pattern between single-sided fracture and fracture of both glass plies can be made clear by Fig. 5.15, for drop weight tests with the rigid indentor on square test samples. Where cracking of the bottom ply only is characterised by a great number of radial cracks and an extensively cracked central area, a fully fractured panel typically shows less radial cracks and an amount of concentric cracks around the edges.

5.3.1 Numerical model

These tests can be used as reference to evaluate the correctness and accuracy that can be attained with the element deletion technique for this type of problem. The failure of glass elements is calculated with the crack delay model, developed in Chapter 2. When the glass breaks, the interlayer can reach locally high deformation. Therefore, the hyper-viscoelastic material model for PVB with elastic behaviour as in Fig. 3.22 is applied. Again, the element configurations of Fig. 5.4 are compared against each other and with experimental results. But first, some practical aspects need to be considered in the setup of the numerical models:

- Shell elements have several integration points through the thickness, or *section points*, at which the bending stresses are calculated. In ABAQUS, integration through the thickness can be computed either with Simpson's rule or by Gauss quadrature. The latter results in a smaller error with

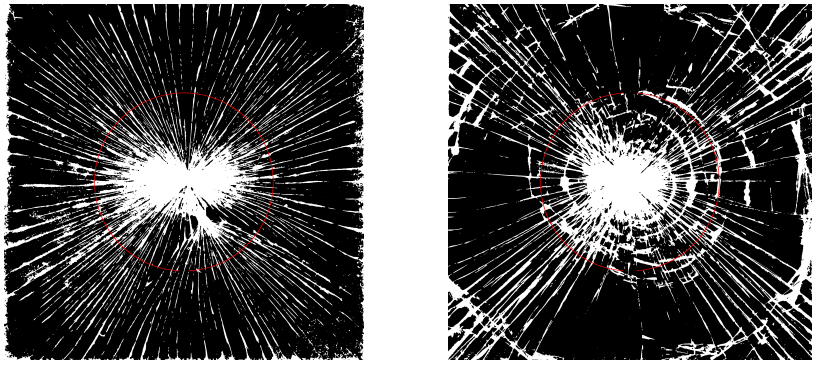

(a) (b)

Figure 5.15: High contrast images of 255 × 255 mm square laminated glass plates with 4 mm thick glass plies and 0.76 mm interlayer under drop weight impact from a drop height of 25 mm: (a) fracture of bottom glass ply, and (b) fracture of both glass plies.

a similar number of section points. However, in the material routine, the critical stress is evaluated not at each location in the thickness of an element, but at the discrete section points. In pure bending, the highest (and lowest) stress is found at the outer surfaces. With Simpson's rule, there is always a section point at these locations, but this is never the case with Gauss quadrature. Therefore, Simpson's rule should be used for shell elements with element deletion. In LS-Dyna, also Lobatto quadrature can be used for the same reason.

- By default, an element is only removed in Abaqus when the failure status is reached at all of its material points. In Chapter 2, solid elements with only a single integration point have been considered, for which deletion occurs immediately. But for shell elements, it is seen that many elements linger with some material points having failed and others still active. In the case of continuum shell elements, the analysis even breaks down by excessive distortions caused in this way. This can be resolved by requiring the element to be removed as soon as failure is reached at one of its section points. To implement this, the `VUMAT` for the crack delay model needs to modified by including the `VUMATXTRARG` subroutine to retrieve the element number for each section point. In the Fortran code, a common array, external to the `VUMAT`, is included to store the status of each element, which is checked at every time increment for each section point.

- The LG2 element configuration uses shell elements for which the nodal surface coincides with the inner surface of the glass plates. A full offset

is used in calculation of the outer surfaces, which are in contact with the frame and the impactor. ABAQUS does not allow the use of MPI parallellisation for surfaces with shell offsets in contact. For larger models, this is a considerable reduction of the computational efficiency.

The mesh topology for the laminated glass part is shown in Fig. 5.16. An unstructured mesh, generated in GMSH, is used with a roughly uniform element length of 3 mm.

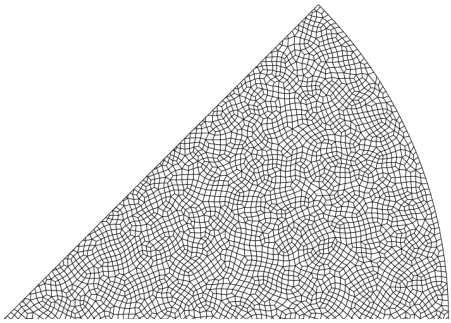

Figure 5.16: Mesh topology for ∅235 mm laminated glass plate; 1/8 shown.

The material properties for glass are given in Table 5.3. These are the same as given before, except for the strength of the glass plate, which has not been determined in the way that it has been for the glass specimens in Chapter 2. Therefore, a generally accepted value is adopted, as described by DIN 18008-4 [215] for glass plates under soft-body impact.

Table 5.3: Material properties for glass.

Young's modulus	E	70 GPa
Poisson's ratio	ν	0.23
Fracture strength	σ_0	81 MPa
Fracture energy	G_{Ic}	8 J/m^2
Max. crack velocity	v_c	1500 m/s
Density	ρ	2500 kg/m^3

5.3.2 Results and discussion

First, the simulations of the test with single ply fracture at a drop height of 650 mm are discussed. In the corresponding LG1 and LG2 models, only the bottom glass ply is allowed to crack, while the top glass plate remains

intact with linear elastic material properties. Because the LG3 configuration represents both glass plies with only 1 shell element through the thickness, single-sided fracture cannot be enforced for this model.

The deceleration of the impactor as simulated with the different element configurations is given in Fig. 5.17, and the corresponding cracking patterns are shown in Fig. 5.18.

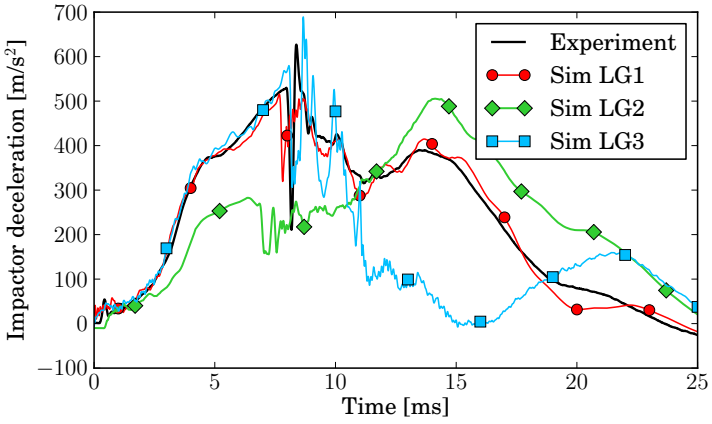

Figure 5.17: Comparison of simulated accelerations with experimental data for drop weight impact test at 650 mm on ∅235 mm laminated glass plate with single-sided fracture.

While the onset of fracture occurs in good correspondence with the experiment for mesh configurations LG1 and LG3, cracking of the LG2 mesh begins much earlier on. The reason for the premature cracking may be found in the large offset used with these elements. The shell offset becomes more significant as the element size decreases, leading to less accurate stress calculation in bending. It is seen that also the initial, elastic response deviates from the other two, while this is not the case in Fig. 5.10.

For the post-fracture response, it is clear that the LG1 simulation is in very good agreement with the experimental measurement. Also the qualitative comparison for the crack pattern matches quite well with Fig. 5.13, showing full fragmentation of the bottom glass plate by radial cracks and an intensely cracked zone at the centre. For the LG3 configuration, it is not possible to model the breakage of a single glass ply. As soon as fracture occurs in this simulation, the resistance of the panel to the impactor drops quickly. After the radial cracks have appeared, the fragments are further bent and broken with concentric cracks that initiate at the top surface.

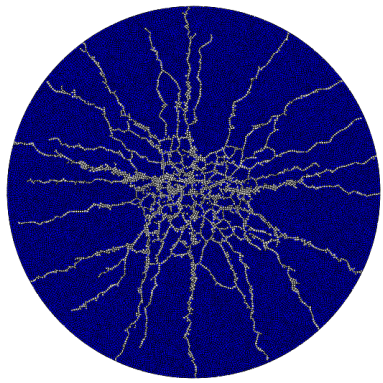

(a) LG1 mesh

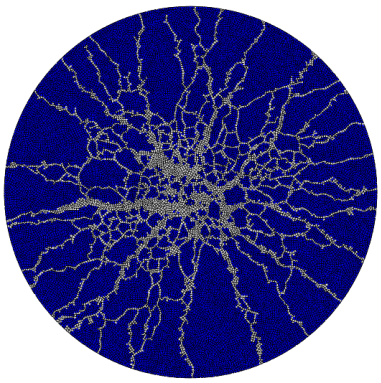

(b) LG2 mesh

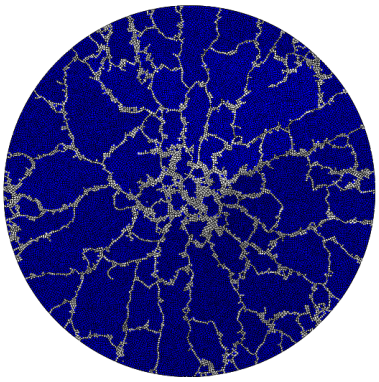

(c) LG3 mesh

Figure 5.18: Cracking of circular laminated glass plate under drop weight impact from 650 mm height: simulated results for element length $L_e = 3\,\text{mm}$.

Thus, all three different mesh types show a quite distinct fracture response. To ascertain the consistency thereof, the simulation is repeated with a finer mesh for the LG1 and LG3 element configurations, with characteristic element length of 1.5 mm. The LG2 mesh is not further considered as it does not seem to be capable of proper stress prediction and requires a high calculation time due to being limited to 1 CPU.

The refined mesh is constructed by the same procedure and has an unstructured mesh topology as well. The resulting response for the LG1 and LG3 configurations is given in Fig. 5.19 and 5.20. These figures show that the global response of the models is consistent when refining the mesh, even though the resulting crack pattern cannot be exactly the same.

Although the single-sided fracture of a laminated glass plate is an interesting

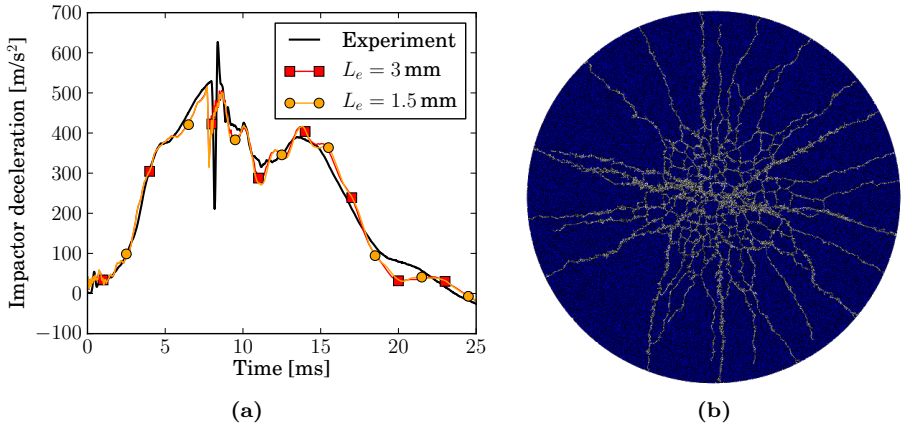

Figure 5.19: Response of LG1 element configuration for drop weight impact at 650mm on ∅235 mm laminated glass plate with single-sided fracture: (a) impactor deceleration, and (b) crack pattern for refined mesh; $L_e = 1.5\,\text{mm}$.

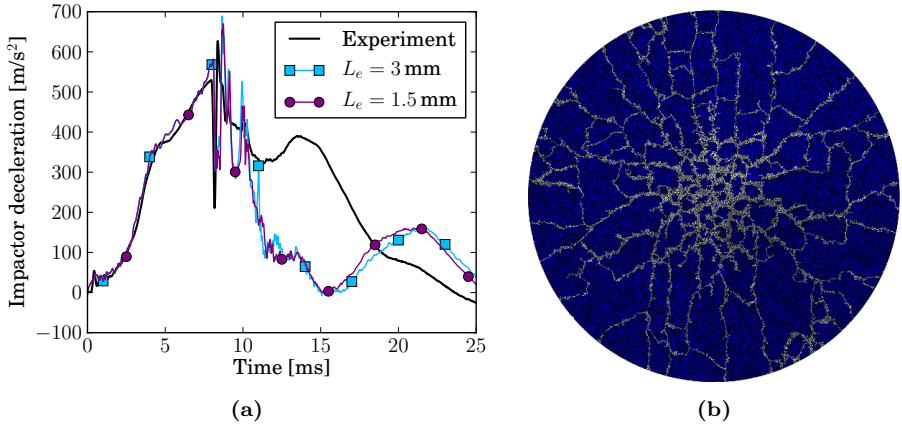

Figure 5.20: Response of LG3 element configuration for drop weight impact at 650mm on ∅235 mm laminated glass plate: (a) impactor deceleration, and (b) crack pattern for refined mesh; $L_e = 1.5\,\text{mm}$.

study case, our main interest goes out to the simulation of fracture in both glass plies of the laminate, where the interlayer dominates the post-fracture response. Therefore, the drop weight impact simulations are repeated for a drop height of 1.20 m. The resulting impactor decelerations are given in Fig. 5.21, where the experimental curve is representative for the average response, given by Experiment 3 in Fig. 5.14. The corresponding cracking patterns are shown in Fig. 5.22.

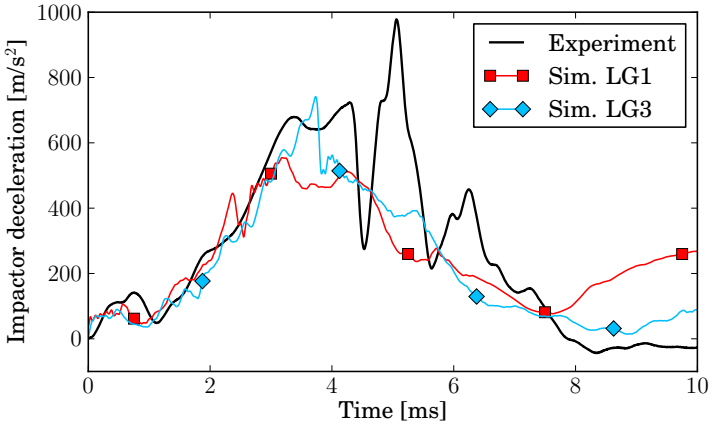

Figure 5.21: Comparison of simulated accelerations with experimental data for drop weight impact test at 1.20 m on ∅235 mm laminated glass plate.

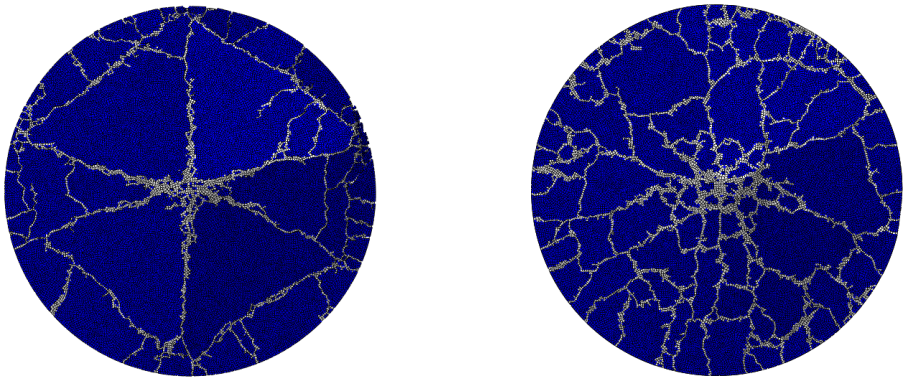

(a) LG1 mesh **(b)** LG3 mesh

Figure 5.22: Cracking of circular laminated glass plate under drop weight impact from 1.20 m height: simulated results (bottom view) for element length $L_e = 3\,\text{mm}$.

In both simulations, fracture takes place earlier than in the experiments, which shows that the strength of the test specimens must have been higher than the critical stress of 81 MPa given by DIN 18008-4 [215]. The loading rate for the impact at 1.20 m is roughly $19 \cdot 10^4$ MPa/s, while this is $11 \cdot 10^4$ MPa/s for a drop height of 0.65 m. With reference to Fig. 2.4, the difference in strength is attributed to the natural variability of glass strength, rather than its rate-dependency. For the simulations, it is also notable that the critical stress is not reached at the same moment for the LG1 and LG3 models. Other than that,

the resisting force of the simulated broken panels on the impactor decreases steadily, but not immediately, which is also seen in the test data. However, for all experiments in Fig. 5.14, the acceleration response shows a peak shortly after the specimen is broken.

The cracking pattern for the LG1 mesh shows significant differences in comparison with the single-sided fracture at a lower drop height: fewer radial cracks are formed and the cracked, central zone is more concentrated. Instead, the plate is further cracked by concentric cracks around the edges. The breakage of the LG3 mesh is similar in appearance as for the drop height of 650 mm and shows more cracking overall in comparison with the LG1 model. It is not easily determined how this difference affects the global response for both models. The most notable difference is seen from $t = 8$ ms on in the acceleration response shown in Fig. 5.21, where the broken plate is in the return stroke and again exerts a higher force on the impactor for the rebound. This takes place earlier for the LG1 model, implying that the LG1 model behaves stiffer in its broken state than the LG3 model.

The numerical simulation for the LG1 element configuration is repeated with an increased fracture strength of 110 MPa. The resulting impactor deceleration and cracking pattern are given in Fig. 5.23. The time of breakage for this simulation is closer to the experiment, as well as the rate by which the force exerted on the impactor decreases. However, the return stroke of the panel, marked by a new rise in the acceleration signal, still takes place earlier: around 9 ms after the impact in the simulation, versus 11 ms for the experiment. This indicates that the elastic stiffness of the broken laminate is overpredicted in the simulation. It could be argued that the hyper-viscoelastic material model for the PVB interlayer overestimates the stiffness at the lower range of strain rates, in combination with the fact that far fewer cracks are formed in the simulation than in reality.

Finally, the energy distribution during the impact event is given in Fig. 5.24 for the simulation with the LG1 mesh and a strength of 110 MPa. The quick release of strain energy upon fracture of the laminated glass plate translates into dissipation as fracture energy and damping of stress waves in the material. Further energy absorption occurs by friction and viscoelastic dissipation by relaxation of the interlayer material. In Abaqus, the latter is included in the curve for the strain energy. However, the kinetic energy, strain energy and dissipations in Fig. 5.24 only add up to 83% of the total energy by the end of the simulation. The remaining portion of the energy is consumed by hourglass and distortion control, used in the solver to maintain stability and reduce further error in the analysis. This may also have an influence on the simulated post-fracture response, although it is not plainly determined what the effect can be.

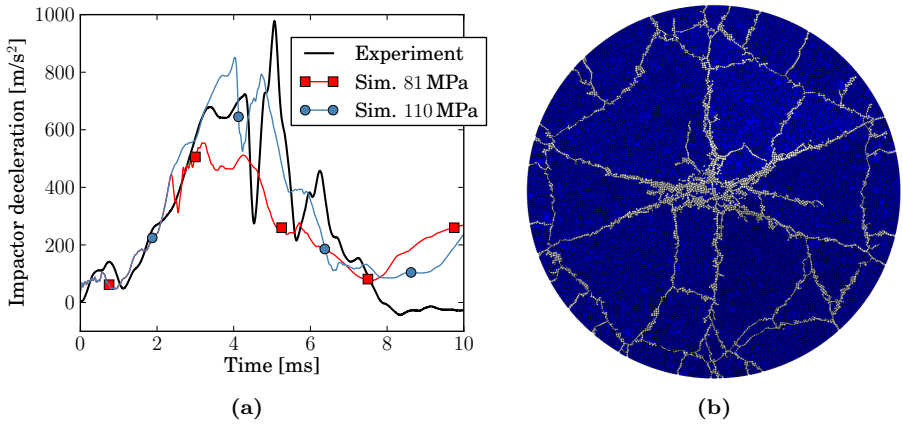

Figure 5.23: Response of LG1 element configuration for drop weight impact at 1200mm on ∅235 mm laminated glass plate with single-sided fracture: (a) impactor deceleration, and (b) crack pattern for increased fracture strength $\sigma_0 = 110\,\text{MPa}$.

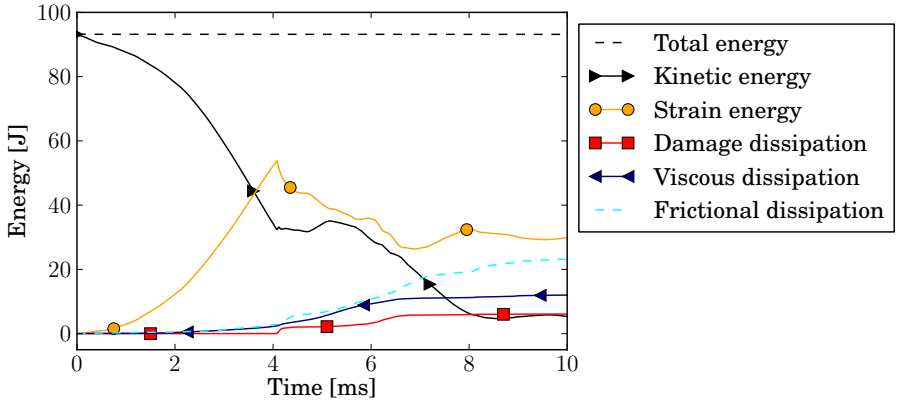

Figure 5.24: Energy balance for LG1 mesh with crack delay model for drop weight impact at 1200mm on ∅235 mm laminated glass plate.

5.4 Conclusions

Three different configurations to model laminated glass have been evaluated with use of the crack delay model and the material model for PVB interlayer that has been conceived in Ch. 3. The intact, elastic responses for all configurations correspond very well with each other, and fairly well with the experimental test data. It is most notable that a simplified representation of the laminate with a single shell of equivalent, monolithic thickness and elastic

properties of glass behaves the same elastically as other representations that do take account of shear transfer by the interlayer. It can be concluded that the PVB interlayer, at low to moderate temperatures, reacts sufficiently stiff to impact loads to assume monolithic behaviour of the laminate.

The differences between the three element configurations become clear when the laminated glass plate breaks. The configuration with full shell offsets (LG2) is not capable of accurate stress calculation at the outer surfaces and reaches the strength criterion prematurely. The other two configurations predict the onset of fracture at a moment close to breakage in the experiment with single-sided fracture at a drop height of 650 mm, with the glass strength being defined as in the standard DIN 18008-4 [215]. This is no longer true for the simulations of impact from a drop height of 1.20 m, where the assumed fracture strength appears too low. Also in the corresponding experiments, there is no one single value for the strength. Yet, the fracture strength remains the singlemost defining factor for the response of a laminated glass panel to the impact. Nonetheless, only a prescribed value can be used when the aim of the numerical model is to make a prediction of the post-fracture response.

Cracking and fragmentation of the glass occurs very quickly with the crack delay model in the simulations, as it does in reality. Especially the configuration with continuum shells (LG1) shows good correspondence for the cracking pattern and sequence in both one- and two-sided glass fracture. The configuration with one shell and one membrane element (LG3) cannot model single-sided fracture, but also captures the cracking of the plate fairly well for the higher drop height.

For single-sided fracture, the continuum shell model shows very good correspondence with the experimental acceleration (and force) data that characterise the global response. For a higher drop height and fracture of both glass plies, the LG1 and LG3 models show a similar post-fracture behaviour with steady decrease of the resisting force of the broken panel to the impactor, at a similar rate as in the test data. However, the return stroke takes place earlier in the simulations, indicating a stiffer response. This could be attributed to the lesser extent of fracture in the numerical simulations, which is most clearly seen for the LG1 models.

Delamination at the glass-PVB interface has not been considered for the drop weight impact, because repeated experiments by Van Dam with different adhesion grade interlayers did not show any discernable influence thereof [6]. For heavy blast loads, both Van Dam and Kuntsche [7] do note different behaviour for high and low adhesion level PVB. Numerical models that include a cohesive zone at the interfaces will be evaluated in the respective chapter. However, in anticipation it can be noted that the mesh sizes required for the peel and TCT models are not practically achievable for full-scale impact and blast simula-

tions. Also, because of the relatively large gaps left by deleted elements, the underlying PVB elements may not reach very high strains by which tearing could be predicted.

Chapter 6

Safety glass under soft body impact: EN 12600

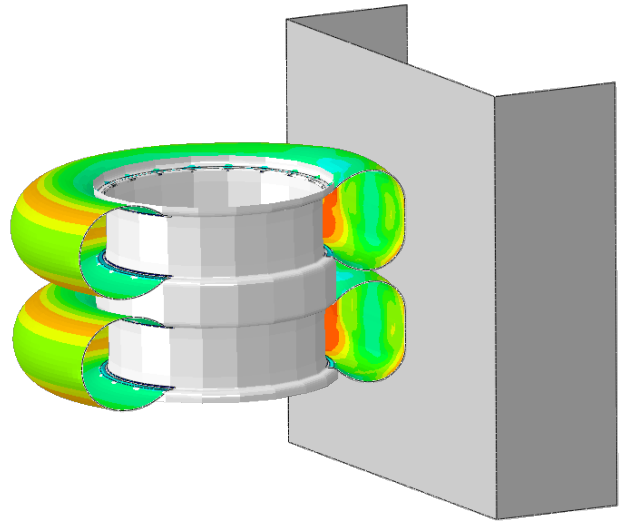

Simulated soft-body impact of twin tyre pendulum setup against rigid wall.

6.1 Introduction

Safety glass has been defined as a glazing composition that reduces the chance of injury upon accidental human impact. Severe and life threatening injuries may be caused by propulsion of sharp glass fragments or in penetration of a window pane. Other accidents may be caused by the collapse of a structural glass element, for example by failure of a glass balustrade or floor. For this reason, several qualification standards have been developed to assess safe response of a glass window when impacted by a human body at a certain speed.

In qualification of automotive windshield, it is common practice to closely mimic the most likely scenario by use of human-like objects. For assessment of human impact from inside the vehicle, crash test dummies are placed in the seats and the vehicle is propelled towards a rigid wall or another vehicle. In Europe, such tests are described by regulations ECE R-33 [216] and ECE R-94 [217]. However, these regulations do not focus on the windshield, but collect data directly from a crash test dummy: acceleration of the head, tensile and shear forces at the neck/head interface and deflection between sternum and spine. Consequently, the entire inside of the car is evaluated: the windshield, but also the airbags, seatbelts, dashboard and steering column.

A testing method directly applicable to automotive windshield is described for pedestrian head impact by the EEVC [218]. A headform impactor, with accelerometer fitted inside, impacts the windshield with a prescribed speed of 40 km/h and at an angle of 65° with ground level. This testing method is not a required qualification standard, but is taken into account in the Euro NCAP safety rating system. Fig. 6.1 shows the impact experiment and the corresponding simulation, where the headform is modelled accurately. In fact, detailed finite element models of crash test dummies and pedestrian headform impactors are made available by both LSTC and SIMULIA for crashworthiness simulations.

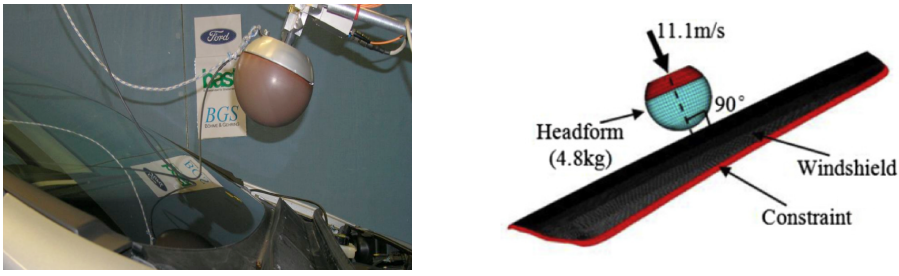

(a) **(b)**

Figure 6.1: Test for pedestrian headform on windshield: (a) EEVC crash test, and (b) finite element simulation (Figure from Peng et al. [116]).

This test has been the subject of study by Zhao et al. [219], Timmel [104], Liu et al. [115] and Peng et al. [116], who all used detailed finite element models of test dummies and pedestrian headform impactors for crashworthiness simulations. In such impact event, fracture of the windshield is beneficial in achieving lower accelerations experienced by the headform. Of course, the headform should not pierce the windshield and glass debris should be avoided as much as possible.

In the construction industry, regulations focus on the impact performance of the glass component directly, rather than the forces experienced by the impacting human body. In the past, the shotbag impact test, described by ANSI Z97.1 [220] was accepted worldwide as a safety standard for window glass. This test method consists of a rigid clamping frame with internal width of 845 mm and internal height of 1911 mm and a 45 kg shotbag covered with a loosely draped cloth towel. The shotbag itself is a leather punching bag (type Everlast 4207) filled with lead shots (see Fig. 6.2), proposed as a reasonable simulator for whole-body human impacts [221].

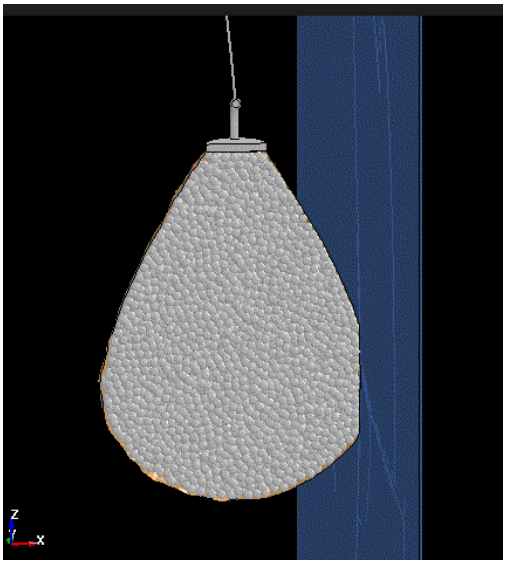

Figure 6.2: Shotbag simulation in LS-DYNA using DEM for the lead shots (Figure from Lancemore Co.)

However, this test method received criticism for doubts over its reproducibility and changing characteristics of the shotbag over time, as demonstrated by Balkow et al. [222]. In Europe, the shotbag impactor has in the meantime been abandoned in favour of a twin-tyre impactor, shown in Fig. 6.3, in the European norm EN 12600 [8]. This norm describes the impactor as a 50 kg mass, consisting of a rigid deadweight surrounded by two tyres that are inflated to 3.5 bar. The test specimens have a size of 876 × 1938 mm and are clamped

on all sides between 10 mm thick rubber linings that should be compressed by 10% when a test panel is installed.

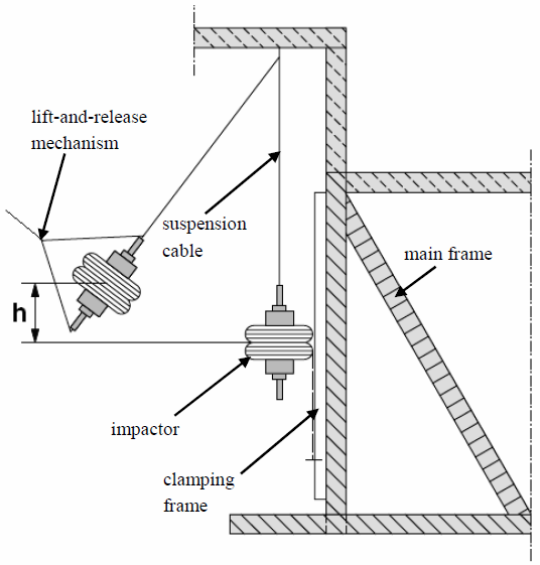

Figure 6.3: Concept drawing of the pendulum impact test setup (Figure from EN 12600 [8]).

Qualification of glazing by this test can become time-consuming and costly. Therefore, in Germany, the TRAV [223] prescribed the design method for defined glass sizes and only required experimental testing with the twin-tyre impactor for deviating glass components. The most recent German norm, DIN 18008-4 [215], now also allows the calculation by either a simplified method or by numerical transient analysis for the geometry and support conditions of the final design. Leading up to this norm, several researchers have drafted validated numerical models for simulation of the impact up to glass breakage. In Schneider [224], and also Müller de Vries [225], the tyres are represented by volume-filling solid elements which are given a Young's modulus that corresponds to the observed stiffness of the tyre for a certain drop height. This approach receives the criticism that simulation results are matched rather than predicted and that they cannot be extrapolated to other glass setups than those for which the model has been validated. Brendler et al. [226] and later Schneider et al. [212] took account of the pressurized air volume in the tyres, but did not yet model the fibre reinforcement in the rubber.

This chapter introduces a numerical representation for the tyres with their actual material properties, which is to be more generally valid. Given the amount of experimental data that exists for this test, such model can further

be used to compare and establish a reliable technique to simulate laminated safety glass into the post-fractured state. In Section 6.2, a model for the tyres is conceived by thorough characterisation of their composition. In the next section, the tyre model is evaluated for the impact against a quasi-rigid plate, in comparison with experimental results. Section 6.4 discusses the verification of the pendulum impact model for repeated impacts on intact glass panels. Simulations of laminated glass specimens that are fractured under the soft body impact are presented in Section 6.5.

6.2 Characterisation and numerical model of the tyres

The tyres used for the pendulum impactor are STARCO TR13 ST11 3.50-8 4PR bias-ply tyres with round section and flat longitudinal tread. The typical build-up of such tyre is shown in Fig. 6.4. The tyres consist of nylon body ply cords, rubber side walls and tread, and steel bead wires. The characteristics of the tyre, necessary for conceiving a numerical model, are not shared by the manufacturer. Therefore, experiments are conducted to look into the mechanical properties of the tyre and its components.

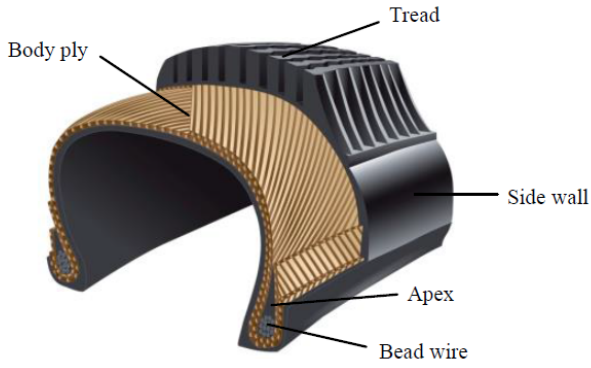

Figure 6.4: Section sketch of a bias-ply tyre (figure courtesy of ClassicTrucks.com).

6.2.1 Material properties

The nearly incompressible rubber material is best characterised by a hyperelastic material law, as large deformation can be expected. The measured Shore-A hardness of 59.5 roughly corresponds to Mooney-Rivlin constants $C_{10} = 0.464\,\text{MPa}$ and $C_{01} = 0.116\,\text{MPa}$ [227]. The bulk modulus of rubber is typically about 2 GPa [214]. This initial estimation proves to be sufficient,

as the simulation results are relatively insensitive to perturbation of rubber material properties. More attention should be given to the nylon reinforcement cords which are placed in the tyre as two angled plies. Micro-CT imaging has been used on a cut-out section of the tyre to reconstruct the geometric configuration of the nylon plies in the rubber matrix. An image of the resulting 3D model is shown in Fig. 6.5. The angle between two nylon cord layers is

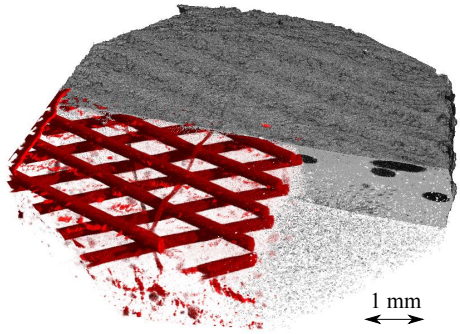

Figure 6.5: Micro-CT image of a cut-out section of bias-ply tyre as used in the pendulum impact test: angled nylon plies in rubber matrix.

60° and their diameter is 0.45 mm. The spacing between the individual nylon wires is 1.60 mm. To determine the Young's modulus of the nylon PA6 cords, a tensile test is executed on a single nylon wire to obtain its stress-strain curve. Four samples were tested, showing a Young's modulus $E = 1.39\,\text{GPa}$. The mechanical properties of the tyre materials are given in Table 6.1.

Table 6.1: Material properties for bias-ply tyre

	Density	Stiffness	Poisson ratio
Steel	$7850\,\text{kg/m}^3$	$E = 210\,\text{GPa}$	$\nu = 0.30$
Nylon	$1400\,\text{kg/m}^3$	$E = 1.39\,\text{GPa}$	$\nu = 0.30$
Rubber	$1100\,\text{kg/m}^3$	$C_{10} = 0.464\,\text{MPa}$	
		$C_{01} = 0.116\,\text{MPa}$	
		$K = 2.0\,\text{GPa}$	

6.2.2 Axisymmetric model

First, an axisymmetric model of the tyre and rim is made to efficiently simulate the mounting and inflation. The resulting stress and displacement fields can subsequently be extrapolated to a full 3D model for further analysis.

The geometry of a symmetric tyre section is drawn in its unstressed state, as shown in Fig. 6.6a. This model is discretised by a finite element mesh of 931 axisymmetric elements, using continuum elements for both the rubber compound and the steel bead wires. Hybrid element formulation is used to prevent volumetric locking for the nearly incompressible rubber material; this formulation includes a hydrostatic stress distribution as additional unknown which must be calculated simultaneously with the displacements. The nylon cord plies can be modelled in ABAQUS by use of a rebar layer, embedded in the elements of the rubber compound [228]. One rebar layer can represent multiple orthotropic reinforcement plies of different materials, thickness, spacing and orientation. In the case of the bias-ply tyre, two equal nylon cord plies are assigned with orientations $+30°$ and $-30°$ with respect to the meridional direction.

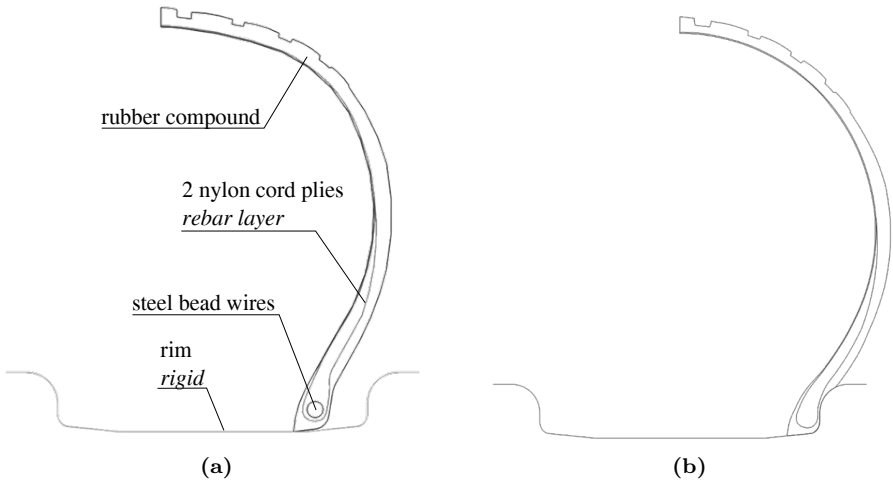

Figure 6.6: Axisymmetric model of bias-ply tyre: (a) initial, unstressed state and (b) after mounting and inflation.

Contact surfaces are defined between the tyre and the rigid rim to allow for frictional sliding during the mounting and inflation stages. An exact value of the frictional coefficient would be difficult to determine due to its dependency of several parameters [229], such as temperature, contact pressure, surface roughness, etc. For this reason, the frictional coefficient μ_f is estimated at 0.7. Figure 6.6b shows the simulated deformation after inflation to 3.5 bar, as prescribed by the standard EN 12600.

Additional simulations with $\mu_f = 0.5$ and $\mu_f = 0.9$ show that variation of the frictional coefficient only has a minor effect on the result. Only the displacement of nodes in the contact zone may vary in the order of 0.1 mm, while nodes away from the contact zone remain relatively unaffected.

6.2.3 Three-dimensional model

A detailed solid model is conceived through Symmetric Model Generation (SMG) in ABAQUS. In essence, the SMG revolves the nodes of the axisymmetric model at regular offsets and connects them to form a 3D continuum elements mesh. The stress and deformation state of the mounting and inflation for the axisymmetric model can easily be transferred to the new 3D model. Three different levels of mesh refinement are studied, for which the characteristics are given in Table 6.2.

For simulation of the impact event using an explicit solving scheme, a more efficient 3D model is preferred. This model is constructed using shell elements with rebar layers defined for the nylon cord plies and the steel bead wires. The shell element thickness is taken to be constant and equal to the sidewall thickness measured on the tyre, i.e. 3.0 mm. Further simplification is required for the implementation of the rebar layers; see Fig. 6.7. Two rebar layers are defined for the nylon cord plies, each at a constant offset from the shell middle surface. An extra rebar layer for the steel bead wires is placed near the inner diameter of the tyre, with 9 wires of 1.0 mm thick. For this model as well, three different levels of mesh refinement are studied. The element length is refined in both meridional and concentric directions.

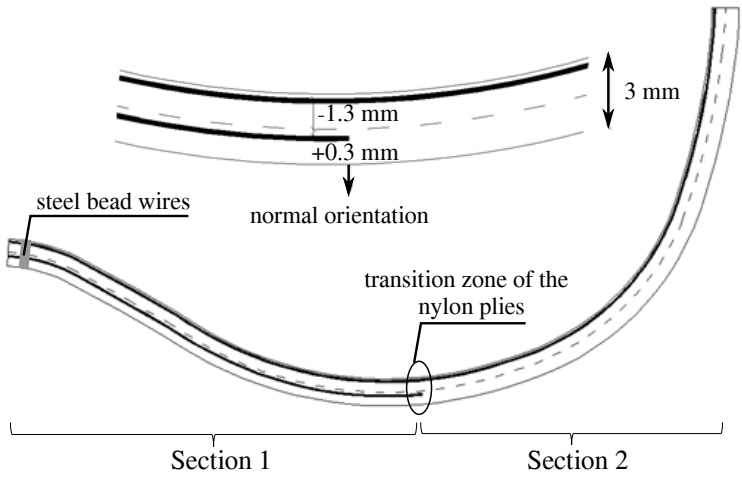

Figure 6.7: Definition of rebar layers and steel bead wire in the efficient shell model of the tyre.

A compression test is performed on the tyre, using an Instron 5800R electromechanical testing bench. The tyre is inflated to 3.0 bar and placed between two rigid plates, as in Fig. 6.8. The upper plate moves downward at a constant rate of 1.0 mm/min, while the force is measured. Three experiments were per-

Table 6.2: Mesh properties for 3D models of the tyre

	Segments in concentric direction	Number of elements
Solid model	90	95,115
	180	201,063
	720	794,397
Shell model	90	2,880
	180	10,440
	720	40,320

formed at this testing speed, for which the average force curve is shown in Fig. 6.9. The maximum standard deviation is 10.2 N.

The numerical model attempts to simulate compression of the tyre closely to the experiment. The simulated tyre is also brought to 3.0 bar internal pressure and placed between two rigid plates. The frictional coefficient between the plates and the rubber is again assumed $\mu_f = 0.7$. The compression of the tyre is computed by the implicit solver ABAQUS/Standard. Fig. 6.8b shows the deformation of the detailed solid model with a 180 segments mesh.

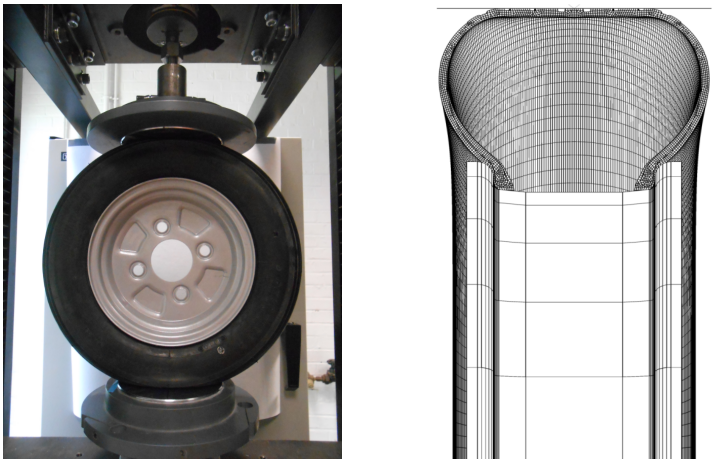

(a) **(b)**

Figure 6.8: Compression test of bias-ply tyre at 1.0 mm/min: (a) experiment and (b) cut view of simulation.

The resulting force vs. displacement relations of Figure 6.9 show that both the detailed and efficient shell models with a sufficiently fine mesh correspond well to the experiment. The shell model with 180 segments is further used for impact simulation.

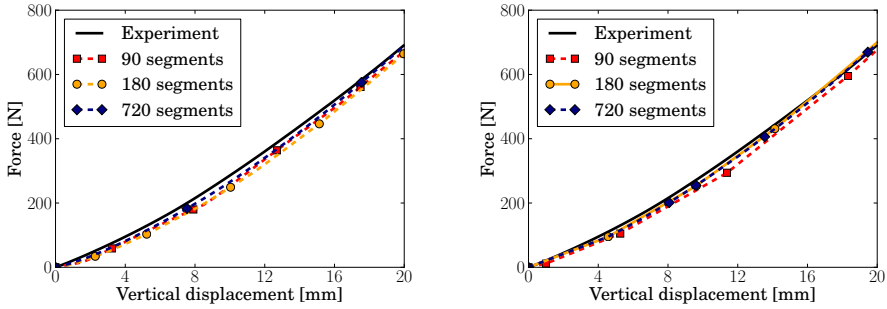

Figure 6.9: Force vs. displacement for compression test of the bias-ply tyre: mean experimental curve and simulated results for (a) solid models and (b) shell models.

6.3 Impact against a quasi-rigid plate

To validate the numerical model, experiments are performed by dropping the pendulum impactor on a force plate and pressure plate setup. This setup is employed as a variation on the drop test against a rigid wall performed by Schneider [224] and Müller de Vries [225], but allowing for more detailed measurement of the impact. Further validation is later established for impact against a 10 mm tempered glass plate, as described for calibration in EN 12600 [8].

6.3.1 Test setup

Force and pressure plate setups are more commonly used in the field of sports biomechanics. They are used in this study to measure the impact forces and to provide an image of the tyre footprint and its pressure distribution during contact. The force plate is of the type KISTLER 9281 B11 and has dimensions of $0.6 \times 0.4 \times 0.1$ m. It is characterized by a high rigidity, implying minimal deflections, and is used in combination with an 8-channel charge amplifier Type 9865E. The force plate is connected to an electronic unit which converts the electrical charges yielded by the force transducers into electrical voltages. Eight transducers allow calculation of the in- and out-of-plane forces. The calibrated range of the vertical force lies between 0 and 20 kN. The pressure plate is a RSscan International Hi-End footscan system with dimensions 0.58×0.42 m. It consists of 4096 sensors, arranged in a 64×64 matrix, and sensor dimensions 7.62×5.08 mm. The measurable pressure range lies between 1 and 127 N/cm^2 and the maximum data acquisition frequency is 500 Hz.

The force and pressure plate are mounted to an already existing test rig, which

is built as described by the European Standard EN 12600. The measurement plates are attached to a 9.8 mm thick steel plate, fixed to the backside of the rear clamping frame. The test setup then looks as in Fig. 6.10a. It should be noted that the impactor and the pressure plate are not in contact when the impactor is at rest. Instead, there exists a gap over a horizontal distance of 147 mm. Consequently, this offset needs to be accounted for in the numerical model as well.

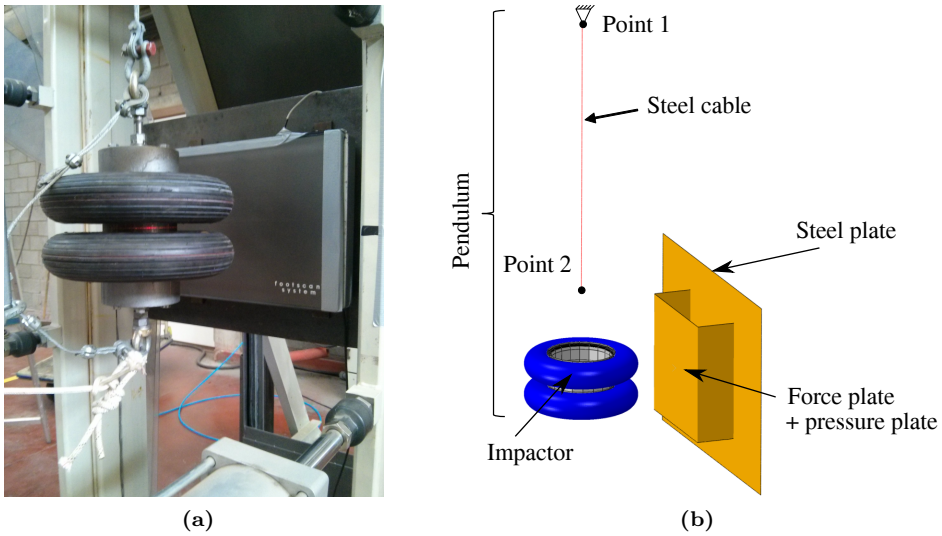

Figure 6.10: Twin-tyre pendulum impact setup with force and pressure plate: (a) experimental setup and (b) FE model representation.

6.3.2 Numerical representation

Fig. 6.10b shows the finite element model of the impact test setup. The impactor consists of two tires and a steel cylinder, and has a total mass of 50 kg. Both tyre models consist of 10,440 elements, as described in Section 6.2. The inertia of the steel cylinder is allocated to a reference point in its gravitational centre. This reference point inside the impactor is coupled to Point 2 on Fig. 6.10b, where the impactor is hinged to a steel cable. Point 1 is at the location of the hinge that is connected to the frame, and its position is held fixed throughout the simulation. The steel cable is discretised by 1000 linear, 2-node truss elements.

Both measurement plates and the steel plate to which they are connected are modelled as in Fig. 6.10b. The force and pressure plate are assumed as rigid, while the steel plate is not. During the tests, it has been observed that the steel plate vibrates upon impact. Therefore, the steel plate is meshed by deformable

shell elements and its vertical edges, which in reality are bolted to the frame, are assigned fixed boundary constraints.

The numerical analysis proceeds in two steps. First, the stresses and deformation of the tyres by inflation to 3.5 bar are calculated with the implicit solver. Subsequently, the impact is simulated, in which the internal pressure and volume of the tyres is governed by the ideal gas equation of state for air in the fluid cavities:

$$\rho(p,T) = \frac{p + p_A}{R(T - T_A)}, \tag{6.1}$$

where $\rho(p,T)$ is the fluid density at the current pressure and temperature, p_A the ambient pressure, p the gauge pressure and $p + p_A$ the absolute pressure. $R = 8.3144\,\mathrm{J/Kmol}$ is the universal gas constant, T the temperature and T_A is the absolute zero temperature.

At the start of the impact analysis, the pendulum impactor, then at its lowest point, is given an initial angular velocity ω_0. This velocity corresponds to the drop height and can be calculated by Eq. 6.2.

$$\omega_0 = \sqrt{\frac{2gh}{L^2}}, \tag{6.2}$$

where h is the drop height, L the length from the fixed hinge to the centre of gravity of the impactor, and g is the gravitational constant. The gravitational acceleration is also taken into account during the impact simulation.

6.3.3 Comparison of simulation and test results

In Fig. 6.11, the experimentally measured impact force is compared with the numerical result for different drop heights. Differences up to 11.1% and 13.5% are observed for the maximum force and corresponding impact time respectively, not including the 20 mm drop height. This deviation most likely has its origin in the experimental testing procedure. The positioning of the impactor to its correct drop height can only be realized with an accuracy of a few millimeters. For small drop heights, the error margin will therefore be larger.

In Fig. 6.12, the contact pressures are compared for impact from a drop height of 700 mm, at the time when the impact force peak is observed, i.e. $t = 24\,\mathrm{ms}$. In general, this study shows that the detailed model is capable of simulating the impact quite realistically, though slightly underpredicting the load. It should be kept in mind that these results have been obtained with a single impactor model that aims to capture the physical properties of the tyres and not by calibrating the model again for every drop height.

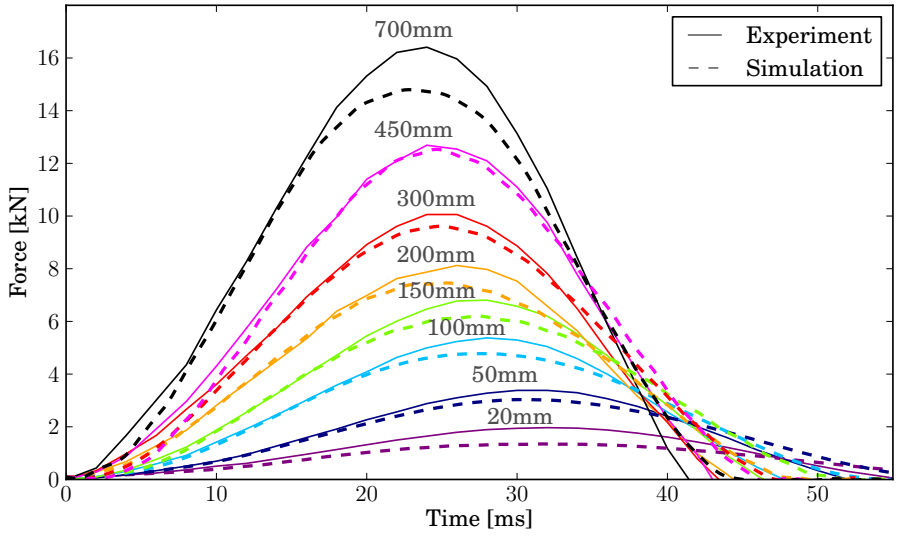

Figure 6.11: Comparison of experimentally measured and simulated impact forces for different drop heights of the twin-tyre pendulum impactor.

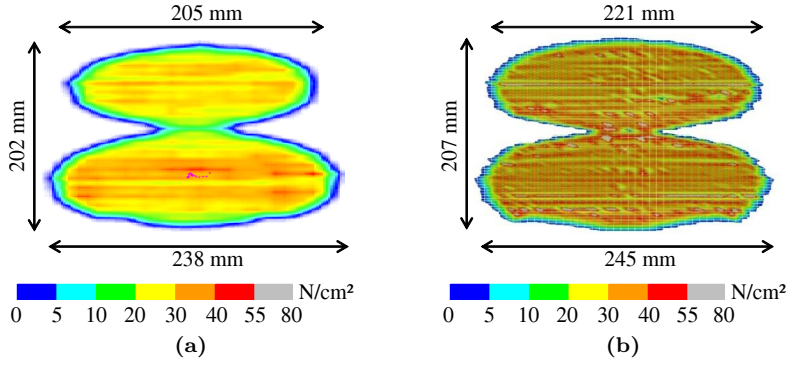

Figure 6.12: Comparison of tyre footprints for a drop height of 700 mm at $t = 24.0$ ms after impact at a drop height of 700 mm: (a) experimental measurement and (b) simulated result.

6.4 Elastic response of glass under impact

Two types of glazing are considered in this section. The first is a monolithic, tempered glass plate that serves as a calibration plate. For this test, the required characteristics of the impact response are described in the EN 12600 standard. The other glass plates are laminated with Saflex® PVB interlayer.

6.4.1 Tempered calibration plate

This setup is fully described by the European Standard EN 12600 [8]. The test plate is a thermally toughened (fully tempered) soda lime silicate glass panel with dimensions of $876 \times 1938 \times 10$ mm. Such panel is required by the standard for calibration of the test rig. The glass panel is clamped between two rigid, steel frames with a 10 mm thick rubber lining of hardness 57 IRHD. When clamped, the rubber strips are to be compressed by 10% of their thickness.

The test rig is calibrated when the maximum strains upon impact, measured in the middle of the test plate, are within prescribed boundaries for each corresponding drop height. Impact testing is performed for drop heights up to 700 mm. The tempered glass plate is not supposed to break during this test. The mechanical properties of the glass are as given in Table 2.1.

The numerical model of the impactor used in these simulations is the same as in the previous sections. Where an initial offset of 120 mm existed between the tyre contact area and the pressure plate, the tyre and glass plate are now 'just touching'. The glass plate is meshed with 10×10 mm reduced linear shell elements. The steel frames are considered rigid, and the 10 mm thick rubber strips are meshed with hexahedral continuum elements. The compressive clamping of the glass plates is simulated in a separate analysis step that precedes the impact simulation. In this step, both frames are moved towards each other by 1 mm each, thus compressing the rubber strips by 10%. The rubber is characterised by a Mooney-Rivlin law, with constants $C_{10} = 0.417$ MPa and $C_{01} = 0.104$ MPa, as derived from the rubber hardness according to Altidis et al. [227], and bulk modulus $K = 2$ GPa.

The horizontal and vertical strains were measured at the centre of the glass plate by use of strain gauges. Figure 6.15 shows the maximum strains in the experiment and in the simulation, along with the boundaries prescribed by the standard, for different drop heights.
The measured strains are slightly lower than required by the standard. This might be ascribed to a slight deviation from the standard in the design of the impactor, in the sense that a part of the deadweight is located between the two rims to avoid bending of the central axle. In the standard, the deadweight is divided in parts above and below the rims, but not in between. This makes no difference for the centre of gravity of the impactor, but the rotational inertia is

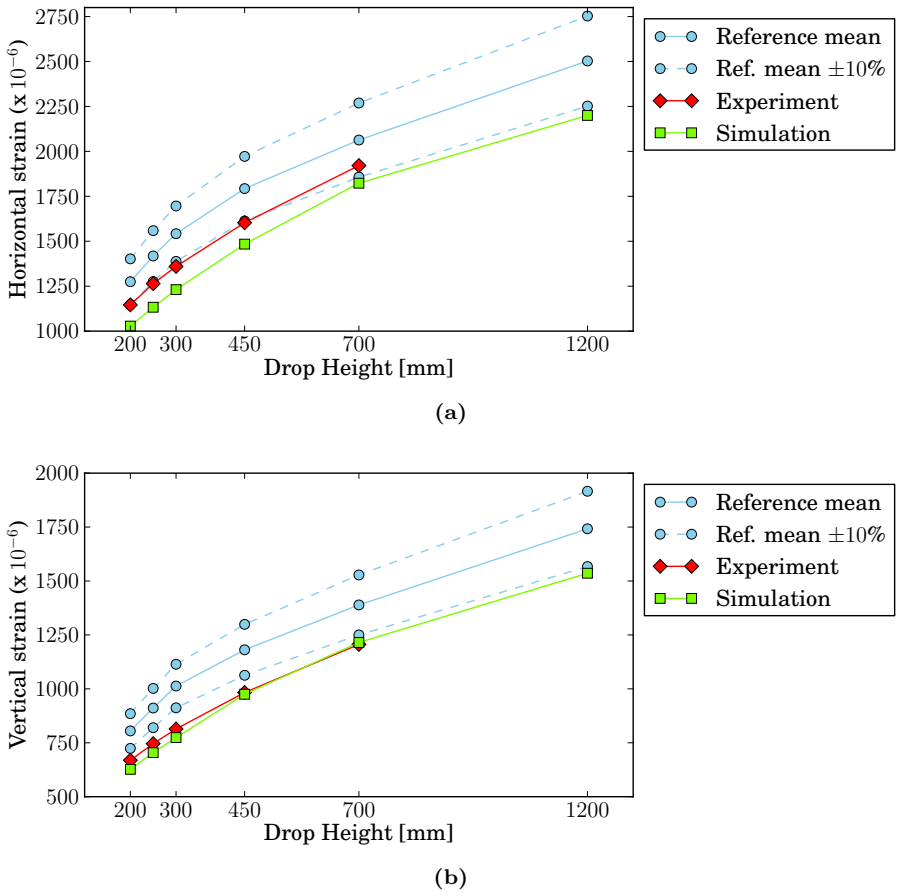

Figure 6.13: Maximum strain at the middle of the backside of the calibration plate for different drop heights: (a) horizontal strain, and (b) vertical strain.

slightly lower than in the configuration of the standard. The central deadweight also causes the spacing between the two STARCO tyres, which appear to be thinner than the tyres that were previously mounted on the test rig in the work of De Pauw [5]. In the glass industry, it is common knowledge that different tyres may produce very different results for the EN 12600 test setup. However, the strains measured with the STARCO tyres are roughly the same as those recorded by De Pauw.

The numerical model is closely representing the experimental setup, including the aforementioned deviations from the standard, although the simulated vertical strains correspond rather well with the experiment, the horizontal strains predicted in the model are somewhat lower.

In analogy with Section 2.3, the analysis can be performed with different boun-

dary conditions, similar to those in Fig. 2.19. The considered boundary conditions are: (i) fixed edges of the glass plate, (ii) a pinned edge at the back of the plate, which allows for rotation of the edge, but no translations, and (iii) clamping between rubber lining and compression by the frame. The resulting deflections at the center of the calibration glass plate in the pendulum test are given in Fig. 6.14 for a drop height of 450 mm. The significant difference in simulated impact response again emphasises the necessity to closely model the clamping of the panel.

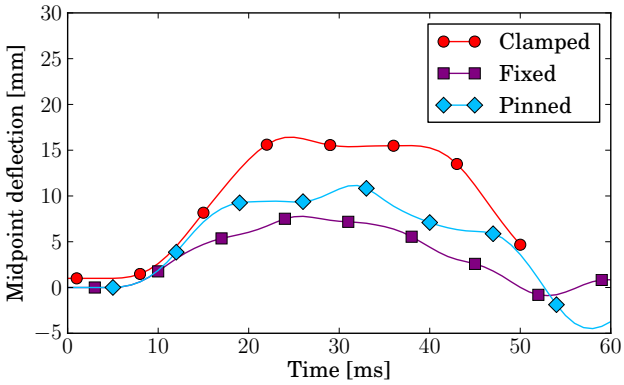

Figure 6.14: Simulated deflections of center of calibration glass plate for different boundary conditions in twin-tyre pendulum impact from a drop height of 450 mm.

Various authors have simulated the same impact on the calibration plate by use of a filled tyre representation. For comparison, the detailed tyre model is replaced by a filled, solid tyre model of the same inflated shape, as shown in Fig. 6.15a. The stiffness of the tyre is characterised by a Neo-Hookean constant $C_{10} = 0.133\,\text{MPa}$, which corresponds to a small-strain modulus of 0.8 MPa, as prescribed for a drop height of 700 mm on a rigid wall by Müller de Vries [225].

The deflection of the centre of the glass plate is given in Fig. 6.15b in comparison with the detailed tyre model for a drop height of 700 mm. It is clear that the filled tyre model exerts a shorter and more severe load on the glass plate. Also the strains at the middle of the panel are notably higher, with a max. horizontal strain of $2130 \cdot 10^{-6}$ and max. vertical strain of $1406 \cdot 10^{-6}$. Nonetheless, Müller de Vries did obtain good simulation results with this tyre representation. The difference in results shows that the filled tyre model cannot be extrapolated to any other impact case, whereas the detailed tyre model is more generally valid.

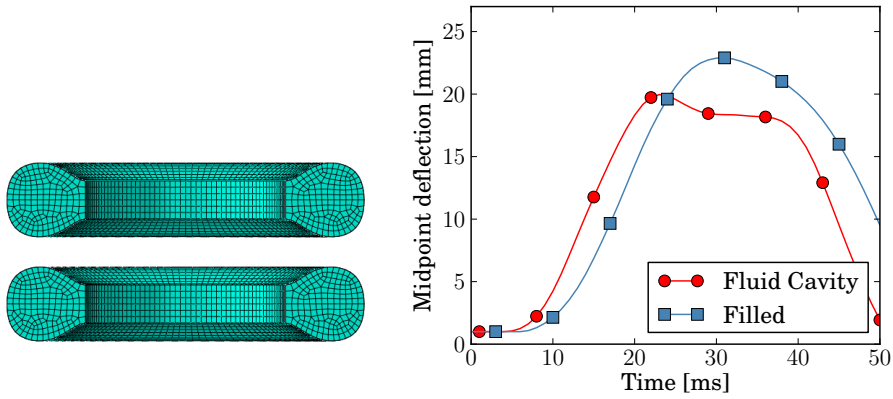

Figure 6.15: Simulation of the twin-tyre pendulum test with a filled tyre representation: (a) Cut view of model, (b) deflection of center of calibration plate.

6.4.2 Laminated glass

The elastic behaviour of laminated glass panels with two glass plies of 3 mm thick and a 1.52 mm thick interlayer is studied under impact. The PVB is of the type Saflex® RB, which has small-strain viscoelastic properties as given by D'haene and Savineau [173]. The same clamping conditions as for the calibration plate are applied on the test rig. The impact response is measured by strain gauges for the horizontal and vertical strain at the centre of the panel and by an accelerometer mounted on the impactor, close to its centre of gravity.

The performed tests are simulated in Abaqus with the impactor model conceived in Sec. 6.2. When the impactor is at rest, the tyre and glass plate are 'just touching'. The glass plates are meshed by 10.0×10.0 mm shell elements which share nodes with two layers of solid elements for the PVB interlayer, i.e. the LG2 mesh type shown in Fig. 5.4.

Similarly, the pendulum impact is simulated using SJ Mepla 3.5.9, which is a finite element software package specifically tailored to the needs of the civil engineering industry.[1] This software includes a simplified manner of representing the impactor as a mass-and-spring system. The spring stiffness C_R is given by Eq. 6.3 and was determined in the work of Schneider [224].

$$C_R = 300 + 2\left|\Delta w_R\right|, \tag{6.3}$$

[1] SJ Mepla analyses have been performed in collaboration with J. Kuntsche at TU Darmstadt.

where Δw_R is the change in distance between the center of the mass and the contact point of the impactor. Furthermore, the laminated glass is represented as a monolithic glass panel of the same total thickness, which has an equivalent elastic response under fast, dynamic loading, as shown in Ch. 5. The clamped boundary conditions are represented by fixed constraints at the edges of the glass panel in perpendicular direction to the surface.

Results of the simulations are compared to the experiments in Fig. 6.16 for a drop height of 450 mm. Fig. 6.17 gives the peak accelerations and peak strains for all simulated and tested drop heights.

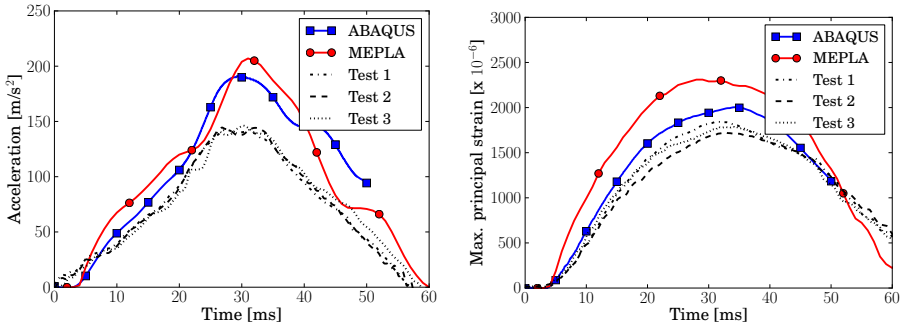

Figure 6.16: Response of laminated glass upon pendulum impact at a drop height of 450 mm: (a) accelerations, and (b) strain.

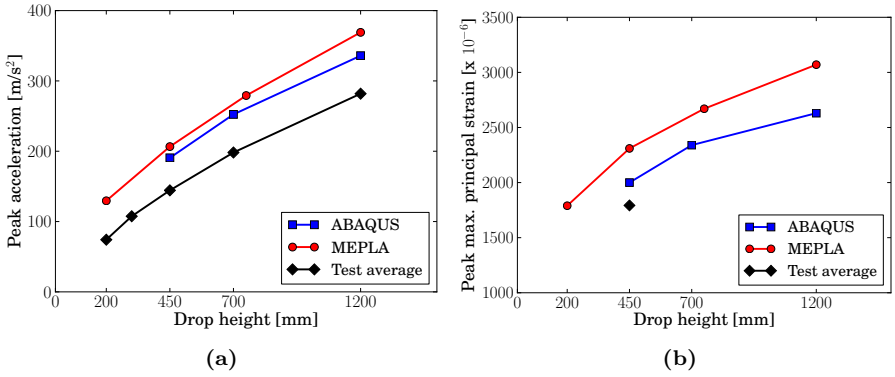

Figure 6.17: Peak values for response of laminated glass upon pendulum impact at various drop heights: (a) acceleration, and (b) strain.

It appears that both simulations are conservative as they consistently overpredict the accelerations and strains. For all considered cases, the detailed model

in ABAQUS captures the impact behaviour marginally better than the model in SJ MEPLA. The modelling technique in SJ MEPLA is known to have been used in qualification in accordance with DIN 18008-4. This indicates that the detailed model may qualify for this standard as well. Nevertheless, the difference in results between both simulations on the one hand and the experiments on the other hand is notable. The reason may lie in the controlling of the experimental setup for these particular tests, where it was neglected to check the pressure in the tyres. Most likely, the tyre pressure during the experiments has been lower than specified in the standard. In Fig. 6.18, additional simulations with lower tyre pressure show that the accelerations and glass strains are lower as well. These results seem to correspond better with the measured response, in particular for a tyre pressure of 2.0bar. Although it can also be noted that the duration of the impact is notably longer in the simulations with lower tyre pressure.

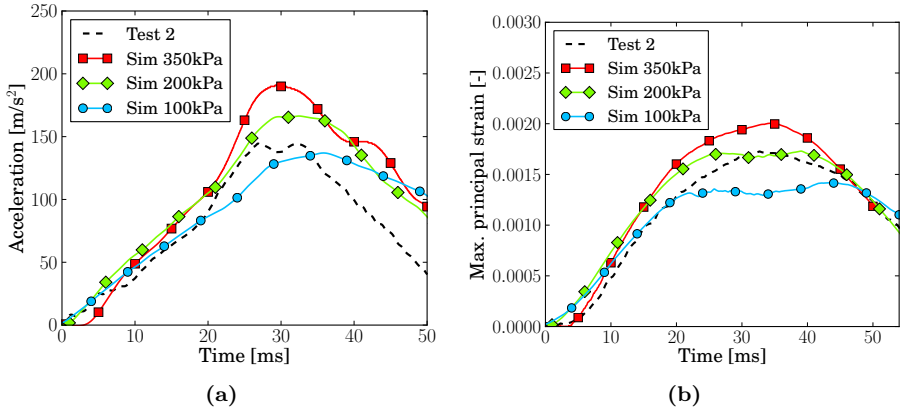

Figure 6.18: Influence of tyre pressure in response of laminated glass upon pendulum impact at a drop height of 450 mm: (a) accelerations, and (b) strain.

6.5 Fractured response of laminated glass plates

6.5.1 Experiments

A series of experiments has been performed by Van Dam [6] to identify the post-fractured behaviour for different compositions of laminated glass. Table 6.3 presents an overview of the performed tests and their qualitative failure performance. It should be mentioned that the tire pressure has been verified at 3.5 bar on the testing days.

Thick and thin panels were tested, with Saflex® R-series PVB. The thin pan-

els have been assembled with three different adhesion grades: RA, RB and RC. However, specimens with different adhesion level showed no discernible difference in response and therefore do not allow to draw any conclusions on the role of delamination in safety performance under the considered soft-body impact.

Table 6.3: Pendulum tests performed on laminated glass.

		Panel thickness	
		$6 + 0.76 + 6$ mm	$3 + 0.76 + 3$ mm
Drop height	450 mm	8(0,0)	
	700 mm	7(1,0)	7(3,0)
	1200 mm	12(6,2)	6(6,1)

A(B,C): A = number of specimens tested, B = number of specimens that cracked, C = number of broken specimens where the interlayer was torn

Along the line of expectation, thin panels break more easily than thicker specimens under the same impulse. For a drop height of 1.2 m, 2 out of 6 broken, thick specimens had their interlayer torn by the impact, while this was the case for only 1 of 6 thin specimens. Moreover, the crack in the PVB at the centre of the plate was rather large for the thick panels, more than 100 mm long, whereas the crack was barely noticeable for the thin panel. Although only few specimens showed interlayer tearing at all, this would lead to conclude that the use of thicker glass plies makes laminated glazing more prone to ultimate failure by tearing. An explanation may be found in the overall load level being higher for thicker panels, which are less flexible, also when broken.

Typical crack patterns for glass plates in the pendulum test are shown in Fig. 6.19. Cracking starts from the centre of the plate, where the tensile stress is the highest. Radial cracks are first formed, mostly oriented along the diagonals. Heavier cracking takes place around the centre of the plate and concentric cracks are formed as well, starting from the impacted side. The total amount or density of the cracks varies among the broken specimens. No clear difference is observed between thick and thin panels.

The deformation of the glazing in response to the impact has been measured for the central zone of each specimen with the Digital Image Correlation technique (DIC) [230]. This method requires the application of a randomised speckle pattern (hence the paint on the back of the glass in Fig. 6.19) and recording by two high-speed cameras for 3D correlation. The highest deflections registered for the broken specimens are given in Fig. 6.20. Unfortunately, data is not available for all of the test panels, as correlation was lost on several occasions upon breakage of the specimen.

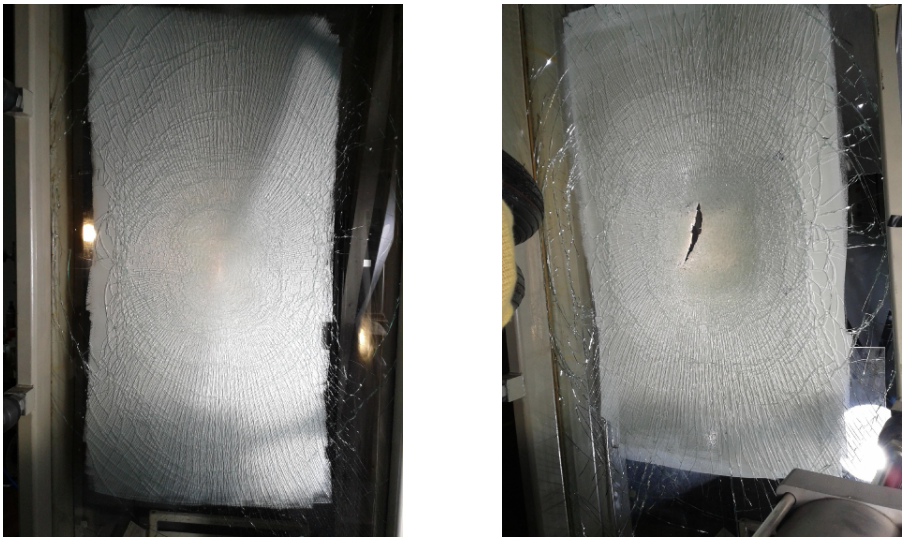

(a) (b)

Figure 6.19: Typical breakage pattern of laminated glass panels in pendulum impact test: (a) broken without tearing, and (b) broken with torn interlayer.

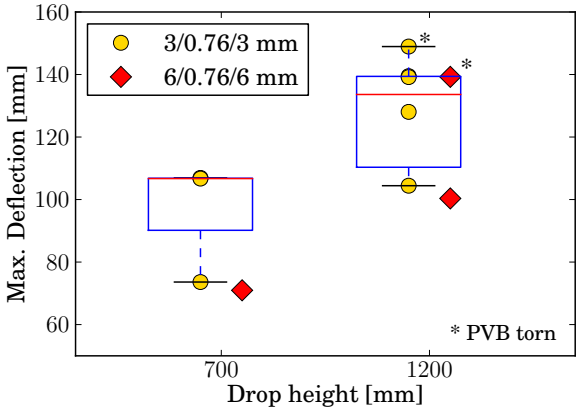

Figure 6.20: Max. deflection of broken laminated glass panels in EN12600 pendulum tests.

6.5.2 Numerical simulations

The setup of the numerical models with glass fracture is largely the same as in Sec. 6.4, except for the representation of the laminated glass panel. The approach of Ch. 5 is followed, with the crack delay model for simulation of

glass cracking and the hyper-viscoelastic material model for Saflex® PVB interlayer (calibrated for a uniaxial tensile test at 0.5 m/s, as given in Sec. 3.5). However, a practical limitation to the use of the crack delay model for shell elements arises, because of the need to import results from a previous, implicit analysis of the mounting and inflation of the tyres. This requires a subdivision of the model into parts, which is incompatible with the use of the `VUMATXTRARG` subroutine that ensures quick fracture upon reaching the stress criterion. Consequently, the crack delay model can still be used for shell elements, but only with the requirement of failure at *all* of the material points within the element. However, this also implies that continuum shell elements cannot be used with this formulation of the fracture model, because they tend to distort when several integration points have failed and others are still active. Therefore, the element configuration with coinciding shell and membrane elements is used (configuration LG3 in Fig. 5.4), which also allows to model the cracking of the glass reasonably well and is more computationally efficient than the other formulations. Material properties for glass are given in Table 5.3. The strength of the glass is taken as 81 MPa, as described in the standard DIN 18008-4 [215] for glass under dynamic soft-body impact. Furthermore, a constant temperature of 20°C is defined for the PVB interlayer, which corresponds to the average lab conditions.

An unstructured mesh topology with characteristic element length of 7.5 mm is used, resulting in a total of 69,000 elements for the laminated glass panel and 130,000 for the entire model. Nevertheless, even with the more computationally efficient element configuration, the calculation time for 100 ms of the impact amounts to nearly 8 days with 4 CPUs. For that reason, further mesh refinement is not investigated for these models.

The resulting crack patterns at the end of the simulations are shown in Fig. 6.21 and Fig. 6.22 for the thick and the thin panels respectively. With the given glass strength, fracture occurred in all simulations, also where this is not on average the case (see the overview of experiments in Table 6.3). It can be argued that the critical stress of 81 MPa is a rather conservative, yet realistic value.

Although the sequence in the formation of the cracks is preserved, the simulated results show markedly fewer cracks than in Fig. 6.19. This comes as no surprise considering the element size, but the difference is substantial also in comparison with the results presented in Ch. 5. It is certain that the requirement for an element to reach the failed status at all of its material points through the thickness prevents more cracks from propagating. This is evidenced in Figs. 6.21 and 6.22 by the contours of damage in the glass, showing that several more cracks have developed at the outer surface, but did not run through the thickness of the element.

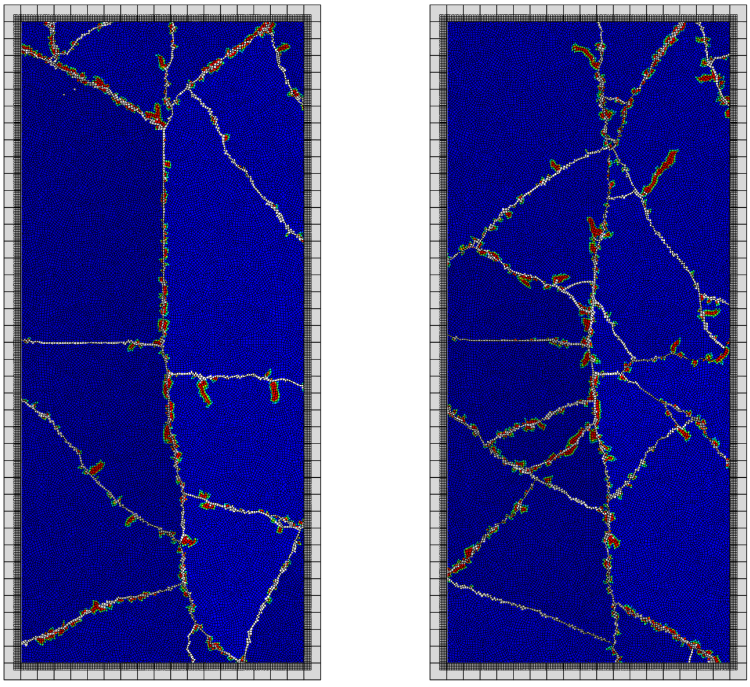

(a) 700 mm **(b)** 1200 mm

Figure 6.21: Cracking of simulated laminated glass panel with $6 + 0.76 + 6$ mm thickness in EN12600 pendulum test, at $t = 100$ ms. Contours of damage at integration point on outward-facing surface: els. in white are deleted, els. in red have failed at outer int. point.

Despite missing the higher degree of fracture that occurs in reality, the deformation of the thick panel under impact does seem to correspond to that of the experiments (without interlayer tearing), as shown in Fig. 6.23. In this figure, the moment at which the test specimens break leads to a quick rise in the outward deflection, which is not experienced in the simulation because the crack propagation by element deletion still takes place slower than in reality. The onset of fracture for the numerical result is seen more clearly in the force or deceleration experienced by the impactor, as marked by a sudden decrease in resistance of the panel to the impactor. Fig. 6.24 shows the deceleration for all four simulations, measured at the central reference point of the rim.

In Fig. 6.25, the deformation of the simulated thin panels is compared to the medians of the experimental curves (see also Fig. 6.20). The correspondence is less convincing than for the thick panels. In the numerical results, the onset of fracture is predicted much earlier and the panel is pushed into higher deflection than in the experiments. Much of the post-fracture response of a laminated

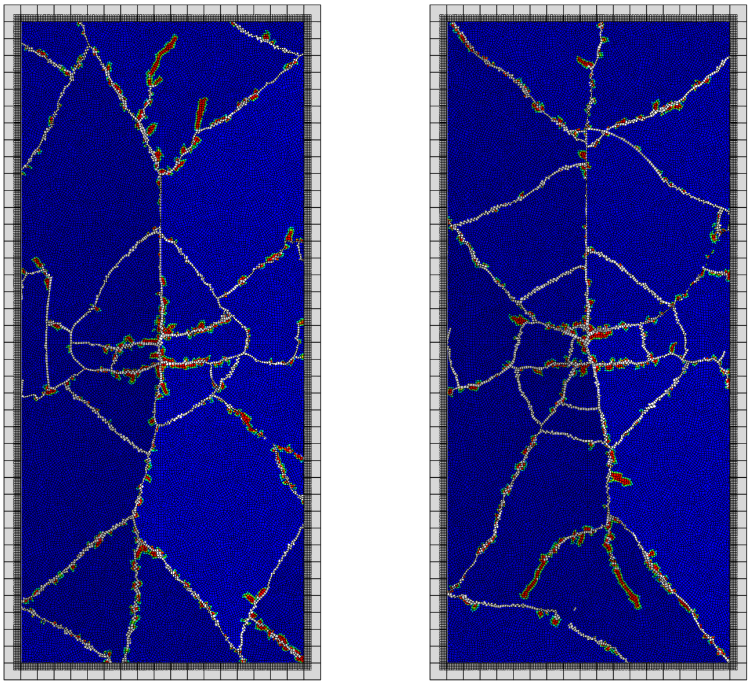

(a) 700 mm **(b)** 1200 mm

Figure 6.22: Cracking of simulated laminated glass panel with $3 + 0.76 + 3$ mm thickness in EN12600 pendulum test, at $t = 100$ ms. Contours of damage at integration point on outward-facing surface: els. in white are deleted, els. in red have failed at outer int. point.

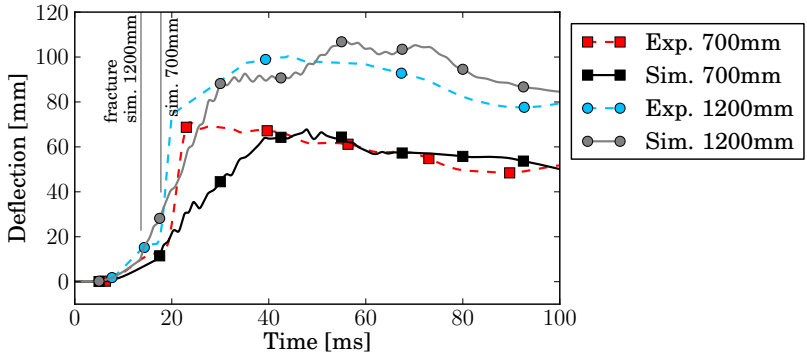

Figure 6.23: Deflection of broken laminated glass panels with $6+0.76+6$ mm thickness in EN12600 pendulum test.

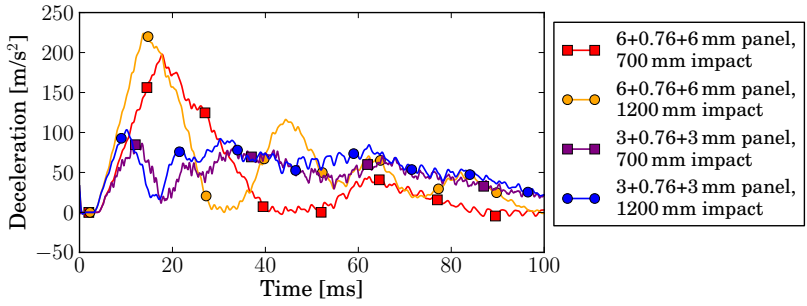

Figure 6.24: Deceleration of the impactor for fracture simulations of the EN12600 pendulum test on laminated glass (results filtered with cutoff frequency of 1.6 kHz).

glass panel depends on the cracking pattern and the straining of the interlayer material bridging those cracks. When so few cracks are formed in the simulations, it is clear that the element deletion technique cannot be regarded as a robust calculation method. However, this aspect is likely to improve when elements can fail as soon as the first material point is fully damaged in the crack delay model.

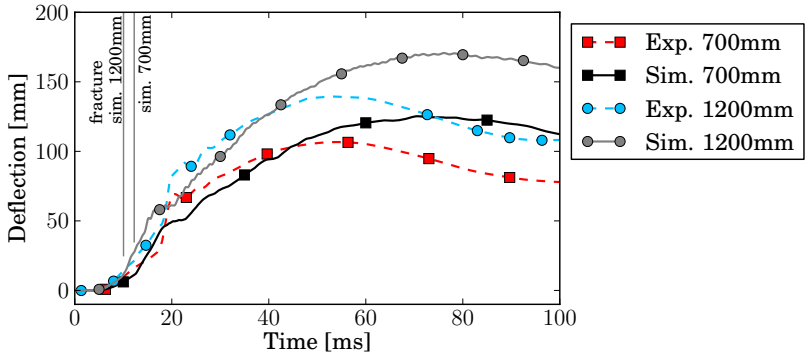

Figure 6.25: Deflection of broken laminated glass panels with 3+0.76+3 mm thickness in EN12600 pendulum test.

One of the main objectives of the study on post-fracture response is the ability to predict ultimate failure of a laminated glass panel under impact and blast loading. This occurs when the interlayer bridging a crack reaches a critical strain level. As observed in the uniaxial tensile tests in Ch. 3, the interlayer tears when reaching 100% true strain, or 170% engineering strain. This value corresponds with the tearing limit observed for similar tests by Schneider et

al. [157].

Table 6.4 gives the maximum interlayer strains in the simulations. In all cases, the highest PVB strain is found in the central zone of the panel. For these simulations an already very high strain level is reached, much higher than the earlier numerical study in Ref. [119] which did not use a verified material model for the PVB interlayer. Nevertheless, the tearing limit is not predicted, even though tearing did occur for several panels tested at the highest drop height. It could be expected that the width of the cracks, here represented by the element size, has great influence on the outcome. This is evaluated further for laminated glass under the more extreme blast loading in the next chapter. However, for practical usage, a conservative tearing limit of 120% engineering strain could be proposed, which corresponds with the highest strains in the simulations of the impact from a drop height of 1.2 m.

Table 6.4: Max. engineering strains in PVB ligaments bridging a crack in simulated results.

		Panel thickness	
		$6 + 0.76 + 6$ mm	$3 + 0.76 + 3$ mm
Drop height	700 mm	55.3% at $t = 100$ ms	91.5% at $t = 55$ ms
	1200 mm	120.4% at $t = 55$ ms	119.1% at $t = 65$ ms

6.6 Conclusions

Numerical models have been conceived to simulate the pendulum impact test, described by the European standard EN 12600 [8]. This standard aims to provide a qualification of glazing towards human body impact, represented in the test method by a 50 kg deadweight surrounded by two tyres. First, the physical properties of the tyres are characterised by experimental investigation of their construction and materials. This allows to develop a detailed model of the impactor which is to be more generally valid than many of the simplified representations described in literature. The impactor model accounts for the compressibility of the pressurised air volume within the tyres, and takes account of the reinforcement wires in the rubber material. Fairly good correspondence is obtained when comparing the simulated response with experimental test data for a compression test, impact on a quasi-rigid force plate and impact on a tempered glass plate. However, the numerical simulations tend to underpredict the impact loads up to 11%.

Experiments and simulations have been conducted on laminated glass plates for different drop heights. These results are also compared to simulations in SJ Mepla, which offers a simplified modelling technique for the pendulum test

and has been used for qualification to the German standard DIN 18008-4 [215]. Both simulation methods predict higher accelerations and strains during the impact when compared with the experimental measurements, which would be conservative from a structural design point of view. However, some doubt exists over the experimental results as the tyre pressure has not been at the prescribed value in the concerned experiments. Even so, it can be concluded that qualification to the standard by simulation would benefit little from the detailed approach as described here, considering the effort required to set up and run the numerical analysis.

Contrary to simplified approaches, the detailed model does allow to simulate the impact response of laminated glass with and beyond fracture of the glass. Thick and thin panels are analysed for two drop heights at which many of the specimens broke in experimental testing. Delamination is not accounted for in the numerical models as no discernible difference in impact response could be seen for test plates with different adhesion grades. Because of the need to import results from the implicit simulation of the inflation of the tyres, it is not possible to use the crack delay model for shell elements as presented in Ch. 5, where an element is deleted as soon as the first material point reaches failure. Instead, the requirement for failure at all material points in the element is used. Partly due to this limitation, cracks propagate slower and appear fewer in number than expected for the simulations. Furthermore, the post-fracture deformation of the panels does not consistently show good correspondence with experimental results, which leads to conclude that the reliability of the investigated method is still lacking. Nonetheless, the post-fracture simulations do show that fairly high strains are reached at the interlayer material bridging the cracks. Eventually, this may allow to assess the ultimate failure of the panel by tearing of the interlayer.

Chapter 7

Laminated glass under blast loading

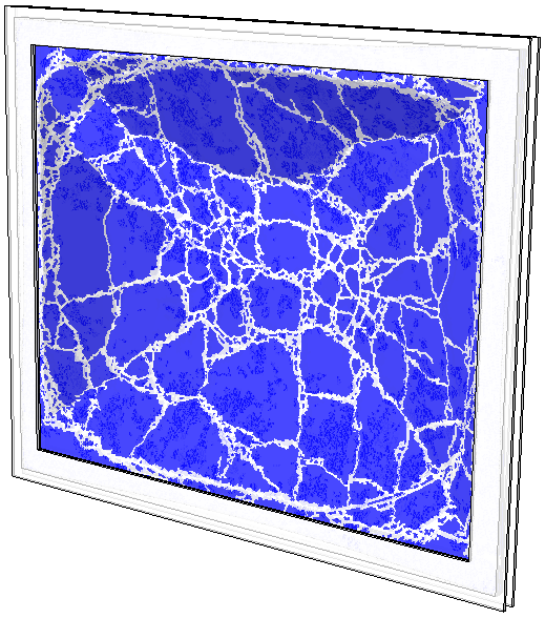

Simulated fracture of a laminated glass window under heavy explosive blast.

7.1 Introduction

Explosions present an extreme load case for any structure, and need to be considered in the design stage of constructions with a higher risk of being subjected to a blast. Because of catastrophes such as accidental gas explosions and terrorist attacks, safety against blast loading has become a qualification demand in the construction and vehicle industry. The supporting structure of the building or vehicle foremost needs to be able to withstand such event. When glass is used, its brittleness presents an increased risk of injury [1–4, 231]. Especially in the building industry, the trend towards light and filigree structures poses a challenge for the current standards in blast-safe window design.

Blast resistant glazing serves two goals: to prevent penetration of the blast wave and to retain the broken glass fragments. Whereas monolithic glass is entirely unfit for this purpose, the use of laminated glass is customary. In the rare event of an explosion, fracture of the glass can be allowed and even be desirable, as a portion of the blast energy gets absorbed by fracture, deformation and delamination of the panel, which in turn reduces the load on the supporting structure. Therefore, a relatively flexible laminate with two glass plies can be preferable, which is quite opposite to the design of burglary and bullet resistant glazing where thick, multi-layer laminates are requisite.

In the fractured state, a certain trade-off exists for the adhesion quality and stiffness of the interlayer. When an interlayer with a high adhesion grade is used, little delamination can take place and the interlayer material at the cracks in the glass is stretched quickly to the point of tearing (see also Fig. 4.1). A lower adhesion level may allow to avoid tearing, but should not be too low in order to prevent the propulsion of glass debris. Similarly, a very soft interlayer may too easily reach the tearing limit, while a very stiff interlayer can result in the window being blown out of its frame altogether.

An overview of the characteristics of loading by blast waves is given in Section 7.2. The numerical simulation of the loading caused by blast waves is discussed in Section 7.3 for two small-scale test cases. Section 7.4 presents the simulation of a small laminated glass plate under free air blast with the crack delay model. The same modelling approach is used in Section 7.5 for larger panels at the end of a shock tube. These simulations are compared with earlier results from LS-Dyna.

7.2 Blast waves

7.2.1 Explosion and explosives

An explosion can be defined as the rapid release of stored potential energy in a very short time. As a result, heat is spread in the surrounding environment and a pressure wave propagates from the point of ignition. Whether the cause of the explosion is natural or intentional as a weapon, it poses an extreme load case that can threaten people's lives and the integrity of buildings and infrastructures. In order to assess the effects, the mechanical processes following an explosion should be well understood. The fundamentals in this field date back to the late nineteenth century work of Rankine, Hugoniot and Lamb. A great body of research was produced in the consecutive decades, in particular during both world wars. The physics of explosions are explained into detail in several books, e.g. Refs. [232–234]. To situate the load cases considered in this work, distinction can be made between the different sources for explosions:

- **Physical explosions:** the sudden relief of a highly pressurised gas without chemical reactions. E.g.: a bursting balloon, Boiling Liquid Expanding Vapour Explosion (BLEVE), etc.
- **Chemical explosions:** caused by a rapid oxidation reaction between oxygen and another chemical component. The oxygen is usually contained within the explosive, such that no additional air is required. The reaction must be triggered upon which it propagates by either of two mechanisms, depending on the explosive:
  - *Deflagration*: combustion propagating through heat transfer, at a velocity lower than the ambient speed of sound. The resulting pressure wave is characterised by a relatively low overpressure, but high impulse.
  - *Detonation*: the reaction front moves at a speed greater than the speed of sound, driving the shock front immediately preceding it. A shock wave expands in the surrounding medium with a high peak overpressure discontinuity and relatively short duration.

  It is possible for a deflagration to change to a detonation, but deflagrating explosives are difficult to bring to this state. They are therefore termed *low explosives*, of which gunpowder is a common example. For *high explosives*, further distinction is made between primary explosives, which detonate by a spark or flame, and secondary explosives, which detonate only by the detonation of a primary explosive. Secondary explosives cause more powerful shock waves and are easier to control.
- **Nuclear explosions:** the sudden (and uncontrolled) release of a great amount of energy by fission or fusion of atomic nuclei.

When blast protection is demanded in the construction energy, it typically concerns the ability to safely withstand a blast wave from the detonation of explosive agents. This is also the type of loading that is considered here.

The effects of explosions are related to the amount of released energy. Each type of explosive has a mass-specific energy, which for TNT amounts to approximately 4.680 MJ/kg when detonated [235]. The mass-specific energy of different high explosives is often expressed as the TNT equivalent; a scaling factor that allows for comparison. TNT equivalents of selected explosives are given in Table 7.1. Composition C-4 consists for 91% of RDX and has been used at the Belgian Royal Military Academy (RMA) for experiments on laminated window glazing in the framework of this study. ANFO is a very common explosive used in the mining industry, and TATP has gained notoriety because of its use by terrorists, a.o. in the Brussels attacks. It should be noted, however, that the mass-specific energy of an explosive is not a consistent value. For TNT alone, deviations up to 50% have been reported [236].

Table 7.1: TNT equivalence factors of explosive agents (Data from Ref. [237])

Explosive	TNT equivalent
TNT	1.00
Composition C-4	1.37
ANFO	0.87
TATP	±0.71

7.2.2 Blast wave propagation

The detonation of an explosive causes a chemical reaction that converts the solid explosive charge into a highly pressurised gas at very high temperature. This concentrated pressure causes a shock wave to propagate, which is essentially a high pressure disturbance moving away radially from the source at a propagation velocity v_s. The energy released by the explosion is distributed over the total volume of the medium where the shock front has passed. As the blast wave propagates, the energy density at the shock front decreases, thus reducing the overpressure, overdensity and velocity.

The typical curve for a blast wave is given in Fig. 7.1, characterised by a discontinuous rise in pressure to p_s at the shock front, followed by an immediate decay to a negative phase of underpressure. The latter can be understood as a dynamic rebound of the air mass behind the shock. The positive phase has a duration t_+ and positive pressure impulse i_+. The peak pressure p_s is the static overpressure, measured at a point in the flow.

Theoretically, for a spherical charge in air, the relationship between p_s, the

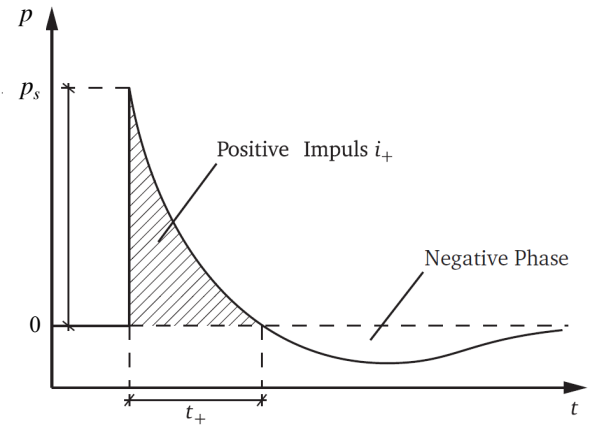

Figure 7.1: Overpressure curve for detonation in air.

distance of the point of measurement from the centre of the explosion R, and the instantaneous energy release Y, also called the *yield*, takes the form:

$$p_s = CY/R^3, \tag{7.1}$$

where C is a non-dimensional constant. The yield can be calculated from the charge mass m_c and the detonation energy density E_{det} of the explosive:

$$\begin{aligned} Y &= m_c E_{det} \\ &= W E_{TNT}, \end{aligned} \tag{7.2}$$

where W is the TNT equivalent mass of the explosive charge. This leads to the definition of the scaled distance; $z = R/W^{1/3}$. Hopkinson, and later Cranz, have formulated scaling laws for explosions, stating that self-similar blast waves are produced at identical scaled distances.

In a TNT explosion, the peak pressure p_s may be up to 20 bar at the point of detonation [233], but rapidly decays with distance. The pressure decay can be expressed as a function of scaled distance, e.g. Eq. 7.3 for spherical charges of TNT as given by Brode [238]. Many similar empirical relations can be found, for spherical charges as well as other shapes. Fig. 7.2 compares often used decay laws by Brode [238], Henrych [239] and Kinney and Graham [240].

$$p_s = \frac{585}{z^3} + \frac{145.5}{z^2} + \frac{97.5}{z} - 1.9 \text{ [kPa]} \tag{7.3}$$

The entire curve in Fig. 7.1 can be described by the Friedlander equation [241]:

$$p = p_s(1 - t/t_+)e^{(-kt/t_+)}, \tag{7.4}$$

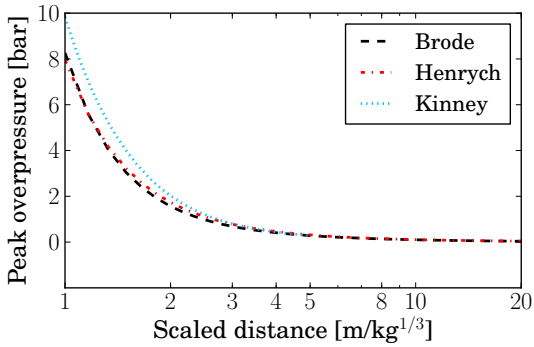

Figure 7.2: Comparison of empirical decay laws for a spherical charge.

where k is the wave form parameter, which is a function of the scaled distance. When $k = 1$, the positive and negative impulses are equal. The wave form parameter can be determined using diagrams, such as from Baker et al. [242]. Larcher [243] has proposed an empirical relation to calculate k, given by Eq. 7.5. This relation is based on the positive impulse and does not describe the negative pressure well. Therefore, Larcher has formulated a correction for the negative phase of the Friedlander curve as well.

$$k = 5.2777 z^{-1.1975} \tag{7.5}$$

The propagation velocity U_s of the shock wave can be calculated from the Hugoniot-Rankine relations, which express the conservation laws across a shock front:

$$U_s = c_0 \sqrt{1 + \frac{\gamma + 1}{2\gamma} p_s}, \tag{7.6}$$

where c_0 is the speed of sound in ambient air and γ is the specific heat ratio, which is 1.4 for air under ambient conditions. Together, the Equations 7.3 to 7.6 can describe the propagation of a blast wave in open air.

7.2.3 Blast wave reflection

When encountering an object in its path, the incident blast wave gets reflected and the total magnitude of the reflected pressure is much higher than the incident pressure. It is the reflected pressure that acts on the structure. The loading depends on the incident blast wave, the angle of incidence and the nature of the surface. Similar to the incident pressure, the reflected pressure can be described by the Friedlander equation (Eq. 7.4).

To calculate the reflected pressure, also the dynamic pressure q of the blast wave needs to be considered. This is essentially the kinetic energy density of the air behind the wave front:

$$q = \frac{1}{2}\rho_s {u_s}^2, \tag{7.7}$$

where ρ_s is the local air density, often referred to as the overdensity, and u_s is the particle velocity of the air behind the shock front. The static overpressure, overdensity and velocity have a similar course in time, but have different positive phase durations [234]. Since the dynamic pressure q stems from the kinetic energy, it can never be negative.

Using the Rankine-Hugoniot equations it can be shown that:

$$q = \frac{p_s^2}{2\gamma p_{atm} + (\gamma - 1)p_s} \tag{7.8}$$

For a blast wave arriving perpendicular to a flat, rigid surface, the reflected pressure is given by Eq. 7.9. Thus, for $\gamma = 1.4$ (air below 17 bar), the reflected pressure is maximally 8 times higher than the static overpressure.[1] The ratio of p_R to p_s is given in Fig. 7.3 for different angles of incidence.

$$p_R = 2p_s + (\gamma + 1)q \tag{7.9}$$

As the reflected pressure is higher than the incident pressure, the reflected shock travels at a greater speed as well. The *triple point* is where the reflected shock front overtakes the incident shock front. Onwards, the fronts merge to form a single outward travelling front, known as the *Mach stem*, which is shown in Fig. 7.4. When an explosive is detonated at ground level, walls and façades are primarily loaded by the Mach stem due to ground reflections. The loading posed by the Mach stem is more intense than by the incident wave. As an example, in the nuclear bombing of Nagasaki, greater destruction was caused in a ring some 500 m away from the center of the explosion due to the Mach effect.

7.2.4 Blast effects on structures

Early, but extensive research programmes for the analysis of blast effects on structures have been conducted during the first half of the 20$^{\text{th}}$ century, which has been marked by both World Wars. The literature from this period has been reviewed by Bulson [233] and by Morison [244], who paid special attention to

[1] This maximum would only be reached at a pressure above 650 bar. Taking into account that γ for air has decreased at such pressures, the theoretical maximum reflection factor becomes ± 14.5 [234]. In reality, a maximum reflection factor of 7 can be reached with moderate to high quantities of explosives.

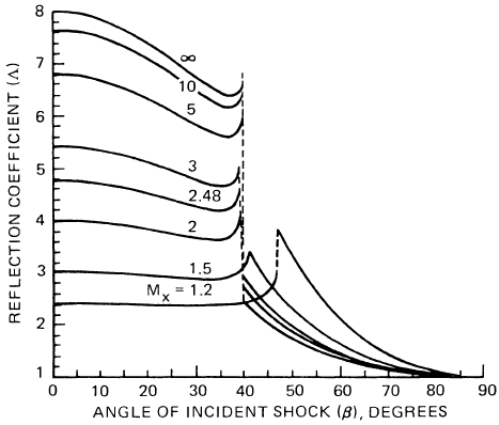

Figure 7.3: Reflection factor in function of incident angle of the shock wave. M_x denotes the Mach number for the incident wave velocity. (Figure from Kinney and Graham [240].)

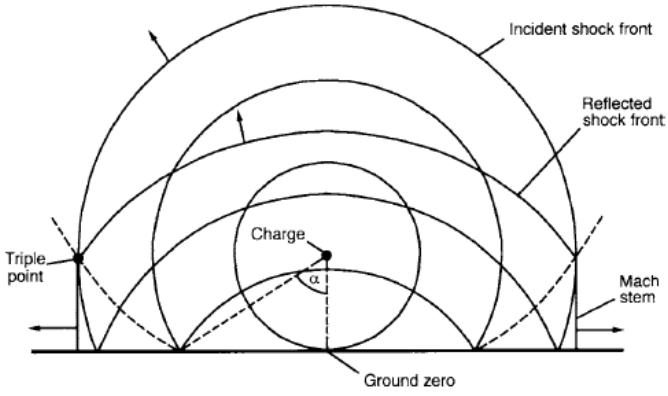

Figure 7.4: Reflection of shock waves for explosions above ground (figure from Bulson [233]).

the response of window glazing. In general, these studies showed that external blast loads cause mostly superficial damage and rarely lead to the collapse of a building. Internal blasts, or external blasts from ground level that penetrate openings, pose a load contrary to what the building was designed for and are generally more damaging. As in many other examples of structural loading, the structural integrity depends highly on the strength or weakness of connections. It is found that clamped connections that rely on friction allow the structure to absorb a larger amount of energy without collapse. As for the construction materials, masonry and stone are significantly less resistant to blast loads than

reinforced concrete. The wartime research served as a basis for design rules, most notably the publication of the US Army Technical Manual on Protective Design (Non-Nuclear) TM 5-855-1 [237], which first appeared in 1965.

Glass and light sheeting are most vulnerable to blast loads, by which they rapidly shatter and produce a great amount of splintered fragments. For these components also the negative suction phase of the blast needs to be considered. The negative phase becomes more important at greater scaled distance, for which the negative impulse can be many times greater than the positive impulse. Wei and Dharani [245] reported that the mid-span deflection and maximum tensile stress of glazing due to negative pressure can be double the corresponding quantities in response to the positive pressure. Contrary to what may be expected, Krauthammer and Altenberg [246] showed that there is no clear, consistent relation between a panel's natural period and its failure on the return stroke due to the negative phase.

Laminated glass offers protection after fracturing by avoiding flying glass debris. The laminated glass panel can also absorb an amount of the blast energy; around 80% according to Hidallana-Gamage et al. [247], based on their numerical modelling of the experiments by Kranzer et al. [248]. As the laminated glass remains attached to its frame or connectors when broken, the joints should also be evaluated for their safe performance. The behaviour of common silicone glazing joints under blast loading has been studied by Hooper [249]. When blast safety is a requirement in the design stage, connections may be designed specifically to absorb a major portion of the blast energy, e.g. different connectors for cable net façades described by Wellershoff et al. [250].

Several current standards address the qualification of glazing under blast loads. In Europe, the standard EN 13541 [9] describes the performance of the (laminated) glass as a building product, while the standards EN 13123 [251,252] and EN 13124 [253,254] specify requirements for windows, doors and shutters, complete with their frames and infills. EN 13541 defines the procedure for shock tube testing of a 0.9×1.1 m glass test specimen, clamped at all sides in a rigid frame. Several load levels are defined as combinations of the positive, reflected peak pressure p_R, positive load duration t_+ and positive specific impulse i_+, as given in Table 7.2. A glass product qualifies for a certain load level when there are no penetrable holes in the panel and no openings to the frame. The EN 13123 and EN 13124 use the same qualification, but without specification of the size or clamping of the glazing.

The US standard ASTM F 1642 [255], which serves as a global reference, treats both the product and the specific design. This standard defines no qualification requirements, but describes the procedure to test glazing and façade systems using a test container and a *witness panel* to assess the size and reach of the debris. World-wide security requirements are specified in the GSA Security

Table 7.2: Blast load levels as defined in EN 13541 [9].

Load level	p_R [kPa]	t_+ [ms]	i_+ [kPa · ms]
ER1	50	20	370
ER2	100	20	900
ER3	150	20	1500
ER4	200	20	2200

Criteria [256]. In this document, protection levels are defined for structural components under several threats, among which blast loading. For the testing of window glazing, referral is made to ASTM F 1642, and to Wingard [257] for calculation.

The international standards ISO 16933 [258] and ISO 16934 [259] specify testing procedures for glass as a building product under open air blast and in a shock tube respectively. The test method of ISO 16934 is identical to that described in EN 13541, except that two additional load levels are defined in the lower range. However, both ISO standards are only rarely used in the building industry [7].

7.3 Simulation of blast loading

An explosion in air causes a highly intense short duration loading which is difficult to measure. When the shape and size of the explosive charge is known, numerical methods allow to analyse the blast wave propagation and reflection in open air or in confined spaces. Consequently, the transient loads acting on a surface of interest may be calculated. The present section aims to evaluate the capablility of numerical methods of fulfilling this goal. Two well-instrumented blast test cases on a quasi-rigid structure are considered, after the experiments performed by Van Dam [6] at the Belgian Royal Military Academy (RMA). Ultimately, the numerical techniques to simulate the blast could be combined with the structural model to study their interaction. First, an overview of relevant techniques to model the blast wave is given.

7.3.1 Modelling techniques

Computational methods for blast prediction can be subdivided into three general categories: empirical methods, computational fluid dynamics (CFD) and hydrocodes. The empirical methods include foremost ConWep [237], a collection of conventional weapons effects calculations that uses the empirical model of Kingery and Bulmash [260] for the calculation of blast loading. ConWep is included in some FE software packages, among which Abaqus and LS-Dyna. An improvement to ConWep with special attention to soil conditions for land mines is the Westine model [261]. Empirical models can be used to calculate

the load on a surface some distance away from an open air blast, but do not take into account important aspects such as the Mach effect, diffraction and multiple reflections.

CFD codes allow for highly detailed simulation of the fluid flow of and around a passing shock wave, including heat losses, boundary layers of viscous flow and turbulent vorticity [262, 263]. However, a very fine mesh is needed for these calculations along with many small time steps. Therefore, CFD simulations of blast are rarely performed for the entire domain [264]. Simulation of the fluid-structure interaction in co-simulation with Lagrangian FEM is even more computationally expensive.

Shocks are treated more naturally by hydrocodes, which can be Eulerian or Lagrangian. Hydrocodes can be defined as codes to solve large deformation, finite strain transient problems that occur on a short time scale [122]. In all hydrocodes, shocks are treated by an artificial viscosity term, based on the approach by Von Neumann and Richtmyer [265], to give the shock a thickness comparable to the element length. This avoids the need for an internal boundary condition to represent the discontinuity and maintains stability of the analysis.
The Lagrangian formulation encompasses the explicit FEM used to simulate structural response to dynamic, transient loading. Eulerian hydrocodes are more suited to model fluid(-like) behaviour. Both can be coupled and efficiently handled by the same solver to allow simulation of fluid-structure interaction. Common techniques to this end are the Arbitrary Lagrangian-Eulerian (ALE) method, developed by Hirt et al. [266], and the Coupled Eulerian-Lagrangian (CEL) method by Noh [267]. In CEL, the Eulerian material is tracked as it flows through the mesh by computing its volume fraction in each element. While CEL provides a coupling between the Eulerian material boundaries and Lagrangian parts through a general contact algorithm, ALE is a truly hybrid method. An ALE formulation consists of two steps: (i) a Lagrangian time step, and (ii) an *advection* step in which computations at the element boundaries are performed and the solution from the distorted mesh is remapped to the smooth mesh [268]. The ALE grid can represent purely Lagrangian behaviour when the vertices move with the material, purely Eulerian behaviour when the boundaries are fixed or a mixture of both. Additional coupling can be provided for a Lagrangian part interacting with the ALE mesh.

Several authors have used hydrocodes to calculate blast wave propagation and reflection on rigid surfaces or with fluid-structure interaction. A similar quality of results for the blast wave model is obtained with Eulerian [269, 270] and ALE [271, 272] methods.

Also the SPH method, introduced in Section 2.5, can be used to model the detonation and expansion of an explosive [273, 274]. SPH is especially suited

to model shaped charges and contact explosions, for which other methods experience difficulties. Because SPH relies on the interpolation of neighbouring particles, the method is less suitable to calculate the far-field blast wave propagation.

7.3.2 Small-scale open air blast

Experiments have been performed in the test bunker of the Laboratory for Explosion Effects (LAEE) at the Belgian RMA. This test facility allows for detonation of explosive charges up to 50 g of Composition C-4. The test setup consists of a thick aluminium plate with dimensions $400 \times 400 \times 20$ mm, mounted on a steel frame that is fixed to the ground. The explosive charge is positioned opposite the centre of the aluminium plate, as in Fig. 7.5.

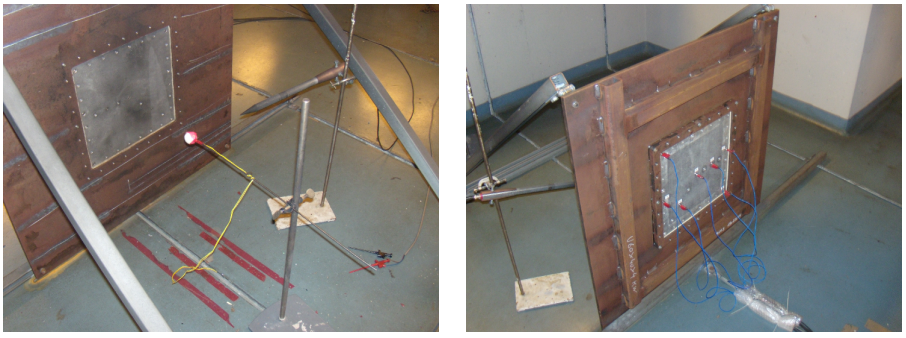

(a) **(b)**

Figure 7.5: Test setup for open air blast on rigid plate: (a) front side with explosive charge and blast pencil, (b) back side with pressure probes.

The incident pressure is measured with a blast pencil that is located at the same distance of the charge as the centre of the test plate. The reflected pressures are measured by pressure probes at various locations on the test plate as indicated on Fig. 7.6.

The explosive charge is a Composition C-4 secondary explosive which is insensitive to most physical shocks, heat or electrical sparks and can safely be used in a test environment. The charge is molded into a spherical shape. A 20 g charge at standoff distance of 300 mm is considered for benchmarking. The distance of the charge to the ground is 500 mm, which is large enough to exclude ground reflection in the pressure measurement of the arriving shock wave. In Fig. 7.7, ten repeated tests show that the blast pressures and pressure impulse acting on the middle of the test plate are consistent, although deviations from the average peak pressure up to 30% are found. For reference, mean curves are

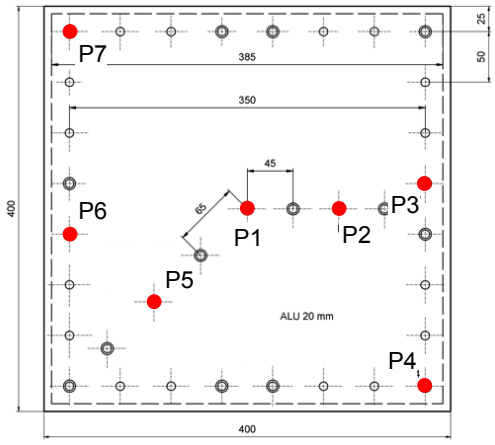

Figure 7.6: Location of pressure probes on the surface of the aluminium test plate.

obtained for each pressure probe by computing the average for each 0.2 µs and filtering with a cut-off frequency of 500 kHz.

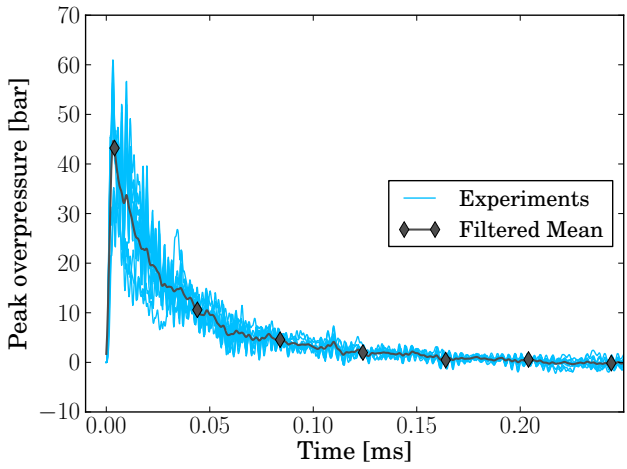

Figure 7.7: Blast pressure at centre of test plate (probe P1); 10 repeated tests with 20 g of C-4 at 300 mm standoff distance.

The mean pressures acting on different locations of the test plate are given in Fig. 7.8, showing the progression of the reflected shock front over the surface. It can be noted that the blast wave is indeed approximately axisymmetric, as the signals of pressure probes at equal distance from the centre of the test plate are alike.

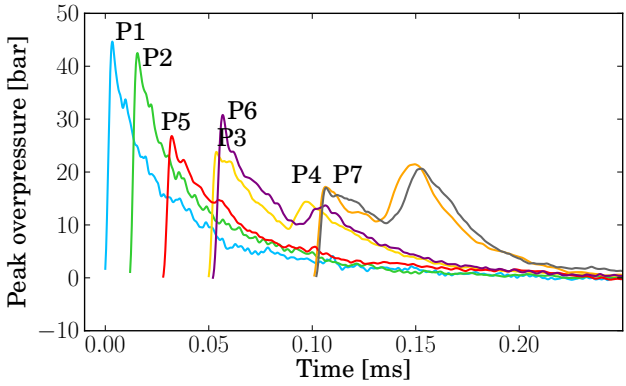

Figure 7.8: Mean blast pressures for all probes on test plate; 20 g of C-4 at 300 mm standoff distance.

In the numerical representation, the aluminium test plate and steel frame are first modelled as deformable solids. For efficiency, only a quarter of both are modelled with use of symmetric boundary conditions, as shown in Fig. 7.9. The element length for the test plate and frame is around 4 mm in the entire mesh. Such a fine mesh is used to evaluate the blast pressures at the contact faces in the locations corresponding to pressure probes in Fig. 7.6.

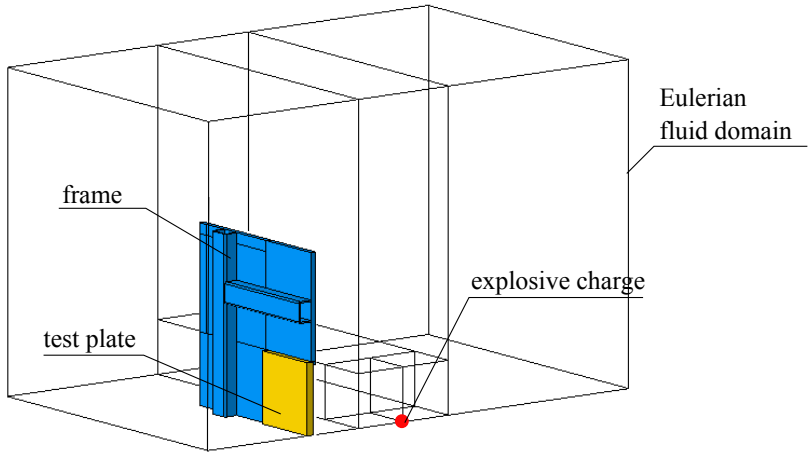

Figure 7.9: Numerical representation of test plate and frame in open air blast; CEL model with fluid domain.

In Abaqus, the blast load can be modelled either with the built-in ConWep module or by simulating the blast expansion in an Eulerian fluid domain, cou-

pled to the Lagrangian structure. The ConWep module requires only the definition of the point of detonation and the TNT equivalent mass, i.e. 27.4 g. In the CEL model, the explosive charge is modelled as a (quarter) sphere with a radius of 14.4 mm in the Eulerian domain. The rest of the Eulerian domain is occupied by air, defined as ideal gas with $\gamma = 1.4$ and density $\rho = 1.205\,\mathrm{kg/m^3}$. The explosive is defined by the Jones-Wilkins-Lee (JWL) equation of state, which describes the thermodynamic properties of detonation products. The JWL equation of state is given by:

$$p = A\left(1 - \frac{\omega}{R_1 V}\right) e^{-R_1 V} + B\left(1 - \frac{\omega}{R_2 V}\right) e^{-R_2 V} + \frac{\omega e_0}{V}, \tag{7.10}$$

where p is the acting pressure of the detonation products, e_0 is the specific internal energy and V is the ratio of the density ρ_e of the solid explosive over the density of the density ρ_d of the detonation products. The terms A, B, R_1, R_2 and ω are empirically determined coefficients. All JWL constants for Composition C-4 are given in Table 7.3.

Table 7.3: JWL constants and properties for Composition C-4 explosive (data from LLNL [275]).

ρ_e	1601 MPa
E_0	8.7 GJ/m^3
A	609.8 GPa
B	12.95 GPa
R_1	4.5
R_2	1.4
ω	0.25
p_{CJ}	28.0 GPa
v_{det}	8193 m/s

The mesh for the Eulerian fluid domain can be refined where high gradients are expected.[2] The Eulerian element length of the initial mesh is 2.5 mm in the vicinity of the charge, and 10 mm elsewhere. In total, this mesh contains 1.14 million elements.

The blast pressures calculated with ConWep in Abaqus are given in comparison with the experimental measurements in Fig. 7.10. Because of symmetry, results for the pressure probe locations P6 and P7 are omitted. The results are generally in good agreement for the arrival time, peak pressure and pressure decay. The latter is less well predicted at locations further away from the centre of the plate where the blast wave has arrived first. ConWep, as an

[2] In newer versions of Abaqus, it is now possible to use adaptive meshing for the Eulerian mesh, based on the pressure gradient. The mesh can also be coarsened again. As such, the mesh refinement can 'move' with the shock front.

empirical calculation tool, can predict the reflected pressure of a shock arriving in a certain point, but does not take account of the propagation of an already reflected wave along the surface. Also, ConWep finds the corresponding load for a TNT equivalent mass, which has slightly different properties than C-4. This may explain why the peak pressure and, particularly, the impulse are somewhat overpredicted at the centre of the test plate.

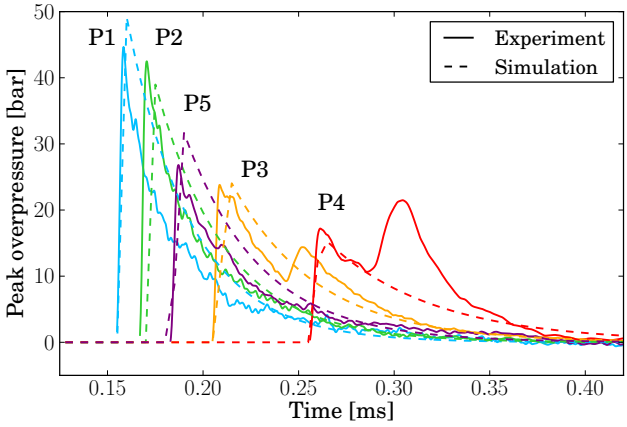

Figure 7.10: Comparison of ConWep simulated blast pressures with experimental measurements; 20 g of C-4 at 300 mm standoff distance.

The deformation of the test plate may be derived from the simulation, in which the maximum deflection at the centre amounts to a mere 2.5 mm in either direction, as shown in Fig. 7.11. Therefore, the frame and test plate could also be regarded as rigid in subsequent models.

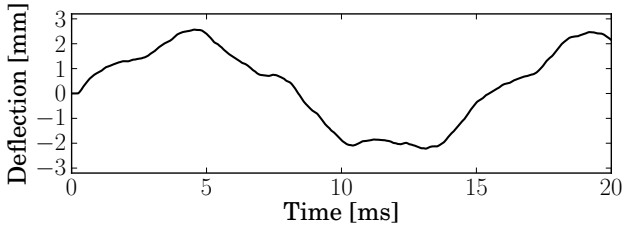

Figure 7.11: Deflection of test plate in blast simulation using ConWep; 20 g of C-4 at 300 mm standoff distance.

In comparison, the CEL approach gives a much less accurate prediction of the blast loading on the test plate with the given mesh size. Pressures at the

different probe locations are given in Fig. 7.12. The peak pressures in the CEL simulation are substantially lower than in the experiment. Also the wave form differs from the expected Friedlander curve, because in hydrocode simulations, the shock front is spread over several elements. To better capture the shock front, a significantly finer mesh would be needed.

However, contrary to ConWep loading, an Eulerian model of the shock wave does take account of the interaction with the reflected wave propagating along the surface of the plate, as seen in the second rise in pressure for location P4. Fig. 7.13 shows the corresponding section view for the air pressure at $t = 0.36\,\text{ms}$. A locally intensified pressure arises when the reflected wave reaches the edge of the aluminium test plate where it meets the frame. Thus, the clamping area is loaded with a greater pressure impulse than what would be predicted by ConWep. This can be taken into consideration for the blast-safe design of window frames.

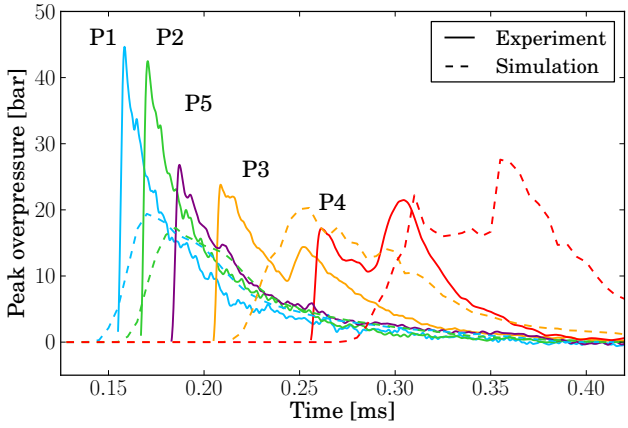

Figure 7.12: Comparison of CEL simulated blast pressures with experimental measurements; 20 g of C-4 at 300 mm standoff distance.

To study the model with a finer mesh, the Eulerian domain can be reduced as in Fig. 7.14a. The results of mesh refinement are given for the blast pressure at the centre of the plate in Fig. 7.14b. The simulated peak pressures increase when smaller elements are used, and also the shock front becomes steeper. However, with an element length of 2.5 mm, the reduced Eulerian mesh contains 5.59 million elements. Further study of the mesh convergence is no longer practically feasable regarding the required computational resources.

In Abaqus, the CEL method can only be applied for three-dimensional models. In LS-Dyna, the similar ALE approach can be used for 1D (spherical symmetry), 2D and 3D models. Moreover, it features the possibility to efficiently

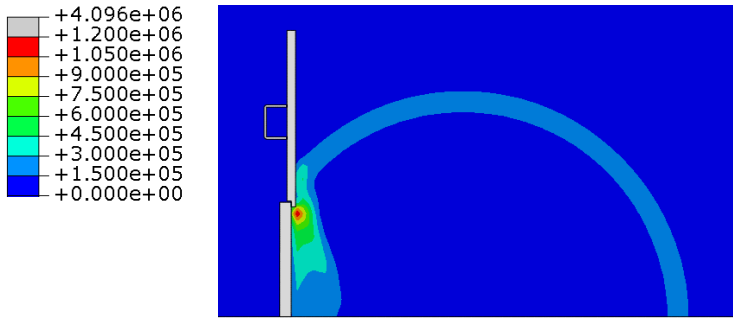

Figure 7.13: Contours of pressure [Pa] at $t = 0.36$ ms for CEL blast simulation; 20 g of C-4 at 300 mm standoff distance. Cut view at 175 mm from symmetry plane.

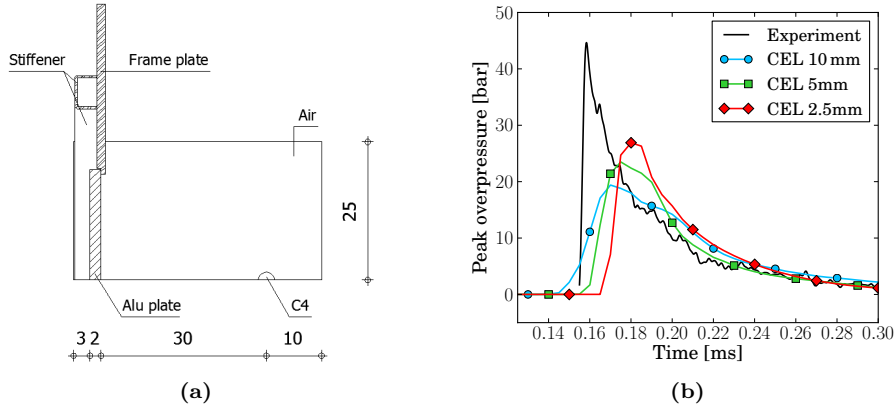

Figure 7.14: CEL simulation of blast with 20 g of C-4 at 300 mm standoff distance: (a) reduced model, (b) blast pressure at probe P1.

map results from one ALE model to another. This technique can be used to calculate the spherical expansion of the blast wave for a very fine meshed 1D model and map the results to a 2D or 3D domain before the shock front meets the test plate. The experiment can be idealised as axisymmetric with a flat, rigid surface, and is represented in a 2D, axisymmetric model.

The 1D model has a length of 300 mm and is meshed with a uniform element length of 33 µm. The 1D simulation is stopped at $t = 0.1$ ms, when the shock wave has propagated 250 mm from its origin. The result is mapped to the 2D axi-symmetric model, as shown in Fig. 7.15. The 2D model has a domain of 300×300 mm and a uniform element length of resp. 1.0 mm and 0.5 mm.
The blast pressure at the centre of the plate is given in Fig. 7.16 for both mesh sizes. Although the peak pressure is 7% higher for the finer mesh, the results

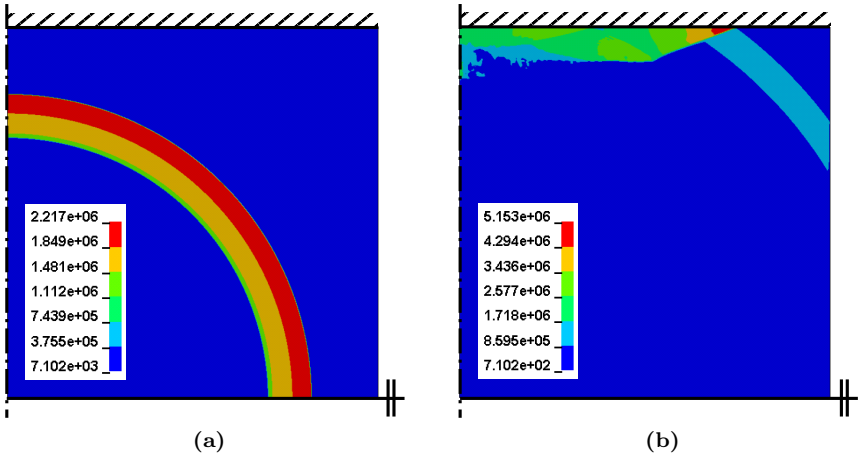

Figure 7.15: Contours of pressure [Pa] for ALE simulation of blast with 20 g of C-4 at 300 mm standoff distance: (a) mapped result at $t = 0.1$ ms, (b) blast reflection at $t = 0.2$ ms.

can be considered as converged for the pressure decay and impulse.

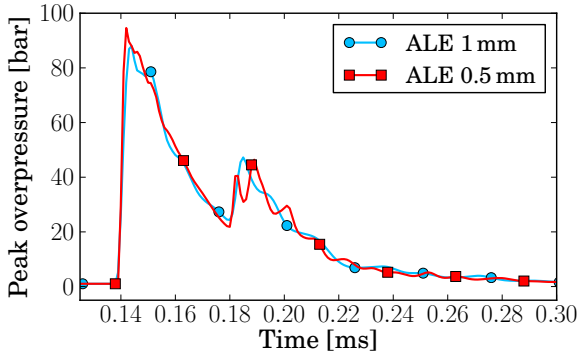

Figure 7.16: Mesh convergence for ALE simulation of blast with 20 g of C-4 at 300 mm standoff distance: pressure at probe P1.

The pressures at all probe locations are compared with the test data in Fig. 7.17. It is clear that the model greatly overpredicts the blast pressure and impulse for the considered case. This result is somewhat disappointing since the ALE method in LS-Dyna has been shown to produce accurate results for larger explosive charges, e.g. by Huang et al. [276] and Trajkovski et al. [277]. Apart from the magnitude of the pressure, also the reflected waveform is different: in the ALE simulation, a secondary shock front arrives in the wake of the initial

shock reflection at the center of the plate. This disappears as the wave travels further along the surface.

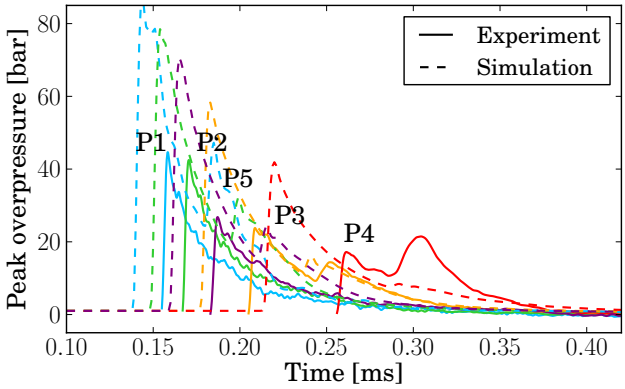

Figure 7.17: Comparison of ALE simulated blast pressures with experimental measurements; 20 g of C-4 at 300 mm standoff distance.

Thus, it can be concluded that the CEL and ALE techniques do not deliver the required accuracy to simulate the blast load on the surface of the test specimen. The emirical calculation tool ConWep does make a close approximation of the blast pressures at the evaluated locations, although it does not account for secondary reflections. Therefore, ConWep is used to apply the loads in further numerical analysis of open air blast.

7.3.3 Small-scale shock tube blast

When a high explosive charge is detonated at relatively large standoff distance from a building, the shock front arrives at the façade as nearly planar with an already much decayed peak pressure, but still high specific impulse. In an experiment, this type of load can be mimicked with a smaller charge (or suddenly opened pressure vessel) in a rigid shock tube. Because of multiple reflections inside the tube, the shock front becomes planar after travelling a certain distance and maintains a high pressure impulse.

A small shock tube has been installed between the charge and the same aluminium test plate in the LAEE test bunker, as shown in Fig. 7.18. The steel tube has dimensions of ∅425 mm × 1.5 m and is anchored to the floor. The charge is placed at the centre of the open end of the shock tube.

Fig. 7.19 shows that the shock front arriving at the test plate is indeed planar and quasi-uniform over the loaded surface. Moreover, the blast loading can be

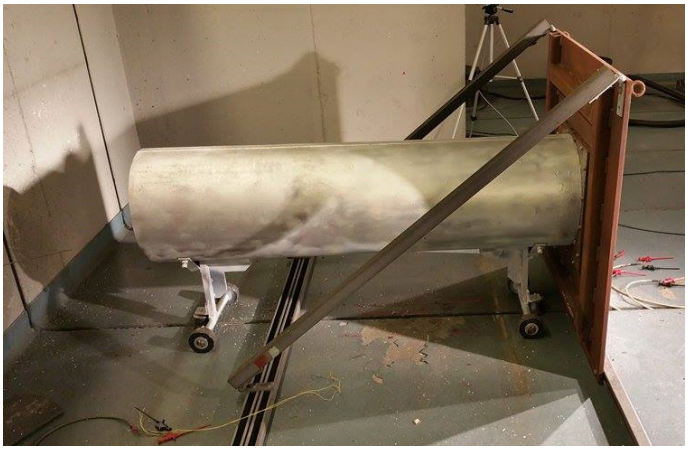

Figure 7.18: Test setup for shock tube blast on rigid plate.

repeated excellently. The average peak pressure is 11.03 bar and the average pressure impulse is 558 kPa ms.

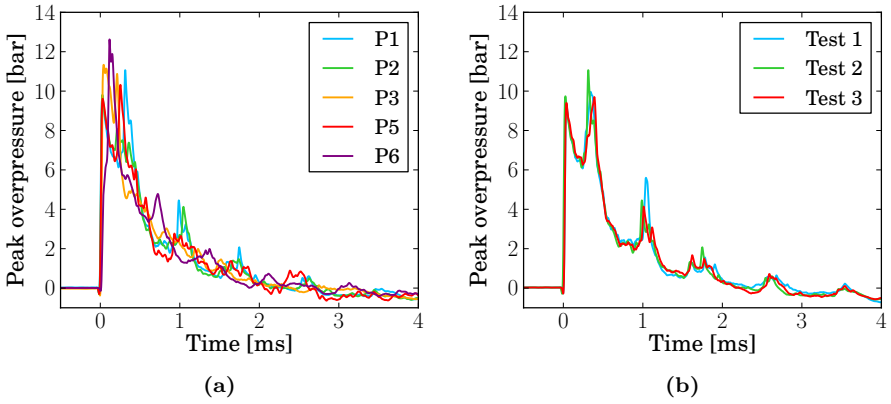

Figure 7.19: Blast pressures on test plate with 15 g charge of C-4 and shock tube: (a) at all probes in single test, (b) at centre (probe P1) in repeated tests.

The shock tube test, with a C-4 charge of 15 g, is simulated with the ALE method by a 2D axisymmetric model with a uniform element length of 1.0 mm. In this case, symmetry conditions are applied at the open end of the tube, while the nodes at the other end and at the side are constrained in all directions. Again, the pressure field is mapped from a 1D model of the detonation. From then on, the shock wave is reflected multiple times until a planar shock front

develops as shown in Fig. 7.20.

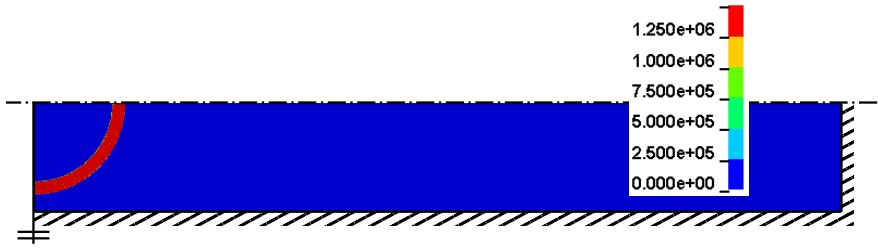

(a) $t = 0.05$ ms: mapped blast wave

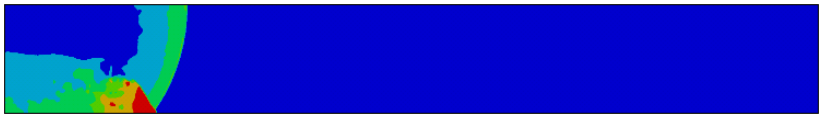

(b) $t = 0.19$ ms: origin of Mach stem

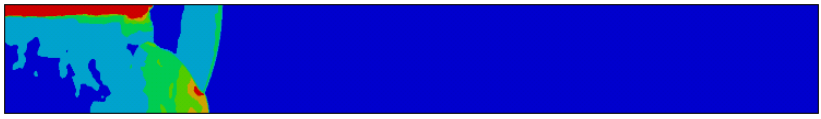

(c) $t = 0.27$ ms: reflected wave meets in center and forms jet

(d) $t = 1.05$ ms: shock front becomes planar

(e) $t = 1.29$ ms: reflection on test plate

Figure 7.20: ALE simulated evolution of blast wave in shock tube with 15 g charge of C-4.

Unfortunately, also in this ALE simulation, the loading on the test plate is overpredicted. Fig. 7.21 shows the pressures at the probe locations. The average peak pressure in the simulations is 43.7 bar and the average specific impulse is 3021 kPa ms.

7.3.4 Conclusions

The loading of a quasi-rigid surface in open air blast and shock tube blast experiments has been studied. Several manners to model the blast load numerically

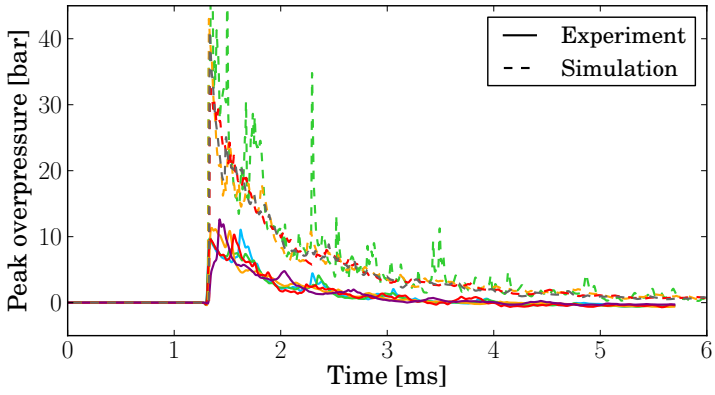

Figure 7.21: Comparions of blast pressures on test plate with 15 g charge of C-4 and shock tube: test data and ALE simulation (fringe values in [Pa]).

are tried and evaluated. It is found that the ConWep empirical calculation method is computationally efficient, easy to use and gives a fair estimation of the blast loading in an open air blast. However, ConWep only calculates the reflected pressures and does not include the effects of a propagating reflected shock wave. Therefore, it cannot be used when ground reflections or fluid-structure interaction become important. Eulerian and ALE hydrocodes do allow to model multiple reflections, formation of a Mach stem and fluid-structure interaction, but need a very fine mesh to reach a convergenced solution that captures the shock. The 1D to 2D ALE mapping approach in LS-Dyna enhances the computational efficiency greatly, but the resulting blast load on the test plate is highly overpredicted for the considered cases.

Because of the poor load predictions, the CEL and ALE methods are not used further to study fluid-structure interaction. For simulation of open air blasts, ConWep is an adequate tool, despite underestimating the impulse further away from the centre of impact. Shock tubes are usually employed in test environments, where the pressure is measured around the objective. Because the blast wave at the end of a shock tube is planar and uniform, the measured pressures can be applied as a load in numerical models. Also, Needham [234] argues that fluid-structure interaction is commonly not a concern in blast events because the duration of the shock load is generally much shorter than the duration of the mechanical response; deformation of a structure only becomes noticeable when the shock wave is long gone. This is also the case here when considering the deflection of the test plate in Fig. 7.11. But the interaction could be more important in the combination of very large glass panels and blast loading at a high scaled distance.

7.4 Laminated glass under small-scale open air blast loading

7.4.1 Experiments

A total of 30 open air blast tests on small 400×400 mm laminated glass plates have been executed by Van Dam [6] in the test bunker of the Belgian RMA. The setup for these tests, as described in the preceding section, does not use a shocktube and allow to exclude ground reflection. The same mounting frame is used for the glass specimens, which consist of two 3.8 mm glass plies, laminated to a 1.14 mm PVB interlayer. C-4 explosive charges of 20, 30 and 40 g were used at standoff distances ranging between 200 and 400 mm. Measurement of the test panel's response is obtained by use of the Digital Image Correlation (DIC) technique [230], which requires the application of a random speckle pattern on the back surface of the glass panel. Two high-speed cameras have been used to allow tracking of three-dimensional deformation and, before fracture, strains at the tension side of a test panel. However, the painted speckle pattern also obscures the observation of the onset of fracture.

The general post-fractured response of laminated glass panels in this test series shows following characteristics:

- The crack pattern for the square specimens describes an inner square of about half the plate dimensions. Heavily cracked zones are found along the diagonals between the inner square and the edges of the glass panel. The central area shows relatively few cracks, except for some of the plates that have been loaded with a high specific impulse. Typical crack patterns are shown in Fig. 7.22.
- No difference in behaviour is seen for specimens with low and high adhesion grade PVB interlayer (resp. Saflex® RC and RA).
- No tearing of the interlayer occurred in any of the performed tests.

Six tests have been subjected to the blast of a 40 g charge at 250 mm; three specimens with a Saflex® RA interlayer and three with Saflex® RC. These are the tests with the highest loading in the test series and are simulated with the methods described in Chapter 5. Measured with a pressure probe at the side of the frame, the average peak reflected pressure is $p_R = 4627$ kPa and the positive impulse is $i_+ = 54.93$ kPa ms. No negative phase is present, implying that the positive phase duration is infinite. However, the pressure has decreased to less than 1% of p_R after 0.21 ms.

Fig. 7.23 shows the deflection at the centre of the 6 considered test specimens. The panels are broken quickly after the arrival of the blast wave, although

(a) (b)

Figure 7.22: Typical crack patterns for laminated glass plates in small scale open air blast tests: (a) 20 g C-4 at 200 mm, and (b) 40 g C-4 at 250 mm.

it is not possible to determine the exact timing from the experimental data. Up to the peak deflection, the deformation of the broken laminates appears as consistent for all specimens, whereas the return stroke exhibits more scatter.

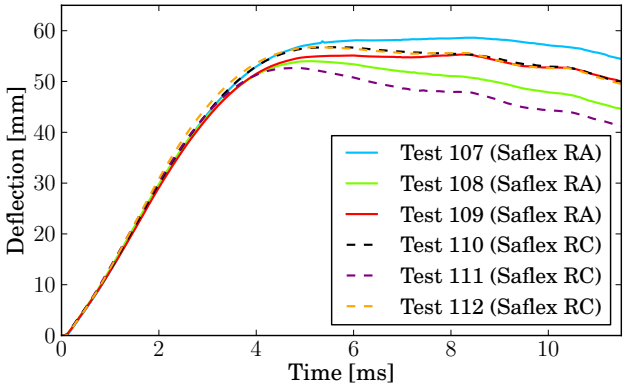

Figure 7.23: Deflection at the centre of laminated glass plates in small scale open air blast tests with 40 g C-4 at 250 mm: experimental data for 6 test specimens.

7.4.2 Numerical model

The numerical model for this test setup with laminated glass uses a simplified representation of the steel frame as a fixed, rigid part. The laminated glass specimens are clamped in the frame between two rings of wool felt. This

material is commonly used for bearing seals, bushings and precision gaskets. Its mechanical properties are given in Table 7.4. The material properties for glass are as given in Table 5.3, and the interlayer is described by the material model of Section 3.5, calibrated for a uniaxial test at 500 mm/s.

Table 7.4: Material properties for Auburn F-1 wool felt [278].

Density	341 kg/m^3
Shear modulus	2.98 MPa
Bulk modulus	1.45 MPa

Two mesh types for the laminated glass part are compared: an unstructured mesh and a structured mesh, suited to the crack pattern. Fig. 7.24 shows the meshes for a characteristic element length of 10 mm. In the simulation, an element size of 2.5 mm is used.

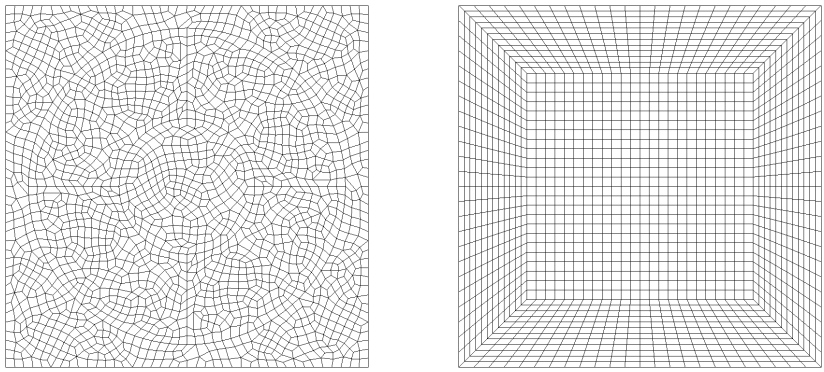

(a) **(b)**

Figure 7.24: Mesh topology for laminated glass plates in small scale open air blast tests: (a) unstructured mesh, and (b) structured mesh.

The glass surface between the edges of the frame is loaded with blast pressures as calculated with ConWep. The TNT-equivalent charge mass is 54.8 g, positioned at 25 mm from the centre of the glass plate.

7.4.3 Simulation results and discussion

The blast wave arrives at the glass surface at 0.1 ms after detonation. Only 0.2 ms later, the first cracks appear on the simulated glass plate. The crack patterns for the unstructured and structured meshes are given in Fig. 7.25 and 7.26. Similar to the experiments, the first and major cracks appear as an inner

square and along the diagonals. Later in the simulation, more cracks appear in the central area of the panel, which is seen for the tested glass panes as well, although not to such extent. For the structured mesh, it is clear that cracks are formed along the grid and rarely deviate into other directions. One of the consequences is that crack branching is handled with greater difficulty. An unstructured mesh allows for a more 'natural' formation of cracks along the direction of the maximum principal stress at fracture, as defined in the crack delay material model.

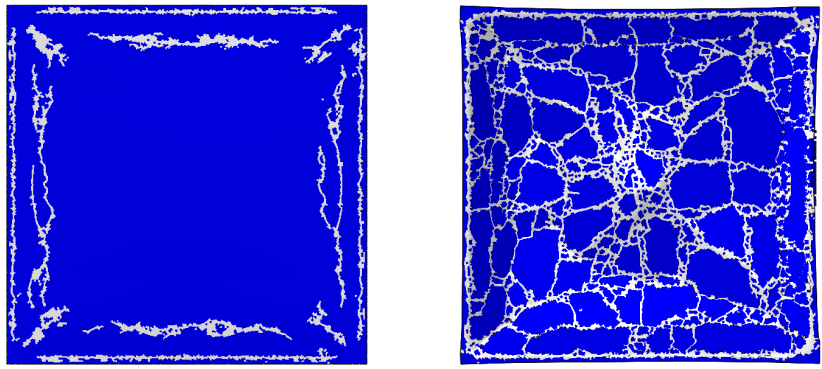

(a) $t = 0.3\,\mathrm{ms}$ **(b)** $t = 4\,\mathrm{ms}$

Figure 7.25: Crack formation for unstructured mesh of laminated glass plate in small scale open air blast tests.

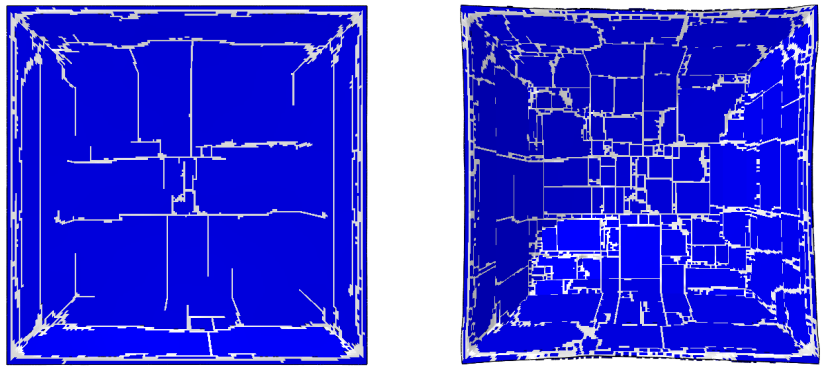

(a) $t = 0.5\,\mathrm{ms}$ **(b)** $t = 4\,\mathrm{ms}$

Figure 7.26: Crack formation for structured mesh of laminated glass plate in small scale open air blast tests.

Fig. 7.27 shows the deflection at the middle of the laminated glass panel for

the simulations in comparison with two of the experiments.

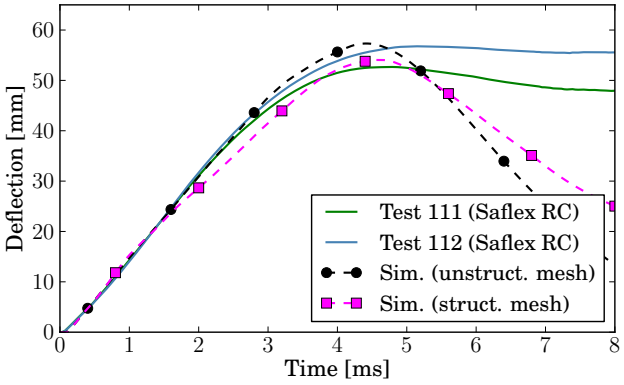

Figure 7.27: Deflection at the centre of laminated glass plates in small scale open air blast tests with 40 g C-4 at 250 mm: simulations vs. experiments.

The simulated results, especially for the unstructured mesh, agree well with the test data for as long as the broken laminate is being stretched out of its frame. On the return stroke, however, the simulated glass panes clearly act more flexible than in reality. The return stroke is also where the responses in the experiments begin to differ (see also Fig. 7.23). At that point, glass fragments come in contact and retain some compressive stiffness across the cracks. Subsequent deformation is determined predominantly by the extent of fracture and the crack topology, both of which may slightly differ for each test panel. However, numerical models with element deletion cannot take account of this behaviour as the simulated cracks are as wide as the size of each element. As such, the technique does not seem capable of capturing the post-fracture behaviour entirely. Nonetheless, the fact that the initial deformation and the maximum deflection are simulated rather well leads to believe that the model does capture some of the features of post-fractured response that allow to evaluate the design of a laminated glass window, including an estimation of the maximum forces exerted on the frame and substructure.

In addition, the deformation of the entire horizontal centre line of the glass pane is given in Fig. 7.28. It is seen that the deflection away from the centre is somewhat higher in reality than in the models. A possible explanation is found in the blast load being higher at these locations than the calculation by ConWep that does not account for the influence of earlier reflections, as seen in Fig. 7.10. It has also been observed in the tests that a portion of the wool felt rings slips out of the frame. Although allowed for in the numerical model, this does not take place in the simulations.

The simulation is repeated for a very fine, unstructured mesh with a charac-

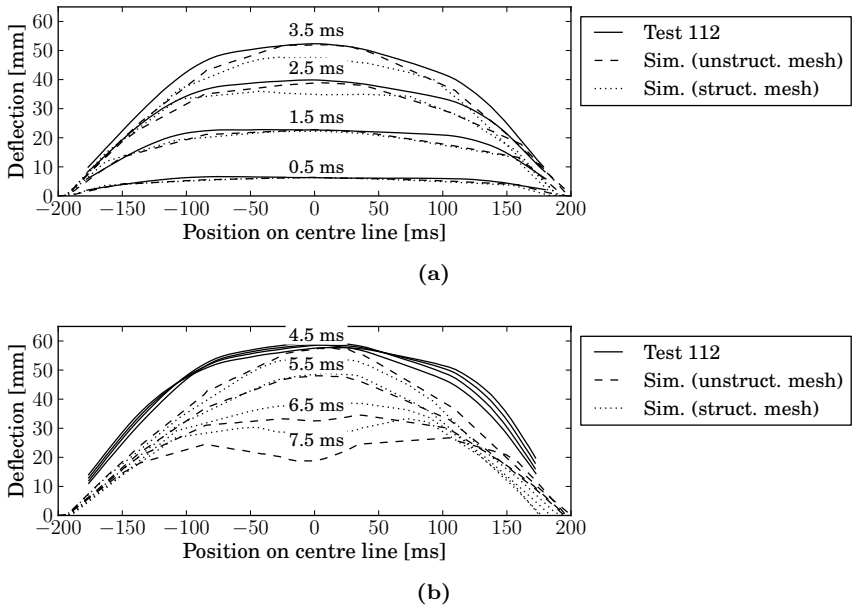

Figure 7.28: Deflection of horizontal centre line of laminated glass plate in small scale open air blast tests: simulation with unstructured mesh vs. experiment: (a) outward deflection, and (b) return stroke.

teristic element length of 0.5 mm to assess whether the post-fracture deflection in the return stroke could show better correspondence with the experiment when contact between different glass fragments is accounted for. However, even though contact between all glass elements is explicitly defined in this model, the continuum shell elements do not recognise penetration at their side faces. Consequently, the post-fracture behaviour is very similar to the results for the coarser mesh.

7.5 Laminated glass under large-scale shock tube blast loading

This section discusses the simulation of experiments that have been conducted in compliance with the standard EN 13541 [9]. The tests were performed by J. Kuntsche of TU Darmstadt using the large shock tube at the Fraunhofer Ernst-Mach-Institut in Germany. The description of the test series and the discussion of experimental results can be found in publications by Kuntsche, i.e. Refs. [7, 190, 211, 279]. A brief review of the experiments is given here for conception of the numerical models and further comparison with simulation results. Early numerical analyses using LS-Dyna software have been performed in collaboration with TU Darmstadt. This work is included here because it

revealed important considerations for numerical stability and sensitivity that have led to the development of the crack delay model, the hyper-viscoelastic material model for PVB and the study on FE representation for laminated glass. Finally, the developed techniques are applied to an ABAQUS model of the same load case and evaluated for their correctness and reliability.

7.5.1 Shock tube experiments

EN 13541 specifies that the 0.9×1.1 m test plate is to be clamped at all sides between rubber lining in a rigid frame with inner dimensions of 0.8×1.0 m. The rubber lining is 4 mm thick and has a hardness of 50 ± 10 IHRD. The clamping force is specified as $14 \pm 3\,\mathrm{N/cm^2}$. The considered laminated glass test panels are composed of two 6 mm annealed glass plies and 1.52 mm PVB interlayer. Plates with different PVB products have been tested, i.e. Trosifol® ES and BG, manufactured by Kuraray™. The ES-variant has a high glass transition temperature and is a stiffer type of PVB, similar to Saflex® DG interlayer. The Trosifol® BG products have elastic properties that are similar to Saflex® R-series and come in different adhesion grades. The results of uniaxial tensile tests for these interlayers are shown in Fig. 7.29 and their adhesion properties are given in Table 7.5.

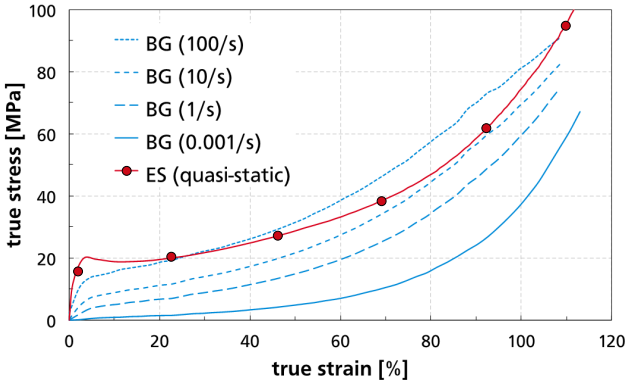

Figure 7.29: Stress-strain relationship of Trosifol® ES- and BG-variants at room temperature (data from Schneider et al. [157]).

The shock tube is shown in Fig. 7.30. After filling the compression section with highly pressurised air, a steel diaphragm is punctured to release the air into the expansion section.
The blast load levels specified in the standard are given in Table 7.2. Because the load step from one level to another is rather high, two intermediate steps have been defined to detect smaller differences in the performance of the interlayer types. These are referred to as ER0.8 and ER1.6, and characterised by

Table 7.5: Adhesion properties of Trosifol® PVB (data from Kuntsche and Schneider [190]).

PVB type (product name)	Pummel value	Bonding shear strength [MPa]
BG R10	3–4	6.5 ± 1.5
BG R15	3–4	7.0 ± 1.0
BG R20	3–4	10.5 ± 2.5
ES	(a)	11.5 ± 2.5

(a) Pummel test at $-18°C$ is not applicable for stiff interlayer material because the interlayer breaks during the test.

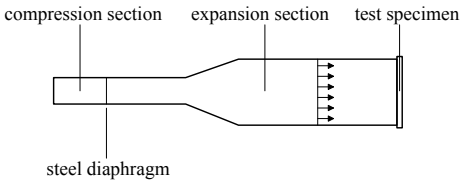

(a)

(b)

Figure 7.30: Blast shock tube at Fraunhofer Ernst-Mach-Institut: (a) schematic representation and (b) image of facility (figures from Ref. [119] and Kuntsche [7]).

the peak reflected pressure and positive impulse as measured during the test, given in Table 7.6.

Table 7.6: Blast load levels, peak pressure (p_R) and positive impulse (i_+) as measured (data from Ref. [119] and Kuntsche [7]).

Load level	p_R [kPa]	i_+ [kPa ms]
ER0.8	47	350
ER1	57	480
ER1.6	87	780
ER2	104	990
ER3	155	2000

In addition to the measurement of the free incident pressure and the reflected pressure, the strains at the middle of the outward-facing glass ply were measured by strain gauges to detect glass breakage. The displacement at the centre of the back-facing glass has been measured by a laser sensor in tests where no

total failure was expected, in order to protect the laser. A high speed camera was used to record the initial breakage of the glass, the breaking pattern and the evolution of the panel deformation. Fig. 7.31 shows the clamping of the test plate and the positioning of instrumentation.

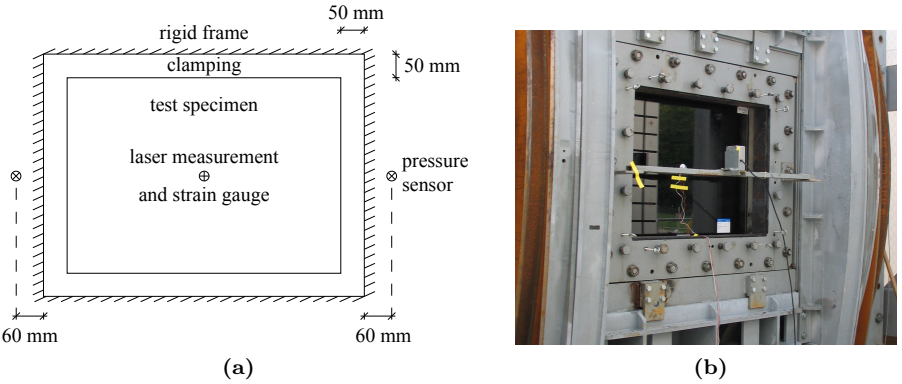

Figure 7.31: Test frame and instrumentation for shock tube: (a) schematic representation and (b) image of facility (figures from Ref. [119] and Kuntsche [7]).

The test is passed when there are no penetrable holes in the (broken) laminate or openings between the glazing and the frame afterwards. Although it is not mandatory in the European standard to indicate whether splinters flew away, an assessment of detachment was made by weighing the test specimens before and after the test. A first assessment of the post-breakage behaviour was done by a classification into four performance levels as illustrated by Fig. 7.32; the observed performance levels for all tests are given in Fig. 7.33. The latter figure shows that a lower adhesion leads to a superior performance under blast loading in terms of ultimate failure by interlayer tearing.

The stiff ES interlayer performed rather poorly in the shock tube tests. These laminates either remained fully intact with no glass fracture, or failed completely. A stiff PVB interlayer does not allow for much deformation to absorb the shock wave energy, and acts more brittle than a soft PVB interlayer. Consequently, a low adhesion level combined with low stiffness of the interlayer enables higher energy absorption of the shock wave by the laminate before its ultimate failure.

Fig. 7.34 shows the loss of weight after testing for load levels ER1.6 and ER2, obtained by weighing the panels before and after each test. The presumption that a stronger adhesion (BG R20) leads to lower mass loss than weaker adhesion (BG R10 and BG R15) cannot be confirmed. In all cases, the adhesion seems to be sufficient to prevent detachment of glass fragments from the inter-

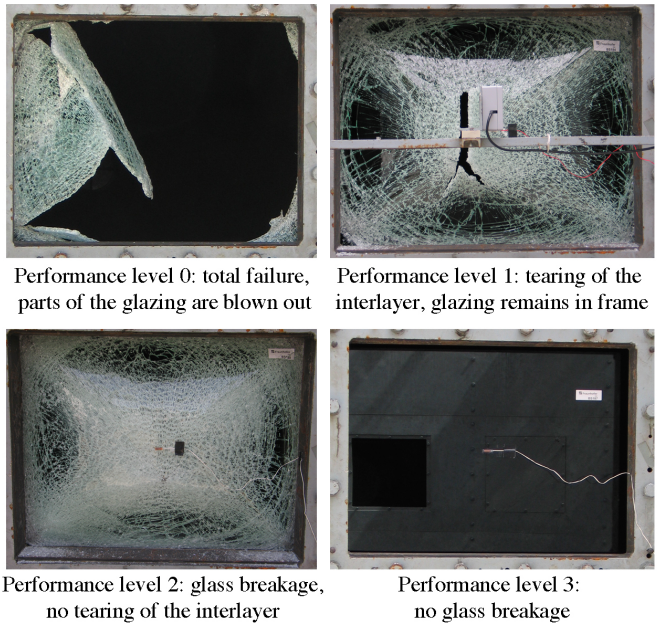

Figure 7.32: Performance levels for window glazing (figure from Ref. [119] and Kuntsche [7]).

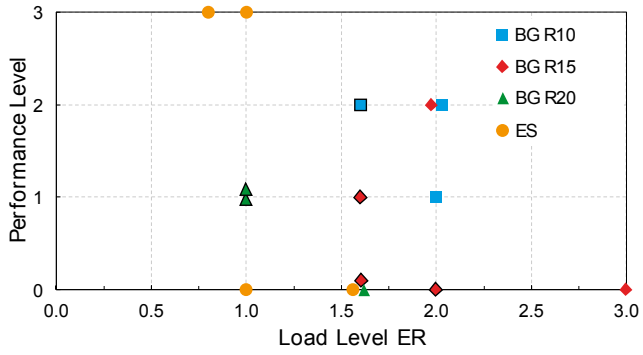

Figure 7.33: Performance level results for shock tube experiments on PVB-laminated glazing (figure from Ref. [119] and Kuntsche [7]).

layer as it is seen that debris is caused primarily by chipping of smaller glass fragments, rather than from delamination.

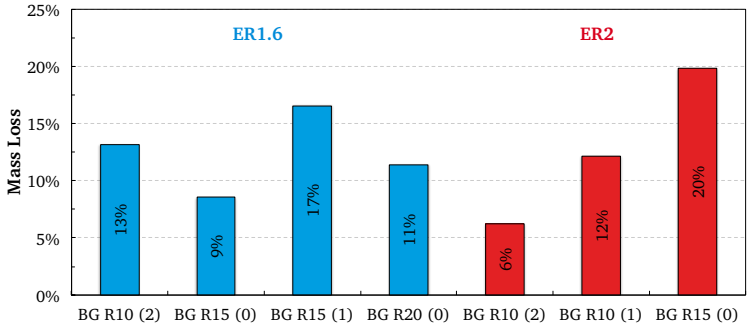

Figure 7.34: Weight loss for the different adhesion levels at load levels ER1.6 and ER2. Performance level of each specimen is indicated between brackets (figure from Ref. [119] and Kuntsche [7]).

7.5.2 Early simulations with LS-Dyna

The simulations aim to explore the possibility of assessing the post-breakage performance of a PVB-laminated glass panel under blast loading. This is only applicable to panels laminated with the soft PVB type, as it is seen that panels with the stiff ES-type PVB either remain intact or fail completely (see Fig. 7.33). The simulations for the soft PVB type are then compared to the experimental tests under ER1 and ER1.6 blast loading, for which sufficient measurement data is available.

The setup of the numerical model is shown schematically in Fig. 7.35. A tied constraint exists at the interface between PVB and glass. For correct representation of shear force transfer in the laminate, the shell nodal surfaces need to coincide with the materials interface, because tied contact in LS-DYNA does not consider the rotational degrees of freedom [280]. This implies that the shell nodes for the glass parts are offset from the mid-plane to coincide with the nodes of the interlayer part at the interfaces. This element configuration is equal to the LG2 configuration as described in Chapter 5 (where it was concluded to be the least favourable configuration, in Abaqus software).

The steel clamping frame is modelled as a deformable, linear elastic solid with outer dimensions of 1.14×0.94 m and a thickness of 6.0 mm, as in Ref. [211]. The nodes at the edges of the frame are constrained with fixed boundary conditions. The uniformly distributed blast load is applied to the free surfaces of the steel and glass parts on the side facing inward to the shock tube. Fig. 7.36 shows the time-varying reflected pressure as measured during the tests with a probe at the side of the frame.

LS-Dyna offers a number of constitutive models to define the material be-

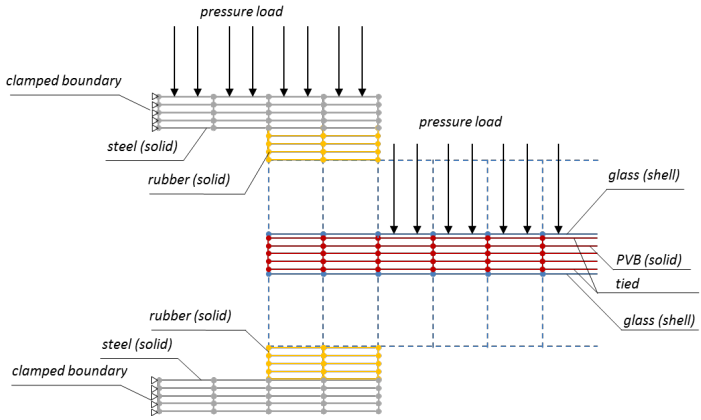

Figure 7.35: Sketch of element configuration, boundary conditions and pressure load for laminated glass under shock tube blast loading.

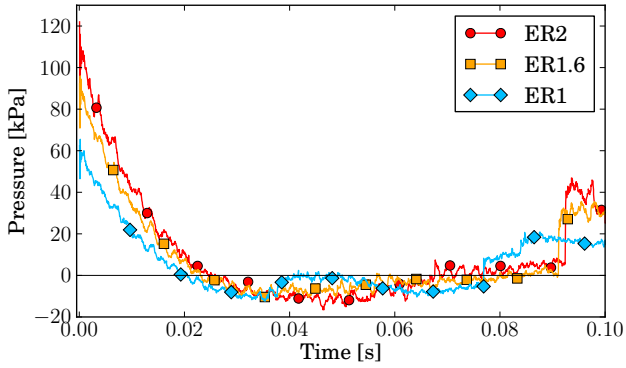

Figure 7.36: Reflected blast pressures for different load levels as measured with pressure probe in shock tube.

haviour of the PVB interlayer. One interesting option, considering the available (uniaxial) test data of Fig. 7.29, is the simplified approach for strain rate-dependent hyperelasticity by Kolling et al. [165], available in the software as MAT181. This material model requires only the input of stress-strain data of uniaxial tensile tests at constant strain rates. Subsequently, the test data is transformed into an Ogden functional not by parameter fitting, but as a tabulated formulation. This produces an exact fit of the input data, which cannot be obtained by a least squares fit to a polynomial function. Rate-dependency of the model is established by interpolation between the different Ogden functions at constant strain rate. Viscoelasticity of the material is not taken into account. As a consequence, the material model responds instantaneously to a

local change in strain rate, without any smoothening by viscous damping.

Although an appealing and elegantly straightforward approach, this material model seems to behave rather disappointingly when simulating the same uniaxial tensile test at 0.5 m/s that was considered in Chapter 3, as demonstrated in Fig. 7.37. The simulated forces are much higher than expected and the analysis turns unstable at an early point. Of course, the considered Trosifol® PVB is not exactly the same as the Saflex® in the experiment and temperature dependency is not included in the material model. But that still does not explain such great difference in the numerical results. Nonetheless, this material model has been used in good faith in the blast simulations with LS-Dyna.

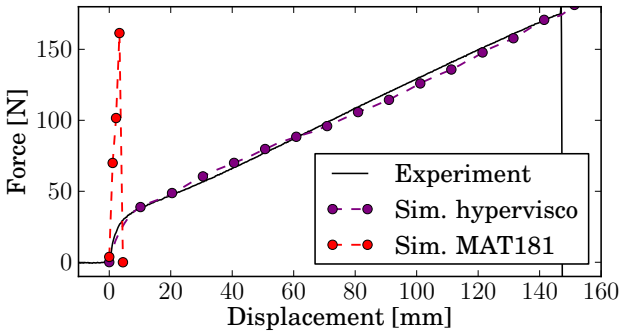

Figure 7.37: Force vs. displacement for uniaxial tensile test at 0.5 m/s and 23.2°C: simulations vs. experiment.

For glass fracture, the Rankine criterion can be used in LS-Dyna with instant element deletion within the same time increment where the critical stress is reached. However, the inability to include any damage softening phase quickly results in excessive deletion of elements at the boundary of glass fragments where reflection of high amplitude stress waves takes place, as shown in Fig. 7.38. As a result, the interlayer with little glass elements left is blown out of its frame. The same occurs when a critical strain criterion (de Venant) is used.

A workaround using a von Mises criterion with a short plastic phase is used instead, as used earlier for glass cracking by Du Bois et al. [102] and Timmel et al. [104]. The critical stress is taken as $\sigma_{cr} = 81\,\text{MPa}$, as described by DIN 18008-4 for glass under soft-body impact [215]. The element is ultimately deleted when a plastic strain ϵ_{pl} is reached. This plastic strain is not physical. Therefore a suitable value is determined by comparing the post-fractured simulation response, as shown in Fig. 7.39. A value of $\epsilon_{pl} = 1 \cdot 10^{-4}$ is further used in all the LS-Dyna models.

Because the element deletion technique is inherently mesh dependent, two diffe-

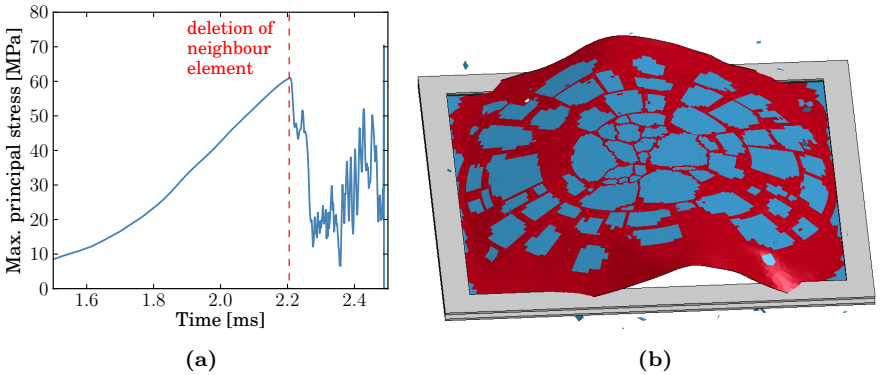

Figure 7.38: Use of Rankine crack criterion for glass in LS-DYNA: (a) stress oscillations in element neighbouring a failing element, and (b) excessive deletion of glass elements at $t = 75\,\text{ms}$ for ER1 load level.

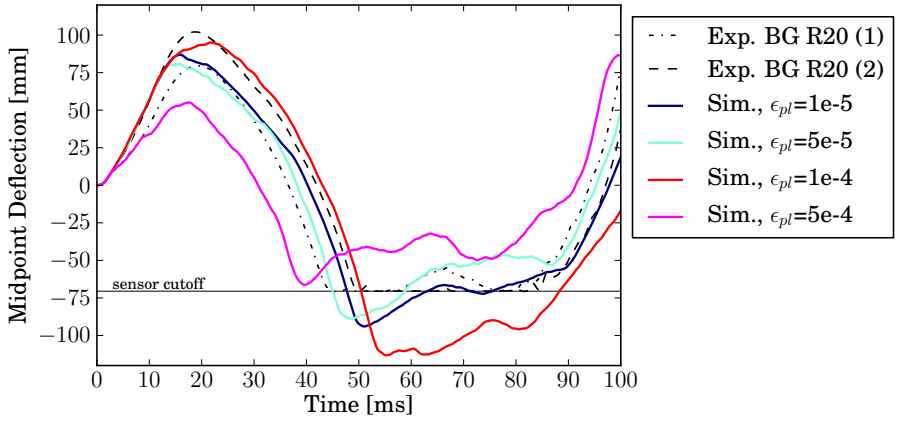

Figure 7.39: Central deflection of laminated glass panels under ER1 blast load: experiments and simulations for unstructured mesh with $L_e = 8\,\text{mm}$; influence of critical plastic strain in glass damage model.

rent mesh topologies are considered: an unstructured and a partially structured mesh, as shown in Fig. 7.40.

The resulting crack formation for the ER1 load is shown in Fig. 7.41. Radial cracks initiate from the middle of the plate at $t = 3\,\text{ms}$. The cracks then rapidly propagate and are most dense along the diagonals of the plate; this is more apparent for the unstructured mesh than for the partially structured mesh. As the blast loading persists, concentric cracks are formed around the edges. The behaviour for the ER1.6 load is similar. Thus, qualitative comparison seems to result in good correspondence, although Fig. 7.42 shows that rather large

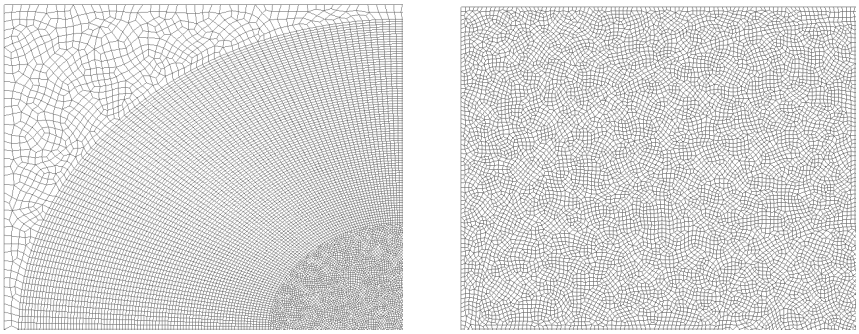

(a) (b)

Figure 7.40: Mesh structures for laminated glass: (a) partially structured mesh with characteristic element size Le = 4mm, and (b) unstructured mesh with Le = 8 mm. A quarter of each mesh is shown.

zones of elements are being deleted by the end of the simulations, especially for the partially structured mesh type.

The global deformation of the simulated panel, evaluated for the central deflection, is in reasonable agreement with experimental measurements, as seen in Fig. 7.43 for the ER1 load level, and Fig. 7.44 for the ER1.6 load level.

The experiments with high-adhesion BG R20-type interlayer at ER1 blast load (see Fig. 7.33) were characterised by early tearing at a time near the end of the positive blast phase. A tearing criterion for PVB is included in the numerical model as well: at a critical true strain of 120% [157], the PVB element is to be deleted. However, strain in PVB ligaments bridging a crack never reach such high values in the simulations; a first maximum is reached at time $t = 9$ ms with a strain amounting to only 14%. This can be explained by the size of the glass elements, i.e. 4 mm to 12 mm for the partially structured mesh and 8 mm for the unstructured mesh. When a crack forms in the simulation, there is immediately a wide gap where glass elements are deleted and the PVB element strains at those locations are bound to remain low. This is felt even more at the centre of the panel where many glass elements have failed. It is concluded that the current numerical models do not allow for prediction of interlayer tearing, unless calculations can be executed with much smaller element lengths.

The simulations at ER1 blast load are repeated for a refined mesh: the unstructured mesh has an element size of 5 mm; the element length in the partially structured mesh varies from 2 mm to 8 mm. With these meshes, the highest interlayer strains in the simulations amount to 30% for the partially structured mesh and 26% for the unstructured mesh. These strains are still too low to model tearing of the interlayer and ultimate failure of the panel. Further re-

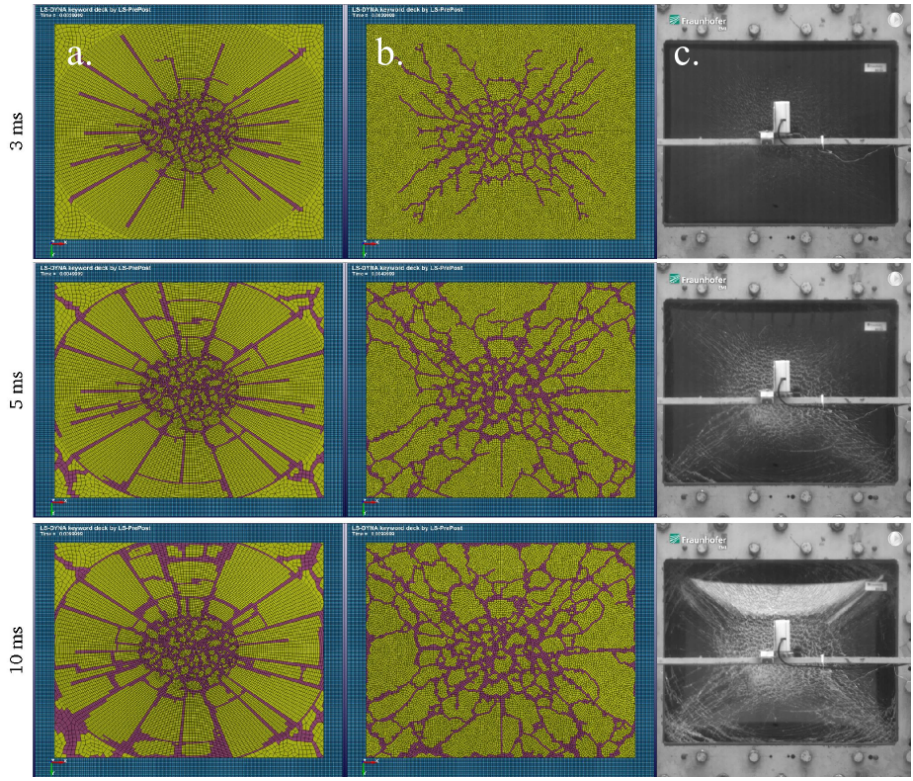

Figure 7.41: Simulated and recorded crack formation of laminated glass panel under ER1 blast load: (a) partially structured mesh, (b) unstructured mesh, and (c) experiment with Trosifol® BG R20 interlayer.

finement of the mesh comes at the cost of very high calculation times, which are already in the order of 50 hrs. using 8 parallel CPUs for the refined mesh analyses.

Laminated glass panels with low- and medium-adhesion PVB interlayer were tested under ER1.6 blast load. Correspondingly, the post-breakage response is simulated with and without delamination by erosion of the tie constraint between glass and PVB in the LS-Dyna model. The delamination model is in effect a cohesive zone with a linear, initially rigid traction-separation law. The bonding strength is taken as 10 MPa for both Mode I and II, while the combined fracture energy is assumed as 1500 J/m^2 for Trosifol® BG R10 interlayer. Unfortunately, the simulation that includes delamination by tiebreak contact at the glass-PVB interface is seen to largely overestimate the glass panel deformation after fracture, as shown in Fig. 7.44. This is ascribed to an unstable performance of the tiebreak contact in LS-Dyna, shown in Fig. 7.45,

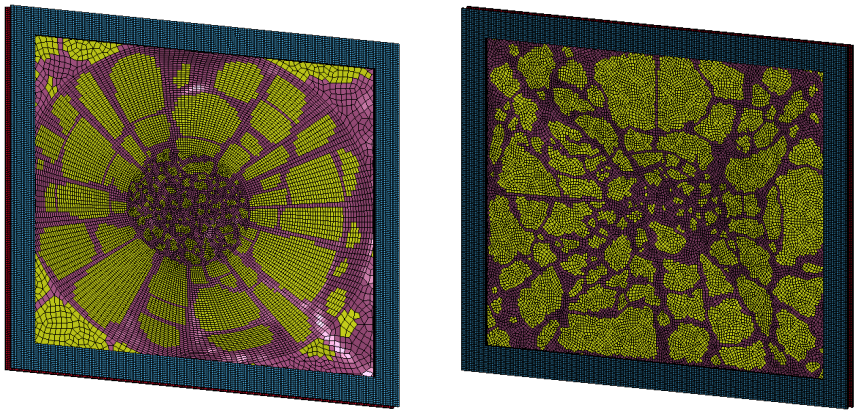

(a) (b)

Figure 7.42: Cracked laminate under ER1 load at $t = 100\,\text{ms}$: (a) partially structured mesh, and (b) unstructured mesh.

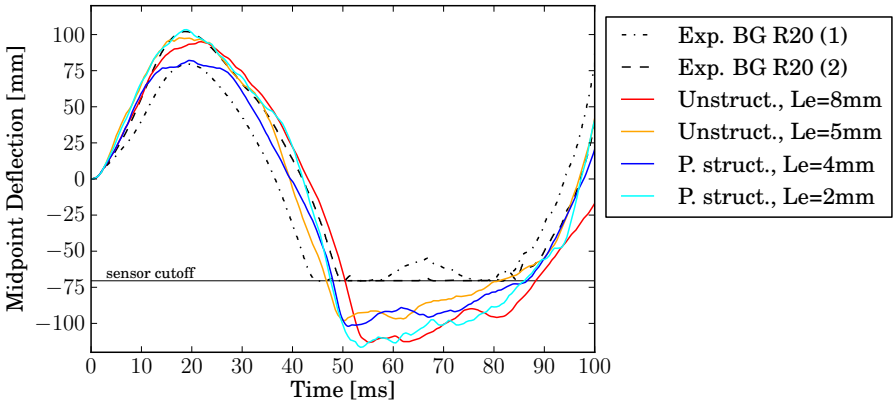

Figure 7.43: Central deflection of laminated glass panels under ER1 blast load: experiments and simulations. Characteristic element lengths are indicated for the simulations.

rather than to the actual simulation of local delamination.

In conclusion, even though seemingly good correspondence with experimental observations can be obtained, certain aspects of these models remain questionable. Furthermore, the need to fit the plasticity failure model for glass with prior access to experimental data is an obstacle when intending to use this modelling technique for reliable prediction. Therefore, simulation of the shock tube blast tests is repeated in Abaqus with the modelling approach developed

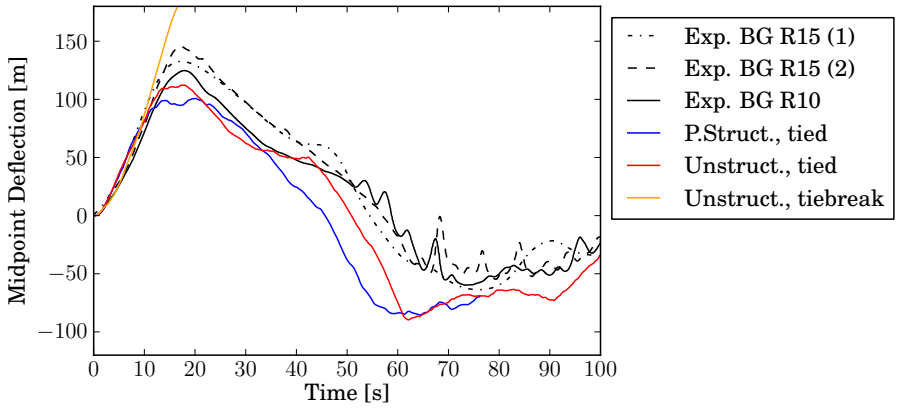

Figure 7.44: Central deflection of laminated glass panels under ER1.6 blast load: experiments and simulations. Characteristic element lengths are indicated for the simulations.

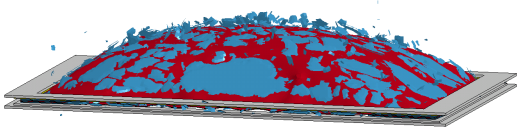

Figure 7.45: Unstable delamination by tiebreak in numerical result for low-adhesion laminated glass panel under ER1.6 blast load, at $t = 20\,\text{ms}$.

in the previous chapters. This approach attempts to stay closer to the physical behaviour of laminated glass with verified material models.

7.5.3 Simulations with crack delay model

The ABAQUS models are constructed in the same way as described in the previous section, except for the formulation of the laminated glass. The glass itself is modelled with the crack delay model and material properties given in Table 5.3. The Trosifol® interlayer behaves as in Fig. 7.29. Unfortunately, the available test data do not allow to fit a hyper-viscoelastic material model in the same way as described in Chapter 3. However, it can safely be assumed that the mechanical properties for Trosifol® BG-series and Saflex® R-series are very similar. Therefore, the material model resulting from Chapter 3, as calibrated for a tensile test at 0.5 m/s, is used for the PVB interlayer in these panels as well. The outside temperature during the tests has not been registered. Thus, the reference temperature of 20°C is assumed in the numerical model.

The mesh for the frame is the same as in the LS-DYNA models. Also the

topology of the meshes for laminated glass is the same, except that continuum shell elements are used for the glass instead of conventional shells with a full offset. Only the unstructured mesh type is further considered, because it has a more uniform element size and is able to capture the crack pattern more realistically.

Fig. 7.46 shows the ongoing fracture in the early stage of the simulation for a ER1 blast load. Unlike for the LS-Dyna models, little cracking takes place after $t = 10\,\text{ms}$ and no large zones of elements are being deleted around the edges of the panel. In comparison with Fig. 7.41, overall less extensive cracking takes place, although the resulting crack pattern is in better accordance with the experimental observation.

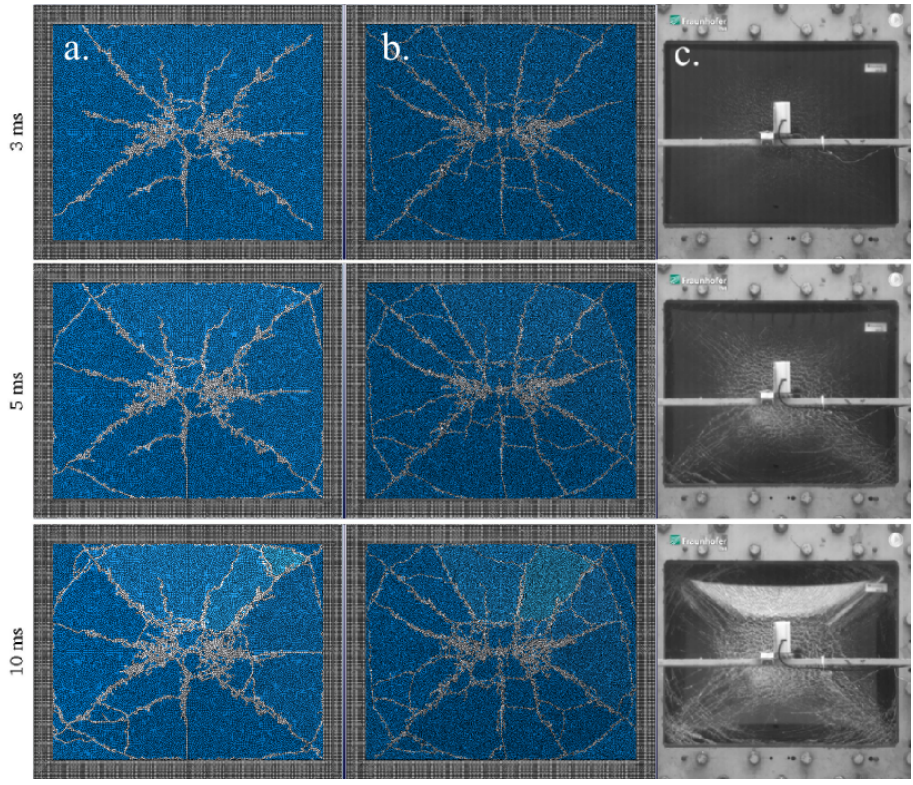

Figure 7.46: Simulated and recorded crack formation of laminated glass panel under ER1 blast load: (a) simulation with element size $L_e = 8\,\text{mm}$, (b) simulation with $L_e = 5\,\text{mm}$, and (c) experiment with Trosifol® BG R20 interlayer.

The deflection at the middle of the panel is compared with the experimental measurement in Fig. 7.47 for both mesh sizes. Similar to what is seen in Sec.

7.4, the deformation of the broken laminate corresponds well to the experiment up until the point of maximum deflection. Afterwards, the laminate rebounds quicker than in reality.

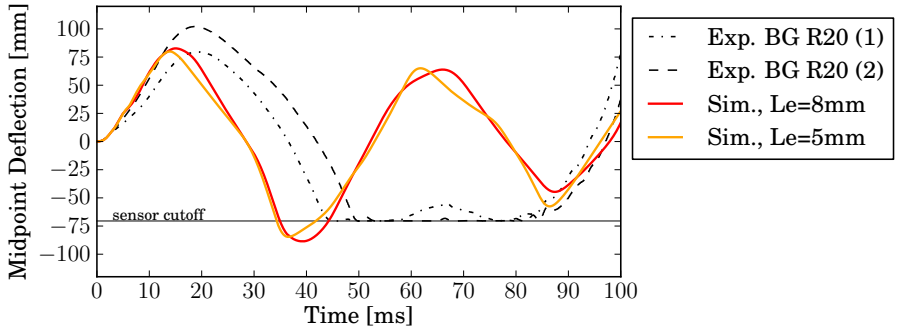

Figure 7.47: Central deflection of laminated glass panels under ER1 blast load: experiments and simulations with different mesh size.

The influence of various parameters is further investigated in Fig. 7.48 for the coarser mesh of the laminated glass panel. Because the outside temperature during the experiments is unknown, the simulation is repeated for $T = 10°\mathrm{C}$. The coefficient of friction between the rubber lining and the glass has been estimated as $\mu_f = 0.7$ in the original models and is repeated with a higher value. The crack patterns that result from variation of these two parameters are very similar to Fig. 7.46. Comparing the panel deflection in Fig. 7.48 shows that a lower temperature and higher coefficient of friction lead to somewhat stiffer behaviour after breakage of the plate, with slightly lower maximum deflection and quicker elastic rebound. However, this behaviour could be expected and the resulting curves are not tremendously different. The glass strength, on the other hand, does have a major effect on the numerical results. The simulated panel shows more extensive breakage when a lower critical stress $\sigma_0 = 50\,\mathrm{MPa}$ is assumed, as shown in Fig. 7.49. As a result, the panel acts softer and more flexible, being pushed out of the frame faster in response to the positive blast phase and reaching a higher maximum deflection. Nevertheless, the subsequent behaviour is in seemingly better correspondence with the deflection measured during the experiment. Whether this would also mean that the actual test panels would have a dynamic strength lower than 81 MPa cannot be concluded solely on this basis. The simulations with element deletion still differ from the experiments in several important characteristics. The number of cracks is certainly one that has a large role, accompanied with the stretching of the interlayer across the cracks. The maximum strain of the interlayer cannot be measured directly during the experiment, but Fig. 7.33 shows that both panels tested at ER1 load level get torn during the experiment, although this occurs

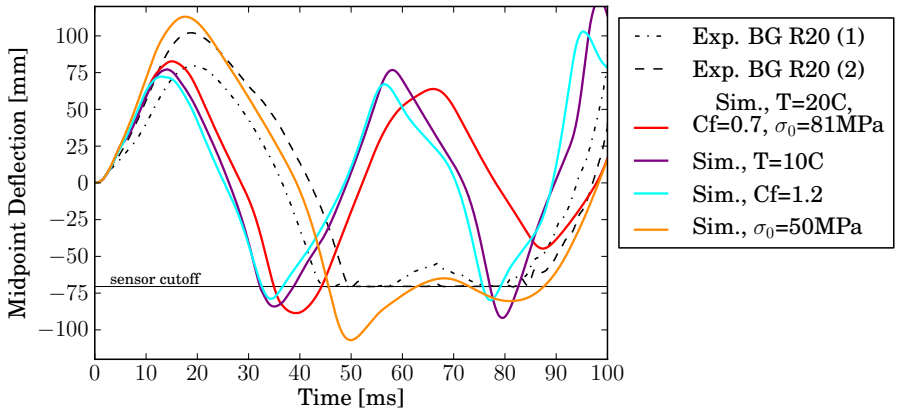

Figure 7.48: Central deflection of laminated glass panels under ER1 blast load: experiments and parameter sensitivity for simulations.

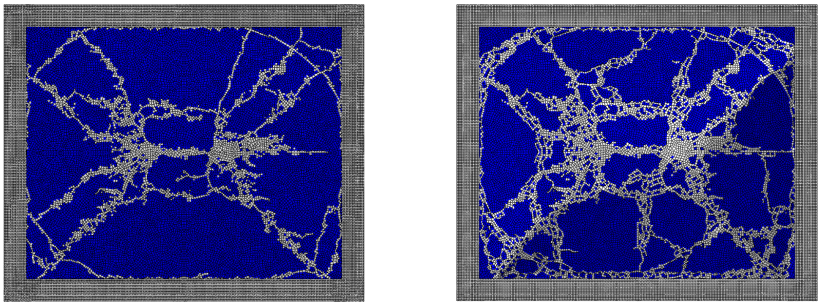

(a) $t = 3\,\text{ms}$ **(b)** $t = 100\,\text{ms}$

Figure 7.49: Cracked laminated glass panel under ER1 load with strength $\sigma_0 = 50\,\text{MPa}$.

at a time later than the recorded 200 ms after arrival of the blast wave. Thus, the PVB must locally experience an engineering strain higher than a minimum tearing limit of 120%. In the simulations, the maximum strain $\epsilon_{E,max}$ is reached around the centre of the plate at a time and value given in Table 7.7.
Although higher than for the LS-Dyna simulations, the strains remain lower than the most conservative tearing limit. Also the hypothesis that a finer mesh would be predicting higher strains for PVB ligaments cannot be confirmed. Because the central zone of the plate is most heavily fractured, the individual cracks are in many places wider than a single element, thus moderating the maximum strain recorded for PVB material between cracks.

Table 7.7: Max. engineering strain in ABAQUS simulations of laminated glass panel under shock tube blast load

Load level	Element size L_e	$\epsilon_{E,max}$	at time
ER1	8 mm	53.7%	16 ms
	8 mm ($\sigma_0 = 50$ MPa)	44.1%	17 ms
	5 mm	59.5%	42 ms
ER1.6	8 mm	107.5%	16 ms
	5 mm	99.4%	16 ms

Under the heavier ER1.6 blast load, the simulated panels show more extensive cracking, as shown in Fig. 7.51. Also in this case, the sequence and pattern of the appearing cracks roughly correspond to the consecutive images from the experiment. The deflection at the centre of the plate, shown in Fig. 7.50, corresponds to the test data in the same way as for the ER1 load, i.e. a good agreement up until the maximum deflection and showing more flexible behaviour during the return stroke and onwards. However, while the responses for the two mesh sizes are alike over the entire analysis duration for the ER1 load, some divergence is noted for the ER1.6 load.

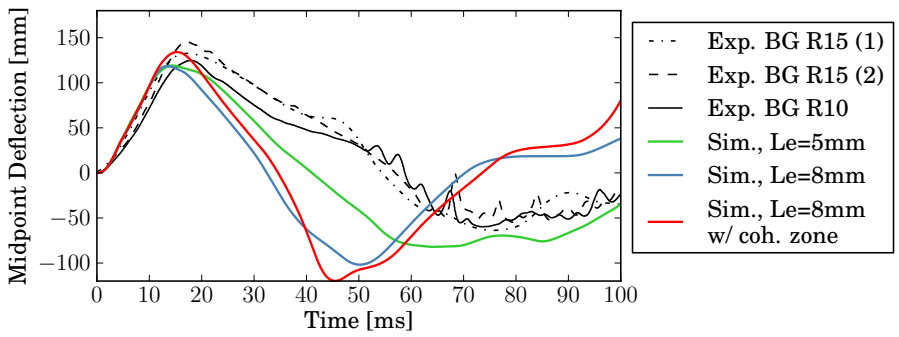

Figure 7.50: Central deflection of laminated glass panels under ER1.6 blast load: experiments and simulations with different mesh size.

The tests at ER1.6 loading show that panels with a lower adhesion grade are capable of absorbing the blast energy without tearing of the interlayer. It is interesting to explore whether the delamination can be included in the numerical models as well, despite the element size being considerably larger than what was required for mesh convergence in Chapter 4. A layer of cohesive elements with zero thickness is inserted at the interfaces between the glass and PVB. Properties for the bilinear traction-separation law are given in Table 4.7. Additionally, the initial stiffness of the cohesive zone needs to be defined. To avoid

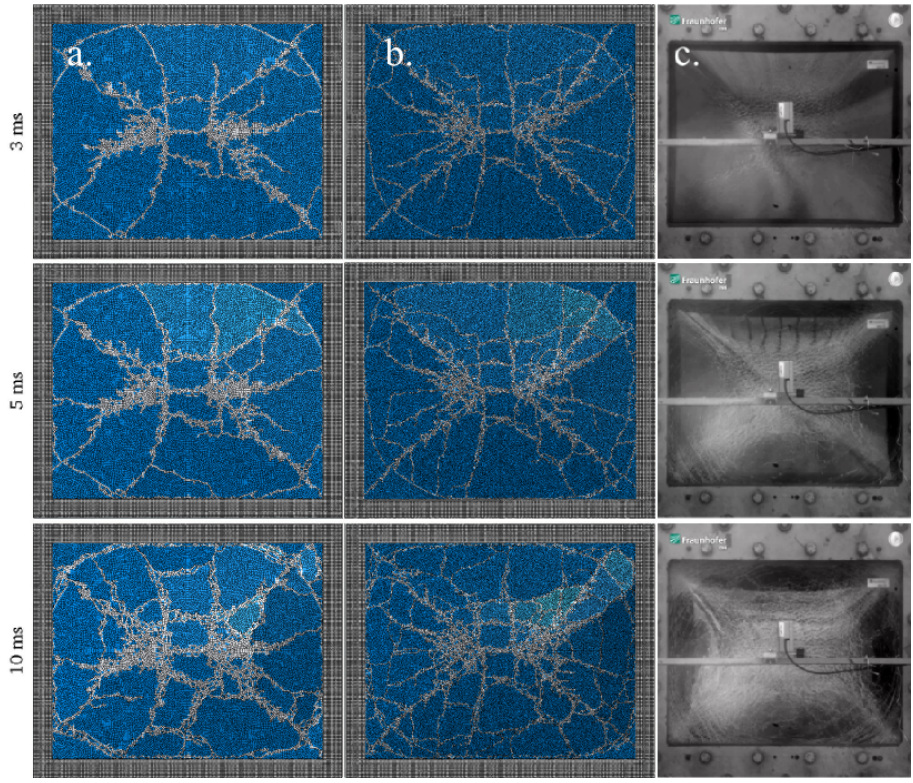

Figure 7.51: Simulated and recorded crack formation of laminated glass panel under ER1.6 blast load: (a) simulation with element size $L_e = 8\,\text{mm}$, (b) simulation with $L_e = 5\,\text{mm}$, and (c) experiment with Trosifol® BG R10 interlayer.

artificial compliance, a very high stiffness should be used, but preferably not so high that it leads to a decrease of the stable time increment. When interface stiffnesses $K_I = K_{II} = 10^{13}\,\text{N/m}^3$ are used, the elastic response is captured well and also the subsequent deflection in the post-crack phase is very similar to the case where delamination is not accounted for, as shown in Fig. 7.50.

However, in Fig. 7.52, it is seen that the model predicts a very high amount of delamination around the glass cracks. It is noted that a very fine mesh with elements of approximately 0.1 mm was needed to reach convergent results for the peel and TCT test simulations in Ch. 4. Such element lengths cannot be used for the cohesive zone in this model without significant loss of computational efficiency. The much coarser mesh used here is most likely at the basis of these unrealistic results.

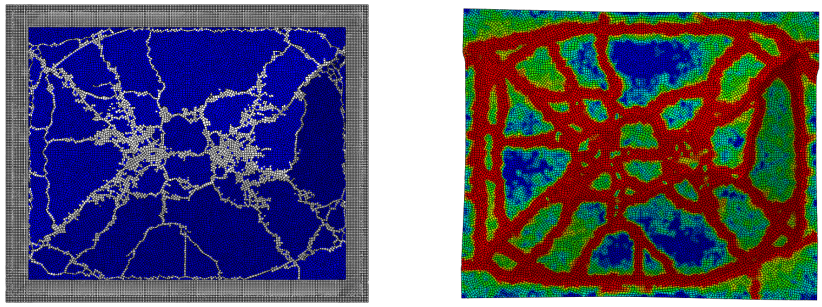

(a) (b)

Figure 7.52: Cracked laminated glass panel with delamination under ER1.6 blast load at $t = 100\,\text{ms}$: (a) cracking pattern, and (b) contours of delamination in cohesive zone between interlayer and outward-facing glass ply (blue: no delamination, red: fully debonded).

Nevertheless, it is seen that the delamination does have a reducing effect on the interlayer strain in the model. When a cohesive zone is present, the highest strain amounts to 46% (at $t = 14\,\text{ms}$), while this is ca. 100% without delamination.

Also the energy balances for simulations with and without delamination can be compared. Fig. 7.53 gives the energies for the simulation of the ER1.6 blast without cohesive zones at the interfaces, while the energies for the simulation with delamination are given in Fig. 7.54. The work performed by the blast load is absorbed by deformation of the panel and by friction at the boundary. When debonding is accounted for, energy is also dissipated in the delamination, which is seen to develop rather quickly as soon as the glass is broken. The dissipation by glass fracture remains realistically low as well as the dissipation by damping of stress waves through bulk viscosity. For hyper-viscoelastic materials in ABAQUS/Explicit, the internal energy includes the elastically recoverable energy and the viscoelastic dissipation in the material. As the recoverable energy would decrease again in the return stroke of the panel and fluctuate afterwards, it can be assumed that viscoelastic dissipation constitutes the greater part of the internal energy by the end of the simulation. For the model with delamination, the internal energy remains at a lower level, indicating that less energy is absorbed by viscoelastic relaxation of the PVB interlayer.

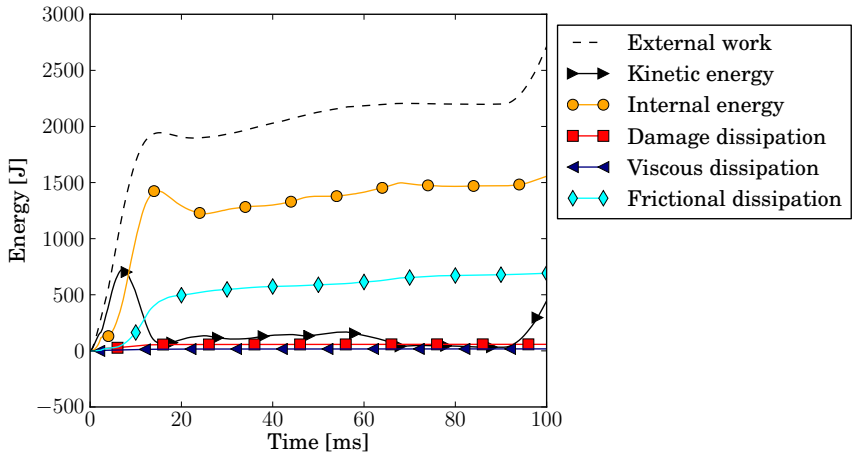

Figure 7.53: Energy balance for simulation of laminated glass panel under ER1.6 blast load; results for fine mesh with element size $L_e = 5\,\text{mm}$.

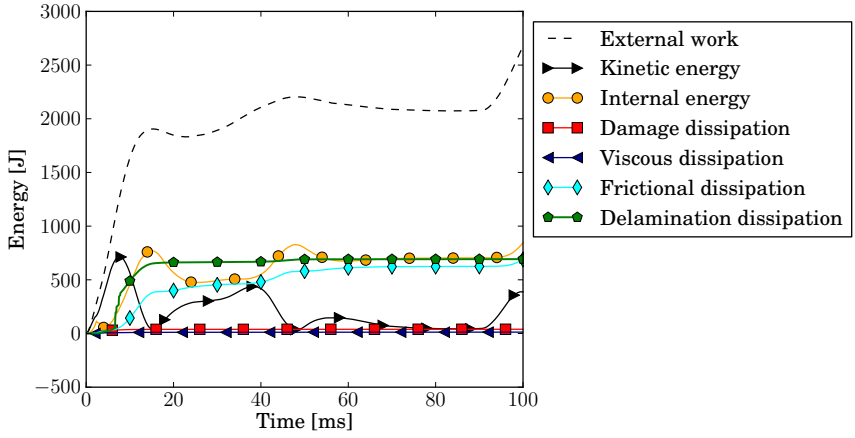

Figure 7.54: Energy balance for simulation of laminated glass panel under ER1.6 blast load with delamination; results for mesh with element size $L_e = 8\,\text{mm}$.

7.5.4 Conclusions

Shock tube experiments on laminated glass panels have shown that the susceptibility to delamination between glass and PVB is influential for the ultimate failure under high pressure loads. It is seen that the interlayer of a broken panel is less likely to be torn when an interlayer with lower adhesion level is used. Also the stiffness of the PVB product matters greatly, seeing that panels with

a very stiff PVB show no post-breakage behaviour at all; they either survive the test intact or disintegrate completely. The combination of lower adhesion and lower stiffness also implies that higher deformations are reached, so that more of the blast energy can be absorbed by the laminated glass panel. In comparison to panels with a higher adhesion grade, no notable difference in the ability to keep glass fragments from propulsion could be observed.

Two of the load cases are modelled numerically for a laminated glass panel with the softer PVB type. In early simulations, the criterion for glass fracture by element deletion consists of a yield stress limit, followed by a short plastic phase. With this approach, the global deformation of the fractured panel can be matched fairly well, but not the local behaviour. It is seen that rather large zones of glass elements are being deleted from the analysis, especially around the corners of the plate. Also the strain in the interlayer material bridging the cracks remains much lower in the simulations than in reality. Consequently, tearing of the interlayer could never be predicted.

When these simulations are repeated with the crack delay model and the hyper-viscoelastic material model for PVB interlayer, an improved cracking pattern can be obtained with finer cracks appearing in the correct locations. Without the modelling of delamination, this entails local interlayer strains that do come close to the tearing limit for the ER1.6 load case. Nonetheless, the same conclusions can be drawn for the deformation of the panel as in Section 7.4: a more flexible response is observed in the numerical result as the deleted elements no longer possess any stiffness in compression.

An attempt has been made to model delamination as well by including cohesive zone elements at the interface, for which the simulation shows that the interlayer strains remain at a lower level than when delamination is not included. Even though this model shows credible elastic response and post-fracture deflection, a very high amount of delamination takes place in the simulation. This rather unrealistic result is likely due to the coarse elements mesh, which is far from the element lengths in the order of 0.1 mm that were needed to reach mesh convergence for the debonding behaviour in Chapter 4.

Chapter 8

General conclusions and outlook

Fireball in a $2 \times 2\,\mathrm{m}$ *shock tube, recorded during field tests on laminated glass at Belgian Armed Forces testing grounds, April 2015. See the work of Sam Van Dam [6] for test results.*

8.1 Conclusions

In this work, an assessment has been made of the numerical simulation of laminated glass response to impact and blast loading. First, fracture models have been analysed for the cracking and fragmentation of annealed float glass, and the mechanical behaviour of PVB interlayer and adhesive debonding at the glass-PVB interface has been characterised. Subsequently, the modelling technique for laminated glass has been evaluated for different load cases.
In all impact and blast models, validation of the elastic response showed the importance of evaluating the representation of the boundary conditions and loads in the model, especially for dynamic behaviour. While this is common knowledge, this study is often not performed in practice.

8.1.1 Simulation of glass fracture

The most encountered modelling technique for the simulation of fracture in structural glazing and windshields is the element deletion technique. Even though this method leaves large gaps in the mesh and is highly mesh sensitive, it is found that element deletion is still the most capable method for the simulation of dynamic crack initiation, propagation, branching, intersection and fragmentation in large and thin glass panels.

The criterion for the failure of an element can be formulated in many different ways. Several damage models have been evaluated for their correctness and numerical implications of the implementation:

- When an element is suddenly removed when the critical stress is reached, the surrounding elements experience high stress oscillations. The reflection and interference of these stress waves may lead to secondary element deletion at the boundaries of fragments in a larger mesh. As a consequence, zones may be developed where little or no glass elements are left, which does not reflect the physical situation.

- The very high stress oscillations and excessive element deletion can be avoided by gradually reducing the element stiffness in a short damage softening phase before deleting the element. This relieves some of the energy from the stress waves and expends it as fracture energy. The softening phase can be regarded as physical, since cracking does not take place instantaneously and the formation of newly cracked surfaces requires some energy.

- The directionality of the crack can be taken into account by softening the stiffness only in the direction of the max. principal stress at the moment when the fracture strength is reached. When the crack direction is not

included in the damage model, the crack pattern may not be captured in a realistic way.

- The built-in *Brittle Cracking model in ABAQUS includes a damage softening phase that is defined foremost by the fracture energy. Because the fracture energy must include the strain energy in the element prior to failure, there exists a maximum element length for which the fracture energy can be correctly represented by a damage phase with monotonously decreasing traction-separation response. However, with the stiffness and strength of glass, this element length is in the order of 0.1 mm, which does not realistically allow to mesh a large glass panel.
  When the *Brittle Cracking model is used with larger element sizes, it is seen to behave as having a pseudo-plastic phase, which ends with the sudden failure of the element within one time increment. This damage phase also consumes far more energy than specified and does not reflect the physical crack formation of glass.

An element deletion model for glass is developed: the *crack delay model*. This model is based on the concept of delay damage, which states that cracking in brittle materials is bounded by a maximum damage rate. The cracking behaviour is defined only by physical material properties: fracture strength, fracture energy and maximum crack velocity. The same element length criterion applies to this damage model, but it is anticipated that the element size will be larger. For this reason, it is accepted that the effective energy dissipated in failure of an element includes the input fracture energy, added with the elastic strain in the element prior to failure. If the maximum damage rate is reached, an extra amount of fracture energy may be expended. However, this is also physically the case for a crack propagating at the maximum crack velocity. Meanwhile, the model ensures the monotonic decrease of the stiffness across the crack in the damage phase, whereby the directionality of the crack is accounted for.
In simulations of larger monolithic and laminated glass plates, it is seen that the energy dissipated by glass fracture, although overestimated, remains at a low level compared to the other energies in the analysis.

Two methods have been explored as alternatives for the element deletion technique. Despite showing some interesting features, their results have been found unsatisfactory for the crack simulation of glass panels.

- The SPH method has been considered because, as a meshfree particle method, there is no need for the deletion of any material; particles can be divided on either side of the crack and any arbitrary crack path can be followed naturally. However, the SPH method cannot be applied to

simulate the fracture of glass panels under low velocity impact or blast for two major reasons:

1. When the critical stress is reached at a point in the mesh, cracks are formed, but full fragmentation does not occur because particles across the cracks are still in each other's influence domain. Consequently, the plate has a softened bending stiffness after breakage, rather than being split by discrete cracks.
2. Practically, it would be too computationally demanding to realistically apply SPH for the modelling of large, thin glazing. No shell-like formulation exists for the particles, and a huge number of particles is needed to provide sufficient resolution.

Nonetheless, SPH is a good choice for simulating the local damage behaviour under high velocity impact, such as ballistic loading. For such application, examples can be found in literature and also in this work, it has been shown that full fragmentation can be simulated for a glass disk impacting at high speed.

- The cohesive zone method is better suited to simulate the propagation of multiple discrete cracks under dynamic loading and advances to the technique are currently still being developed. In the current version of ABAQUS/Explicit only the intrinsic approach with cohesive interface elements can be used. In this formulation the cohesive zone method suffers from artificial compliance when zero-thickness elements are present in the mesh. This problem can be resolved by assigning a small thickness to the cohesive elements, although this leaves small gaps in the mesh at the edges of all bulk elements. In the simulation, cracks are quickly initiated when the fracture strength is reached and the failed cohesive elements leave very thin cracks, which is more realistic for glass. However, a great number of cracks are formed simultaneously, thus instantly reducing the stiffness of the entire plate. Because of this, the cracks do not propagate any further and no fragmentation of the glass is simulated.

8.1.2 Characterisation of PVB interlayer

In all experiments with laminated glass at Ghent University, Saflex® PVB was used. Tensile testing of this material showed that the deformation rate has a very outspoken influence on the stiffness of PVB, as well as the temperature. At the higher deformation rates, the force-displacement curves show a defined turning point that bears similarity to a yield point, followed by a plastic hardening phase. But PVB does not show any permanent set, even after large deformation, and is best modelled as a nonlinear viscoelastic material. In literature, however, only simplified representations for the mechanical behaviour

of PVB are found. This can be justified for most common load cases, but for the dynamic failure analysis of laminated glass and for quasi-static analysis of adhesive debonding, it is absolutely necessary to use a nonlinear viscoelastic model for the PVB interlayer. In both cases, large strains and high strain rates are locally reached.

A material model for PVB interlayer can be formulated as a combination of viscoelasticity in a Prony series formulation and a reduced polynomial strain energy potential for the instantaneous behaviour. This model can be calibrated to fit the tensile test data by simulation of the tensile tests. At higher strain rates, a high order polynomial formulation is required for the strain energy potential; firstly, to capture the quick change in stiffness at small strains, and secondly, to avoid undulations in the stress-strain curve that might lead to instability of the numerical analysis.

The resulting material models are calibrated for a specified range of strain rates (and temperature). Outside of this range, the material behaviour at moderate to large strains is no longer described accurately. Thus, care should be taken to correctly apply the PVB material model that is calibrated for the expected deformation behaviour.

8.1.3 Characterisation of adhesive debonding at the glass-PVB interface

The adhesion between glass and PVB has an important role in the safety performance of laminated glass when fractured. Sufficient adhesive strength is required to withhold glass fragments from projection. However, allowing for some delamination can be beneficial, as this relieves the strain of the PVB material across the glass cracks and may prevent failure by tearing at these locations. Moreover, a portion of the impact or blast energy is absorbed by the delamination.

The adhesion in laminated glass can be characterised by several test methods. With the exception of the pull-off test to identify the interfacial strength, the quantities measured in these tests are characteristic for the bond, but not a direct measure for the adhesive properties between glass and PVB. Therefore, a numerical approach with the cohesive zone method can be used to analyse the peel test and through-cracked tensile (TCT) test in detail. This allows to capture the steady state response by iteratively finding the cohesive zone properties. In the development of the numerical models, it was found that the simulation of these tests does not allow for much simplification and several influential parameters could be identified:

- For the peel test, the plasticity of the aluminium backing foil should be included in the analysis. If not, the interfacial debonding energy

is greatly overestimated in the simulation. Also, the plastic deformation absorbs some energy of the exerted work, as well as the dissipation by viscoelastic relaxation in the PVB interlayer. These energy absorptions are overlooked when the delamination energy is determined from the force-displacement test data only.

- In both the peel and the TCT tests, the PVB material is being strained to a high extent: 42% around the crack tip in the peel test, and 170% in the TCT test (both eng. strain). Moreover, a quick change of the strain rate is found close to the crack tip in both cases. For these reasons, it is absolutely necessary to account for the highly nonlinear viscoelastic nature of the PVB interlayer in the calculations.

- Contrary to common assumptions, debonding in the peel test is not purely Mode I, and in the TCT test it is not purely Mode II. The analysis of both tests requires a mixed-mode formulation of the cohesive zone.

- In TCT tests, the interlayer shows notable contraction at the middle section, which is more correctly captured in a 3D simulation. Comparison with a simplified 2D, plane strain representation of the same TCT test showed that the 2D simulation overpredicts the steady state force and underestimates the crack propagation speed.

- The simulation method allows to identify the Mode I and Mode II debonding energy, but not the interfacial strength. For this reason, additional tests need to be performed, such as the pull-off test to characterise the Mode I strength.

8.1.4 Characterisation of pendulum impact and blast loading

A detailed numerical model has been developed for the pendulum impact setup, described by the European standard EN 12600 [8]. The model aims to represent the tyres close to their physical composition and could be validated for quasi-static compression, impacts at different drop heights against a force and pressure plate setup, and against a thick, monolithic glass panel. For the simulation of impact against a laminated glass panel, the detailed model shows very similar response as the simplified, but highly efficient modelling approach in SJ Mepla software. This indicates that the use of a detailed numerical model would not be beneficial as a calculation method for qualification to the standard.

For fluid pressures acting on a surface, such as in an explosive blast, it may be interesting to account for the fluid-structure interaction in numerical simulation, as the acting pressures may be altered by deformation of the surface. However, in blast loading of a structure, it is most often seen that the blast

wave has already passed when the structure begins to show any noticeable deformation. Therefore, it may be assumed that the influence of fluid-structure interaction is negligible for the blast response. Consequently, the load may be represented by the equivalent pressures acting on a rigid surface. In a finite element model, the pressure load can be applied either directly or by use of an empirical calculation method such as ConWep.

8.1.5 Simulation of laminated glass under impact and blast loading

To efficiently model larger laminated glass plates, an element configuration can be used where the glass is discretised by shell elements, rather than different layers of solid elements. This also implies that a crack always runs through the full thickness of the glass ply, once an element is deleted. In the default formulation for element deletion in ABAQUS, an element is only deleted when all of its integration points have reached failure. Consequently, many elements remain active in the simulation with some of their integration points no longer capable of bearing stress. Because of this, the propagation of many cracks is halted. For continuum elements, the semi-failed state often leads to excessive element distortion, which causes the analysis to abort. However, in reality, a sharp crack tip is present, by which the glass is quickly split through its thickness. Therefore, the adapted formulation of the crack delay model for shell elements requires an element to fail as soon as full damage is reached at its first integration point through the thickness.

Three different element configurations for laminated glass have been evaluated:

- The configuration with a continuum shell element for each glass ply, coupled with solid elements for the PVB interlayer allows to model the transfer of shear stresses by the interlayer. Very good correspondence with experimental observations for an impact test with single-sided glass fracture could be obtained, both for the cracking pattern and for the acting forces acting in post-fracture response. For fracture at both sides of a laminated glass panel, models with this element configuration are capable of realistically simulating the global post-fracture response as well.
  However, further simulation of laminated glass panels under blast loading shows that the broken panels respond more flexibly in the return stroke of their deflection than observed in experiments. This may be due to a lack of compressive stiffness across the glass cracks, because the deleted elements leave rather large gaps by which the neighbouring elements do not get into contact at the compressive side. This presumption could not yet be verified by simulation with a very fine mesh, as sideways contact between continuum shell elements is not recognised.

- A configuration with solid elements for the PVB, coupled with shell el-

ements with full nodal offsets from the midplane has been abandoned because the stress at the outer surfaces is no longer calculated well in ABAQUS/Explicit when the aspect ratio of the shell thickness to element length becomes too high. Consequently, elements failed prematurely and post-fracture response was not at all captured well, even though the simulated cracking pattern does appear as realistic.
It should be noted that the large errors in the stress calculation are not experienced when the same configuration is used in LS-DYNA software.

- An efficient configuration with a coinciding shell and membrane element can also be used, though not for single-sided fracture. Elastic response to an impact is captured well when the shell element is given the same thickness as the laminate. This shows that the PVB interlayer behaves sufficiently stiff under dynamic loading to assume equivalent monolithic behaviour of the laminate.
  When fracture takes place, the resulting crack pattern is more dense than for continuum shells, but a similar, global post-fracture response is achieved.

Consequently, the element configuration with continuum shell elements is preferred. Also contact is treated more easily with this configuration, because no offsets need to be taken into account.

For all simulated test cases, the fracture strength remains the singlemost defining factor for the response of a glass panel. However, this parameter is not so easily determined because of the high variability that can be found in different glass samples. When the aim of the numerical model is to make a prediction of the post-fracture response, only a prescribed value can be used, which may not always reflect the reality so well.

The mesh topology for the laminated glass panel can either be random and unstructured with a quasi-uniform element size, or structured in a way that is suited for the expected cracking pattern. Both approaches show a similar result for the post-fracture response. In this work, an unstructured mesh was generally preferred because it allows the crack paths to be found more naturally. Also, because the crack delay model uses the element length in calculation of the maximum damage rate, a more uniform element size is preferred.

Mesh refinement generally results in very similar global behaviour of the plate in the post-crack phase, but with more discrete cracks being formed. It would be expected that mesh refinement leads to higher local strains in the PVB, because the cracks are thinner. But this is not confirmed in the simulation results, where the maximum interlayer strains are of similar magnitude as with a coarser mesh. In simulations of test cases in which several laminated glass specimens were torn, the following maximum engineering strains are found:

ca. 120% for both thick and thin panels under pendulum impact as described by EN 12600, and ca. 100% for a laminated glass panel under ER1.6 level shock tube blast loading. In these models, the highest strains are found at interlayer ligaments in between the cracks in the central area of the panel, which corresponds with the location of tearing in the corresponding experiments. However, these maximum strains are still lower than the experimentally found tearing limit of PVB, which is found at 170% engineering strain. Nonetheless, a lower, conservative critical strain could be used to evaluate the qualification of a laminated glass panel for a certain load level by numerical modelling. A more severe criterion is also more realistic, to compensate for the inability of the numerical method to capture the cutting of interlayer ligaments by the sharp glass fragments. However, to determine the critical value for qualification, the reliability of this method should be further investigated by application of the proposed simulation technique to more and different tests with interlayer tearing than the two cases discussed in this work.

Delamination of the laminated glazing can be taken into account in the impact and blast models by including an intrinsic, zero-thickness cohesive zone at the glass-PVB interfaces. A sufficiently high cohesive stiffness should be defined to preserve the elastic response of the laminate. The analysis of shock tube blast on a laminated glass panel showed that delamination takes place in the simulation after cracking of the glass, and results in lower interlayer strains than when delamination is not included in the model. But the delamination in the numerical result occurs to a rather high extent that does not seem realistic. This may be due to the element size, since the analysis of peel and TCT tests showed that a very fine mesh (element length in the order of 0.1 mm) is needed to find a converged solution for the debonding.

In general, although showing fairly good correspondence of the global post-fracture response up to a certain point, it cannot be concluded that the robustness of this method has been established. Also, to truly predict the ultimate failure, the model should be capable of more accurately capturing the local behaviour for the strain in the PVB material at the gaps between the cracks and for delamination at the crack edges. The ability to do so is highly related to the element size. Therefore, this would remain the greatest challenge when the glass fracture is modelled by a different method that does allow for the simulation of very thin cracks.
However, the effect of delamination on the safety performance is only really observed for the higher blast loads in shock tube testing. It can be assumed that for many, more common impact cases, it is not necessary to account for delamination in a numerical model.
Nonetheless, the presented simulation method can be used to assess the maximum forces and interaction with an impacting human body or the supporting structure of the glazing into the post-cracked phase.

8.2 Recommendations for future research

This research work has focused on the development of a modelling technique to simulate the post-fracture response of laminated glass under dynamic loading. Some suggestions of the topics requiring further attention and areas for investigation that were not covered in this dissertation are given here.

- Up until now, the element deletion method is still the best option for simulation of the post-fracture response of glass under dynamic loading. Some promising alternative methods are currently still being developed and are not (yet) available for use in commercial FE software. In Ch. 2, it has already been mentioned that the discontinuous Galerkin formulation for the cohesive zone method (CZM) [91] overcomes the most critical shortcomings of the intrinsic and extrinsic CZM approaches. Recent advances in this field show the application of this method to the dynamic fracture of large, brittle shell structures [144, 145].
  Another method that could be considered is the Applied Elements Method (AEM) [281], in which the material is discretised by rigid body elements that are connected via zero length springs at the interfaces, which can be removed upon reaching of a failure criterion. This method has recently been applied to model the fracture of monolithic glass under blast loading [282], and can also be applied to model the collapse of entire buildings [283].
  However, these methods can only be applied to the simulation of laminated glass response when the coupling with highly nonlinear material behaviour and contact with finite elements can be established. Also, just because these methods allow for the simulation of very thin cracks, the interaction with an underlying finite elements mesh for the interlayer becomes a new challenge. This problem could partly be solved by including a cohesive zone for delamination, but still a very fine mesh would be needed to capture the local debonding correctly.

- The rate-dependency of the strength of soda-lime glass is still unknown. In Sec. 2.2.3, a relation is derived from published data for borosilicate glass. A study on the strength increase for soda-lime glass at loading rates between 1 MPa/s and 10^6 MPa/s would be highly valuable. The approach by Nie et al. [70] consists of axisymmetric bending tests with a Split-Hopkinson Pressure Bar (SHPB) setup and appears fit to cover loading rates between 100 MPa/s and 10^6 MPa/s.

- The developed hyper-viscoelastic material model for PVB interlayer is shown to capture the material behaviour well within the range for which it is calibrated, but much less accurately outside of this range. Also the behaviour in unloading has not been evaluated. It could be possible to expand the material model by describing the PVB in a parallel network

formulation. To properly validate such model, additional biaxial tests and hysteresis tests are required.

- The pull-off tests to measure the interfacial strength did not yield very consistent results: the measured values are lower than those found by Franz [179] for similar tests and show more scatter. In these tests, specimens were cut from a larger laminated glass plate. The specimens could be produced in a different manner, e.g. by laminating a small, circular piece of PVB interlayer between two slightly larger square glass plates, such as performed by Franz. Alternatively, specimens could be produced similar to those for the peel test: bonded on one side with a glass substrate and glued on the other side to a metal pull stub. In this way, there can be no two-sided failure, as long as a very strong adhesive is used on the metal side.

- When reliable values for the interfacial strength can be found, the simulation of the peel and TCT tests should also be repeated, since it was shown that the debonding strength has a major influence on the rest of the numerical result.
  This study can also be expanded to other interlayer materials.

- The presented study on the post-fracture response of laminated glass has focused on the verification of numerical models in comparison with experimental results. Using the developed methods, different compositions for the laminated glazing could be further studied and evaluated for an optimal setup. This can be performed for the thicknesses of the glass and interlayer plies, but also the case where interlayer plies with different elastic properties are combined could be considered.

- The element deletion technique allows to simulate tearing of the interlayer as well. This would allow to compare simulation results with experiments for the case of a steel ball impact in which the laminate is completely penetrated (EN356 P2A [60] or smaller setups). Such test setup is commonly used in the glass industry and the effect of temperature, PVB thickness and adhesion are well known for this case.

- The role of the supporting structure of the glass in response to an impact or blast has not been treated. Nonetheless, this is a very important study as well, because separation at the frame is one of the most common failure mechanisms. The performance of silicone glazing joints has already been studied by Hooper [249]. Also the study of hinged joints and cable net façades are relevant topics.

Bibliography

[1] B. Karger, M.A. Rothschild, and H. Pfeiffer. Accidental sharp force fatalities - beware of architectural glass, not knives. *Forensic Science International*, 123(2-3):135–139, 2001.

[2] J.R. Avner and M.D. Baker. Lacerations involving glass. The role of routine roentgenograms. *American Journal of Diseases of Children*, 146(5):600–602, 1992.

[3] S. Mallonee, S. Shariat, G. Stennies, R. Waxweiler, D. Hogan, and F. Jordan. Physical injuries and fatalities resulting from the Oklahoma City bombing. *Journal of the American Medical Association*, 276(5):382–387, 1996.

[4] M. Mines, A. Thack, S. Mallonee, L. Hildebrand, and S. Shariat. Ocular injuries sustained by survivors of the Oklahoma City bombing. *Ophthalmology*, 107(5):837–843, 2000.

[5] S. De Pauw. *Experimental and numerical study of impact on window glass fitted with safety window film.* Doctoral thesis, Ghent University, 2010.

[6] S. Van Dam. Doctoral thesis (forthcoming), Ghent University, 2016.

[7] J. Kuntsche. *Mechanisches Verhalten von Verbundglas unter zeitabhängiger Belastung und Explosionsbeanspruchung.* PhD thesis, Technische Universität Darmstadt, 2015.

[8] EN 12600:2002. *Glass in builing - Pendulum test - Impact test method and classification for flat glass.* CEN, 2002.

[9] DIN EN 13541. *Glas im Bauwesen - Sicherheitssonderverglasung - Prüfverfahren.* CEN, 2012.

[10] M. Haldimann, A. Luible, and M. Overend. *Structural Use of Glass*, volume 10 of *Structural Engineering Documents.* IABSE-AIPC-IVBH, 2008.

[11] J.H. Nielsen. *Tempered glass: bolted connections and related problems.* Doctoral thesis, Denmark Technical University, 2009.

[12] R. Weissmann. Fundamental properties of float glass surfaces. In *Glass Performance Days*, pages 40–43, 1997.

[13] M.H. Krohn, J.R. Hellman, D.L. Shelleman, G.C. Pantano, and G.E. Sakoske. Biaxial flexure strength and dynamic fatigue of soda-lime-silica float glass. *Journal of the American Ceramic Society*, 85(7):1777–1782, 2002.

[14] Kuraray Europe GmbH. *Technical manual: the processing of Trosifol® PVB film.* Troisdorf, Germany, 6 edition, 2012.

[15] R. Nijsse and E.H.J. ten Brincke. Glass columns. In C. Louter, F. Bos, J. Belis, and J.-P. Lebet, editors, *Challenging Glass 4*, pages 625–632. Taylor & Francis, UK, 2014.

[16] P. Oikonomopoulou, F. Veer, R. Nijsse, and K. Baardolf. A completely transparent, adhesively bonded soda-lime glass block masonry system. *Journal of Facade Design and Engineering*, 2:201–221, 2014.

[17] J.-D. Wörner, J. Schneider, and A. Fink. *Glasbau - Grundlagen, Berechnung, Konstruktion.* Springer-Verlag, 2001.

[18] J. Belis. *Kipsterkte van monolithische en gelamineerde glazen liggers.* Doctoral thesis, Ghent University, 2005.

[19] A.A. Griffith. The phenomena of rupture and flow in solids. *Philosophical Transactions of the Royal Society of London*, 221:163–198, 1921.

[20] A. Fink. *Ein Beitrag zum Einsatz von Floatglas als dauerhaft tragender Konstruktionswerkstoff im Bauwesen.* Doctoral thesis, Technische Universität Darmstadt, 2000.

[21] G. Molnár, L.M. Molnár, and I. Bojtár. Preparing a comprehensive analysis of the mechanical classification of structural glass. *Materials Engineering - Materiálové inžinierstvo*, 18(71-81), 2011.

[22] M. Vandebroek, C. Louter, R. Caspeele, F. Ensslen, and J. Belis. Size effect model for the edge strength of glass with cut and ground edge finishing. *Engineering Structures*, 79:96–105, 2014.

[23] ASTM E1300-04. *Standard Practice for Determining Load Resistance of Glass in Buildings. American Society for Testing Materials*, 2004.

[24] EN 1288-3:2000. *Glass in building - Determination of the bending strength of glass - Part 3: Test specimen supported at two points (four point bending).* CEN, 2000.

[25] ASTM C158-02. *Standard Test Methods for Strength of Glass by Flexure (Determination of Modulus of Rupture)*, 2009.

[26] EN 1288-2:2000. *Glass in building - Determination of the bending strength of glass - Part 2: Coaxial double ring test on flat specimens with large test surface areas.* CEN, 2000.

[27] EN 1288-5:2000. *Glass in building - Determination of the bending strength of glass - Part 5: Coaxial double ring test on flat specimens with small test surface areas.* CEN, 2000.

[28] ASTM C1499. *Standard Test Method for Monotonic Equibiaxial Flexural strength of Advanced Ceramics at Ambient Temperature*, 2009.

[29] DIN 1249-10. *Glass in building - Design and construction rules.* Beuth, Berlin, 1990.

[30] W. Weibull. A statistical distribution function of wide applicability. *Journal of Applied Mechanics*, 18:293–297, 1951.

[31] R.A. Behr, M.J. Karson, and J.E. Minor. Reliability analysis of window glass failure pressure data. *Structural Safety*, 11:43–58, 1991.

[32] M. Overend, G.A.R. Parke, and D. Buhagiar. Predicting failure in glass - a general crack growth model. *Journal of Structural Engineering*, 133(8):1146–1155, 2007.

[33] M. Haldimann. *Fracture strength of structural glass elements - analytical and numerical modelling, testing and design.* Doctoral thesis, EPFL, Switzerland, 2006.

[34] F.A. Veer, J. Zuidema, and F.P. Bos. The strength and failure of glass in bending. In *Glass Performance Days, Tampere, Finland*, 2003.

[35] F.A. Veer, P.C. Louter, and F.P. Bos. The strength of annealed, heat-strengthened and tempered float glass. *Fatigue and Fracture of Engineering Materials and Structures*, 32:18–25, 2008.

[36] J.A. Veer and Y.M. Rodichev. The structural strength of glass: hidden damage. *Strength of Materials*, 43(3):302–315, 2011.

[37] O.S. Narayanaswamy. A model for structural relaxation in glass. *Journal of the American Ceramic Society*, 54(10):491–498, 1971.

[38] G.R. Irwin. Analysis of stresses and strains near the end of a crack traversing a plate. *Journal of Applied Mechanics*, 24:361–364, 1957.

[39] E.E. Gdoutos. *Fracture mechanics*, volume 123 of *Solid mechanics and its applications.* Springer, 2nd edition, 2005.

[40] D. Gross and T. Seelig. *Fracture mechanics with an Introduction to Micromechanics*. Mechanical Engineering. Springer, 2nd edition, 2011.

[41] B. Lawn. *Fracture of Brittle Solids*. Cambridge solid state science series. Cambridge University Press, UK, 2 edition, 1993.

[42] S.M. Wiederhorn. Influence of water vapor on crack propagation in soda-lime glass. *Journal of the American Ceramic Society*, 50:407–414, 1967.

[43] E. Gehrke, C. Ullner, and M. Hähnert. Correlation between multistage crack growth and time-dependent strength in commercial silicate glasses, part 1. Influence of ambient media and types of initial cracks. *Glastechnisches Bericht*, 60(8):268–278, 1987.

[44] E. Gehrke, C. Ullner, and M. Hähnert. Correlation between multistage crack growth and time-dependent strength in commercial silicate glasses, part 2. Influence of surface treatment. *Glastechnisches Bericht*, 60(10):340–345, 1987.

[45] A.G. Atkins and Y.W. Mai. *Elastic and plastic fracture*. Ellis Horwood Ltd., 1988.

[46] J. Mencik. *Strength and fracture of glass and ceramics*. Elsevier, 1992.

[47] C. Ullner. *Untersuchungen zum Festigkeitsverhalten von Kalk-Natronsilikatglas nach mechanischer Vorschädigung durch Korundberieselung*. BAM, Berlin, 1993.

[48] N.D. Surdyka, C.G. Pantano, and S.H. Kim. Environmental effects on initiation and propagation of surface defects on silicate glasses: scratch and fracture toughness study. *Applied Physics A*, 116:519–528, 2014.

[49] S.M. Wiederhorn. Stress corrosion and static fatigue of glass. *Journal of the American Ceramic Society*, 53:543–548, 1970.

[50] L.B. Freund. *Dynamic Fracture Mechanics*. Cambridge University Press, 1990.

[51] K. Ravi-Chandar and W.G. Knauss. An experimental investigation into dynamic fracture III: on steady-state crack propagation and crack branching. *Internation Journal of Fracture*, 26(2):141–154, 1984.

[52] C.J. Clif. Fracture of glass under various liquids and gases. *Journal of the Society of Glass Technology*, 41:157–167, 1957.

[53] K.R. Linger and D.G. Holloway. The fracture energy of glass. *Philosophical Magazine*, 18(156):1269–1280, 1968.

[54] S.M. Wiederhorn. Fracture Surface Energy of Glass. *Journal of the American Ceramic Society*, 52(2):99–105, 1969.

[55] M. Inagaki, K. Urashima, S. Toyomasu, Y. Goto, and M. Sakai. Work of fracture and crack healing in glass. *Journal of the American Ceramic Society*, 68(12):704–706, 1985.

[56] F. Yuan and L. Huang. Molecular dynamics simulation of amorphous silica under uniaxial tension: from bulk to nanowire. *Journal of Non-Crystalline Solids*, 358(24):3481–3487, 2012.

[57] E. Sharon and J. Fineberg. Confirming the continuum theory of dynamic brittle fracture for fast cracks. *Nature*, 397:333–335, 1999.

[58] S. Reich and M.R.S. Vanapalli. Ball drops and equilibrium of brittle fractures. In J. Schneider and B. Weller, editors, *Engineered transparency, International Conference at glasstec, Düsseldorf, Germany*, 2014.

[59] N.F. Mott. Brittle fracture in mild steels. *Engineering*, 165:16–18, 1948.

[60] EN 356:2000. *Glass in builing - Security Glazing - Testing and classification of resistance against manual attack*. CEN, 2000.

[61] D.S. Dugdale. Yielding of steel sheets containing slits. *Journal of Mechanics and Physics of Solids*, 8:100–104, 1960.

[62] G.I. Barenblatt. The mathematical theory of equilibrium cracks in brittle solids. *Advances in Applied Mechanics*, 7:55–129, 1962.

[63] X.P. Xu and A. Needleman. Void nucleation by inclusion debonding in a crystal matrix. *Modelling and Simulation in Materials Science Engineering*, 1(2):111–132, 1993.

[64] P. Gaubelle and J. Baylor. Impact-induced delamination of composites: a 2D simulation. *Composites B*, 29B:589–602.

[65] V. Tvergaard. Effect of fibre debonding in a whisker-reinforced metal. *Materials Science Engineering A*, 125:203–213, 1990.

[66] G.T. Camacho and M. Ortiz. Computational modeling of impact damage in brittle materials. *International Journal of Solids and Structures*, 33(20-22):2899–2983, 1996.

[67] R.J. Charles. Dynamic fatigue of glass. *Journal of Applied Physics*, 29:1657–1662, 1958.

[68] J.E. Ritter. Dynamic fatigue of soda-lime silica glass. *Journal of Applied Physics*, 40:340–344, 1969.

[69] W.G. Brown. A practicable formulation for the strength of glass and its special application to large plates. *National Research Council of Canada*, 1974.

[70] X. Nie, W.W. Chen, and D.W. Templeton. Dynamic ring-on-ring equibiaxial flexural strength of borosilicate glass. *International Journal of Applied Ceramic Technology*, 7(5):616–624, 2010.

[71] W.L. Beason and J.R. Morgan. Glass failure prediction model. *Journal of Structural Engineering*, 110(2):197–212, 1984.

[72] G. Sedlacek, K. Blank, and J. Gusgen. Glass in structural engineering. *Structural Engineering*, 73(2):17–22, 1995.

[73] M. Overend and K. Zammit. A computer algorithm for determining the tensile stress of float glass. *Engineering Structures*, 45:68–77, 2012.

[74] F. Veer. The failure strength of glass, a non-transparent value. In *Glass Performance Days*, pages 610–614, 2007.

[75] M. Larcher, G. Solomos, S. Casadei, and N. Gebbeken. Experimental and numerical investigations of laminated glass subjected to blast loading. *International Journal of Impact Engineering*, 39:42–50, 2012.

[76] X. Brajer, P. Forquin, R. Gy, and F. Hild. The role of surface and volume defects in the fracture of glass under quasi-static and dynamic loadings. *Journal of Non-Crystalline Solids*, 316:42–53, 2003.

[77] M. Grujicic, B. Pandurangan, N. Coutris, B.A. Cheeseman, C. Fountzoulas, P. Patel, D.W. Templeton, and K.D. Bishnoi. A simple ballistic material model for soda-lime glass. *International Journal of Impact Engineering*, 36:386–401, 2009.

[78] M. Peroni, G. Solomos, V. Pizzinato, and M. Larcher. Experimental investigation of high strain rate behaviour of glass. *Applied Mechanics and Materials*, 82:63–68, 2011.

[79] X. Zhang, H. Hao, and G. Ma. Dynamic material model of annealed soda-lime glass. *International Journal of Impact Engineering*, 77:108–119, 2015.

[80] G.I. Kanel, A.A. Bogatch, S.V. Rozarenov, and Z. Chen. Transformation of Shock Compression Pulses in Glass due to the Failure Wave Phenomena. *Journal of Applied Physics*, 92(9):5045–5052, 2002.

[81] M. Grujicic, B. Pandurangan, W.C. Bell, N. Coutris, B.A. Cheeseman, P. Patel, D.W. Templeton, and K.D. Bishnoi. An improved mechanical material model for ballistic soda-lime glass. *Journal of Materials Engineering and Performance*, 18(8):1012–1028, 2009.

[82] S. Bouzid, A. Nyoungue, Z. Azari, N. Bouaouadja, and G. Pluvinage. Fracture criterion for glass under impact loading. *International Journal of Impact Engineering*, 25:831–845, 2001.

[83] X. Zhang, Y. Zou, H. Hao, X. Li, G. Ma, and K. Liu. Laboratory Test on Dynamic Material Properties of Annealed Float Glass. *International Journal of Protective Structures*, 3(4):407–430, 2012.

[84] F.L.L.B. Carneiro. A new method to determine the tensile strength of concrete. In *5th meeting of the Brazilian Association for Technical Rules*. Associacao Brasileira de Normas Tecnicas, 1943.

[85] T.J. Holmquist and G.R. Johnson. A computational constitutive model for glass subjected to large strains, high strain rates and high pressure. *Journal of Applied Mechanics*, 78:051003–2, 2011.

[86] Y. Bao, J. Yang, Y. Qiu, and Y. Song. Space and time effects of stress on cracking of glass. *Materials Science and Engineering A*, 512:45–52, 2009.

[87] S. Monserez. Impact behavior of laminated glass for use in large glass facades. Master's thesis, Ghent University, 2013.

[88] S. Van Dam, J. Pelfrene, W. Van Paepegem, J. Degrieck, D. Lecompte, and J. Vantomme. A new experimental test set-up for investigating impact resistance of laminated glass. In J. Belis, C. Louter, and D. Mocibob, editors, *COST Action TU0905: Mid-term Conference On Structural Glass*, pages 359–366, 2013.

[89] S. Van Dam, J. Pelfrene, S. De Pauw, and W. Van Paepegem. Experimental study on the dynamic behaviour of glass fitted with safety window film with a small-scale drop weight set-up. *International Journal of Impact Engineering*, 73:101–111, 2014.

[90] T. Dekeukelaere. Study of safety film for protection of window glass against impact. Master's thesis, Ghent University, 2008.

[91] A. Seagraves and R. Radovitzky. *Dynamic Failure of Materials and Structures*, chapter 12. Springer, 2010.

[92] N. Moës, J. Dolbow, and T. Belytschko. A finite element method for crack growth without remeshing. *International Journal of Numerical Methods in Engineering*, 46:131–150, 1999.

[93] T. Belytschko, Y.Y. Lu, and L. Gu. Crack propagation by element-free Galerkin methods. *Engineering Fracture Mechanics*, 51:295–315, 1995.

[94] G.R. Johnson, R.A. Stryk, S.R. Beissel, and T.J. Holmquist. An algorithm to automatically convert distorted finite elements into meshless particles during dynamic deformation. *International Journal of Impact Engineering*, 27:997–1013, 2002.

[95] M. Unosson and L. Nilsson. Projectile penetration and perforation of high performance concrete: experimental results and macroscopic modelling. *International Journal of Impact Engineering*, 32:1068–1085, 2005.

[96] M. Unosson, L. Olovsson, and K. Simonsson. Failure modelling in finite element analyses: Random material imperfections. *Mechanics of Materials*, 37(12):1175–1179, 2005.

[97] M. Unosson, L. Olovsson, and K. Simonsson. Weakest link model with imperfection density function: Application to three point bend of a tungsten carbide. *International Journal of Refractory Materials and Hard Materials*, 25(1):6–10, 2007.

[98] M. Unosson, L. Olovsson, and K. Simonsson. Failure modelling in finite element analyses: element erosion with crack tip enhancement. *Finite Elements in Analysis and Design*, 42:283–297, 2006.

[99] J.-H. Song, H. Wang, and T. Belytschko. Comparative study on finite element methods for dynamic fracture. *Computational Mechanics*, 42:239–250, 2006.

[100] B. Bourdin, G.A. Francfort, and J.-J. Marigo. Numerical experiments in revisited brittle fracture. *Journal of the Mechanics and Physics of Solids*, 48:797–826, 2000.

[101] D.S. Cronin, K. Bui, C. Kaufmann, G. McIntosh, and T. Berstad. Implementation and validation of the Johnson-Holmquist ceramic material model in LS-DYNA. In *4th European LS-DYNA User Conference*, pages 47–60, 2003.

[102] P.A. Du Bois, S. Kolling, and W. Fassnacht. Modeling of safety glass for crash simulation. *Computational Materials Science*, 28:675–683, 2003.

[103] D.-Z. Sun, F. Andrieux, A. Ockewitz, H. Klamser, and J. Hogenmuller. Modelling of the failure behaviour of windscreens and component tests. In *5th European LS-DYNA Users Conference*, 2005.

[104] M. Timmel. A finite element model for impact simulation with glass. *International Journal of Impact Engineering*, 34:1465–1478, 2007.

[105] M. Larcher. Simulation of Several Glass Types Loaded by Air Blast Waves. Technical report, European Commission Joint Research Center, Ispra, Italy, 2008.

[106] M. Larcher and G. Solomos. Laminated glass loaded by air blast waves - Experiments and numerical simulations. Technical report, European Commission Joint Research Center, Ispra, Italy, 2010.

[107] C.D. Wu, X.Q. Yan, and L.M. Shen. A numerical study of dynamic failure of nanomaterial enhanced laminated glass under impact. In *Materials Science and Engineering*, volume 10, 2010. article number 012176.

[108] T. Pyttel, H. Liebertz, and J. Cai. Failure criterion for laminated glass under impact loading and its application in finite element simulation. *International Journal of Impact Engineering*, 38:252–263, 2011.

[109] I.V. Ivanov and T. Sadowski. Advanced laminated glass modelling for safety FEA. In *9. LS-Dyna forum, Bamberg*, 2010.

[110] M. Konrad and M. Gevers. Advanced laminated glass modelling for safety FEA. In *9. LS-Dyna forum, Bamberg*, 2010.

[111] M. Konrad and M. Gevers. Model Optimization of Laminated Glass for Impact Simulations. *ATZ*, pages 10–14, 2012.

[112] C. Amadio and C. Bedon. Dynamic Response of Cable-Supported Façades Subjected to High-Level Air Blast Loads: Numerical Simulations andMitigation Techniques. *Modelling and Simulation in Engineering*, 2012:13, 2012.

[113] C. Amadio and C. Bedon. Blast Analysis of Laminated Glass Curtain Walls Equipped by Viscoelastic Dissipative Devices. *Buildings*, 2:359–383, 2012.

[114] C. Amadio and C. Bedon. Viscoelastic spider connectors for the mitigation of cable-supported façades subjected to air blast loading. *Engineering Structures*, 42:190–200, 2012.

[115] Q. Liu, J. Liu, Q. Miao, D. Wang, and X. Tang. Simulation and test validation of windscreen subject to pedestrian head impact. In *12th International LS-DYNA Users Conference*, 2012.

[116] Y. Peng, J. Yang, C. Deck, and R. Willinger. Finite element modeling of crash test behavior for windshield laminated glass. *International Journal of Impact Engineering*, 57:27–35, 2013.

[117] X. Zhang, H. Hao, and G. Ma. Laboratory test and numerical simulation of laminated glass window vulnerability to debris impact. *International Journal of Impact Engineering*, 55:49–62, 2013.

[118] J. Pelfrene, S. Van Dam, W. Van Paepegem, and J. Degrieck. Numerical simulation of elastic, fracture and post-failure response of monolithic and laminated glass under impact loading. In J. Belis, C. Louter, and D. Mocibob, editors, *COST Action TU0905: Mid-term Conference On Structural Glass*, pages 413–420, 2013.

[119] J. Pelfrene, J. Kuntsche, S. Van Dam, W. Van Paepegem, and J. Schneider. Critical assessment of the post-breakage performance of blast loaded laminated glazing: experiments and simulations. *International Journal of Impact Engineering*, 88:61–71, 2016.

[120] A. Hillerborg, M. Modeer, and P.-E. Petersson. Analysis of crack formation and crack growth in concrete by means of fracture mechanics and finite elements. *Cement and concrete research*, 6:773–782, 1976.

[121] Dassault Systèmes Simulia. *Abaqus 6.14 Analysis User's Manual*, 2014.

[122] D.J. Benson. Computational methods in Lagrangian and Eulerian hydrocodes. University of California, 1990.

[123] C. Geuzaine and J.-F. Remacle. Gmsh: a three-dimensional finite element mesh generator with built-in pre- and post-processing facilities. *International Journal of Numerical Methods in Engineering*, 79(11):1309–1331, 2009.

[124] O. Allix, P. Feissel, and P. Thevenet. A delay damage mesomodel of laminates under dynamic loading: basic aspects and identification issues. *Computers and Structures*, 81:1171–1191, 2003.

[125] R. A. Gingold and J. J. Monaghan. Smooth particle hydrodynamics: theory and application to non-spherical stars. *Mon. Not. R. Astron. Soc.*, 181:375–389, 1977.

[126] G.L. Vaughan. Completeness, conservation and error in SPH for fluids. *International Journal for Numerical Methods in Fluids*, 56:37–62, 2008.

[127] G. R. Liu and M. B. Liu. *Smoothed Particle Hydrodynamics, a meshfree particle method.* World Scientific Publishing Company, Incorporated, 2003.

[128] G. R. Johnson. SPH for high velocity impact computations. *Computer methods in applied mechanics and engineering*, 139:347–373, 1996.

[129] J. J. Monaghan and R. A. Gingold. Shock simulation by the particle method of SPH. *Journal of Computational Physics*, 52:374–381, 1983.

[130] W. Benz and E. Asphaug. Simulations of brittle solids using smoothed particle hydrodynamics. *Computer Physics Communications*, 87:253–265, 1995.

[131] Y. Michel, J.-M. Chevalier, C. Durin, C. Espinosa, F. Malaise, and J.-J. Barrau. Meshless modelling of dynamic behaviour of glasses under intense shock loadings: Application to matter ejection during high velocity impacts on thin brittle targets. *Journal de Physique IV*, 134:1077–1083, 2006.

[132] R. Das and P.W. Cleary. Effect of rock shapes on brittle fracture using Smoothed Particle Hydrodynamics. *Theoretical and Applied Fracture Mechanics*, 53:47–60, 2010.

[133] G.W. Ma, X.J. Wang, and F. Ren. Numerical simulation of compressive failure of heterogeneous rock-like materials using SPH method. *International Journal of Rock Mechanics and Mining Sciences*, 48:353–363, 2011.

[134] V. Gupta, S. Rajagopal, and N. Gupta. A comparative study of mesh-free methods for fracture. *International Journal of Damage Mechanics*, 20:729–751, 2011.

[135] T.J. Holmquist, G.R. Johnson, D.E. Grady, C.M. Lopatin, and E.S. Hertel. High strain rate properties and constitutive modelling of glass. In *Proceedings of the 15th International Symposium on Ballistics*, pages 47–60, Jerusalem, Israel, 1995.

[136] D. Price. Smoothed Particle Hydrodynamics and Magnetohydrodynamics. ASTROSIM Summer School, Turon, Poland, 2010.

[137] H.D. Espinosa, P.D. Zavattieri, and S.K. Dwivedi. A finite deformation continuum/discrete model for the description of fragmentation and damage in brittle materials. *Journal of Mechanics and Physics of Solids*, 46(10):1909–1942, 1998.

[138] X.P. Xu and A. Needleman. Numerical simulation of fast crack growth in brittle solids. *Journal of the Mechanics and Physics of Solids*, 42(9):1394–1434, 1994.

[139] A. Needleman. A continuum model for void nucleation by inclusion debonding. *Journal of Applied Mechanics*, 54:525–531, 1987.

[140] A. Pandolfi and M. Ortiz. Solid modeling aspects of three-dimensional fragmentation. *Engineering with Computers*, 14:287–308, 1998.

[141] A. Pandolfi and M. Ortiz. An efficient adaptive procedure for three-dimensional fragmentation. *Engineering with Computers*, 18:148–159, 2002.

[142] P.H. Geubelle and J.S. Baylor. Impact-induced delamination of composites: a 2D simulation. *Composites B*, 29B:589–602, 1998.

[143] J. Mergheim, E. Kuhl, and P. Steinmann. A hybrid discontinuous Galerkin/interface method for the computational modelling of failure. *Numerical Methods in Engineering*, 20(7):511–519, 2004.

[144] G. Becker and L. Noels. Validation tests of the full-discontinuous Galerkin/extrinsic cohesive law framework of Kirchhoff-Love shells. *International Journal of Fracture*, 178:299–322, 2012.

[145] G. Becker and L. Noels. A full-discontinuous Galerkin formulation of nonlinear Kirchhoff-Love shells: elasto-plastic finite deformations, parallel computation and fracture applications. *Internation Journal for Numerical Methods in Engineering*, 93:80–117, 2013.

[146] V.P. Nguyen. Discontinuous Galerkin/extrinsic cohesive zone modeling: Implementation caveats and applications in computational fracture mechanics. *Engineering Fracture Mechanics*, 128:37–68, 2014.

[147] I. Scheider. Cohesive model for crack propagation analyses of structures with elastic-plastic material behavior: foundations and implementation. GKSS Research Center Geesthacht, Dept. WMS, April 2001.

[148] X. Su. Finite element modelling of compelx 3D static and dynamic crack propagation by embedding cohesive elements in ABAQUS. *Acta Mechanica Solida Sinica*, 23(3):271–282, 2010.

[149] V.P. Nguyen. An open source program to generate zero-thickness cohesive interface elements. *Advances in Engineering Software*, 74:27–39, 2014.

[150] B.G. Trunk. *Einfluss der Bauteilgroesse auf die Bruchenergie von Beton.* PhD thesis, ETH Zürich, 1999.

[151] P.M.A. Areias and T. Belytschko. Analysis of three-dimensional crack initiation and propagation using the extended finite element method. *International Journal for Numerical Methods in Engineering*, 2005.

[152] Y.-J. Juang, L. James Lee, and K.W. Koelling. Rheological analysis of polyvinyl butyral near the glass transition temperature. *Polymer Engineering and Science*, 41(2):275–292, 2001.

[153] V. Ungureanu. Laminated glass and interlayers. European Erasmus Mundus Master Course - Sustainable constructions under natural hazards and catastrophic events, 2011.

[154] U. Keller and H. Mortelmans. Adhesion in laminated glass; what makes it work? In *Glass Performance Days*, pages 353–356, 1999.

[155] C. Morison, M. Zobec, and A. Frenceschet. The measurement of PVB properties at high strain rates, and their application in the design of laminated glass under bomb blast. In *International Symposium on the Interaction of the Effects of Munitions with Structures*, 2007.

[156] P.A. Hooper. The mechanical behaviour of poly(vinyl butyral) at different strain magnitudes and strain rates. *Journal of Materials Science*, 47:3564–3576, 2012.

[157] J. Schneider, S. Kolling, J. Kuntsche, and S. Moennich. Tensile properties of different polymer interlayers under high strain rates. In *Engineered Transparancy, International Conference at Glasstec, Duesseldorf, Germany*, pages 427–437, 2012.

[158] J.D. Ferry. *Viscoelastic Properties of Polymers*. John Wiley and Sons, USA, 1980.

[159] J. Bergström. *Mechanics of Solid Polymers*. Plastics Design Library. Elsevier Inc., 2015.

[160] M.-J. Potvin. *Comparison of Time-domain finite element Modelling of Viscoelastic structures using an efficient fractional Kelvin-Voight Model or Prony series*. PhD thesis, McGill University, Montreal, Canada, 2001.

[161] L. Hoss and R.J. Marczak. A new constitutive model fmaterials-like materials. *Mecanica Computacional*, 29:2759–2773, 2010.

[162] O.H. Yeoh. Characterization of elastic properties of carbon-black-filled rubber vulcanizates. *Rubber Chemistry and Technology*, 63:793–805, 1990.

[163] E. M. Arruda and M. C. Boyce. A three-dimensional model for the large stretch behavior of rubber elastic materials. *Jounal of the Mechanics and Physics of Solids*, 41(2):389–412, 1993.

[164] A.N. Gent. A new constitutive relation for rubber. *Rubber Chemistry and Technology*, 69:59–61, 1996.

[165] S. Kolling, P.A. Du Bois, and D.J. Benson. A tabulated formulation of hyperelasticity with rate effects and damage. *Computational Mechanics*, 40:885–899, 2007.

[166] T. Dalrymple, J. Choi, and K. Miller. Elastomer rate-dependence: a testing and material modeling methodology. In *172nd Technical Meeting of the Rubber Division of the American Chemical Society, Inc.*, Cleveland, OH, 2007.

[167] H. Khajehsaeid, J. Arghavani, and S. Sohrabpour. A visco-hyperelastic constitutive model for rubber-like materials: A rate-dependent relaxation time scheme. *International Journal of Engineering Science*, 79:44–58, 2014.

[168] I. Lapczyk, J.A. Hurtado, and S.M. Govindarajan. A parallel Rheological framework for modelling Elastomers and polymers. In *182nd Technical Meeting of the Rubber Division of the American Chemical Society Inc.*, Cincinatti, OH, 2012.

[169] R. Behr, J.E.. Minor, and M.P. Linden. Load duration and interlayer thickness effects on laminated glass. *Journal of Structural Engineering*, 112(6):1441–1453, 1986.

[170] C.V.G. Vallabhan, J.E. Minor, and S.R. Nagalla. StStress in layered glass units and monolithic glass plates. *Journal of Structural Engineering*, 113(1):36–43, 1987.

[171] C.V.G. Vallabhan, Y.C. Das, and M. Ramasamudra. Properties of PVB interlayer used in laminated glass. *Journal of Materials in Civil Engineering*, 4(1):71–76, 1992.

[172] S.J. Bennison and A. Jagota. Fracture of Glass/Poly(vinyl butyral)(Butacite) Laminates in Biaxial Flexure. *Journal of the American Ceramics Society*, 82(7):1761–1770, 1999.

[173] P. D'haene and G. Savineau. Mechanical properties of laminated safety glass - FEM study. In *Glass Performance Days*, pages 594–598, 2007.

[174] R. Iwasaki. Experimental Study on the interface fracture toughness of PVB/glass at high strain rates. *International Journal of Impact Engineering*, 12(3):293–298, 2011.

[175] H. Khajehsaeid, R. Naghdabadi, and J. Arghavani. A strain energy function for rubber-like materials. *Constitutive Models for Rubber*, 8:205–210, 2013.

[176] J.-C. Nugue, E. Nourry, and G. Savineau. Toughness, resiliency and adhesion of polyvinyl butyral (PVB) interlayers with regard to impact resistance. In *Glass Performance Days*, pages 437–440, 2003.

[177] C. Butchart and M. Overend. Influence of moisture on the post-fracture performance of laminated glass. In *Glass Performance Days*, pages 59–61, 2013.

[178] R. Speelman and G. Savineau. Laminated glass and interlayers - breaking the myths. In *Glass Performance Days*, pages 235–237, 2013.

[179] J. Franz. *Untersuchungen zur Resttragfähigkeit von gebrochenen Verglasungen*. PhD thesis, Technische Universität Darmstadt, 2015. Springer Verlag.

[180] J.O. Aguilar, J.M. Rodriguez-Lelis, M. Carrasco de la Fuente, C. Lopez-Mata, J.A. Arellano-Cabrera, and F. Chan. Adhesion strength in laminated glazings containing multilayer solar control coatings. *Mechanical science and technology*, 26(6):1725–1730, 2012.

[181] ISO 8510-1:1990. *Adhesives - Peel test for flexible-bonded-to-rigid test speciment assembly*. CEN.

[182] Y. Sha, C.Y. Hui, E.J. Kramer, P.D. Garrett, and J.W. Knapczyk. Analysis of adhesion and interface debonding in laminated safety glass. *Journal of Adhesion Science and Technology*, 11(1):49–63, 1997.

[183] S. Muralidhar, A. Jagota, S.J. Bennison, and S. Saigal. Mechanical behaviour in tension of cracked glass bridged by an elastomeric ligament. *Acta Materialia*, 48:4577–4588, 2000.

[184] C. Butchart and M. Overend. Delamination in fractured laminated glass. In *Engineered Transparancy, International Conference at Glasstec, Duesseldorf, Germany*, 2012.

[185] J. Franz and J. Schneider. Through-cracked tensile tests with polyvinyl butyral (PVB) and different adhesion grades. In J. Schneider and B. Weller, editors, *Engineered Transparency*, pages 135–142, 2014.

[186] F.W. Flocker and L.R. Dharani. Modeling interply debonding in laminated architectural glass subject to low velocity impact. *Structural Engineering and Mechanics*, 6(5):485–496, 1998.

[187] D.H. Kaelble. Theory and analysis of peel adhesion: mechanisms and mechanics. *Transactions of the Society of Rheology*, 3:161–180, 1959.

[188] D.H. Kaelble. Theory and analysis of peel adhesion: bond stresses and distributions. *Transactions of the Society of Rheology*, 4:45–73, 1960.

[189] P.A. Hooper. On the blast resistance of laminated glass. *International Journal of Solids and Structures*, 49:899–918, 2012.

[190] J. Kuntsche and J. Schneider. Mechanical behavior of polymer interlayers in explosion resistant glazing. In C. Louter, J. Belis, F. Bos, and J.P. Lebet, editors, *Challenging Glass 4 and COST Action TU0905 Final Conference*, pages 447–454. Taylor and Francis Group, 2014.

[191] M. Seshadri. *Interfacial delamination in polymer coated metal sheet, a numerical-experimental study.* doctoral thesis, Carnegie Mellon University, 2001.

[192] S. Bati, M. Fagoni, and G. Ranocchiai. Analysis of the post-crack behaviour of a laminated glass beam. In *Glass Performance Days*, pages 349–352, 2009.

[193] S. Nhamoinesu and M. Overend. Simple models for predicting the post-fracture behaviour of laminated glass. In *XXV A.T.I.V. 2010 International Conference, Parma, Italy*, 2010.

[194] F. Bernard, B. Krour, S. Benyoucef, and B. Fahsi. Numerical analysis of the debonding of the adhesive interlayer in a laminated glass plate. In C. Louter, J. Belis, F. Bos, and J.P. Lebet, editors, *Challenging Glass 4*

and COST Action TU0905 Final Conference, pages 491–498. Taylor and Francis Group, 2014.

[195] A. Jagota, S.J. Bennison, and C.A. Smith. Analysis of a compressive shear test for adhesion between elastomeric polymers and rigid substrates. *International Journal of Fracture*, 104:105–130, 2000.

[196] J. Schneider and J. Franz. Classification of material properties of interlayers for laminated glass regarding the post-breakage behaviour. In *Engineered Transparancy, International Conference at Glasstec, Duesseldorf, Germany*, pages 417–426, 2012.

[197] P. Rahul-Kumar, A. Jagota, S.J. Bennison, and S. Saigal. Interfacial failures in a compressive shear strength test of glass/polymer laminates. *International Journal of Solids and Structures*, 37:7281–7305, 2000.

[198] A. Van Duser, A. Jagota, and S.J. Bennison. Analysis of glass/polyvinyl butyral laminates subjected to uniform pressure. *Journal of Engineering Mechanics*, 125(4):435–442, 1999.

[199] T. Diehl. On using a penalty-based cohesive-zone finite element approach, part I: elastic solution benchmarks. *International Journal of Adhesion and Adhesives*, (28):237–255, 2008.

[200] P. Rahul-Kumar, A. Jagota, S.J. Bennison, and S. Saigal. Cohesive element modeling of viscoelastic fracture: application to peel testing of polymers. *International Journal of Solids and Structures*, 37:1873–1897, 2000.

[201] J.A. Williams and J.J. Kauzlarich. The influence of peel angle on the mechanics of peeling flexible adherends with arbitrary load-extension characteristics. *Tribology international*, 38:951–958, 2005.

[202] W.G. Knauss. On the steady propagation of a crack in a viscoelastic sheet: experiments and analysis. In H.H. Kausch, J.A. Hassell, and R.I. Jaffe, editors, *Deformation and fracture of high polymers*, pages 501–540. Plenum Press: New York, 1973.

[203] K. Allaer, I. De Baere, W. Van Paepegem, and J. Degrieck. Numerical study of the interfacial stress distribution in dolly pull-off adhesion tests for thin sheet materials. *International Journal of Adhesion and Adhesives (Submitted)*, 2015.

[204] B. Mukherjee, D.A. Dillard, R.B. Moore, and R.C. Batra. Debonding of confined elastomeric interlayer using cohesive zone method. *International Journal of Adhesion and Adhesives*, 66:114–127, 2016.

[205] D. Delincé, D. Sonck, J. Belis, D. Callewaert, and R. Van Impe. Experimental investigation of the local bridging behaviour of the interlayer in broken laminated glass. In G. Siebert, T. Hermann, and A. Haese, editors, *International Symposium on the Application of Architectural Glass ISAAG 2008 Conference Proceedings*, pages 41–49, Munich, Germany, 2008.

[206] D. Ferretti, M. Rossi, and G. Royer-Carfagni. Through-cracked tensile delamination tests with photoelastic measurements. In F. Bos, C. Louter, R. Nijsse, and F. Veer, editors, *Challenging Glass 3*, pages 641–652, 2012.

[207] M.L. Benzeggagh and M. Kenane. Measurement of mixed-mode delamination fracture toughness of unidirectional glass/epoxy composites with mixed mode bending apparatus. *Composites Science and Technology*, 56:439–449, 1996.

[208] F.W. Flocker and L.R. Dharani. Modeling fracture in laminated architectural glass subject to low velocity impact. *Journal of Materials Science*, 32:2587–2594, 1997.

[209] H.S. Norville, K.W. King, and J.L. Swofford. Behavior and strength of laminated glass. *Journal of Engineering Mechanics*, 124(1):46–53, 1998.

[210] M. Kutterer. Verbundglasplatten - Schubverbund und Membrantragwirkung. *Stahlbau*, 74:39–46, 2005.

[211] J. Kuntsche and J. Schneider. Explosion resistant glazing - experimental tests and numerical simulation. In *Glass Performance Days*, pages 173–177, 2013.

[212] J. Schneider, S. Schula, and A. Burmeister. Zwei Verfahren zum rechnerischen Nachweis der dynamischen Beanspruchung von Verglasungen durch weichen Stoss, Teil 1: numerische transiente Simulationsberechnung und vereinfachte Verfahren mit statischen Ersatzlasten. *Stahlbau*, 80:81–87, 2011.

[213] M. Wagner and R. Müller. Berechnung Sprengwirkungshemmender Fenster- und Fassadenkonstruktionen. In *5. LS-DYNA Anwenderforum*, Ulm, Germany, 2006.

[214] D. Tabor. The bulk modulus of rubber. *Polymer*, 35(13):2759–2763, 1994.

[215] DIN 18008-4. *Glass in building - Design and Construction Rules - Part 4: Additional Requirements for Barrier Glazing.* Beuth Verlag, Berlin, 2013.

[216] ECE R-33. *Uniform provisions concerning the approval of vehicles with regard to the behaviour of the structure of the impacted vehicle in a head-on collision*. United Nations, 1993.

[217] ECE R-94. *Uniform provisions concerning the approval of vehicles with regard to the protection of the occupants of the impacted vehicle in a head-on collision*. United Nations, 2002.

[218] European Enhanced Vehicle-safety Committee. *Working Group 17 Report: Improved Test Methods to Evaluate Pedestrian Protection Afforded by Passenger Cars*, 1998.

[219] S. Zhao, L.R. Dharani, L. Chai, and S. Barbat. Analysis of damage in automotive glazing subjected to simulated head impact. *Engineering Failure Analysis*, 13:582–597, 2006.

[220] Z97.1. *American National Standard for Safety Glazing Materials Used in Buildings - Safety Performance Specifications and Methods of Test*. ANSI, 1975.

[221] R. V. Foss, T. Murakami, M. Kikuta, and S. Aratani. Safety glass testing: human head impactor by dynamic transient analysis. In *Glass Performance Days*, pages 444–450, 1999.

[222] K. Balkow, H. von Bock, H. Krewinkel, and R. Rinkens. Glas am Bau - Technischer Leitfaden. Deutsche Verlags-Anstalt, Stuttgart, 1980.

[223] Deutsches Institut für Bautechnik (DIBt), Berlin. *Technische Regeln für die Verwendung von absturzsichernden Verglasungen (TRAV)*, 2003.

[224] J. Schneider. *Festigkeit und Bemessung punktgelagerter Gläser und stossbeanspruchter Gläser*. Doctoral thesis, Technische Universität Darmstadt, 2001.

[225] C. Müller de Vries. Numerical simulation of façade / window fracture under impact loading. In Bos, Louter, Nijsse, Veer, editor, *Challenging Glass 3*, pages 489–500, 2012.

[226] S.A. Brendler. *Rechnerisches Bemessungskonzept für absturzsichernden Glastafeln*. PhD thesis, Technische Universität Carolo-Wilhelmina, Braunschweig, 2007.

[227] P. Altidis, B. Warner, and V. Adams. Analyzing hyperelastic materials with some practical considerations. presentation, May 2005.

[228] N. Korunovic, M. Trajanovic, and M. Stojkovic. FEA of tires subjected to static loading. *Journal of the Serbian Society for Computational Mechanics*, 1(1):87–98, 2007.

[229] Yi Sang, Martin Dubé, and Martin Grant. Dependence of friction on roughness, velocity, and temperature. *Physical Review E*, 77:036123, 2008.

[230] F. Hild and S. Roux. *Optical methods for solid mechanics: A full-field approach*, chapter 5, pages 183–228. Wiley-VCH, 2012.

[231] S. Norville, N. Harvill, E. Conrath, and S. Shariat. Glass-related injuries in Oklahoma City Bombing. *Journal of Performance of Constructed Facilities*, 13:50–56, 1999.

[232] P.D. Smith and J.D. Hetherington. *Blast and ballistic loading of structures*. Butterworth-Heinemann, 1994.

[233] P.S. Bulson. *Explosive loading of engineering structures*. E & FN Spon, 1997.

[234] C.E. Needham. *Blast waves*. Springer, 2009.

[235] C.N. Kingery and G. Bulmash. Air blast parameters from TNT spherical air burst and hemispherical surface burst. Technical Report BRL 02555, U.S. Army Ballistic Research Laboratory, 1984.

[236] P.M. Locking. The trouble with TNT equivalence. In *26th International Ballistics Symposium*, 2012.

[237] Fundamentals of protective design from conventional weapons. Technical Report TM 5-855-1, U.S. Department of the Army, 1986.

[238] H.L. Brode. Numerical solution of spherical blast waves. *Journal of Applied Physics*, 26(2):766ff, 1955.

[239] J. Henrych. *The dynamics of explosion and its use*. Elsevier, Amsterdam, Netherlands, 1979.

[240] G.F. Kinney and K.J. Graham. *Explosive shocks in air*. Springer-Verlag, Berlin, Germany, 1985.

[241] F.G. Friedlander. Note on the diffraction of blast waves by a wall. Technical report, UK Home Office ARP Department, 1939.

[242] W. Baker, P. Cox, P. Westine, J. Kulesz, and R. Strehlow. *Explosion hazards and evolution*. Elsevier, 1983.

[243] M. Larcher. Simulation of the effects of an air blast wave. Technical report, European Commission Joint Research Center, Ispra, Italy, 2007.

[244] C. Morison. *The resistance of laminated glass to blast pressure loading and the coefficients for single degree of freedom analysis of laminated glass*. PhD thesis, Cranfield University, 2007.

[245] J. Wei and L.R. Dharani. Response of laminated architectural glazing subjected to blast loading. *International Journal of Impact Engineering*, 32(12):2032–2047, 2006.

[246] T. Krauthammer and A. Altenberg. Negative phase blast effects on glass panels. *International Journal of Impact Engineering*, 24:1–18, 2000.

[247] H.D. Hidallana-Gamage, D.P. Thambiratnam, and N.J. Perera. Failure analysis of laminated glass panels subjected to blast loads. *Engineering Failure Analysis*, 36:14–29, 2014.

[248] C. Kranzer, G. Gürke, and C. Mayrhofer. Testing of bomb resistant glazing systems: experimental investigation of the time dependent deflection of blast loaded 7.5 mm laminated glass. In *Glass processing days*, Fraunhofer Institute for High-Speed Dynamics, Ernst-Mach-Institut, Efringen-Kirchen, Germany, 2005.

[249] P.A. Hooper. *Blast performance of silicone bonded laminated glass.* Doctoral thesis, Imperial College London, 2011.

[250] F. Wellershoff, M. Teich, G. Nehring, and N. Gebbeken. Konstruktion und Berechnung von explosionshemmenden Seilnetzfassaden. *Stahlbau*, 81:13–25, 2012.

[251] DIN EN 13123-1. *Fenster, Türen, Abschlüsse - Sprengwirkungshemmung - Anforderungen und Klassifizierung - Teil 1: Stossrohr.* CEN, 2001.

[252] DIN EN 13123-2. *Fenster, Türen, Abschlüsse - Sprengwirkungshemmung - Anforderungen und Klassifizierung - Teil 2: Freilandversuch.* CEN, 2004.

[253] DIN EN 13124-1. *Fenster, Türen, Abschlüsse - Sprengwirkungshemmung - Prüfverfahren - Teil 1: Stossrohr.* CEN, 2001.

[254] DIN EN 13124-2. *Fenster, Türen, Abschlüsse - Sprengwirkungshemmung - Prüfverfahren - Teil 2: Freilandversuch.* CEN, 2004.

[255] ASTM F 1624. *Standard Test Method for Glazing and Glazing Systems Subject to Airblast Loadings*, 2004.

[256] GSA. *Security Criteria*, 2003.

[257] ARA. *Applied Research Associates: Window Glazing Analysis Response & Design WINGARD: Technical Manual*, 2005.

[258] ISO 16933. *Glass in builduing - Explosion-resistant security in glazing - Test and classification for arena air-blast loading*, 2007.

[259] ISO 16934. *Glass in builduing - Explosion-resistant security in glazing - Test and classification for shock-tube loading*, 2007.

[260] C.N. Kingery and G. Bulmash. Air blast parameters from TNT spherical air burst and hemispherical surface burst. Technical report, U.S. Army Ballistic Research Laboratory, USA, 1984.

[261] P.S. Westine, B.L. Morris, P.A. Cox, and E.Z. Polch. Development of computer program for floor plate response from land mine explosions. Technical Report 13045, U.S. Army Tank-Automotive Command, Warren, MI, 1985.

[262] K.J. Badcock. A numerical simulation of boundary layer effects in a shock tube. *International Journal of Numerical Methods in Fluids*, 14:1151–1171, 1992.

[263] R.J. Gooze, P.A. Jacobs, and D.R. Buttsworth. Simulation of a complete reflected shock tunnel showing a vortex mechanism for flow contamination. *Shock Waves*, 15:165–176, 2006.

[264] M. Lamnaouer. *Numerical modeling of the shock tube flow fields before and during ignition delay time experiments at practical conditions.* PhD thesis, University of Central Florida, 2010.

[265] J. Von Neumann and R.D. Richtmyer. A method for the numerical calculation of hydrodynamic shocks. *Journal of Applied Physics*, 21, 1950.

[266] C.W. Hirt, A.A. Amsden, and J.L. Cook. An Arbitrary Lagrangian-Eulerian Computing Method for All Flow Speeds. *Journal of Computational Physics*, 14:227–253, 1972.

[267] W.F. Noh. CEL: a time-dependent, two-space-dimensional coupled Eulerian-Lagrangian code. In *Fundamental Methods in Hydrodynamics*, volume 3 of *Methods in Computational Physics*, pages 117–179. Academic Press, 1964.

[268] John O. Hallquist. LS-Dyna *Theory Manual.* Livermore Software Technology Corporation, 2006.

[269] B. Luccioni, D. Ambrosini, and R. Danesi. Blast load assessment using hydrocodes. *Engineering Structures*, 28:1736–1744, 2005.

[270] Palanivelu Sivakumar. *Energy absorption of crushable tubes for protective structures under static, impact and blast loading.* PhD thesis, Ghent University, 2011.

[271] A. Alia and M. Souli. High explosive simulation using multi-material formulations. *Applied Thermal Engineering*, 26(10):1032–1042, 2006.

[272] D. Kakogiannis, D. Van Hemelrijck, Wastiels, S. J., Palanivelu, W. Van Paepegem, J. Vantomme, A Kotzakolios, and V. Kostopoulos. Assessment of pressure waves generated by explosive loading. *Computer Modelling in Engineering and Structures*, 65(1):75–92, 2010.

[273] G. Toussaint and A. Bouamoul. Comparison of ALE and SPH methods for simulation mine blast effects on structures. Technical report, Defence Research and Development Canada, 2010.

[274] M.B. Liu, D.L. Feng, and Z.M. Guo. Recent developments of SPH in modeling explosion and impact problems. In M. Bischoff, E. Oñate, D.R.J. Owen, E. Ramm, and P. Wriggers, editors, *III International Conference on Particle-Based Methods PARTICLES*, pages 428–435, 2013.

[275] B.M. Dobratz and P.C. Crawford. *LLNL Explosives Handbook: Properties of chemical explosives and explosive simulants*. Lawrence Livermore National Laboratory, 1985.

[276] Y. Huang, M. Willford, and L. Schwer. Validation of LS-Dyna MMALE with blast experiments. In *12th International LS-Dyna Conference*, 2012.

[277] J. Trajkovski, R. Kunc, J. Perenda, and I. Prebil. Minimum mesh design criteria for blast wave development and structural response - MMALE method. *Latin American Journal of Solids and Structures*, 11(11):1999–2017, 2014.

[278] Auburn Manufacturing Company. SAE F-1 Wool Felt (Typical Properties). Technical data sheet.

[279] J. Kuntsche and J. Schneider. Experimental and numerical investigation of the mechanical behavior of explosion resistant glazing. In *Proceedings of engineered transparency*, pages 175–184, Düsseldorf, Germany, 2014.

[280] Livermore Software Technology Corporation. LS-Dyna *keyword user's manual*, 2007.

[281] K. Meguro and H. Tagel-Din. Applied element method for structural analysis: theory and application for linear materials. *Journal of Structural Mechanics in Earthquake Engineering*, 17(1):21–35, 2000.

[282] R. Johns and S.K. Clubley. Post-fracture response of blast loaded monolithic glass. In *ICE Proceedings Structures and Buildings*, page 168, 2015.

[283] H.S. Kim and H.H. Wee. Separation strain for progressive collapse analysis of reinforced concrete building using applied element method. *Construction & Building Technology*, 19(3):437–448, 2016.

Publications

List of scientific publications by Joren Pelfrene.

A1 - Peer reviewed journal publications included in Science Citation Index

1. S. Van Dam, **J. Pelfrene**, S. De Pauw and W. Van Paepegem. Experimental study on the dynamic behaviour of glass fitted with safety window film with a small-scale drop weight set-up. *International Journal of Impact Engineering*, 73:101-111, 2014.

2. **J. Pelfrene**, S. Van Dam and W. Van Paepegem. Numerical analysis of the peel test for characterisation of interfacial debonding in laminated glass. *International Journal of Adhesion and Adhesives*, 62:146-153, 2015.

3. **J. Pelfrene**, J. Kuntsche, S. Van Dam, W. Van Paepegem and J. Schneider. Critical assessment of the post-breakage performance of blast loaded laminated glazing: experiments and simulations. *International Journal of Impact Engineering*, 88:61-71, 2016.

P1 - Publications in conference proceedings included in Science Citation Index

1. **J. Pelfrene**, S. Van Dam, W. Van Paepegem and J. Degrieck. Numerical simulation of elastic, fracture and post-failure response of monolithic and laminated glass under impact loading. In: J. Belis, C. Louter and D. Mocibob, editors, *COST Action TU0905: Mid-term Conference On Structural Glass*, pages 413-420, 2013.

2. S. Van Dam, **J. Pelfrene**, W. Van Paepegem, J. Degrieck, D. Lecompte and J. Vantomme. A new experimental test set-up for investigating im-

pact resistance of laminated glass. In: J. Belis, C. Louter and D. Mocibob, editors, *COST Action TU0905: Mid-term Conference On Structural Glass*, pages 359-366, 2013.

C1 - Publications in conference proceedings

1. S. Van Dam, **J. Pelfrene**. Study on the mechanical response of glass facades under air blast loading. In: J. Belis, editor, *Recent, Current and Near-Future Research on Structural Glass*, pages 39-44, 2012.

2. S. Van Dam, **J. Pelfrene**, K. Spranghers, D. Lecompte and W. Van Paepegem. Digital Image Correlation technique applied to laminated glass plates under free air blast loading. In: *Conference Proceedings of the 21st DYMAT Technical Meeting, High speed imaging for dynamic testing of materials and structures*, pages 43-46, 2013.

3. **J. Pelfrene**, S. Van Dam and W. Van Paepegem. Numerical and experimental study of the peel test for assessment of the glass-PVB interface properties in laminated glass. In: C. Louter, J. Belis, F. Bos and J.P. Lebet, editors, *Challenging Glass 4 & COST Action TU0905 Final Conference*, pages 513-519, 2014.

4. S. Van Dam, **J. Pelfrene**, W. Van Paepegem and D. Lecompte. Mechanical response of laminated glass plates subjected to impact loading. In: C. Louter, J. Belis, F. Bos and J.P. Lebet, editors, *Challenging Glass 4 & COST Action TU0905 Final Conference*, pages 473-480, 2014.

5. **J. Pelfrene**, S. Van Dam, J. Kuntsche and W. Van Paepegem. Numerical simulation of the EN12600 pendulum test for structural glass. In: J. Belis, F. Bos and C. Louter, editors, *Challenging Glass Conference 5*, 2016.

6. **J. Pelfrene**, S. Van Dam and W. Van Paepegem. Fracture simulation of structural glass by element deletion in explicit FEM. In: J. Belis, F. Bos and C. Louter, editors, *Challenging Glass Conference 5*, 2016.

C3 - Conference abstracts

1. **J. Pelfrene**, S. Van Dam and W. Van Paepegem. Simulating dynamic glass fracture in an air blast event. In: *13th UGent FEA Phd Symposium*, 2012.

2. **J. Pelfrene**, S. Van Dam and W. Van Paepegem. Numerical simulation of the 'human impact' pendulum test for structural glass. In: *SIMULIA Benelux User's Meeting*, 2014. **Best academic presentation award.**

3. W. Van Paepegem, L. Daelemans, **J. Pelfrene**, I. De Baere, N. Lammens, G. Chiesura, G. Luyckx, S. Jacques, J. Vanwalleghem and J. Degrieck. Added value of micro-tomography measurements in mechanical characterization of materials: some case studies in engineering applications. In: *2nd UGCT seminar*, Ghent, Belgium, 2015.